CRANFIELD UNIVERSITY

CHONG WANG

HIGH DEPOSITION RATE WIRE BASED ADDITIVE MANUFACTURE OF TI-6AL-4V

SCHOOL OF AEROSPACE, TRANSPORT AND MANUFACTURING
Welding Engineering And Laser Processing Centre

PhD Thesis
Academic Year: 2020 - 2021

Supervisor: Dr. Wojciech Suder
Associate Supervisor: Dr. Jialuo Ding
December 2020

CRANFIELD UNIVERSITY

SCHOOL OF AEROSPACE, TRANSPORT AND MANUFACTURING
Welding Engineering And Laser Processing Centre

PhD Thesis

Academic Year 2020 - 2021

CHONG WANG

High deposition rate wire based additive manufacture of Ti-6Al-4V

Supervisor: Dr. Wojciech Suder
Associate Supervisor: Dr. Jialuo Ding
December 2020

This thesis is submitted in partial fulfilment of the requirements for the degree of Doctor of Philosophy

© Cranfield University 2020. All rights reserved. No part of this publication may be reproduced without the written permission of the copyright owner.

ABSTRACT

Wire + arc additive manufacture (WAAM) is characterised by high deposition rate, short lead-time and relatively low cost, making it suitable for building large-scale metal components. In practical production, high deposition rates are required to reduce the lead-time and overall costs of the components. However, there is a trade-off between the productivity and quality of the deposited components. This is because the fundamental building block of each part, the shape of each individually deposited bead, is dictated by the melt pool dynamics, which is more challenging to control at high heat inputs with any single axisymmetric heat source. Therefore, this thesis undertakes a study of a novel wire based additive manufacture (AM) process, which combines a plasma transferred arc (PTA) and a laser heat sources, aiming to achieve high deposition rates and near-net shape.

First, the limitations of a single PTA deposition process, in terms of the deposition rate and process tolerance were obtained. It was found that the deposition rate can be improved by changing the energy distribution between the wire and the workpiece. This can be done by increasing the wire diameter or changing the position of the wire with respect to the arc column. To enable a further increase of energy input and deposition rate but without increasing the likelihood of keyhole defects formation, a novel configuration of the PTA process with the vertical wire and inclined torch was examined. Although this process is not omnidirectional, it could reduce the likelihood of keyhole formation.

The interaction between the PTA and laser was studied using a finite element (FE) model. This model could predict thermal conditions, such as melt pool geometry, for different process parameters. A wire based PTA-laser hybrid AM process was developed, and the possibility of independent control of deposition rate and bead shape was studied. It has been demonstrated that near-net-shape parts at high deposition rates could be achieved with the PTA-laser hybrid AM. In addition, with the PTA to melt the wire and the laser to control the melt pool size, the deposition rate and bead shape could be controlled independently in the hybrid process. This was then extended to a multi-energy source (MES) approach

with two lasers and a PTA. Despite the increased complexity of such a process, it is easier to control the bead dimensions and thermal cycle independently.

Keywords: Wire + arc additive manufacture (WAAM); Plasma arc-laser hybrid additive manufacture; Metal transfer; Melting efficiency; Keyhole; Bead shape control; Finite element model; Multi-energy source.

ACKNOWLEDGEMENTS

First of all, I would like to thank Welding Engineering and Laser Processing Centre (WELPC) of Cranfield University and China Scholarship Council (No. 201706450041) for funding my research and making my PhD study possible.

I would like to express my deepest gratitude to my supervisors Dr. Wojciech Suder and Dr. Jialuo Ding for their consistent guidance, support and encouragement. Numerous help was received from them in the last three years, without which I could not have a memorable experience like this. Also, their rigorous attitude to research and great patience to people set an example for me.

I am grateful to Professor Stewart Williams, who offered me this position and provided me with numerous helpful advice on my PhD project in the last three years. I also would like to thank Professor Karl Jenkins for chairing my review meetings.

I am thankful to the technicians, Flemming Nielsen, John Thrower, Nisar Shah, from WELPC for helping me set up equipment and solve engineering issues during my study. Also, Steve Pope and Dr. Tracey Roberts, from the metallographic laboratory are much appreciated.

I would like to thank my amazing colleagues, Dr. Sonia Meco, Dr. Goncalo Pardal, Dr. Supriyo Ganguly, Guangyu Chen, Chenglei Diao, Armando Caballero, Leonor Neto, Dr. Eloise Eimer, Dr. Xiangfang Xu, Junny Lai, Dr. Kuladeep Rajamudili, Rongdong Qu, Philippe Bridgeman, Dr. Filomeno Martina, Dr. Yipeng Wang, Shariq Akhtar, Joao Bento, Dr. Gianrocco Marinelli, Anne Fiorucci, Dr. Romali Biswal, Dr. Yongle Sun, Mete Demirorer, Osas Ehigiator, etc. for giving me countless help on both my study and my life, and made me feel like being a part of the big family.

Special gratitude goes to Dr. Xin Chen not only for the full discussions on scientific issues but also for his advice on how to become a good researcher.

Last but not least, I would like to express my gratitude to my family, including my parents and my sister, who always give me their unconditional support. Also, I

would like to thank my beloved girlfriend, Dr. Yu Wan, whose endless love helped me go through the hard times and become a better me.

TABLE OF CONTENTS

ABSTRACT i
ACKNOWLEDGEMENTS iii
LIST OF FIGURES ix
LIST OF TABLES xvii
LIST OF EQUATIONS xviii
LIST OF ABBREVIATIONS xx
NOMENCLATURE xxi
1 Introduction 1
1.1 Research background 1
1.2 Aim and objectives 5
1.3 Thesis structure 5
1.4 References 12
2 Literature review 13
2.1 Additive manufacture 13
2.1.1 Introduction 13
2.1.2 Classification of metal AM processes 14
2.1.3 High deposition rate AM processes 16
2.2 Fundamentals of plasma arc and laser 20
2.2.1 Plasma arc 20
2.2.2 Laser 22
2.3 Thermal efficiencies 27
2.3.1 Energy transfer efficiency 27
2.3.2 Melting efficiency 29
2.3.3 Process efficiency 30
2.4 Bead shape control 30
2.5 Research gap 35
2.6 Summary 35
2.7 References 36
3 Understanding the limitations of a single axisymmetric heat source – PTA 45
3.1 The effect of wire size on high deposition rate wire and plasma arc additive manufacture of Ti-6Al-4V 45
3.1.1 Introduction 46
3.1.2 Experimental procedure 48
3.1.2.1 Materials and setup 48
3.1.2.2 Methods 50
3.1.3 Results and discussion 52
3.1.3.1 Limitation of deposition rate 52
3.1.3.2 The effect of wire size on bead shape 56
3.1.3.3 Keyhole behaviour 59
3.1.3.4 Wire feeding position 63

3.1.4 Conclusions 67
3.1.5 Acknowledgement 68
3.1.6 References 68
3.2 Process characteristics of wire and plasma arc additive manufacture with a vertical wire feed 71
3.2.1 Introduction 72
3.2.2 Experimental procedure 75
3.2.2.1 Materials and setup 75
3.2.2.2 Methods 75
3.2.3 Results and discussion 78
3.2.3.1 Effect of travel direction on bead shape 78
3.2.3.2 Comparison with the traditional process 80
3.2.3.2.1 Keyhole behaviour 80
3.2.3.2.2 Deposition rate 81
3.2.3.3 Metal transfer behaviour 83
3.2.3.3.1 Effect of WFS 83
3.2.3.3.2 Effect of current 85
3.2.3.3.3 Effect of plasma gas flowrate 86
3.2.3.3.4 Forces acting on droplets 87
3.2.4 Conclusions 91
3.2.5 Acknowledgement 92
3.2.6 References 92
4 The interaction between the PTA and laser 97
4.1 Finite element analysis of thermal behaviour in hybrid plasma arc-laser melting of Ti-6Al-4V 97
4.1.1 Introduction 98
4.1.2 Experimental procedure 101
4.1.2.1 Materials and setup 101
4.1.2.2 Methods 102
4.1.3 Finite element model 103
4.1.3.1 Geometrical model and FE mesh 103
4.1.3.2 Heat source model 104
4.1.3.3 Boundary and initial conditions 105
4.1.3.4 Material properties 105
4.1.3.5 Model calibration 106
4.1.4 Results and discussion 109
4.1.4.1 Model validation 109
4.1.4.2 Melt pool geometry 110
4.1.4.3 Cooling rate and solidification parameters 116
4.1.4.3.1 Cooling rate 117
4.1.4.3.2 Solidification parameters 119
4.1.5 Conclusions 122

4.1.6 Acknowledgement 123
4.1.7 References 123
5 Wire based PTA-laser hybrid additive manufacture 129
5.1 Wire based plasma arc and laser hybrid additive manufacture of Ti-6Al-4V 129
5.1.1 Introduction 130
5.1.2 Experimental procedure 132
5.1.2.1 Materials and setup 132
5.1.2.2 Methods 134
5.1.2.2.1 Processing conditions in the hybrid process 134
5.1.2.2.2 Deposition rate in different AM processes 136
5.1.2.2.3 Tolerance of WLAM 138
5.1.2.2.4 Limitation of WAAM 138
5.1.2.2.5 Multi-layer wall building 139
5.1.2.2.6 Multi-energy source deposition 140
5.1.3 Results and discussion 142
5.1.3.1 Processing conditions of the hybrid AM 142
5.1.3.1.1 Configuration 142
5.1.3.1.2 Wire feeding position 143
5.1.3.1.3 Arc-laser separation distance 145
5.1.3.2 Benefits of the hybrid process 147
5.1.3.2.1 Deposition rate 147
5.1.3.2.2 Tolerance of WLAM 152
5.1.3.2.3 Limitation of WAAM 152
5.1.3.3 Multi-layer wall building 155
5.1.3.4 Multi-energy source deposition 156
5.1.4 Conclusions 157
5.1.5 Acknowledgement 158
5.1.6 References 159
5.2 Bead shape control in wire based plasma arc and laser hybrid additive manufacture of Ti-6Al-4V 162
5.2.1 Introduction 163
5.2.2 Experimental procedure 165
5.2.2.1 Materials and setup 165
5.2.2.2 Methods 167
5.2.3 Results and discussion 170
5.2.3.1 Different process parameters on bead shape 170
5.2.3.1.1 Effect of laser power 170
5.2.3.1.2 Effect of ratio of arc power to laser power 171
5.2.3.1.3 Effect of wire feed speed 173
5.2.3.1.4 Effect of travel speed 174
5.2.3.1.5 Effect of laser beam size 176

5.2.3.2 Procedure for bead shape control 179
5.2.3.3 Multi-layer single-pass walls 182
5.2.4 Conclusions 183
5.2.5 Acknowledgement 184
5.2.6 References 185
6 Summary, Conclusions, and Future work 187
6.1 Summary 187
6.2 Conclusions 190
6.3 Future work 192
6.3.1 FE modelling 192
6.3.2 Wire preheating for higher deposition rate 192
6.3.3 Multi-energy source 193
6.3.4 Mechanical properties and microstructure 193

LIST OF FIGURES

Figure 1-1 Example of large-scale parts built by WAAM: (a) a pressure vessel made in Ti-6Al-4V for space application (1 m in height), and (b) a rear frame also made in Ti-6Al-4V for an aircraft (2.5 m × 1.5 m in the planar area). Image credit: Cranfield University. 2

Figure 1-2 Cost as a function of the deposition rate in WAAM. Curves are plotted for different machine costs [1]. 3

Figure 1-3 Titanium parts built by PTA deposition process: (a) a relatively low deposition rate with high surface finish (image credit: Cranfield University), and (b) a high deposition rate with low surface finish (image credit: Norsk Titanium). 4

Figure 1-4 Outline of research methodology. 11

Figure 2-1 Classification of metal AM processes based on the heat source, feedstock form and delivered way of the material. 14

Figure 2-2 PTA based WAAM system with dual plasma torch (image credit: Norsk Titanium). 17

Figure 2-3 (a) Experimental setup for GMA based WAAM process with a tandem torch, and (b) single-pass walls deposited at different WFSs with the process. Images are adapted from Ref. [27]. 18

Figure 2-4 (a) Schematic shows the configuration of the WAAM process with GMA torch and external cold wire, and (b) cross-section of the part built by the process. Images are adapted from Ref. [28]. 19

Figure 2-5 (a) Schematic shows the configuration of the PTA deposition process with dual wire, and (b) cross-section of the part built by the process. Images are adapted from Ref. [29]. 19

Figure 2-6 (a) The EBAM system developed by Sciaky, and (b) the part deposited by the EBAM process (Image credit: Sciaky). 20

Figure 2-7 Schematic of a plasma torch showing the components and working principle. 21

Figure 2-8 Cross-sectional profiles obtained with conduction and keyhole regimes in autogenous laser welding processes [41]. 23

Figure 2-9 Spatters occur during the laser welding process in keyhole regime [47]. 24

Figure 2-10 Laser absorptivity of different materials as a function of wavelength [40]. 25

Figure 2-11 Laser absorptivity of different materials as a function of temperature for two different lasers: (a) fibre laser with 1.07 μm beam, and (b) CO_2 laser with 10.7 μm beam. Images are adapted from Ref. [52]. 25

Figure 2-12 Laser absorptivity as a function of power density [54]. 26

Figure 2-13 Process map of laser applications based on interaction time and power density [55]. 26

Figure 2-14 Schematic shows the applied power of a power source ($\boldsymbol{Pa}$), power transferred to the workpiece ($\boldsymbol{Pt}$), power for the generation of melt pool ($\boldsymbol{Pm}$), and power lost through workpiece ($\boldsymbol{Pw}$). 28

Figure 2-15 Temperature and velocity field during PTA based deposition process of Ti-6Al-4V on the (a) longitudinal cross-section, and (b) transverse cross-section at x=26 mm. Red arrow indicates the torch travel direction. Images are adapted from Ref. [37]. 32

Figure 2-16 Temperature and velocity field during laser based deposition process of maraging steel; (a) longitudinal cross-section, and (b) transverse cross-section. Images are adapted from Ref. [72]. 33

Figure 2-17 Penetration depth as a function of WFS (i.e. deposition rate) for different TSs [73]. 34

Figure 3-1 Schematic diagram showing the experimental setup. 50

Figure 3-2 Wire feeding position in PTA-based deposition process (side view). 51

Figure 3-3 Comparison between (a) a stable deposition process at a WFS of 5.4 m/min, and (b) an unstable deposition process at a WFS of 6.0 m/min. 52

Figure 3-4 Effect of wire size and current on maximum WFS. 53

Figure 3-5 Effect of wire size and current on the limitation of deposition rate. . 54

Figure 3-6 Diagram (top view) showing the projected areas of wires with different diameters under the PTA: (a) 1.2 mm and (b) 2.4 mm. 54

Figure 3-7 The temperature contours of (a) 1.2 mm wire, and (b) 2.4 mm wire in the FE modelling. 55

Figure 3-8 (a) Schematic representation of deposition efficiency; (b) a high surface waviness and low deposition efficiency obtained with the bead with low aspect ratio, and (c) a low surface waviness and high deposition efficiency obtained with the bead with high aspect ratio. 57

Figure 3-9 Bead dimensions as a function of deposition rate for 1.2 and 2.4 mm wires: (a) bead width, and (b) bead height. 58

Figure 3-10 Cross-section of the beads at different deposition rates obtained with (a) 1.2 mm wire, and (b) 2.4 mm wire at the current of 250 A. 59

Figure 3-11 Bead shape changes with the increasing WFS during the deposition of 1.2 mm wire at 250 A: (a) bead width increases as the WFS increases from 3 to 5 m/min, and (b) bead width decreases as the WFS increases from 5 to 7 m/min. The pink arrows indicate the torch travel direction. 59

Figure 3-12 Keyhole appearance with (a) a stationary and (b) a moving plasma torch..... 60

Figure 3-13 Cross-section of the samples with different currents and nozzle diameters: (a) 3.0 mm nozzle, and (b) 3.9 mm nozzle. The plasma torch was stationary. 61

Figure 3-14 Appearance of the samples obtained with different currents and nozzle diameters: (a) 3.0 mm nozzle, and (b) 3.9 mm nozzle. The torch travel speed was 9.0 mm/s in these cases. 62

Figure 3-15 Effect of wire size on keyhole formation at 300 A for the following wire diameters: (a) 1.2 mm, (b) 1.6 mm, (c) 2.0 mm, and (d) 2.4 mm. 63

Figure 3-16 Deposition process with different wire feeding positions at the WFS of (a) 3.2 m/min (deposition rate: 0.98 kg/h), and (b) 4.4 m/min (deposition rate: 1.35 kg/h) with a 1.2 mm wire. Bead width and metal transfer mode as a function of *h*: (c) WFS=3.2 m/min, (d) WFS=4.4 m/min. 64

Figure 3-17 Deposition process with different wire feeding positions at the WFS of (a) 0.8 m/min (deposition rate: 0.98 kg/h), and (b) 1.1 m/min (deposition rate: 1.35 kg/h) with a 2.4 mm wire. Bead width and metal transfer mode as a function of *h*: (c) WFS=0.8 m/min, (d) WFS=1.1 m/min. 65

Figure 3-18 Experimental setup for the PTA-based WAAM system with a vertical wire and inclined torch. 75

Figure 3-19 Schematic showing the definition of different parameters for the deposition process. 76

Figure 3-20 Deposition processes at different travel directions (indicated by the pink arrows): (a) torch leading, (b) torch on the side, and (c) torch trailing. 79

Figure 3-21 Cross-section of the beads obtained with different travel directions: (a) torch leading, (b) torch on the side, and (c) torch trailing. 79

Figure 3-22 Comparison of the deposition processes between the (a) new process and (b) traditional process. 81

Figure 3-23 Deposition processes at different torch angles: (a) 60°, (b) 45°, and (c) 30°. 82

Figure 3-24 Maximum wire feeding rates obtained with the new and traditional processes at the same current of 200 A. 83

Figure 3-25 Droplet transfer and voltage waveform at different WFSs: (a) 2.5 m/min, (b) 3.0 m/min, and (c) 3.5 m/min. 84

Figure 3-26 Droplet transfer at different levels of current: (a) 160 A, (b) 180 A, and (c) 200 A. 85

Figure 3-27 Droplet transfer with different plasma gas flowrates: (a) 0.6 L/min, (b) 0.7 L/min, and (c) 0.8 L/min. 86

Figure 3-28 Forces acting on a droplet in (a) the traditional PTA deposition process, and (b) the new PTA deposition process. 88

Figure 3-29 Bead appearance as a function of different process parameters: (a) WFS, (b) current, and (c) plasma gas flowrate. All parameters used in each case can be seen in Table 3-5..... 89

Figure 3-30 The (a) deposition process and (b) bead appearance obtained with the traditional process at a current of 200 A, WFS of 2.5 m/min, and plasma gas flowrate of 0.8 L/min..... 90

Figure 4-1 (a) Experimental setup for the hybrid PTA-laser system, and (b) the configuration inside the tent..... 101

Figure 4-2 Geometry and mesh used in the FE model..... 104

Figure 4-3 The melt pool obtained with (a) FE model, and (b) experiment. The yellow arrows indicate the travel direction. 107

Figure 4-4 Comparison between simulation and experimental results: (a) melt pool at cross-section, (b) HAZ at cross-section, (c) melt pool at top surface, and (d) thermal cycle. 108

Figure 4-5 Comparison of melt pool and HAZ between simulation and experiment with different process parameters (Cases 2 to 5 in Table 4-2): (a) melt pool at cross-section, (b) HAZ at cross-section, and (c) melt pool form top view. 109

Figure 4-6 The effect of laser power on the melt pool dimensions (all the process parameters used except laser power are the same as those of Case 1 in Table 4-2). 111

Figure 4-7 The effect of laser power on the melt pool geometry from different views: (a) top surface, (b) longitudinal section, and (c) cross-section..... 111

Figure 4-8 The effect of travel speed on the melt pool dimensions (all the process parameters used except travel speed are the same as those of Case 1 in Table 4-2). 112

Figure 4-9 The effect of travel speed on the melt pool geometry from different views: (a) top surface, (b) longitudinal section, and (c) cross-section..... 112

Figure 4-10 The effect of the separation distance between the PTA and laser on the melt pool dimensions (all the process parameters used except separation distance are the same as those of Case 1 in Table 4-2). 113

Figure 4-11 The effect of arc-laser separation distance on the melt pool geometry from different views: (a) top view, (b) longitudinal section, and (c) cross-section. 114

Figure 4-12 The effect of the laser beam diameter on the melt pool dimensions (all the process parameters used except laser beam diameter are the same as those of Case 1 in Table 4-2)..... 115

Figure 4-13 The melt pool geometry obtained with the laser beam diameters of 4 and 12 mm from different views: (a) top view, (b) longitudinal section, and (c) cross-section. 115

Figure 4-14 The thermal cycle as a function of different process parameters: (a) laser power, (b) travel speed, (c) separation distance, and (d) laser beam diameter..... 118

Figure 4-15 The effect of (a) laser power, and (b) travel speed on cooling rate. 118

Figure 4-16 The effect of laser power on solidification rate (travel speed was kept fixed), and the effect of travel speed on solidification rate (laser power was kept fixed). 120

Figure 4-17 Melt pool contour including the solidification front and the angle $\boldsymbol{\theta}$. 120

Figure 4-18 The effect of laser power on thermal gradient (travel speed was kept fixed), and the effect of travel speed on thermal gradient (laser power was kept fixed). 121

Figure 5-1 (a) Experimental setup for PTA-laser hybrid AM system, and (b) view from inside of the tent, which is indicated by a red dashed square in (a). 134

Figure 5-2 Different configurations and travel directions (indicated by pink arrows) used: (a) the wire is first irradiated by the PTA, and (b) the wire is first irradiated by the laser. 135

Figure 5-3 Illustration of the definition of d_1 and d_2..... 136

Figure 5-4 Measured output power of PTA as a function of applied current... 137

Figure 5-5 Schematic diagram showing the deposited bead with a cross-sectional area of $\boldsymbol{Ab}$ and remelting area of $\boldsymbol{Ar}$. 139

Figure 5-6 Schematic shows (a) the configuration of MES with one PTA and two separate lasers, and (b) the relative position of the three energy sources. Pink arrows indicate the travel direction. 141

Figure 5-7 The effect of wire orientation and leading source on the deposition process and bead appearance for 7 kW laser and 200 A current: (a) wire melted by the PTA, and (b) wire melted by the laser. (c) and (d) show the bead appearance obtained with (a) and (b) respectively. Pink arrows indicate the travel direction. 142

Figure 5-8 The effect of wire feeding direction on the hybrid deposition process: (a) back feeding, and (b) front feeding. The laser power used in both cases was 3 kW. 143

Figure 5-9 The effect of wire-workpiece distance on the deposition process: (a) d_1=0, (b) d_1=1 mm, (c) d_1=2 mm, (d) d_1=3 mm, and (e) d_1=4 mm..... 144

Figure 5-10 (a) Bead appearance and (b) bead width obtained with different wire-workpiece distances: (a1) d_1=0, (a2) d_1=1 mm, (a3) d_1=2 mm, (a4) d_1=3 mm, and (a5) d_1=4 mm. 145

Figure 5-11 The effect of arc-laser separation distance on the deposition process: (a) d_2=10 mm, (b) d_2=12 mm, (c) d_2=14 mm, (d) d_2=16 mm, and (e) d_2=18 mm..... 145

Figure 5-12 The effect of arc-laser separation distance on (a) bead appearance, and (b) bead width. The pink arrow indicates the deposition direction. ... 146

Figure 5-13 Comparison of maximum deposition rates obtained with a single laser and a single PTA processes. 148

Figure 5-14 Schematic shows the wire under a single power source (PTA or laser). Blue arrow indicates wire feeding direction. 148

Figure 5-15 The deposition processes with the power source of (a) PTA, and (b) laser, at the same applied power of 6 kW. 149

Figure 5-16 Comparison of maximum deposition rates obtained with the hybrid process, PTA only process, and laser only process with a total power input of 8 kW in each case. 149

Figure 5-17 Hybrid and PTA only deposition process with a total power input of 8 kW: (a) 2 kW arc and 6 kW laser, (b) 4 kW arc and 4 kW laser, (c) 6 kW arc and 2 kW laser, and (d) 8 kW arc. Yellow dashed line indicates the melt pool boundary..... 150

Figure 5-18 Schematic shows the positions of the wire in (a) the hybrid PTA-laser process, and (b) single PTA process. 151

Figure 5-19 Tolerance of WLAM to wire-workpiece distance: (a) d_1=0, (b) d_1=1 mm, (c) d_1=2 mm, (d) d_1=3 mm, and (e) d_1=4 mm. 152

Figure 5-20 The effect of current on keyhole formation: (a) bead with a good appearance at 205 A, and (b) bead with defects at 283 A. 153

Figure 5-21 (a) Deposition rate and (b) bead appearance at different applied powers obtained with WAAM and hybrid processes. 154

Figure 5-22 The cross-sections of the multi-layer single-pass walls with different WFSs show good surface finish: (a) wall 1: 4 m/min, (b) wall 2: 6 m/min, and (c) wall 3: 8 m/min. The parameters used are shown in Table 5-2. 155

Figure 5-23 The deposition process with (a) one PTA (200 A) and one laser (3 kW), and (b) one PTA (200 A) and two lasers (1.5 kW for each laser). (c) and (d) shows the cross-section of the deposited beads obtained with (a) and (b) respectively..... 157

Figure 5-24 Experimental setup for the wire based PTA-laser hybrid AM system. 166

Figure 5-25 Configuration for the wire based PTA-laser hybrid deposition process (side view). 167

Figure 5-26 Schematic diagram of the cross-section showing the bead width and bead height. 168

Figure 5-27 The effect of laser power on (a) deposition process, and (b) bead shape with a constant arc power of 4.8 kW. 170

Figure 5-28 The effect of laser power on (a) bead width, and (b) bead height. All the parameters used are shown in Cases (1-5) of Table 5-5. 171

Figure 5-29 The deposition processes with different ratios of arc power to laser power at a constant total applied power of 8 kW. Red arrows indicate the laser positions. 172

Figure 5-30 The effect of the ratio of arc power to laser power on (a) bead width, and (b) bead height. All the parameters used are shown in Cases (6-11) of Table 5-5. 173

Figure 5-31 The hybrid deposition processes at different WFSs: (a) 2 m/min, (b) 3 m/min, (c) 4 m/min, (d) 5 m/min, and (e) 6 m/min. Red arrows indicate the laser positions. 173

Figure 5-32 The effect of WFS on (a) bead width, and (b) bead height. All the parameters used are shown in Cases (12-16) of Table 5-5. 174

Figure 5-33 Hybrid deposition processes at different TSs: (a) 4 mm/s, (b) 6 mm/s, (c) 8 mm/s, (d) 10 mm/s, and (e) 12 mm/s. Pink arrow indicates the travel direction whilst the red arrows indicate the laser positions. 175

Figure 5-34 The effect of TS on (a) bead width, and (b) bead height. All the parameters used are shown in Cases (17-21) of Table 5-5. 176

Figure 5-35 The effect of laser beam size on bead width at an arc power of 4.8 kW and laser power of 5 kW. All the parameters used are shown in Cases (23-27) of Table 5-5. 177

Figure 5-36 The cross-section of the beads obtained with different laser beam diameters: (a) 4 mm, (b) 6 mm, (c) 8 mm, (d) 10 mm, and (e) 12 mm. 178

Figure 5-37 The effect of laser beam size on bead width at different laser powers. 178

Figure 5-38 The effect of laser beam size on the deposition process and bead appearance at a constant laser power of 5 kW and arc power of 4.8 kW. Note, LBD stands for laser beam diameter. 179

Figure 5-39 Procedure for bead shape control in wire based PTA-laser hybrid AM process. Note: BW and BH stand for bead width and bead height, respectively. 181

Figure 5-40 Two single-pass multi-layer walls with the same width but different deposition rates: (a) Wall 1 and (b) its cross-section at a deposition rate of 1.2 kg/h, and (c) Wall 2 and (d) its cross-section at a deposition rate of 1.8 kg/h..... 183

LIST OF TABLES

Table 1-1 Thesis structure, status of paper submissions, and key conclusions of each paper..... 9

Table 3-1 Chemical composition (in wt.%) of the Ti-6Al-4V substrate and wire. 49

Table 3-2 Fixed process parameters used during the experiments..... 50

Table 3-3 Fixed parameters used in all experiments..... 76

Table 3-4 Parameters used for the study of travel direction effect. 77

Table 3-5 Parameters used for the metal transfer behaviour study..... 78

Table 4-1 Fixed parameters used during the experiments. 102

Table 4-2 Parameters used in the experiments for calibration and validation of the FE model. 103

Table 4-3 The dimensions of melt pool and HAZ obtained with experiment and FE model. 108

Table 5-1 Fixed process parameters used during the experiments..... 136

Table 5-2 Process parameters used for deposition of the multi-layer single-pass walls..... 140

Table 5-3 Process parameters used for the standard PTA-laser hybrid process and MES deposition process. 141

Table 5-4 Geometric properties of the multi-layer single-pass walls..... 156

Table 5-5 Process parameters used to study the effect of each parameters on the bead shape..... 169

Table 5-6 Process parameters used for the deposition of multi-layer single-pass walls..... 182

Table 5-7 Features of the two multi-layer single-pass walls. 183

LIST OF EQUATIONS

(2-1)..... 28
(2-2)..... 29
(2-3)..... 29
(2-4)..... 29
(2-5)..... 29
(2-6)..... 30
(3-1)..... 53
(3-2)..... 56
(3-3)..... 59
(3-4)..... 80
(3-5)..... 87
(4-1)..... 104
(4-2)..... 104
(4-3)..... 104
(4-4)..... 105
(4-5)..... 105
(4-6)..... 105
(4-7)..... 111
(4-8)..... 119
(4-9)..... 120
(5-1)..... 136
(5-2)..... 137
(5-3)..... 138
(5-4)..... 138
(5-5)..... 140
(5-6)..... 147
(5-7)..... 147
(5-8)..... 147

(5-9)..... 175
(5-10)..... 175
(5-11)..... 177
(5-12)..... 177
(5-13)..... 180

LIST OF ABBREVIATIONS

2D	Two Dimensional
3D	Three Dimensional
AM	Additive Manufacture
BTF	Buy To Fly
CAD	Computer Aided Design
CET	Columnar to Equiaxied Transition
CFD	Computational Fluid Dynamics
CMT	Cold Metal Transfer
CNC	Computer Numerical Control
DED	Directed Energy Deposition
DoE	Design of Experiment
EBAM	Electron Beam Additive Manufacture
EBF^3	Electron Beam Freeform Fabrication
EBM	Electron Beam Melting
FE	Finite Element
GMA	Gas Metal Arc
GTA	Gas Tungsten Arc
HAZ	Heat Affected Zone
LMD	Laser Metal Deposition
MES	Multiple Energy Source
PBF	Powder Bed Fusion
PTA	Plasma Transferred Arc
SLM	Selective Laser Melting
TS	Travel Speed
WAAM	Wire + Arc Additive Manufacture
WFS	Wire Feed Speed
WLAM	Wire + Laser Additive Manufacture

NOMENCLATURE

A_b	Cross-sectional area of bead
A_r	Remelting area
A_w	Cross-sectional area of wire
d	The distance between wire and copper nozzle in PTA process
d_1	The distance between wire tip and workpiece in PTA-laser hybrid process
d_2	Separation distance between laser and PTA
d_l	Laser beam diameter
d_w	Wire diameter
D	Power source beam diameter
E	Power density
f	Mass flow rate per area
F	The resultant force acting on a droplet in vertical direction
F_a	Plasma drag force
F_{em}	Electromagnetic force
F_g	Gravitational force
F_p	Driving force of the wire
F_v	Vapour jet force
F_σ	Surface tension
G_0	Thermal gradient
h	The distance between wire tip and workpiece in PTA process
I	Arc current
k	Thermal conductivity
k_{xx}	The component of thermal conductivity in X direction
k_{yy}	The component of thermal conductivity in Y direction
k_{zz}	The component of thermal conductivity in Z direction
M_1	The melting efficiency for welds with two-dimensional flow
M_2	The melting efficiency for welds with three-dimensional flow

n	The unit outward normal vector
p	The total arc pressure
p_e	The arc pressure caused by electromagnetic force
p_g	The arc pressure caused by plasma gas flow
p_n	The arc pressure normal to the workpiece
P	Power absorbed per unit length by wire
P_a	The total applied power
P_e	The power lost to the environment
P_l	Laser power
P_m	The power for the generation of melt pool
P_o	Output power
P_t	The power transferred to the workpiece
P_w	The power lost through workpiece
q	The heat flux received by the surface
Q	Heat input
Q_a	Heat input of the PTA
Q_l	Heat input of the laser
r	The radial distance from a given point to the heat source centre
r_0	The effective radius of the region where 95% of the heat flux is applied
r_1	The radius of arc at the workpiece
r_2	The radius of arc at the electrode
R	Deposition rate
R_0	Solidification rate
t	Time
t_i	Interaction time
T_0	Initial temperature
T_s	Solidus
T_t	Beta transus temperature
u_z	Flow velocity of the plasma gas
U	Arc voltage

v_t	Travel speed
v_w	Wire feed speed
Y	Dimensionless parameter
α	Torch angle
Λ	Line energy
τ	Thermal diffusivity at 300 K
μ	Convection coefficient
μ_0	Magnetic permeability
ε	Deposition efficiency
ε_0	Emissivity coefficient
σ	Stefan-Boltzmann constant
ρ	Material density
ρ_w	The density of wire
ρ_g	The density of plasma gas
η	Process efficiency
η_1	Energy transfer efficiency
η_2	Melting efficiency
η_a	Arc efficiency
η_l	Laser absorptivity
δh	The enthalpy change to melt
ν	Kinematic viscosity at the melting point
θ	The angle between travel direction and the tangential direction at a location on the solidification front
$\frac{\partial T}{\partial t}$	Cooling rate

1 Introduction

1.1 Research background

Additive manufacture (AM), or commonly referred to as 3D printing, has developed rapidly in the last few decades and shows great advantages over traditional manufacture methods. For example, compared to subtractive manufacture methods, such as machining, AM helps reduce a large amount of material wastage. Compared to formative manufacture methods, such as forging and casting, AM does not need dies or moulds and therefore saves the costs. In addition, it offers shorter production lead-time and higher design flexibility. In fact, all the metal AM processes share the same principle, which is using a heat source to melt the feedstock and thus to deposit components upon layer-by-layer manner. The movement in AM is provided by a computer numerical controlled (CNC) gantry system or a robot. AM can be used to deposit almost all commonly-used metallic materials, but it is particularly beneficial to fabricate the materials that are expensive and difficult to process with traditional processing routes. Ti-6Al-4V is an excellent example, as one of the most extensively used materials in the aerospace industry, that benefits significantly from the advantages of AM due to its poor machinability and high material cost.

There are numerous variants of metal AM. Depending on the feedstock, they can be classified into powder based processes and wire based processes, whilst depending on the heat source, they can be divided into laser, electron beam, and electric arc based processes. Amongst these processes, wire + arc additive manufacture (WAAM) is characterised by a high deposition rate and a relatively low equipment cost, making it one of the most cost-effective processes to build large engineering components (metres in scale) with low to medium complexity. There are many large-scale components deposited successfully by WAAM, demonstrating the high capability of the process. Figure 1-1 shows two examples built using WAAM for the aerospace sector at Cranfield University. A titanium pressure vessel having a weight of 8.5 kg built by WAAM is shown in Figure 1-1a, which saved more than 200 kg of raw material compared to the traditional

manufacturing by forging and machining. The lead time was cut significantly from several months to a few days. Similarly, a titanium rear frame for an aircraft built by WAAM is shown in Figure 1-1b, which also saved significant material and lead time (from year to month).

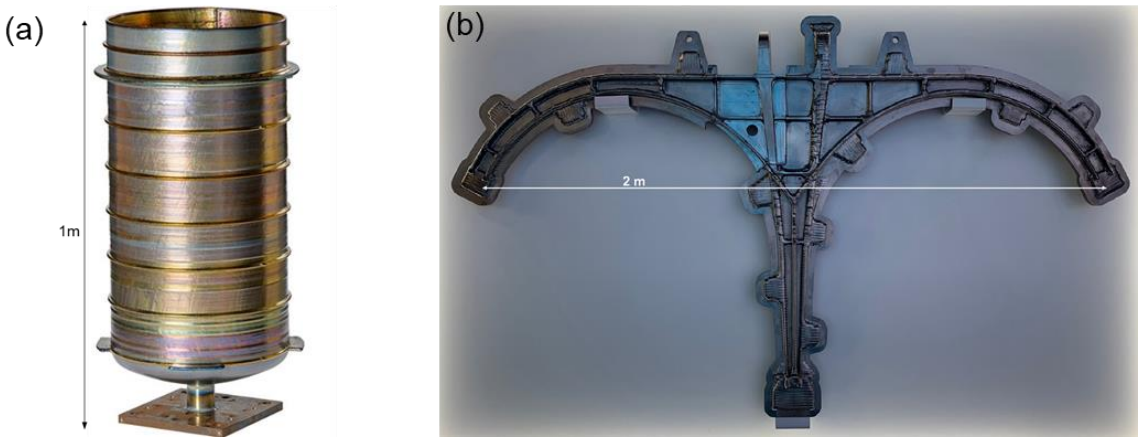


Figure 1-1 Example of large-scale parts built by WAAM: (a) a pressure vessel made in Ti-6Al-4V for space application (1 m in height), and (b) a rear frame also made in Ti-6Al-4V for an aircraft (2.5 m × 1.5 m in the planar area). Image credit: Cranfield University.

In WAAM, an electric arc, such as gas metal arc (GMA), gas tungsten arc (GTA), and plasma transferred arc (PTA) can be used as the heat source. Amongst these, PTA-based WAAM exhibits more benefits than the other two processes when depositing titanium, as it does not have arc wandering issues compared to the GMA process and has much higher process tolerance than the GTA process. Normally, the deposition rates for titanium are 0.4-1.2 kg/h when using a single PTA heat source. Higher deposition rates are required in practical production to reduce the lead time and overall costs. For example, landing gear of an average-size aircraft is around 2 t, and with regular deposition rate it would take 2000 hours to build it. To make the process viable for large aerospace components like this, the deposition rate should be increased by a factor of 10. Also, Figure 1-2 shows the cost of titanium parts built by WAAM as a function of the deposition rate. It can be seen that the cost will be reduced by increasing the deposition rate.

Specifically, at a machine cost of £0.18M, the cost can be halved by increasing the deposition rate from 1 to 4 kg/h.

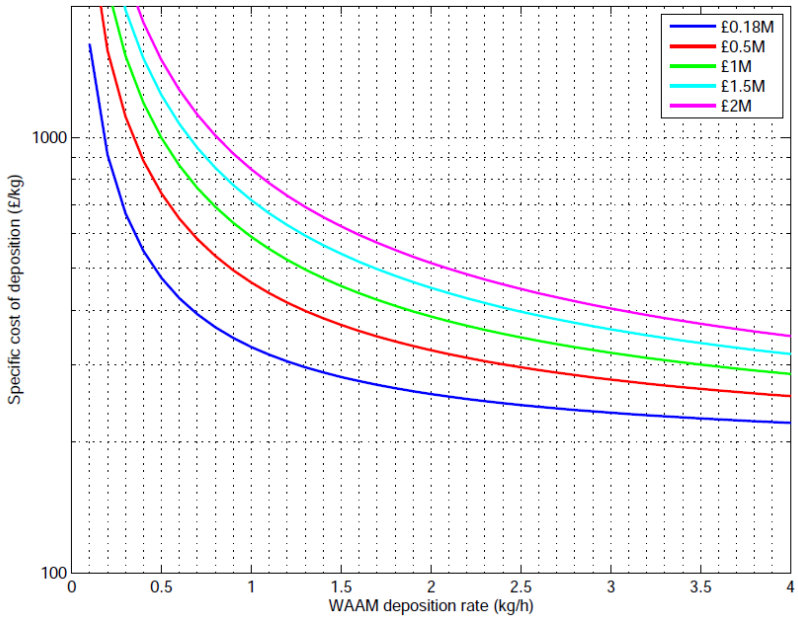


Figure 1-2 Cost as a function of the deposition rate in WAAM. Curves are plotted for different machine costs [1].

However, there is a trade-off between the deposition rate and surface quality, meaning that higher deposition rate can be achieved but at the cost of lower surface finish and geometric accuracy. This is because the surface finish and geometric accuracy are dictated by the process stability and the melt pool behaviour, which are more difficult to control at higher deposition rates. As shown in Figure 1-3, two titanium components were built with the PTA deposition process, of which the first one that exhibits smooth surface and high geometric accuracy was deposited at a regular deposition rate of 1 kg/h (Figure 1-3a), whilst the second one with rough surface and relatively low geometric accuracy was deposited at a high deposition rate of 5 kg/h (Figure 1-3b). The second approach allows shorter deposition time which can be translated into shorter duty cycle and lower cost. However, the lower surface quality requires extra material to be deposited to compensate for any dimensional inaccuracies, which at certain point offsets the benefits of higher deposition rate. In addition, this additional material needs to be machined off, which increases material waste and machining cost

and time. Therefore, ideally, the deposition rate needs to be improved without compromising the accuracy of the deposited components.

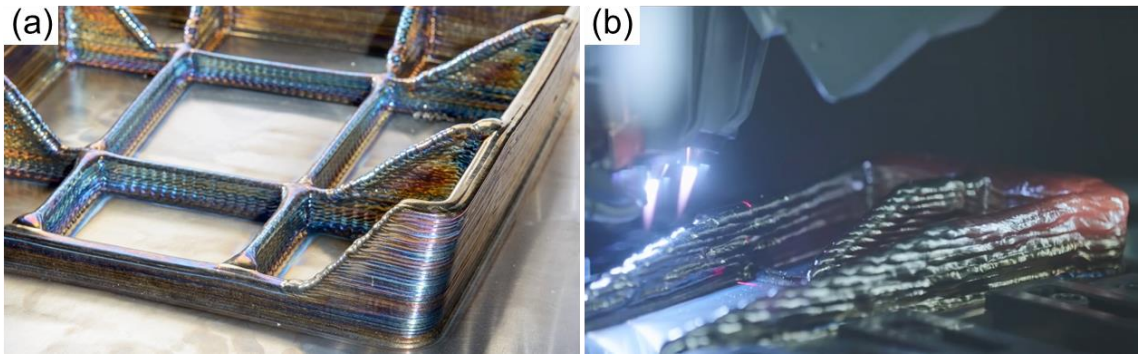


Figure 1-3 Titanium parts built by PTA deposition process: (a) a relatively low deposition rate with high surface finish (image credit: Cranfield University), and (b) a high deposition rate with low surface finish (image credit: Norsk Titanium).

To date, most wire based AM processes use standard axisymmetric heat sources (e.g. laser, arc), which were designed for welding or other applications. With such heat sources, it is hard to satisfy all requirements for AM applications, such as efficient melting of feedstock material, low magnitude of convective flow, and accurate control of bead shape with right thermal cycle. Hence, most wire based AM processes are optimised for one of these requirements based on engineering optimisation. In this work, a new approach with multi-heat source is applied. All aspects of feedstock melting and melt pool control are understood to develop a new science-based process optimised for AM application.

First, the limitations of the single PTA and its interaction with feedstock were investigated. Aspects such as most optimum wire diameter, the position of wire with respect to the arc column, and distribution of energy between wire and workpiece on the melting efficiency and deposition rate were investigated. Then, the ability of a laser source to tailor its energy to the required conditions by independent control of spot size and applied power was investigated. The thesis presents results on process fundamental based on instrumented experiments, numerical modelling, and analysis of built demonstrators. The process shows high flexibility and capability of independent control of deposition rate and melt

pool shape required for the achievement of near-net-shape components at high deposition rates.

1.2 Aim and objectives

The overall aim of this research is to investigate the capability of a wire based PTA-laser hybrid process for deposition of near-net-shape Ti-6Al-4V parts at a high deposition rate of 4 kg/h. There are seven individual objectives, which are listed below.

1. To understand the limits in terms of deposition rate and process tolerance of single PTA process.
2. To understand the effect of processing conditions on the efficiency of feedstock melting and deposition rate.
3. To evaluate the process tolerance and deposition rate of a novel PTA process with the vertical wire and inclined torch.
4. To understand forces responsible for the control of melt pool shape and resulting surface waviness of deposited components.
5. To understand the interaction between the PTA and laser as a function of different process parameters.
6. To develop a wire based PTA-laser hybrid process with independent control of bead shape and deposition rate.
7. To develop a process control algorithm for the achievement of various bead dimensions required for printing of complex parts.

1.3 Thesis structure

This thesis is presented in a paper-format structure which is based on several papers being prepared for submission or published. The thesis structure, the status of the paper submissions, and the key conclusions of each paper are shown in Table1-1. It consists of six chapters altogether. Chapters 1 and 2 are introduction and literature review respectively, while Chapter 6 is the overall summary and future work of the research. Chapters 3 to 5 are the technical parts including the main outcomes of the research, of which Chapter 3 discusses the

limitations of the single PTA process, Chapter 4 presents the results of the PTA-laser hybrid melting process, and Chapter 5 is focused on the PTA-laser hybrid deposition process. It is worth noticing that a separate literature review is not required in a paper-format thesis as the technical chapters have their own literature review as part of the papers. But a short literature review is presented in Chapter 2 to enrich the thesis. The detailed introduction of each chapter is shown below.

Chapter 1 shows the overall introduction of the thesis, which includes the research background, the aim and objectives, and the thesis structure.

Chapter 2 presents the literature review, including a brief introduction of metal AM processes, fundamentals of the PTA and laser, different thermal efficiencies, and bead shape control in wire based AM processes. In addition, the barriers to the building of large-scale and near-net-shape metal parts at high deposition rates have been highlighted.

Chapter 3 discusses the limits of using a single PTA heat source and the process characteristics of a newly proposed configuration of the PTA process. This chapter consists of two papers. Paper 1 presents an experimental study on the effect of the wire size on the deposition rate, process behaviour and defect formation in the PTA deposition process. The results from Paper 1 show that there are limits to achieve high deposition rates with a traditional PTA deposition process in terms of keyhole formation, process tolerance, bead shape, and maximum deposition rate that can be achieved. To achieve higher deposition rates, lower likelihood of keyhole formation and higher bead quality, Paper 2 examines a new PTA deposition process which, unlike the traditional configuration, has a configuration with an inclined plasma torch and vertical wire. The process tolerance, keyhole behaviour, deposition rate, and melt transfer behaviour were investigated and compared with the traditional process. The results from Paper 1 and Paper 2 demonstrate that it is difficult to achieve both high deposition rate and near-net-shape using a single PTA heat source. This is because it is difficult to control the deposition rate and bead shape independently

with one heat source. Therefore, a hybrid process with two independent heat sources (i.e., PTA and laser) is investigated in the following chapters.

Chapter 4 studies the interaction between the PTA and the laser. This chapter contains data from one paper. The paper discusses the thermal behaviour, including the melt pool geometry, cooling rate, and solidification parameters, as a function of different process parameters in PTA-laser hybrid melting process using finite element (FE) modelling and instrumented experiments. The results from this chapter reveal that the melt pool geometry can be controlled by manipulating the parameters of the two heat sources. However, the wire feeding effect is not considered, which is needed in practical application. In addition, the feasibility of using the hybrid deposition process to achieve high deposition rates and near-net-shape is unknown, which is investigated in Chapter 5.

Chapter 5 presents the development of a wire based PTA-laser hybrid deposition process and its ability to control the bead shape. This chapter consists of two papers. Paper 4 discusses different processing conditions in the hybrid process and the benefits of using the hybrid process over the PTA and laser processes on their own. In addition, a multi-energy source (MES) approach with one PTA and double laser was introduced to expand the capabilities of the standard hybrid process. Paper 5 discusses the bead shape control as a function of different process parameters in the hybrid process. A procedure for selection of process parameters to achieve a particular bead shape was proposed and its feasibility was demonstrated by the deposition of multi-layer walls. The results from this chapter demonstrate that the hybrid deposition process shows more benefits than the PTA and laser processes on their own. Using the PTA to melt the wire and laser to control the melt pool, the deposition rate and bead shape can be controlled independently. As a result, high deposition rates and near-net-shape can be achieved.

Chapter 6 presents the key findings and a summary of all findings presented in this thesis. In addition, suggestions for future development and how this research could be taken forward are proposed.

Figure 1-4 shows the methodological approach of this research with the objectives highlighted. The research started with the investigation of the limitations of the conventional PTA deposition process. Then, a novel PTA process with the vertical wire and an inclined torch was examined. After that, the interaction between both heat sources (PTA and laser) on the material response was studied. At last, a wire based PTA-laser hybrid deposition process was developed, and the bead shape control in the hybrid process was investigated.

Table 1-1 Thesis structure, status of paper submissions, and key conclusions of each paper.

Chapter	Title	Papers	Objectives	Key conclusions
1	Introduction	N/A	N/A	N/A
2	Literature review	N/A	N/A	N/A
3	Understanding the limitations of a single axisymmetric heat source – PTA	Paper 1: The effect of wire size on high deposition rate wire and plasma arc additive manufacture of Ti-6Al-4V (Published - Journal of Materials Processing Technology)	1, 2	• The melting efficiency and deposition rate can be improved by using thick wires. • The bead becomes narrower when the wire reaches the melt pool. • The likelihood of keyhole formation can be reduced by using thick wires. • Thin wire is more sensitive to wire feeding position in terms of melt transfer compared to thick wire.
		Paper 2: Process characteristics of wire and plasma arc additive manufacture with a vertical wire feed (In preparation - Journal of Manufacturing Processes)	3, 4	• The new process is not omnidirectional, having an optimum configuration of torch trailing. • The new process has lower likelihood of keyhole formation compared to traditional process. • With the same wire-to-nozzle distance, similar deposition rates were achieved with the new and traditional processes. • The droplet transfer behaviour is determined by different process parameters, having significant effect on bead quality.
4	The interaction between the PTA and laser	Paper 3: Finite element analysis of thermal behaviour in plasma arc-	5	• The established FE model is suitable for predicting the thermal behaviour in hybrid PTA-laser melting process.

		laser hybrid melting of Ti-6Al-4V (In preparation - Applied thermal engineering)		• The melt pool geometry responds more significantly to laser power and travel speed than laser beam size and arc-laser separation distance. • The cooling rate decreases with increasing laser power and decreasing travel speed. • The solidification rate increases significantly with travel speed but has a minor response to laser power.
5	Wire based PTA-laser hybrid additive manufacture	Paper 4: Wire based plasma arc and laser hybrid additive manufacture of Ti-6Al-4V (Published - Journal of Materials Processing Technology)	6	• The best configuration for the hybrid process is the PTA leading, combined with front feeding of the wire. • Compared to laser and PTA processes on their own, the hybrid process has a higher deposition rate. • Compared to the laser process, the hybrid process has a much higher wire melting efficiency and tolerance to wire positioning accuracy. • The likelihood of keyhole formation in the hybrid process is lower than that in the single PTA process.
		Paper 5: Bead shape control in wire based plasma arc and laser hybrid additive manufacture of Ti-6Al-4V (Under review - Journal of Manufacturing Processes)	7	• The optimum operating regime for the hybrid process is the wire being melted by the PTA and the melt pool being controlled by the laser. • The effect of different processing parameters on bead shape was obtained. • A procedure for selecting process parameters for the achievement of required bead dimensions and deposition rate was proposed.
6	Summary, conclusions, and future work	N/A	N/A	N/A

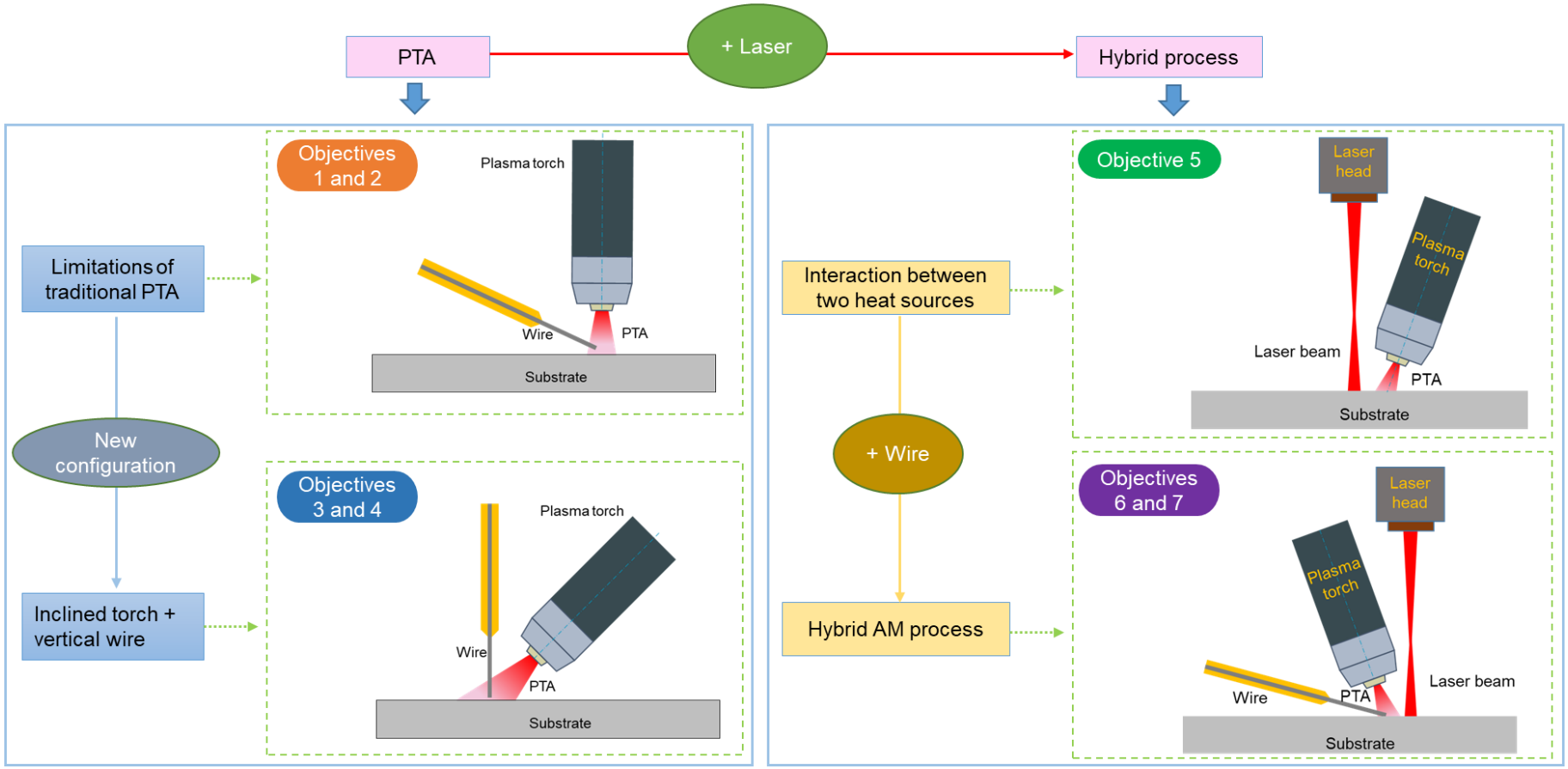


Figure 1-4 Outline of research methodology.

1.4 References

[1] S. Williams, F. Martina, Wire+ arc additive manufacturing vs. traditional machining from solid: a cost comparison, Technical report, Cranfield University, 2015.

2 Literature review

2.1 Additive manufacture

2.1.1 Introduction

Additive manufacture (AM) has developed rapidly over the last few decades, transforming from rapid prototyping and rapid tooling to rapid manufacture applications, which now stands out as a valid and convenient alternative to other traditional manufacture methods [1-3]. The concept of AM is to fabricate desired components by depositing successive layers of a material based on a three-dimensional (3D) computer-aided design (CAD) model [4-6]. In metal AM processes, the feedstock with the form of wire or powder is melted by the heat source, such as laser, electron beam or electric arc and is consolidated in subsequent cooling to form a fully-dense part [7]. In some cases, post-machining and cold working are needed to meet the requirements of surface quality, dimensional accuracy and mechanical properties.

The unique features of AM bring significant advantages compared with traditional manufacture techniques. First, it has high design flexibility, allowing the fabrication of complex and customised components that are challenging to manufacture with traditional manufacture methods [2]. Second, it allows a significant reduction of material wastage, making it more environmentally friendly. For example, most structural components in the aerospace industry fabricated by traditional manufacture suffer from a high buy-to-fly (BTF) ratio of 10-20 [8]. This can potentially be reduced to nearly 1 when the same parts are produced by AM techniques. Third, it saves production lead-time due to the fewer processing steps and independent supply chain. For some parts, the production lead-time can be reduced to a few hours instead of weeks and months when fabricated with the traditional manufacture methods [9]. Based on these advantages, metal AM has been widely researched in aerospace, automotive, marine, and medical fields [10]. In addition, different materials such as steels [11], aluminium alloys [5], titanium alloys [12], nickel alloys [13,14], and some refractory metals [15,16] can be deposited.

2.1.2 Classification of metal AM processes

A large number of metal AM techniques have been developed which can be classified based upon heat source, feedstock form, or delivery way of the material. Figure 2-1 schematically shows the classification of metal AM techniques. As mentioned earlier, there are mainly three types of heat sources that can be used for metal AM, which are laser beam, electron beam and electric arc. For electric arc, there are gas metal arc (GMA), gas tungsten arc (GTA), and plasma transferred arc (PTA). Depending on the form of feedstock, there are powder and wire based processes. Therefore, based on different combinations of heat source and feedstock, there are mainly six types of metal AM processes, namely selective laser melting (SLM), laser metal deposition (LMD), wire + laser additive manufacture (WLAM), electron beam melting (EBM), electron beam freeform fabrication (EBF^3), and wire + arc additive manufacture (WAAM). In addition, depending on the way the material is delivered (pre-placed bed or direct feed), AM can be broken into powder bed fusion (PBF) and directed energy deposition (DED) processes.

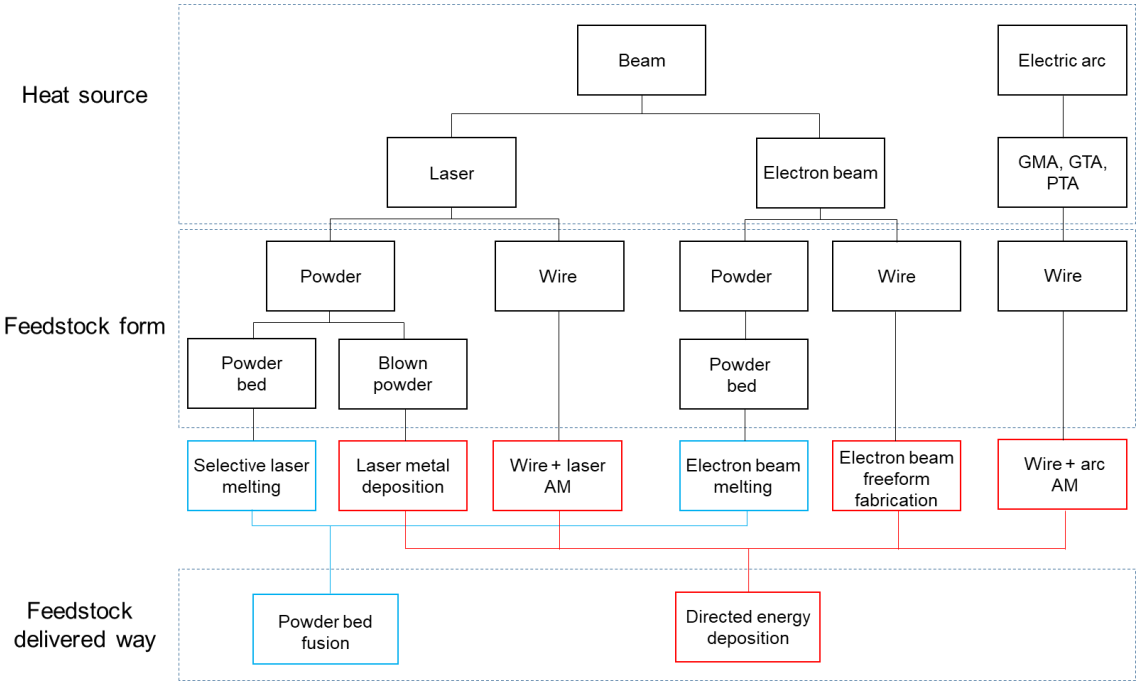


Figure 2-1 Classification of metal AM processes based on the heat source, feedstock form and delivered way of the material.

Based on the intrinsic characteristics, each process is suitable for certain applications. SLM and LMD with the combination of laser and powder are the most popular processes due to the capability of building very complex parts with net shape. Among these two processes, in SLM process the material is pre-placed on the powder bed and then is fully melted by the laser beam according to the planned scanning pattern [17], whilst in LMD process the powder is delivered by the shielding gas through a coaxial or multi-jet nozzle and fed directly into the melt pool created by the laser beam [18]. Another laser based process is WLAM, in which wire is used as a feedstock instead of powder. The setup in WLAM is much simpler than in powder based processes due to the much easier handling of wire compared to powder. Amongst the three processes, SLM has the lowest deposition rate, LMD has a higher deposition rate than SLM, whilst WLAM has the highest deposition rate. This means the capability for deposition of large build volume is increasing for the three corresponding processes. However, as a compromise, there is a decrease in the capability of achieving high geometrical complexity.

For the two electron beam based processes, EBM and EBF^3, the former is similar to the SLM process, whilst the latter is similar to the WLAM process. Instead of using a laser as the heat source, an electron beam is used to melt the feedstock. However, unlike the laser based processes which are normally conducted in an inert atmosphere, the electron beam needs to be enclosed in a vacuum chamber ($< 10^{-2}$ Pa [1]) in order to avoid scattering of the electrons by air molecules. In addition, in the EBM process very low quantity of helium is injected to the work area during the melting process to reduce the electrical charging of the powder [19]. It should be noted that due to the lack of convective cooling in a vacuum environment, the cooling rates upon solidification of the material are typically lower than with other processes.

Compared to laser and electron beam processes, the electric arc processes have higher efficiency and relatively low equipment cost [9]. Therefore, WAAM is the most cost-effective process for deposition of parts with large volume. Amongst different arc processes, GMA process has higher tolerance in terms of the path

planning and omnidirectionality than GTA and PTA processes, owing to the coaxial configuration of the consumable electrode (i.e. wire) and torch [9,20]. Therefore, it is the first choice whenever possible, to deposit materials. However, for some materials like titanium, the process with GMA has high instability due to the occurrence of arc wandering [21]. GTA and PTA based processes with non-consumable tungsten electrode are then more suitable for deposition of these materials due to better stability of arc. Between GTA and PTA, the latter provides a more focused arc and enables longer stand-off distance between electrode and workpiece, making it a better choice for AM [22].

To avoid contamination and oxidation of built parts by the surrounding atmosphere, usually the parts have to be deposited in an inert atmosphere. In WAAM, there are two options to provide an inert gas atmosphere. The first option is to use an enclosure filled with inert gas. The second option is to use a local shielding device, integrated with the process torch and wire, which provides positive pressure locally near the melt pool and freshly solidified material to expel ambient air [23].

Due to the high deposition rate of WAAM, the surface quality is lower as compared to other processes [24], meaning that WAAM is not a net-shape process. Typically, it is possible to distinguish each individual layer on the side of the components, referred to as surface waviness. In addition, due to the relatively large melt pool, it is not suitable for the building of very complex components. Therefore, WAAM is suitable for deposition of large components with low to medium complexity.

2.1.3 High deposition rate AM processes

The practical requirements for producing large engineering structures with better economic efficiency have driven the rapid development of high deposition rate metal AM techniques. Of all the metal AM processes available, wire based processes are more suitable for high deposition rate applications compared to powder based processes due to the higher power that can be used [24,25]. As described previously, there are three heat sources (electric arc, laser, and

electron beam) that can be used for melting metallic wires. Among these processes, WAAM is most competitive due to the relatively low equipment cost and high efficiency. In WAAM, if the deposition rate is kept at a medium level (e.g. 3 kg/h for steel, and 1 kg/h for aluminium and titanium), a relatively low BTF ratio of 1.5 is always achievable [9].

In addition to traditional WAAM processes, various research groups are exploring novel WAAM process in order to achieve higher deposition rates and lower costs. Norsk Titanium [26] developed a PTA deposition process with a dual plasma torch, as shown in Figure 2-2. This process gives higher heat input compared with the traditional PTA process with one plasma torch, and therefore allows higher wire feed speed (WFS). As a result, this leads to much higher deposition rates. However, the process dynamics and melt pool are not controlled precisely, leading to low dimensional accuracy and poor surface finish of the deposited parts, as can be seen from Figure 1-3b. This means that significant material needs to be machined off to meet the final requirement of surface quality.

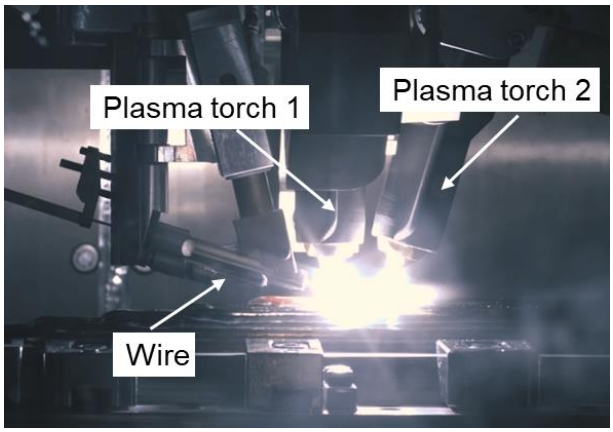


Figure 2-2 PTA based WAAM system with dual plasma torch (image credit: Norsk Titanium).

Martina et al. [27] investigated the feasibility of using pulse tandem GMA to deposit 17-4PH stainless steel for high productivity application. This process allows dual wire deposition as shown in Figure 2-3a, and a very high deposition rate of 9.5 kg/h was achieved without defects, as shown in Figure 2-3b. In abovementioned two examples, the deposition rate was increased by increasing

heat input using more than one heat sources, thereby allowing more wire can be fed into the melt pool. However, high heat input produced by the two heat sources resulted in deep remelting and poor surface finish of the deposited parts.

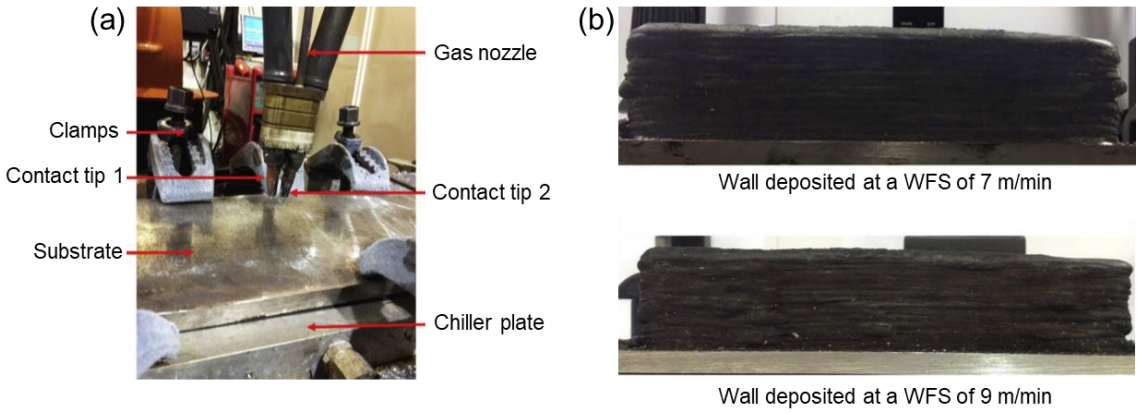


Figure 2-3 (a) Experimental setup for GMA based WAAM process with a tandem torch, and (b) single-pass walls deposited at different WFSs with the process. Images are adapted from Ref. [27].

Another example of high productivity WAAM includes the combination of one arc heat source and two wires. Liu and Xiong [28] developed a WAAM process with a GMA torch and an external cold wire for deposition of aluminium, the configuration of which is schematically shown in Figure 2-4a. The purpose of this process was to increase the deposition rate as well as to reduce the remelting to the underlying layers. By increasing the WFS of the cold wire whilst keeping all the GMA related parameters constant, the ratio between heat input and volume of the deposited material was reduced, leading to an increase of 80% in deposition rate and reduction in remelting ratio compared to that of the GMA only process.

Feng et al. [29] developed a PTA deposition process with dual wire, as shown in Figure 2-5a. The deposition rate was increased by 106% compared with the traditional PTA process with a single wire. In the abovementioned two cases, due to more energy was taken directly by the wire, higher deposition rates were achieved. In addition, the remelting was reduced significantly due to less energy transferred to the underlying layers. However, the bead shape could not be

controlled very precisely with two wires being fed into a common melt pool, which resulted in low surface finish and low dimensional accuracy, as demonstrated in Figure 2-4(b) and Figure 2-5(b).

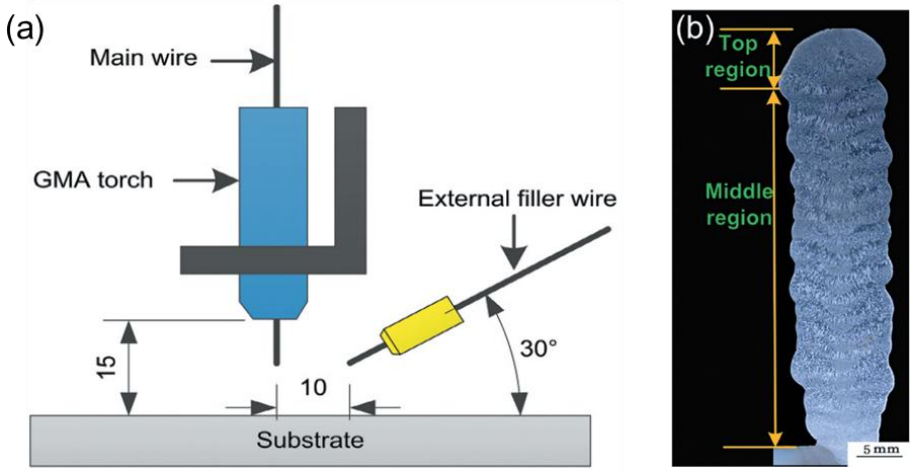


Figure 2-4 (a) Schematic shows the configuration of the WAAM process with GMA torch and external cold wire, and (b) cross-section of the part built by the process. Images are adapted from Ref. [28].

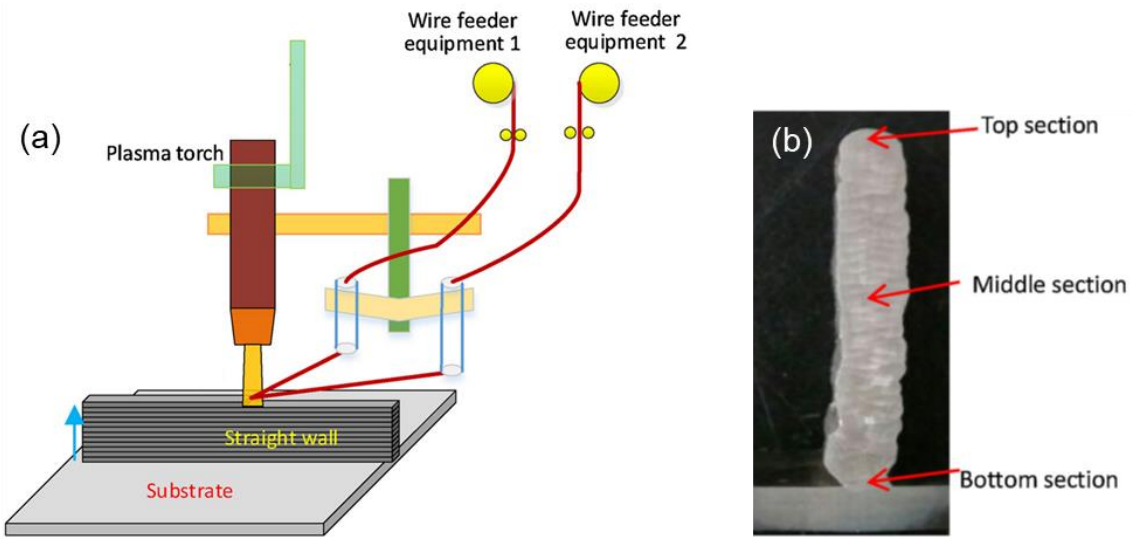


Figure 2-5 (a) Schematic shows the configuration of the PTA deposition process with dual wire, and (b) cross-section of the part built by the process. Images are adapted from Ref. [29].

In addition to WAAM, EBF^3 is also suitable for high deposition rate application but with a relatively high cost. This technology was first patented and developed by

NASA [30], and then commercialised by Sciaky and called electron beam additive manufacture (EBAM) [31]. Figure 2-6 shows the EBAM system and example of a part built with this process. Common materials including titanium, aluminium, copper, steel, Inconel, and some refectory metals can all be deposited by the EBAM process with the deposition rates of up to 10 kg/h. However, it can be seen from Figure 2-6b that the resolution of the process is relatively low, meaning that a large amount of material needs to be machined off. In addition, Sciaky developed an EBAM process with dual wire feed to achieve higher deposition rates, which also can be used to fabricate graded parts.

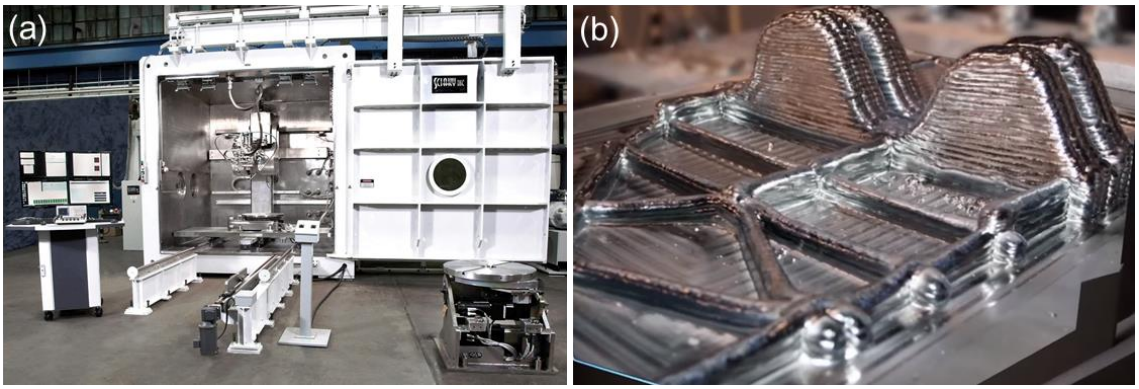


Figure 2-6 (a) The EBAM system developed by Sciaky, and (b) the part deposited by the EBAM process (Image credit: Sciaky).

2.2 Fundamentals of plasma arc and laser

2.2.1 Plasma arc

Plasma is a state of matter, in which a gas is ionised and becomes electrically conductive [32]. The overall charge of a plasma is zero, but it consists of both positive and negative particles. Plasma is the state of the matter presented between the electrodes in all electric arcs. Figure 2-7 shows the structure of a plasma torch. The key difference in the structure of GTA and PTA torch is that there is a water-cooled copper nozzle in the latter, which allows plasma gas to flow through. Due to the constriction effect of the plasma gas, PTA has higher arc pressure, temperature and power density, and is more concentrated and stable than GTA [33].

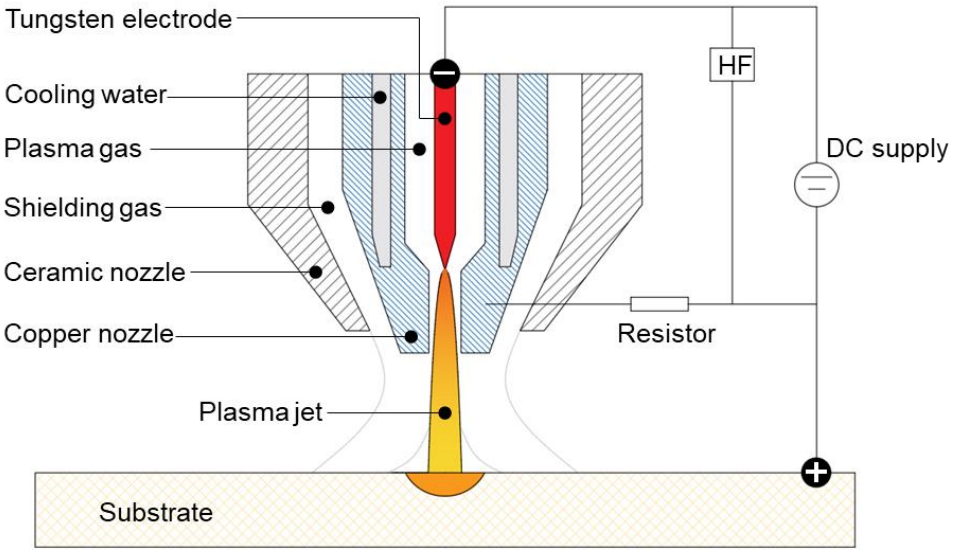


Figure 2-7 Schematic of a plasma torch showing the components and working principle.

There are two types of plasma arc, which are transferred arc and non-transferred arc (or pilot arc). The non-transferred arc is formed between the electrode and the copper nozzle, whilst the transferred arc is formed between the electrode and the workpiece [33]. Normally, the non-transferred arc is used to initiate the PTA and will be switched off once the PTA is ignited. In some cases, it also can be used for welding applications. In the non-transferred arc process, the workpiece is not in the arc circuit and therefore receives relatively low energy and arc pressure. In a plasma torch, two separate gases are used, which are plasma gas and shielding gas. The plasma gas flows through the copper nozzle and is ionised by the electric current to form the arc plasma. The shielding gas flows through the space between the copper nozzle and the ceramic nozzle to shield the arc plasma and melt pool [33].

Due to the relatively high energy density, PTA is widely used for welding application [34]. Especially keyhole PTA welding, which is characterised by deep penetration and relatively high fit-up tolerance, is suitable for joining plates with medium thickness both efficiently and cost-effectively [35]. Due to the stable arc characteristics, which allows high tolerance of stand-off distance, PTA has been used for AM applications and has been developed rapidly in the last decade

[29,36,37]. By using higher plasma gas flowrate and lower diameter of the copper nozzle, the PTA is further constricted, which can be used for metal cutting application [38]. In addition, it can be used for spraying and other applications [39].

2.2.2 Laser

A laser is a precise heat source with high versatility due to the independent control of laser power and beam size. It allows much higher flexibility of tailoring the energy delivered to the workpiece than electric arc [40]. For example, by varying the optical magnification, the laser beam can be highly focused to tens of microns and also can be enlarged to tens of millimetres, allowing a wide range of power densities and interaction times. Besides, different energy distributions of the laser beam, such as Gaussian, top-hat, doughnut, and higher-order modes can be achieved by manipulating the optical setups.

Depending upon the processing conditions, there are two main process regimes in laser based processes, which are conduction regime and keyhole regime [41]. The regime is determined by the power density and thermal properties of the material. Normally, it is considered that the threshold power density between the two regimes for steel is 10^6 W/cm^2 [42-44]. Below this value, the conduction regime is present. The cross-section of the melted region in the conduction regime has a low depth-to-width ratio. Above this value, the keyhole regime occurs, and the cross-section of the melted region has a high depth-to-width ratio [45]. Figure 2-8 shows the typical cross-sectional profiles of the melted regions obtained with the two operational regimes.

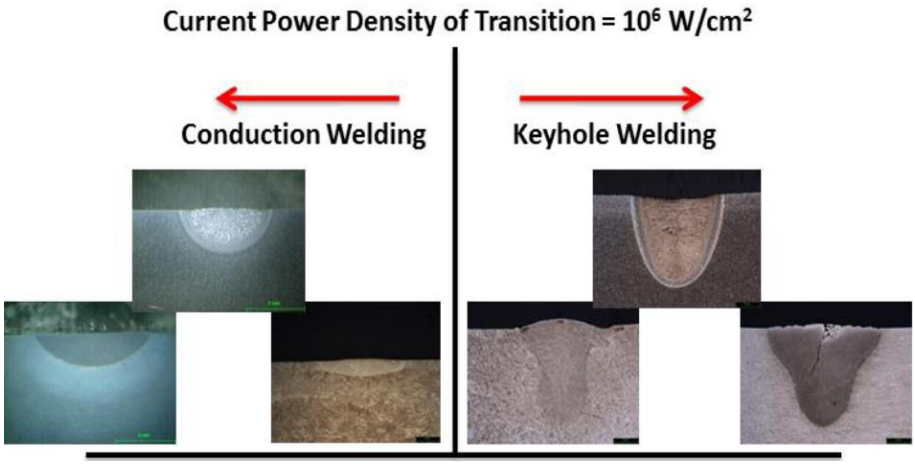


Figure 2-8 Cross-sectional profiles obtained with conduction and keyhole regimes in autogenous laser welding processes [41].

Due to the relatively low power density in the conduction regime, the melt pool is shallow. Besides, the low temperature gradient leads to weak convective flow and hence the melt pool is still and stable, which normally results in high quality. In contrast, due to the high power density in the keyhole regime, the melt pool is heated to a very high temperature, where vaporisation occurs. The high recoil pressure produced by the vaporised metal along with the steep temperature gradient induce strong and complex melt flow in the melt pool [46]. This results in a violent process, where spatters and instabilities are often observed. Figure 2-9 shows a laser welding process in keyhole regime, where spatters can be seen clearly. In addition, the interactions between vapour gases and liquid metal often lead to the intermittent closure of the keyhole and can cause porosity due to gas entrapment [42]. Although this regime is very efficient in some applications, such as welding and cutting, it is not suitable for AM due to the high penetration and low process stability.

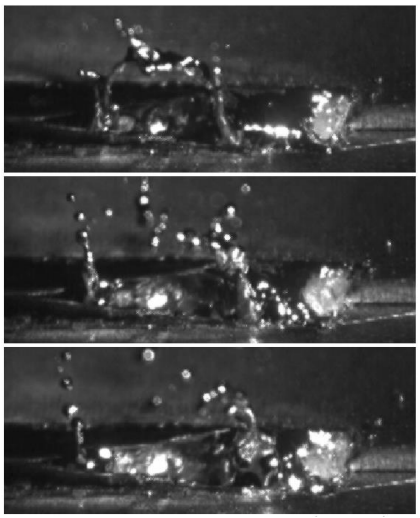


Figure 2-9 Spatters occur during the laser welding process in keyhole regime [47].

Absorptivity is a critical factor in laser material processing, which determines the thermal efficiency of the process. Normally, laser absorptivity varies significantly (from less than 0.1 to more than 0.9) depending on the wavelength of the laser, process regime, material type and its surface conditions, and processing conditions [48-51]. Figure 2-10 shows the laser absorptivity for different metals as a function of wavelength. It can be seen that higher absorptivity can be achieved with lower wavelength lasers for most metals. Therefore, a fibre laser with a 1.07 µm wavelength has a higher absorptivity than a CO_2 laser with a 10.7 µm wavelength. This phenomenon also can be seen in Figure 2-11, which shows the absorptivity of three commonly-used materials as a function of temperature for fibre laser and CO_2 laser measured by Kwon et al. [52]. It also can be seen from Figure 2-11 that the absorptivity also depends on the material, where titanium has the highest absorptivity, followed by steel and aluminium. For titanium and steel, the absorptivity is increased after 700 °C, which is attributed to the occurrence of oxidation. However, there is no significant change for aluminium due to the negligible oxidation (around 0.1%) at elevated temperature.

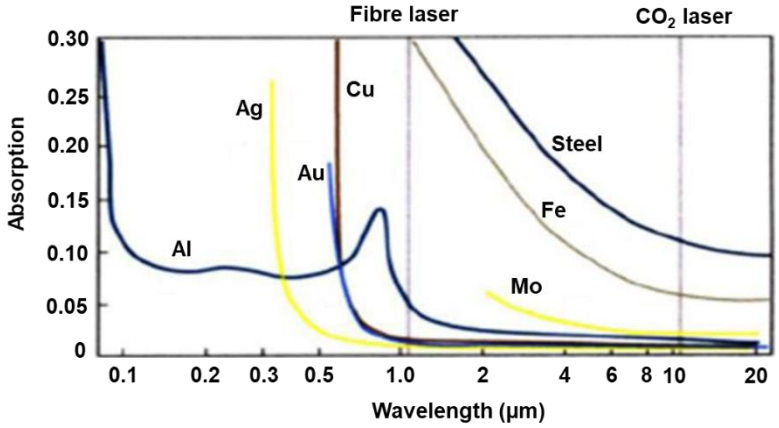


Figure 2-10 Laser absorptivity of different materials as a function of wavelength [40].

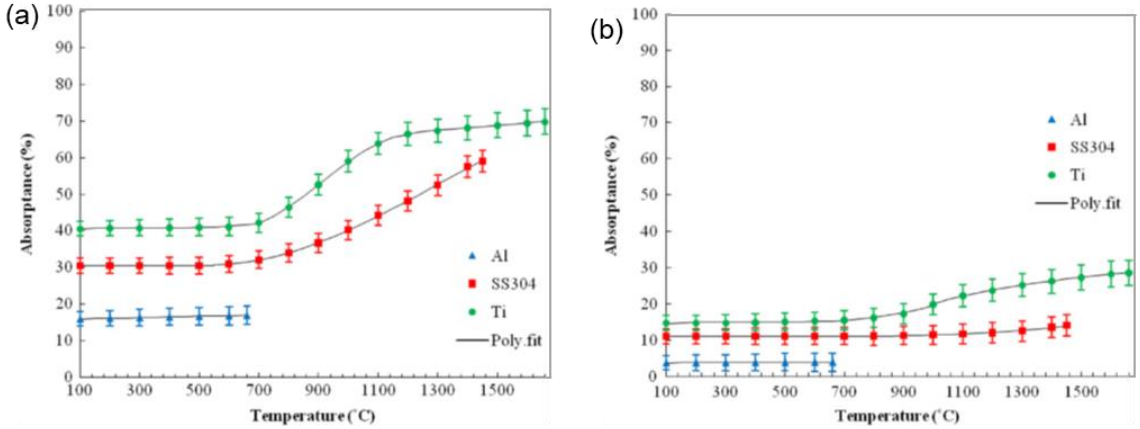


Figure 2-11 Laser absorptivity of different materials as a function of temperature for two different lasers: (a) fibre laser with 1.07 μm beam, and (b) CO_2 laser with 10.7 μm beam. Images are adapted from Ref. [52].

In addition, for a particular laser and a particular material, the absorptivity in conduction regime is lower than in the keyhole regime. Figure 2-12 shows the laser absorptivity as a function of power density. It can be seen that as the laser power density increases, the penetration becomes deeper with the absorptivity increasing significantly from around 0.3 to 0.9. This is because compared to the conduction regime, in keyhole regime multiple reflections of the laser beam is trapped inside the melt pool [53].

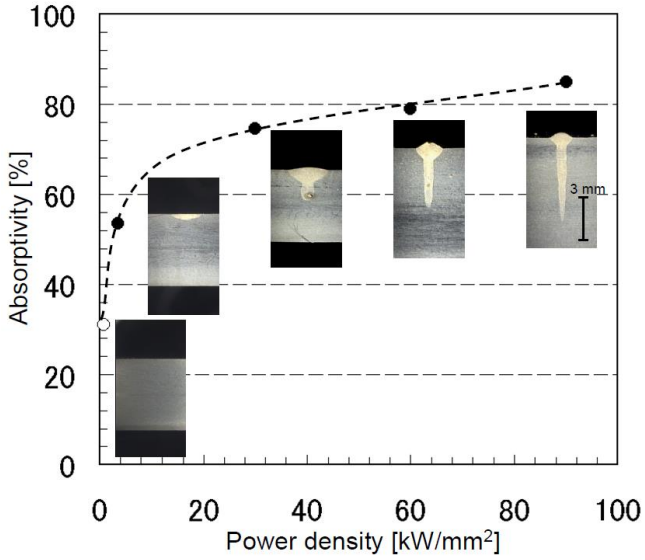


Figure 2-12 Laser absorptivity as a function of power density [54].

Owing to its versatility, precision and non-contact interaction with materials, lasers are widely used for material processing. By changing the laser power and beam size, different power densities and interaction times can be achieved, satisfying many applications, as shown in Figure 2-13. These processes can be divided into three groups, depending upon if the material is melted or vaporised. It should be noted that laser based AM processes are in the area around melting and cladding in this process map.

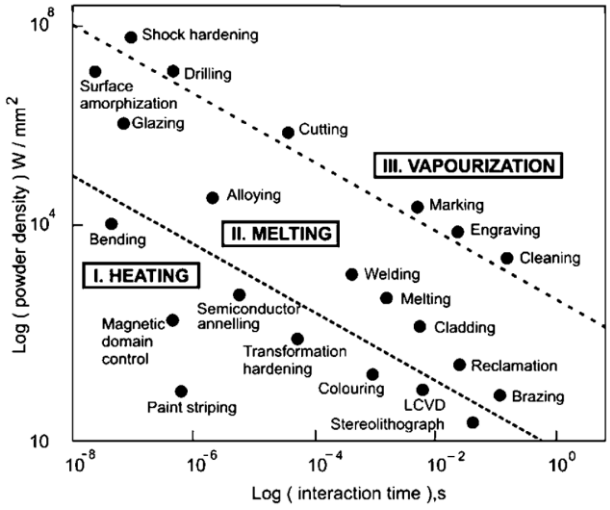


Figure 2-13 Process map of laser applications based on interaction time and power density [55].

2.3 Thermal efficiencies

In welding or AM, thermal efficiencies, such as energy transfer efficiency, melting efficiency, and process efficiency, are important parameters when assessing the performance of a process. For example, in welding, it is expected that the majority of energy is used to generate a weld zone rather than wasted for the generation of the heat-affected zone (HAZ) or heat loss. Similarly, in AM, the more feedstock can be melted with the same amount of applied power, the better the efficiency of the process. In practice, this means a higher deposition rate can be achieved with particular equipment or lower power heat source can be utilised for the same deposition rate. Since the efficiency is fundamental to the improvement of deposition rate, it is important to understand how to improve the energy utilisation at different processing conditions, thus to maximise the specific thermal efficiencies.

2.3.1 Energy transfer efficiency

Figure 2-14 schematically shows the distributions of the total applied power (P_a) generated by a power source, where P_t is the power transferred to the workpiece, and P_e is the power lost to the environment. In laser based processes, P_e is mainly the reflected radiation, whilst in arc based processes, it is primarily the radiative and convective energy from the arc plasma to surroundings. It should be mentioned that in PTA based processes, a significant proportion of energy is dissipated through the copper nozzle and tungsten electrode.

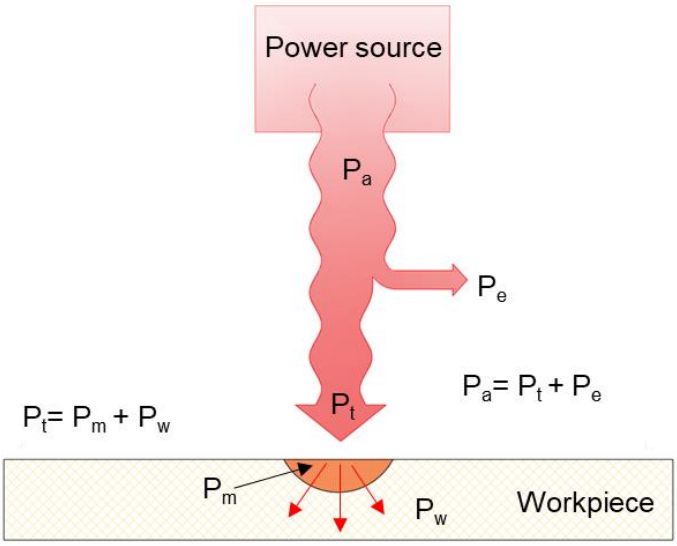


Figure 2-14 Schematic shows the applied power of a power source (P_a), power transferred to the workpiece (P_t), power for the generation of melt pool (P_m), and power lost through workpiece (P_w).

The energy transfer efficiency (also called energy coupling efficiency) is defined as the power transferred to the workpiece (P_t) divided by the total applied power of a power source (P_a) [56], which is expressed as:

$$\eta_1 = \frac{P_t}{P_a} \tag{2-1}$$

In arc based processes, it is commonly known as arc efficiency, whilst in laser based processes it is called laser absorptivity or laser coupling coefficient. The energy transfer efficiency in arc and laser processes are normally measured by calorimetric methods [57,58] or by integrating spheres [59]. It has been found by several authors that the GMA exhibits the highest arc efficiency of 0.84, followed by the GTA (0.67-0.8) and the PTA (0.47-0.75) [57,58]. For a given arc process, the arc efficiency has very low dependence on the process parameters and environmental conditions. But it is affected by the anode material as 60% of the transferred energy is attributed to the anode work function [57]. However, in laser based processes, the absorptivity is largely dependent on the processing conditions, as described in Section 2.2.2.

2.3.2 Melting efficiency

As shown in Figure 2-14, the power transferred to the workpiece (P_t) can be split into two parts. One is used to generate the melt pool (P_m), and the other is dissipated by thermal losses through the workpiece (P_w). Melting efficiency is defined as the ratio of the power used for the generation of melt pool to the power transferred to the workpiece, which is expressed as:

$$\eta_2 = \frac{P_m}{P_t} \quad \textbf{(2-2)}$$

In welding or AM, higher melting efficiency is desired as it will reduce HAZ size, wasted process energy, and distortion [58]. The melting efficiency is dependent on the processing conditions. For example, Fuerschbach and Knorovsky [57] investigated the melting efficiency of PTA and GTA welding processes. They determined a dimensionless parameter, *Y*, which correlates well with the measured melting efficiency. It is expressed as:

$$Y = P_a v_t / \delta h \nu \tau \quad \textbf{(2-3)}$$

where P_a is applied power, v_t is travel speed (TS), δh is enthalpy change to melt, ν is kinematic viscosity at the melting point, and τ is thermal diffusivity at 300 K. The melting efficiency for welds with the two-dimensional flow (e.g. edge welds) is expressed as:

$$M_1 = 0.407\mathrm{e}^{-29.6/Y} \quad \textbf{(2-4)}$$

The melting efficiency for welds with the three-dimensional flow (e.g. bead on plate or square-groove welds) is expressed as:

$$M_2 = 0.346\mathrm{e}^{-0.90/Y} \quad \textbf{(2-5)}$$

It can be seen that the melting efficiency varies with TS, applied power, material property, weld type, etc. Specifically, the experimental results showed that in GTA and PTA welding processes the melting efficiency increased with the TS, and reached a maximum value of 0.46 and 0.37 for two-dimensional and three-

dimensional welds, respectively [57]. These values are in good agreement with the values of 0.41 and 0.35 obtained with Equations (2-4) and (2-5) when *Y* goes to infinity. In addition, the melting efficiency can vary with the electrode tip angle, shielding gas, etc. [60].

2.3.3 Process efficiency

Process efficiency is defined as a ratio of the power used for the generation of melt pool (P_m) to the total applied power of the power source (P_a). Therefore, it is expressed by:

$$\eta = \eta_1 \cdot \eta_2 = \frac{P_m}{P_a} \quad \textbf{(2-6)}$$

It can be seen that process efficiency is a product of energy transfer efficiency and melting efficiency. It represents the applied power needed to achieve the expected melt pool (i.e. fusion zone in welding, or melted feedstock in AM). It can be seen that the process efficiency is dependent on both the energy transfer efficiency and melting efficiency. Therefore, in order to achieve higher deposition rates, the process efficiency needs to be addressed.

2.4 Bead shape control

In wire based AM processes, a single bead is the smallest and fundamental feature, which determines the final quality of the parts. For example, there are mainly three deposition tool-paths when building a part, which are single pass, oscillated pass, and parallel pass [61]. Wang et al. [22] demonstrated that in a single-pass deposition strategy, a flatter bead would lead to a lower surface waviness of final parts, meaning less material needs to be machined away. Also, in oscillated and parallel deposition strategies, the bead geometry will determine the overlapping principle, which consequently determines the surface finish and dimensional accuracy of the final parts [62-64]. Therefore, it is of significant importance to understand the mechanisms of bead formation and how different parameters affect the final bead shape after solidification.

Numerous studies have investigated the variation in the bead shape as a function of different process parameters in a single power source deposition process (arc or laser) and achieved some common conclusions [65-71]. For example, the beads become wider and shallower with the increase in applied power. By increasing the WFS (or TS) at a constant ratio of WFS to TS, the bead becomes narrower and taller. In addition, the process windows for PTA and laser deposition processes have been investigated. Most of these studies used empirical models, design of experiment (DoE), or neural networks to establish the relationship between the bead shape and process parameters. However, most of them omitted the complex effect of melt flow and energy distribution and other fundamental mechanisms that affect the bead formation.

The deposited bead shape is a consequence of fluid flow and heat transfer in the melt pool before solidification takes place. During the PTA or laser deposition process, there are different forces acting in the melt pool, contributing to the heat and mass transfer. Taking the PTA process as an example, there are electromagnetic force, Marangoni force, arc shear stress, gravity, buoyance force, surface tension, etc. This indicates that an accurate prediction of bead shape requires an understanding of all the forces and their net effect acting on the melt pool.

Bai et al. [37] developed a computational fluid dynamics (CFD) model to investigate the heat transfer and fluid flow behaviour in the PTA deposition process of Ti-6Al-4V, and also carried out experiments to validate the numerical results. Figure 2-15 shows the temperature and fluid flow field obtained. It can be seen from Figure 2-15a that a depression is formed at the front of the melt pool (under the heat source), which is attributed to the high arc pressure. Besides, there is a big clockwise circulation formed in the melt pool, which is caused by a combined effect of all the forces acting on the melt pool. The velocity of the flow decreases as the distance from the heat source increases. Since the melt pool is supported by the substrate, the influence of gravity and buoyancy is relatively low. In addition, the arc shear stress and Marangoni force have contradicting effects on the back slope of the depressed region, where the former is driving the

flow outward from the lowest position, and the latter is driving the flow downward from the mass input location (wire transfer position). Since the arc shear stress (around 80 Pa) is much lower than the Marangoni force (around 400 Pa), the latter is the dominant force for the surface flow. Figure 2-15b shows the flow pattern in the melt pool at the transverse cross-section. It can be seen that the metal liquid flows outward on the surface, and flows upward inside the melt pool, which indicates that Marangoni force plays a dominant role in determining the flow direction in this plane. It should be mentioned that the contribution of different forces changes with process parameters, hence affecting the net flow. This shows the complexity of the problem.

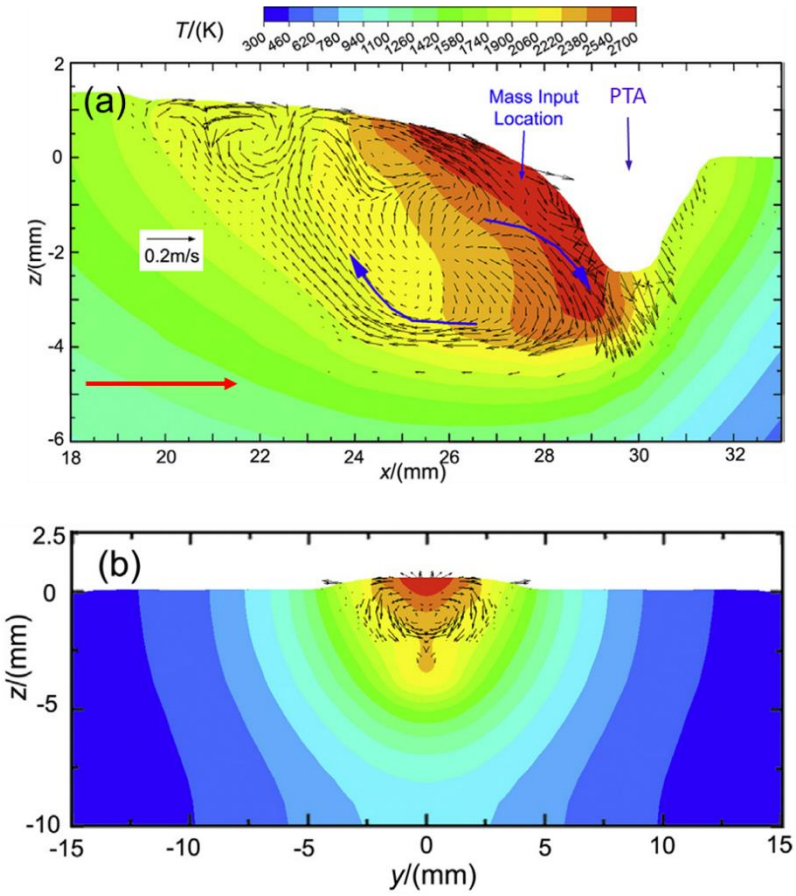


Figure 2-15 Temperature and velocity field during PTA based deposition process of Ti-6Al-4V on the (a) longitudinal cross-section, and (b) transverse cross-section at x=26 mm. Red arrow indicates the torch travel direction. Images are adapted from Ref. [37].

As described earlier, in the laser deposition process, conduction regime is desirable as it can produce wide beads with shallow penetration and allows high process stability. Compared to the PTA deposition process, the bead formation in laser deposition process is relatively straightforward due to the lack of arc-related forces. Also, unlike in PTA where the Gaussian profile of arc results in high temperature gradient, in laser the energy distribution can be tailored, leading to more thermally balanced melt pools and less significant Marangoni convection.

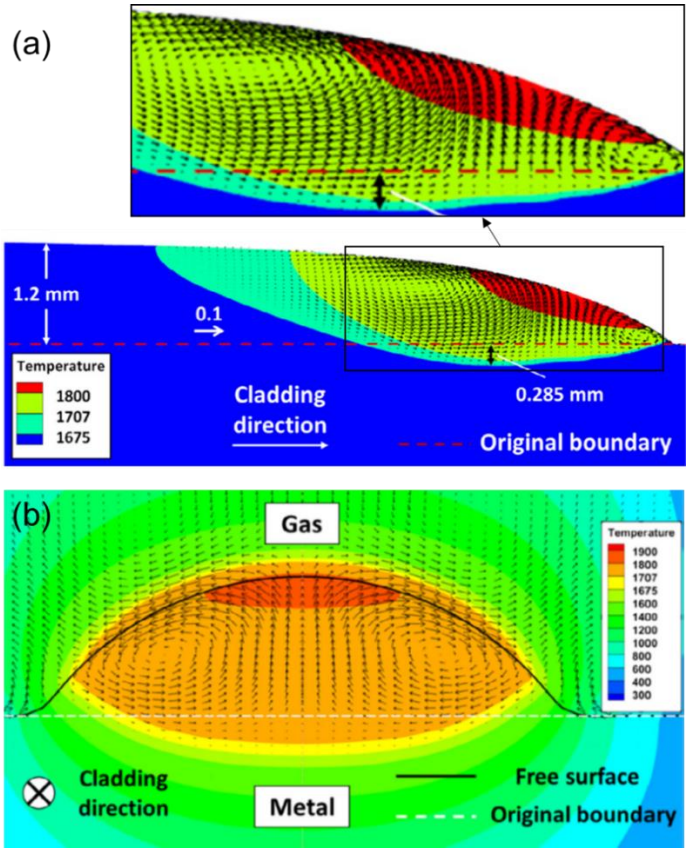


Figure 2-16 Temperature and velocity field during laser based deposition process of maraging steel; (a) longitudinal cross-section, and (b) transverse cross-section. Images are adapted from Ref. [72].

Wei et al. [72] developed a CFD model to investigate the laser wire deposition process, the temperature and the fluid field of which is shown in Figure 2-16. It can be seen from Figure 2-16a that a small clockwise circulation and a big anticlockwise circulation are formed at the front and back of the melt pool, respectively. Besides, the metal liquid on the surface flows from the position with

high temperature to the position with low temperature caused by the Marangoni force. Figure 2-16b shows the flow pattern at the transverse cross-section, which is similar to that in the PTA process shown in Figure 2-15b. Two symmetric circulations are formed about the mid-width line with outward flow direction on the surface.

It can be seen that the melt flow in the melt pool is very complex. However, to increase the deposition rate in WAAM, higher WFS should be used along with the higher current. The means the bead shape will be more difficult to control due to the more agitated melt pool caused by the higher current. In addition, increasing the current will result in larger remelting to the underlying layers, leading to lower process efficiency and unnecessary thermal damage. Figure 2-17 shows the penetration depth as a function of WFS in the cold metal transfer (CMT) process [73]. It should be mentioned that the CMT process is a variant of the GTA process, which has low heat input. In this process the WFS is associated with the arc current and voltage, meaning that the current is increased with the increasing WFS. It can be seen that a higher deposition rate was achieved but at the cost of larger remelting. Actually, this issue is difficult to overcome with a single axisymmetric heat source, and therefore two heat sources are needed.

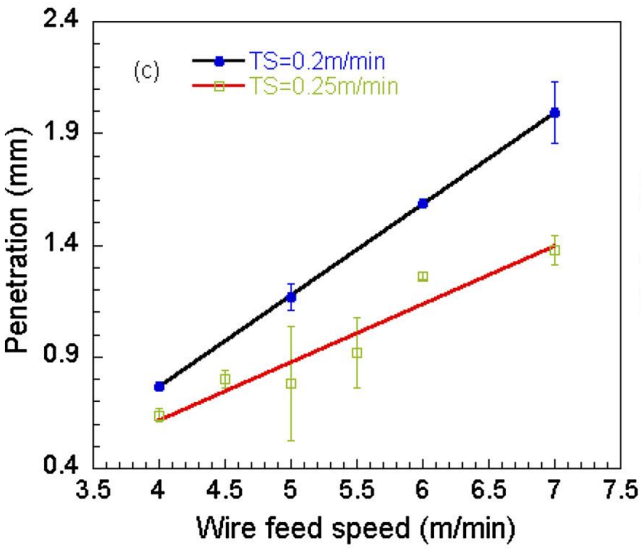


Figure 2-17 Penetration depth as a function of WFS (i.e. deposition rate) for different TSs [73].

2.5 Research gap

From the literature review, it can be concluded that for all metal AM processes, WAAM is the most cost-effective for large-scale components. Amongst different WAAM processes, PTA based process is most suitable for the deposition of titanium due to the high stability and process tolerance. Some new PTA processes, such as the dual PTA system, were developed for a much higher deposition rate. However, it is more difficult to control the melt flow and bead shape with two PTA sources. More importantly, the limitations of the deposition rate using a single PTA heat source have not been studied. In addition, the melting efficiency is an important factor affecting the deposition rate, and its limits have not been studied for a single PTA heat source.

To achieve higher deposition rates as well as to better control the melt pool, another heat source is needed. A laser is then selected as the second heat source due to its features of high precision and easy-to-control. Between the PTA and laser, the former has better efficiency and is very suitable for melting wire, whilst the latter allows control of energy distribution and should be better for control of bead profile and reduction of remelting. Therefore, a wire based PTA-laser hybrid deposition process needs to be investigated. However, the best operating conditions and other aspects, such as process efficiency and process tolerance, are not understood, which needs to be studied.

Compared to PTA or laser deposition processes with a single heat source, the bead shape control in the PTA-laser hybrid process with two heat sources is more complicated owing to the more process parameters that can be used. Therefore, how these different process parameters affect the bead shape needs to be studied, and the selection criteria of process parameters for the achievement of a required bead shape in the hybrid process needs to be investigated.

2.6 Summary

The literature review has summarised the characteristics of different metal AM techniques and introduced some AM processes that could be potentially used for

high deposition rate applications. The fundamentals of the PTA and laser were introduced, summarising the benefits and challenges of the two heat sources used separately. Thermal efficiencies, including energy transfer efficiency, melting efficiency, and process efficiency have been described, which will provide guidance to understand how to improve the energy utilisation in the AM process. It has been shown how complex the forces acting on the melt pool are and how difficult it is to control the bead shape at high deposition rate with a single axisymmetric heat source. In addition, the research gap has been summarised.

2.7 References

[1] D. Herzog, V. Seyda, E. Wycisk, C. Emmelmann, Additive manufacturing of metals, Acta Mater. 117 (2016) 371–392.

[2] T. DebRoy, H.L. Wei, J.S. Zuback, T. Mukherjee, J.W. Elmer, J.O. Milewski, A.M. Beese, A. Wilson-Heid, A. De, W. Zhang, Additive manufacturing of metallic components – Process, structure and properties, Prog. Mater. Sci. 92 (2018) 112–224.

[3] T.D. Ngo, A. Kashani, G. Imbalzano, K.T.Q. Nguyen, D. Hui, Additive manufacturing (3D printing): A review of materials, methods, applications and challenges, Compos. Part B Eng. 143 (2018) 172–196.

[4] K. Ha, T. Kim, G.Y. Baek, J.B. Jeon, D. Shim, Y.H. Moon, W. Lee, Numerical study of the effect of progressive solidification on residual stress in single-bead-on-plate additive manufacturing, Addit. Manuf. 34 (2020) 101245.

[5] N.T. Aboulkhair, M. Simonelli, L. Parry, I. Ashcroft, C. Tuck, R. Hague, 3D printing of Aluminium alloys: Additive Manufacturing of Aluminium alloys using selective laser melting, Prog. Mater. Sci. 106 (2019) 100578.

[6] Y. Huang, M.C. Leu, J. Mazumder, A. Donmez, Additive manufacturing: Current state, future potential, gaps and needs, and recommendations, J. Manuf. Sci. Eng. Trans. ASME. 137 (2015) 1–10.

[7] B.E. Carroll, T.A. Palmer, A.M. Beese, Anisotropic tensile behavior of Ti-6Al-4V components fabricated with directed energy deposition additive manufacturing, Acta Mater. 87 (2015) 309–320.

[8] B.A. Szost, S. Terzi, F. Martina, D. Boisselier, A. Prytuliak, T. Pirling, M. Hofmann, D.J. Jarvis, A comparative study of additive manufacturing techniques: Residual stress and microstructural analysis of CLAD and WAAM printed Ti-6Al-4V components, Mater. Des. 89 (2016) 559–567.

[9] S.W. Williams, F. Martina, A.C. Addison, J. Ding, G. Pardal, P. Colegrove, Wire + arc additive manufacturing, Mater. Sci. Technol. 32 (2016) 641–647.

[10] T. DebRoy, T. Mukherjee, J.O. Milewski, J.W. Elmer, B. Ribic, J.J. Blecher, W. Zhang, Scientific, technological and economic issues in metal printing and their solutions, Nat. Mater. 18 (2019) 1026–1032.

[11] P. Bajaj, A. Hariharan, A. Kini, P. Kürnsteiner, D. Raabe, E.A. Jägle, Steels in additive manufacturing: A review of their microstructure and properties, Mater. Sci. Eng. A. 772 (2020) 138633.

[12] B. Dutta, F.H.S. Froes, The Additive Manufacturing (AM) of titanium alloys, Met. Powder Rep. 72 (2017) 96–106.

[13] M. Komarasamy, S. Shukla, S. Williams, K. Kandasamy, S. Kelly, R.S. Mishra, Microstructure, fatigue, and impact toughness properties of additively manufactured nickel alloy 718, Addit. Manuf. 28 (2019) 661–675.

[14] H. Hack, R. Link, E. Knudsen, B. Baker, S. Olig, Mechanical properties of additive manufactured nickel alloy 625, Addit. Manuf. 14 (2017) 105–115.

[15] G. Marinelli, F. Martina, S. Ganguly, S. Williams, Microstructure, hardness and mechanical properties of two different unalloyed tantalum wires deposited via wire + arc additive manufacture, Int. J. Refract. Met. Hard Mater. 83 (2019) 104974.

[16] G. Marinelli, F. Martina, S. Ganguly, S. Williams, Development of Wire + Arc additive manufacture for the production of large-scale unalloyed tungsten components, Int. J. Refract. Met. Hard Mater. 82 (2019) 329–335.

[17] C.Y. Yap, C.K. Chua, Z.L. Dong, Z.H. Liu, D.Q. Zhang, L.E. Loh, S.L. Sing, Review of selective laser melting: Materials and applications, Appl. Phys. Rev. 2 (2015) 041101.

[18] A. Singh, S. Kapil, M. Das, A comprehensive review of the methods and mechanisms for powder feedstock handling in directed energy deposition, Addit. Manuf. 35 (2020) 101388.

[19] W.J. Sames, Additive manufacturing of Inconel 718 using electron beam melting: processing, post-processing and mechanical properties, PhD thesis, Texas A&M University, 2015.

[20] B. Wu, Z. Pan, D. Ding, D. Cuiuri, H. Li, J. Xu, J. Norrish, A review of the wire arc additive manufacturing of metals: properties, defects and quality improvement, J. Manuf. Process. 35 (2018) 127–139.

[21] B.W. Shinn, D.F. Farson, P.E. Denney, Laser stabilisation of arc cathode spots in titanium welding, Sci. Technol. Weld. Join. 10 (2005) 475–481.

[22] C. Wang, W. Suder, J. Ding, S. Williams, The effect of wire size on high deposition rate wire and plasma arc additive manufacture of Ti-6Al-4V, J. Mater. Process. Tech. 288 (2021) 116842.

[23] J. Ding, P. Colegrove, F. Martina, S. Williams, R. Wiktorowicz, M.R. Palt, Development of a laminar flow local shielding device for wire + arc additive manufacture, J. Mater. Process. Technol. 226 (2015) 99–105.

[24] D. Ding, Z. Pan, D. Cuiuri, H. Li, Wire-feed additive manufacturing of metal components: technologies, developments and future interests, Int. J. Adv. Manuf. Technol. 81 (2015) 465–481.

[25] A. Ho, H. Zhao, J.W. Fellowes, F. Martina, A.E. Davis, P.B. Prangnell, On the origin of microstructural banding in Ti-6Al4V wire-arc based high deposition rate additive manufacturing, Acta Mater. 166 (2019) 306–323.

[26] Norsk Titanium receives Thales Alenia Space contract to build structural additive manufactured components for orbital missions. https://www.businesswire.com/news/home/20160713005335/en/Norsk-Titanium-Receives-Thales-Alenia-Space-Contract-to-Build-Structural-Additive-Manufactured-Components-for-Orbital-Missions.

[27] F. Martina, J. Ding, S. Williams, A. Caballero, G. Pardal, L. Quintino, Tandem metal inert gas process for high productivity wire arc additive manufacturing in stainless steel, Addit. Manuf. 25 (2019) 545–550.

[28] G. Liu, J. Xiong, External filler wire based GMA-AM process of 2219 aluminum alloy, Mater. Manuf. Process. 35 (2020) 1268–1277.

[29] Y. Feng, B. Zhan, J. He, K. Wang, The double-wire feed and plasma arc additive manufacturing process for deposition in Cr-Ni stainless steel, J. Mater. Process. Technol. 259 (2018) 206–215.

[30] K.M. Taminger, R.A. Hafley, Electron beam freeform fabrication for cost effective near-net shape manufacturing, NATO/RTOAVT-139 specialists' meeting on cost effective manufacture via net shape processing, Amsterdam, 2006.

[31] Make metal parts faster & cheaper with EBAM® metal 3D printing technology. https://www.sciaky.com/additive-manufacturing/electron-beam-additive-manufacturing-technology.

[32] D.A. Gurnett, A. Bhattacharjee, Introduction to plasma physics: with space and laboratory applications, Cambridge University Press, Cambridge, 2005.

[33] C.S. Wu, L. Wang, W.J. Ren, X.Y. Zhang, Plasma arc welding: Process, sensing, control and modeling, J. Manuf. Process. 16 (2014) 74–85.

[34] T.Q. Li, C.S. Wu, Y.H. Feng, L.C. Zheng, Modeling of the thermal fluid flow and keyhole shape in stationary plasma arc welding, Int. J. Heat Fluid Flow. 34 (2012) 117–125.

[35] X. Jian, C.S. Wu, Numerical analysis of the coupled arc-weld pool-keyhole behaviors in stationary plasma arc welding, Int. J. Heat Mass Transf. 84 (2015) 839–847.

[36] J.J. Lin, Y.H. Lv, Y.X. Liu, B.S. Xu, Z. Sun, Z.G. Li, Y.X. Wu, Microstructural evolution and mechanical properties of Ti-6Al-4V wall deposited by pulsed plasma arc additive manufacturing, Mater. Des. 102 (2016) 30–40.

[37] X. Bai, P. Colegrove, J. Ding, X. Zhou, C. Diao, P. Bridgeman, J. Hönnige, H. Zhang, S. Williams, Numerical analysis of heat transfer and fluid flow in multilayer deposition of PAW-based wire and arc additive manufacturing, Int. J. Heat Mass Transf. 124 (2018) 504–516.

[38] R. Bini, B.M. Colosimo, A.E. Kutlu, M. Monno, Experimental study of the features of the kerf generated by a 200 A high tolerance plasma arc cutting system, J. Mater. Process. Technol. 196 (2008) 345–355.

[39] H.Y. Zhang, C.X. Li, S.H. Liu, L. Li, G.J. Yang, C.J. Li, S.L. Zhang, Splash involved deposition behavior and erosion mechanism of long laminar plasma sprayed NiCrBSi coatings, Surf. Coatings Technol. 395 (2020) 125939.

[40] W. Suder, Study of fundamental parameters in hybrid laser welding, PhD thesis, Cranfield University, 2011.

[41] E. Goncalves Assuncao, Investigation of conduction to keyhole mode transition, PhD thesis, Cranfield University, 2012.

[42] J.M. Sánchez-Amaya, T. Delgado, J.J. De Damborenea, V. Lopez, F.J. Botana, Laser welding of AA 5083 samples by high power diode laser, Sci. Technol. Weld. Join. 14 (2009) 78–86.

[43] J.C. Ion, Laser processing of engineering materials: principles, procedure and industrial application, Elsevier, Oxford, 2005.

[44] T. Sibillano, A. Ancona, V. Berardi, E. Schingaro, G. Basile, P.M. Lugarà, Optical detection of conduction/keyhole mode transition in laser welding, J. Mater. Process. Technol. 191 (2007) 364–367.

[45] R. Rai, G.G. Roy, T. Debroy, A computationally efficient model of convective heat transfer and solidification characteristics during keyhole mode laser welding, J. Appl. Phys. 101 (2007) 054909.

[46] W.E. King, H.D. Barth, V.M. Castillo, G.F. Gallegos, J.W. Gibbs, D.E. Hahn, C. Kamath, A.M. Rubenchik, Observation of keyhole-mode laser melting in laser powder-bed fusion additive manufacturing, J. Mater. Process. Technol. 214 (2014) 2915–2925.

[47] I. Eriksson, A.F. Kaplan, Evaluation of laser weld monitoring - A case study, ICALEO, LIA, (2009) 1419–1425.

[48] J. Weston, Surface related features of laser welding of aluminium alloys. ISIJ Int. 40 (2000) S6-S9.

[49] A.K. Nath, R. Sridhar, P. Ganesh, R. Kaul, Laser power coupling efficiency in conduction and keyhole welding of austenitic stainless steel. Sadhana - Academy proceedings in engineering sciences, 27 (2002) 383–392.

[50] R. Indhu, V. Vivek, S. Loganathan, A. Bharatish, S. Soundarapandian, Overview of laser absorptivity measurement techniques for material processing, Lasers Manuf. Mater. Process. 5 (2018) 458–481.

[51] P.W. Fuerschbach, D.O. MacCallum, Variation of laser energy transfer efficiency with weld pool depth, ICALEO, LIA, (1995) 497–503.

[52] H. Kwon, W.K. Baek, M.S. Kim, W.S. Shin, J.J. Yoh, Temperature-dependent absorptance of painted aluminum, stainless steel 304, and titanium for 1.07 μm and 10.6 μm laser beams, Opt. Lasers Eng. 50 (2012) 114–121.

[53] S. Patel, M. Vlasea, Melting modes in laser powder bed fusion, Materialia 9 (2020) 100591.

[54] S. Katayama, Y. Kawahito, K. Kinoshita, N. Matsumoto, M. Mizutani, Weld penetration and phenomena in 10 kW fiber laser welding, ICALEO, LIA, (2007) 540.

[55] W.M. Steen, K. Watkins, Laser material processing, Springer, London, 2003.

[56] D. Hipp, A. Mahrle, S. Jäckel, E. Beyer, C. Leyens, U. Füssel, Method for high accuracy measurements of energy coupling and melting efficiency under welding conditions, J. Laser Appl. 30 (2018) 032414.

[57] P.W. Fuerschbach, G.A. Knorovsky, A study of melting efficiency in plasma arc and gas tungsten arc welding, Weld. J. 70 (1991) 287–297.

[58] J.N. DuPont, A.R. Marder, Thermal efficiency of arc welding processes. Weld. J. 74 (1995) 406–416.

[59] D. Bergström, The absorption of laser light by rough metal surfaces, PhD thesis, Luleå University of Technology, 2008.

[60] R.W. Niles, C.E. Jackson, Weld thermal efficiency of the GTAW process, Weld. J. 54 (1975) 25–32.

[61] A. Caballero, J. Ding, S. Ganguly, S. Williams, Wire + Arc Additive Manufacture of 17-4 PH stainless steel: Effect of different processing conditions on microstructure, hardness, and tensile strength, J. Mater. Process. Technol. 268 (2019) 54–62.

[62] J. Xiong, G. Zhang, H. Gao, L. Wu, Modeling of bead section profile and overlapping beads with experimental validation for robotic GMAW-based rapid manufacturing, Robot. Comput. Integr. Manuf. 29 (2013) 417–423.

[63] D. Ding, Z. Pan, D. Cuiuri, H. Li, A multi-bead overlapping model for robotic wire and arc additive manufacturing (WAAM), Robot. Comput. Integr. Manuf. 31 (2015) 101–110.

[64] S. Suryakumar, K.P. Karunakaran, A. Bernard, U. Chandrasekhar, N. Raghavender, D. Sharma, Weld bead modeling and process optimization in hybrid layered manufacturing, CAD Comput. Aided Des. 43 (2011) 331–344.

[65] M. Dinovitzer, X. Chen, J. Laliberte, X. Huang, H. Frei, Effect of wire and arc additive manufacturing (WAAM) process parameters on bead geometry and microstructure, Addit. Manuf. 26 (2019) 138–146.

[66] F. Martina, J. Mehnen, S.W. Williams, P. Colegrove, F. Wang, Investigation of the benefits of plasma deposition for the additive layer manufacture of Ti-6Al-4V, J. Mater. Process. Technol. 212 (2012) 1377–1386.

[67] M. Schulz, F. Klocke, J. Riepe, N. Klingbeil, K. Arntz, Process optimization of wire-based laser metal deposition of titanium, J. Eng. Gas Turbines Power. 141 (2019) 052102.

[68] T.E. Abioye, J. Folkes, A.T. Clare, A parametric study of Inconel 625 wire laser deposition, J. Mater. Process. Technol. 213 (2013) 2145–2151.

[69] S.H. Mok, G. Bi, J. Folkes, I. Pashby, Deposition of Ti-6Al-4V using a high power diode laser and wire, Part I: Investigation on the process characteristics, Surf. Coatings Technol. 202 (2008) 3933–3939.

[70] D. Ding, Z. Pan, D. Cuiuri, H. Li, S. Van Duin, N. Larkin, Bead modelling and implementation of adaptive MAT path in wire and arc additive manufacturing, Robot. Comput. Integr. Manuf. 39 (2016) 32–42.

[71] J. Xiong, G. Zhang, J. Hu, L. Wu, Bead geometry prediction for robotic GMAW-based rapid manufacturing through a neural network and a second-order regression analysis, J. Intell. Manuf. 25 (2014) 157–163.

[72] S. Wei, G. Wang, Y.C. Shin, Y. Rong, Comprehensive modeling of transport phenomena in laser hot-wire deposition process, Int. J. Heat Mass Transf. 125 (2018) 1356–1368.

[73] L. Sun, F. Jiang, R. Huang, D. Yuan, Y. Su, C. Guo, J. Wang, Investigation on the process window with liner energy density for single-layer parts fabricated by wire and arc additive manufacturing, J. Manuf. Process. 56 (2020) 898–907.

3 Understanding the limitations of a single axisymmetric heat source – PTA

3.1 The effect of wire size on high deposition rate wire and plasma arc additive manufacture of Ti-6Al-4V

Chong Wang, Wojciech Suder, Jialuo Ding, Stewart Williams

Welding Engineering and Laser Processing Centre, Cranfield University, Cranfield, Bedfordshire, MK43 0AL, UK

Abstract: Wire + arc additive manufacture (WAAM) is suitable for building large-scale components at high deposition rates. However, in order to further increase the deposition rate of Ti-6Al-4V to improve productivity and reduce manufacture costs without significantly compromising the quality, some fundamental process characteristics need to be investigated. In this paper, the effect of wire size on the limitation of deposition rate and bead shape in plasma arc additive manufacture was studied along with the process tolerance and melting characteristics, such as the effect of current and nozzle size on keyhole behaviour and the effect of wire feeding position on the deposition process. The results show that with the same heat input, the deposition rate increases linearly with the wire size due to the increasing melting efficiency. The bead geometry obtained with a thinner wire has a higher aspect ratio, which can be attributed to the difference in the distribution of the energy between wire and workpiece. The likelihood of keyhole increases with increasing current and decreasing nozzle size, and it can be mitigated by using thicker wires. The wire feeding position plays a significant role in determining the metal transfer mode, which has a significant impact on the bead shape and process stability. Also, as the deposition rate changes, thin wire is more sensitive to wire feeding position than the thick wire in terms of metal transfer behaviour.

Keywords: Wire + arc additive manufacture; plasma transferred arc; titanium; high deposition rate; keyhole.

3.1.1 Introduction

Additive manufacture (AM) is a promising technology that can be used to build components by layer-upon-layer deposition of materials [1]. Compared to traditional subtractive manufacture, AM has distinctive advantages in the reduction of material wastage and machining effort required [2]. Furthermore, it offers a relatively short lead-time, high design freedom and low overall part costs [3]. Numerous AM techniques have been developed to produce metallic structures, which can be classified based upon feedstock and heat source [4]. Depending on the feedstock, AM techniques can be classified into powder based and wire based processes. In general, the powder based processes offer higher resolution and fidelity, whilst the wire based processes allow higher deposition rates. The layer thickness in a powder based process can be up to 200 μm [5], while a typical layer thickness in a wire based process is 1-2 mm [6]. This means that the wire based processes are more suitable for manufacturing of large-scale components where high volumes of deposited material are required. In addition, depending on the heat source, AM techniques can be split into laser, electron beam, and electric arc based processes. Amongst these, the arc based processes are the most cost-effective, as unlike electron beam they do not require a vacuum chamber and are more efficient than lasers. The electric arc fusion processes have been designed to efficiently melt the feedstock of wire and are widely used for welding and AM processes. They can be operated either in a global enclosure or out-of-chamber using a local shielding device [7]. Hence, wire + arc additive manufacture (WAAM) offers potentially an unlimited working envelope and high deposition rate, which is optimum for the fabrication of large-scale and medium-complex components.

In WAAM, various arc processes can be employed to serve as an energy source, including gas metal arc (GMA), gas tungsten arc (GTA), and plasma transferred arc (PTA). GMA with coaxially incorporated filler wire is commonly used for the deposition of steel and aluminium alloys, but it suffers from a significant arc wandering, spatter and poor surface quality in alloys with low work function, including titanium [8]. GTA and PTA with non-consumable electrodes do not

suffer from these issues and allow high-quality deposition with a wide range of materials. Compared to GTA, PTA has a higher stand-off distance and lower risk of tungsten contamination, thereby giving a higher process tolerance. Martina et al. [9] first used PTA to deposit titanium and developed a working envelope for the process. They concluded that PTA based WAAM process gives a higher deposition rate and larger effective wall width than other WAAM processes.

Depending on different deposition strategies, the deposition rate of titanium in WAAM processes ranges from 0.4 to 1.2 kg/h. A higher deposition rate would be desirable in order to reduce production times and therefore the overall costs, but the limit of productivity is dictated by the process physics and ability to control the melt pool shape. High deposition rate but with poor process control leads to an excessive amount of material needing to be deposited and subsequently machined away, which is counterproductive from the economic point of view [6]. Therefore, it is of critical significance to increase the deposition rate without compromising the quality and fidelity of the components.

Another factor limiting the deposition rate in the PTA deposition process is arc pressure. The high current induces the arc pressure upon the melt pool due to the electromagnetic force, and above a certain current level a keyhole is generated [10]. In welding, the keyhole is beneficial as a means of improving penetration depth and productivity [11]. In AM, however, the keyhole is undesirable as it leads to defects formation and poor efficiency. High penetration depth means unnecessary remelting of the underlying layers, which consequently reduces the process efficiency and may increase distortion in the components. Therefore it is important to understand the process limit and melting behaviour in order to maximise the feedstock melting and minimise penetration into the underlying layers.

Efficient feedstock melting is another important aspect in high deposition rate WAAM. One of the effective ways of improving deposition rate is to increase the wire feed speed (WFS) whilst increasing the energy input by using a higher current. For a given energy input, in order to feed the material more quickly, there

are different combinations of the wire size and WFS. For example, we can use either a thin wire with a high WFS or a thick wire with a low WFS. However, it needs to be understood which combination is more efficient. Moreover, with the same deposition rate and energy input, the bead shape and its quality are dependent on the melting behaviour of the wire. Ríos et al. [12] studied the metal transfer behaviour in the PTA deposition process by analysing the voltage waveform and video imaging, and stated that depending on the position of the feedstock in the arc, different metal transfer modes can be achieved, which affects the process stability and even bead quality. Chu and Lian [13] reported that the arc source does not have a uniform energy distribution and therefore there is a steep temperature gradient across the plasma arc, which means different regions of the arc have different temperature distributions. Therefore, the process is sensitive to the wire position with respect to the arc column. Furthermore, the wire diameter should play an important role in melting efficiency of wire and metal transfer mode, which is a key factor in improving the deposition rate of WAAM. However, all the effects of wire size on process characteristics and deposition rate in the PTA deposition process are not well understood.

In this work, the effect of wire diameter and feeding rate on the deposition rate and melting characteristics in the PTA deposition process of Ti-6Al-4V was studied. The main focus was to investigate which combination of wire diameter and WFS can give a higher deposition rate and better bead geometry and how to control the process and avoid defects at high deposition rates. All aspects of the limitations of deposition rate, bead shape control, keyhole formation and metal transfer were studied.

3.1.2 Experimental procedure

3.1.2.1 Materials and setup

The deposition was performed on Ti-6Al-4V substrates with dimensions of 300 mm × 200 mm × 7 mm. Four different sized Ti-6Al-4V wires with 1.2, 1.6, 2.0 and 2.4 mm diameters were used as feedstock. The grade and supplier of the wires are Ti6Al/4V and Perryman company, respectively. The chemical compositions

of the substrates and wires are listed in Table 3-1. The shielding gas and the plasma gas were pure argon (99.999 %). Figure 3-1 shows a schematic diagram of the experimental setup. The substrate was fixed onto an aluminium baseplate by means of M8 bolts, and the baseplate was clamped on the workbench. Before deposition, the substrates were polished and then cleaned with acetone to remove any surface contamination. For the WAAM system, a DC plasma power supply (EWM Tetrix 352) was used, and an arc monitor (AMV 4000) was used to record the arc voltage and current. The motion of the torch was provided by a computer numerical controlled (CNC) gantry system. A Lincoln wire feeder was used to feed the wire, and a CMOS process camera (Xiris XVC-1000) was used to record the melt pool and the wire melting behaviour. The camera recording rate and resolution were 55 fps and 1280×1024, respectively. The experiments were conducted in an argon-filled chamber to prevent the material from oxidation, where the chamber was purged until the oxygen level was below 500 ppm as verified by an oxygen analyser. This oxygen level was found to be optimum based on a previous study by Caballero et al. [14]. Also, the front feeding configuration was used. During the experiments, some process parameters were kept constant, as listed in Table 3-2.

Table 3-1 Chemical composition (in wt.%) of the Ti-6Al-4V substrate and wire.

	Al	V	Fe	C	N	H	O	Ti
Substrate	6.39	4.20	0.17	0.01	0.01	0.006	0.16	Balance
Wire	6.08	3.80	0.122	0.019	0.008	0.001	0.15	Balance

Table 3-2 Fixed process parameters used during the experiments.

Parameters	Value (unit)
Torch travel speed	4.5 mm/s
Bead length	120 mm
Plasma gas flowrate	0.8 L/min
Shielding gas flowrate	8 L/min
Wire feeding angle	25°
Nozzle to substrate stand-off	8 mm

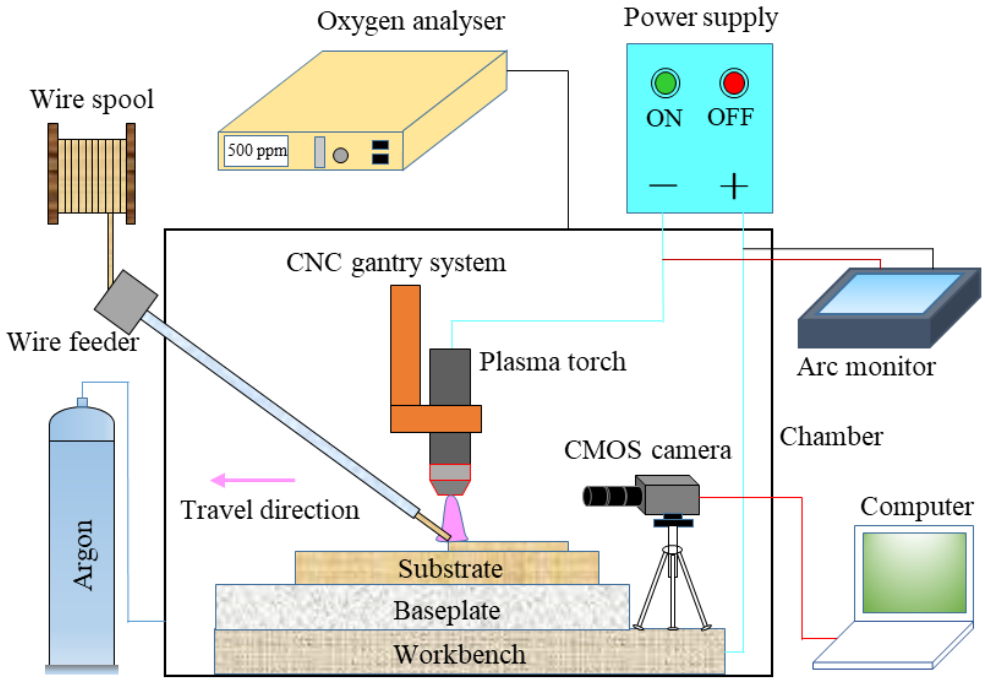


Figure 3-1 Schematic diagram showing the experimental setup.

3.1.2.2 Methods

Four different sized wires with diameters of 1.2, 1.6, 2.0 and 2.4 mm were used to identify the optimum combination of wire diameter and WFS for high deposition rate. For each size of the wire, the current was increased from 200 to 300 A with an increment of 50 A to study the effect of current on deposition rate. At each

current level, the WFS was increased until a limit value of melting and stabbing, which was determined from the process camera.

The effect of wire size on bead shape was studied using 1.2 and 2.4 mm wires at a constant current of 250 A. The WFSs for both wires were increased from low to high values, and the range of the deposition rates for both wires were same. After deposition, the samples were cross-sectioned, polished and etched to check the bead profile and remelting area.

The PTA is constricted by a water-cooled copper nozzle, which means the nozzle size affects the arc pressure and consequently keyhole formation. Therefore, in this study, two different sized nozzles with diameters of 3.0 and 3.9 mm were used to investigate the effect of nozzle size on keyhole behaviour. For each size of the nozzle, different levels of current were applied to study the effect of current on keyhole behaviour.

Two wires with diameters of 1.2 and 2.4 mm were used to study the effect of wire feeding position on the deposition process. Figure 3-2 schematically shows the definition of the wire feeding position, where the distance between the wire and the substrate along the centreline of the torch is defined as *h*. For each size of the wire, *h* was increased from 0 to 3.0 mm with an increment of 0.5 mm. The metal transfer behaviour was monitored using the process camera, and the bead dimensions were measured using a digital vernier calliper.

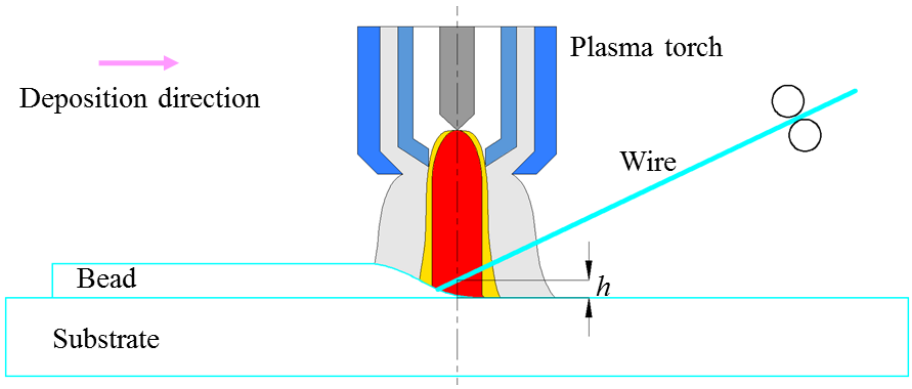


Figure 3-2 Wire feeding position in PTA-based deposition process (side view).

3.1.3 Results and discussion

3.1.3.1 Limitation of deposition rate

Figure 3-3 shows the melt pools for two different WFSs for a 1.6 mm wire at a current of 300 A. Up to a WFS of 5.4 m/min, the wire was completely melted, and the deposition process was stable (Figure 3-3a). However, when the WFS was increased to 6.0 m/min, the wire could not be melted completely and some violent disturbances occurred in the melt pool, as exhibited in Figure 3-3b. This is because when the WFS is too high, the volume of feedstock is too high for given energy input to fully melt the wire, and this causes stabbing of the wire tip which disturbs the melt pool.

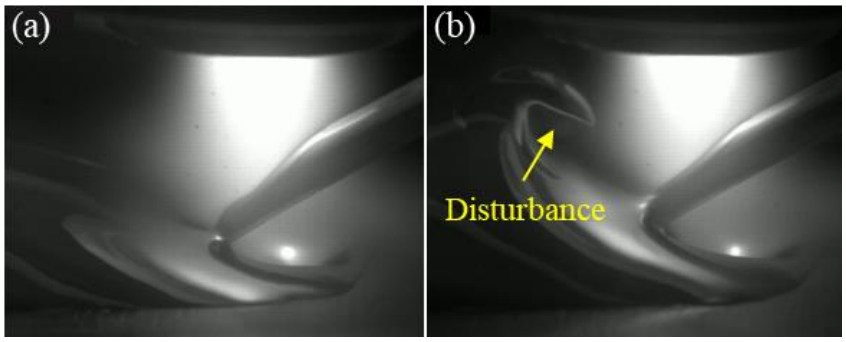


Figure 3-3 Comparison between (a) a stable deposition process at a WFS of 5.4 m/min, and (b) an unstable deposition process at a WFS of 6.0 m/min.

The same experiment was repeated for all the remaining wire diameters. The maximum WFS for different sized wires under different currents is shown in Figure 3-4. It can be seen that for each size of wire the maximum WFS increases with current. This is attributed to the increasing heat input as the current increases.

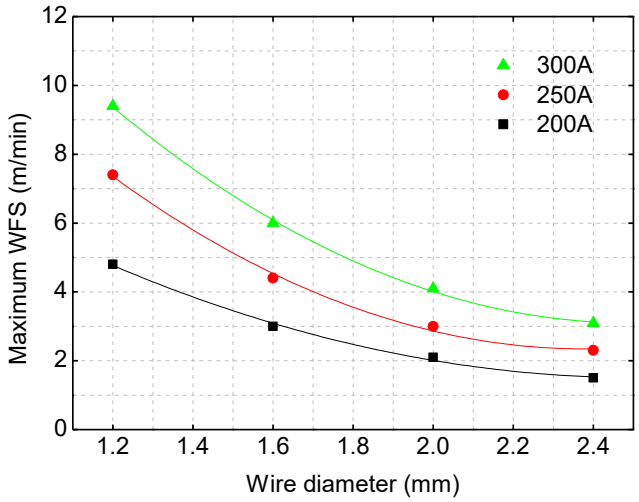


Figure 3-4 Effect of wire size and current on maximum WFS.

From Figure 3-4, one also can see that at the same current, the maximum WFS decreases with the increasing wire thickness. However, the deposition rate, R, is expressed as:

$$R = \frac{\pi d_w^2 v_w \rho_w}{4} \quad \textbf{(3-1)}$$

where d_w is the wire diameter, v_w is WFS and ρ_w is the density of the wire. Therefore, with Equation (3-1) and the data from Figure 3-4, the deposition rate as a function of wire diameter was achieved, as shown in Figure 3-5. It can be seen that for a particular current, the deposition rate increases linearly with wire size. This means that for the same energy input, a higher deposition rate can be achieved by using a thicker wire. This is because thick wire has a larger width and consequently a larger projected area under the arc, which enables it to capture more energy from the arc compared to a thin wire.

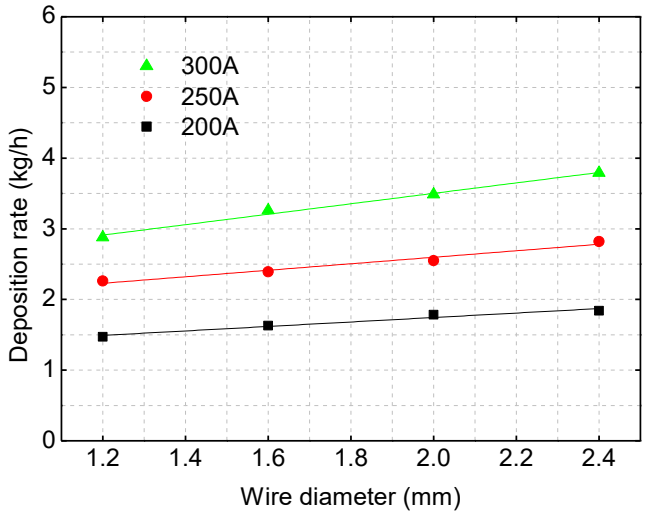


Figure 3-5 Effect of wire size and current on the limitation of deposition rate.

The effect of wire diameter has been schematically shown in Figure 3-6 with the projected areas of both wires under the plasma arc. It is assumed that the distribution of energy intensity in plasma arc is uniform, and the wire is melted by arc only (i.e. not reaches melt pool). It can be seen that the projected area of 2.4 mm wire (area B) is twice as that of 1.2 mm wire (area A). Therefore, in a unit time 2.4 mm wire absorbs twice the energy as 1.2 mm wire regardless of their WFSs. This indicates that twice the volume of 2.4 mm wire can be melted as that of 1.2 mm wire per unit time.

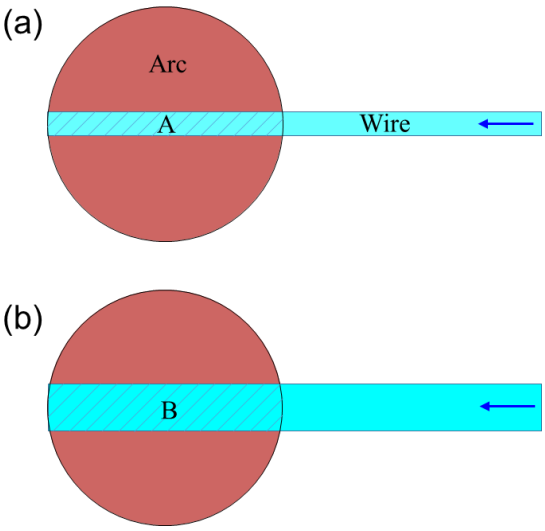


Figure 3-6 Diagram (top view) showing the projected areas of wires with different diameters under the PTA: (a) 1.2 mm and (b) 2.4 mm.

Also, a finite element (FE) modelling was conducted to support this explanation using 1.2 and 2.4 mm wires. In the modelling work, a power of 2000 W was applied on both wires. To make both wires fully melted, the maximum WFSs obtained for 1.2 and 2.4 mm wires were 3.00 and 1.38 m/min respectively. The temperature distributions of the two wires can be seen in Figure 3-7. According to Equation (3-1), the deposition rate of the 2.4 mm wire is around 1.84 times as that of 1.2 mm wire in this modelling work, which is close to the theoretical analysis. The difference is mainly because the heat source applied in the modelling work is a Gaussian distribution instead of a uniform distribution.

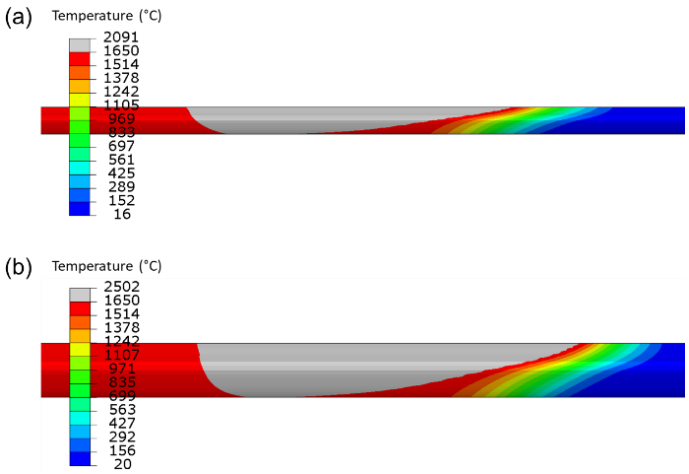


Figure 3-7 The temperature contours of (a) 1.2 mm wire, and (b) 2.4 mm wire in the FE modelling.

In reality, the thick wire is not as efficient as both theoretical analysis and FE modelling (e.g., deposition rates of 1.84 and 1.47 kg/h for 2.4 and 1.2 mm wires respectively at 200 A, see Figure 3-5). This is because that in theoretical analysis and FE modelling, the wires are only melted by the PTA. In practice, however, at high WFS the PTA does not melt the feedstock completely. Hence, both 1.2 and 2.4 mm wires reach the melt pool, which provided extra energy to fully melt the wires (take Figure 3-3 as an example). However, because the 2.4 mm wire screened more energy from the PTA so that the temperature in its melt pool was relatively low. Therefore, the energy absorbed from the melt pool by the 2.4 mm wire could not be as much as that of the 1.2 mm wire, resulting in only a bit higher deposition rate with the 2.4 mm wire.

In the deposition process, a significant proportion of the total arc energy absorbed by the workpiece is dissipated for conduction losses, and only a small proportion is utilised for melting [15,16]. Therefore, due to the less thermal loss of the wire compared to the workpiece, the melting efficiency is higher when using a thicker wire.

3.1.3.2 The effect of wire size on bead shape

In WAAM, a single bead is the smallest and fundamental unit of a built part. Therefore, the bead shape will determine the final surface waviness and consequently the deposition efficiency of the component. Figure 3-8 shows a schematic representation of different regions in a generic part cross-section (Figure 3-8a) and the surface waviness of two single-pass walls with different bead shapes (Figure 3-8b and 3-8c). Note that the volume of each single bead is the same for the two walls in Figure 3-8b and 3-8c. The deposition efficiency, ε, is defined as [9]:

$$\varepsilon = \frac{A}{A + B + C + D} \quad \textbf{(3-2)}$$

where area A corresponds to the material that can be used in the final part, whilst areas B, C and D correspond to the material that needs to be machined off. It can be seen that a low aspect ratio (i.e., the ratio of bead width to bead height) of the bead will lead to a high surface waviness and low deposition efficiency (Figure 3-8b), while a high aspect ratio of the bead with low and wide layer will ensure the near-net shape and high deposition efficiency (Figure 3-8c). This means that for the same deposited volume, more material needs to be machined away in the first wall (Figure 3-8b), and hence the second approach is more cost-effective and desirable (Figure 3-8c). Therefore, at a given cross-sectional area of the bead, the higher the aspect ratio of the bead, the better the surface finish and higher deposition efficiency of the component.

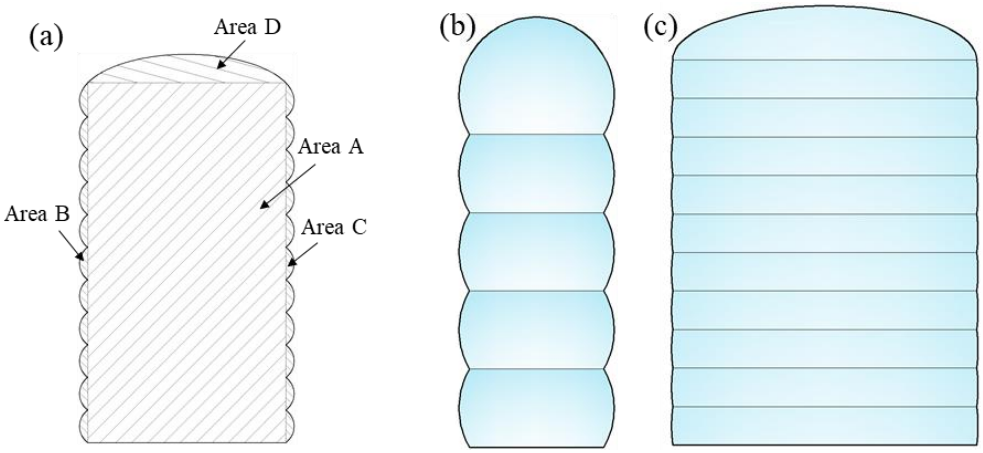


Figure 3-8 (a) Schematic representation of deposition efficiency; (b) a high surface waviness and low deposition efficiency obtained with the bead with low aspect ratio, and (c) a low surface waviness and high deposition efficiency obtained with the bead with high aspect ratio.

Two wire diameters were used to deposit single-layer beads with the same deposition rate, and their dimensions were compared. Figure 3-9 shows a comparison of the bead shape obtained with 1.2 and 2.4 mm wires at 250 A, and Figure 3-10 shows the corresponding cross-sections. In Figure 3-9a, it can be seen that for both wires, as the deposition rate (controlled by WFS) increases, the bead width increases gradually at first and then decreases very slightly. The width of the melt pool without feeding the wire (8.07 mm) is also shown in Figure 3-9a, which is less than those with the wire feeding. The increasing bead width at relatively low deposition rates (from 0.5 to 1.5 kg/h) is due to the increased melting efficiency. This is because as the WFS increases, more energy is absorbed by wire, and less energy is dissipated through the workpiece. Therefore, this leads to an increased melting efficiency and consequently wider beads. However, as the deposition rate further increases (from 1.5 kg/h), the melt pool is being depleted of the heat, and there is not enough heat to provide sufficient wetting with the substrate and this results in narrow and tall beads. An extra experiment was conducted to prove this, as shown in Figure 3-11, where the WFS was increased from 3 to 5 m/min in the first deposit and from 5 to 7 m/min in the second deposit. From the first case (Figure 3-11a), it can be clearly seen that the bead width increases as the WFS increases. However, in the

second case (Figure 3-11b) the bead width decreases due to the wire dipping into the melt pool. As for the bead height (Figure 3-9b), it increases constantly as the deposition rate increases due to the increase of the feeding material.

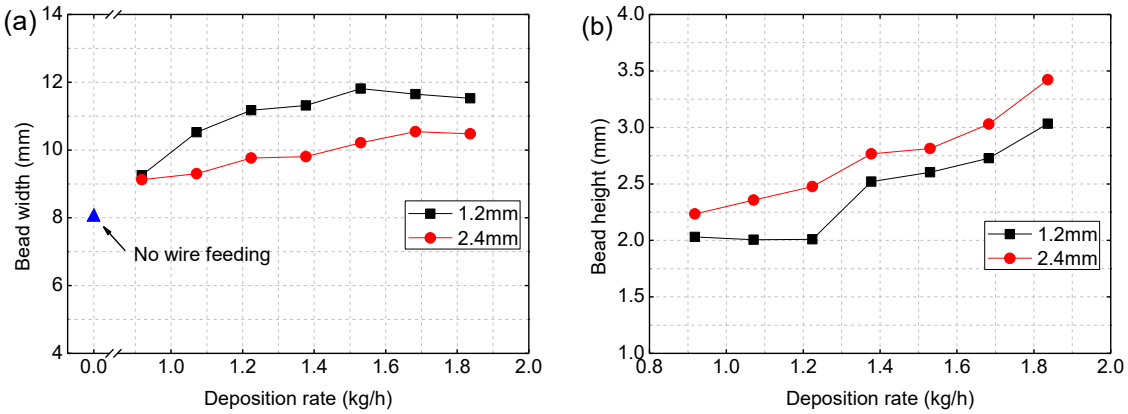


Figure 3-9 Bead dimensions as a function of deposition rate for 1.2 and 2.4 mm wires: (a) bead width, and (b) bead height.

Moreover, by comparing the bead shapes obtained with the two wires in Figure 3-9, one can see that at the same deposition rate the bead obtained with 1.2 mm wire is wider and lower compared to that of 2.4 mm wire, meaning that the former has a higher aspect ratio. As discussed in Section 3.1.3.1, due to the larger projected area under the arc, more energy goes to the thicker wire directly, and less energy goes to the workpiece, leading to a smaller melt pool and remelting area in the workpiece. This is consistent with the results presented in Figure 3-10, where at the same deposition rate the remelting area in the workpiece with 2.4 mm wire is smaller than that with 1.2 mm wire (note, the remelting area is hard to identify, but its size can be reflected by the heat-affected zone). Therefore, it can be concluded that at a same current and deposition rate, a higher aspect ratio of the bead can be obtained with a thinner wire, which will lead to a better surface finish and higher deposition efficiency of the component.

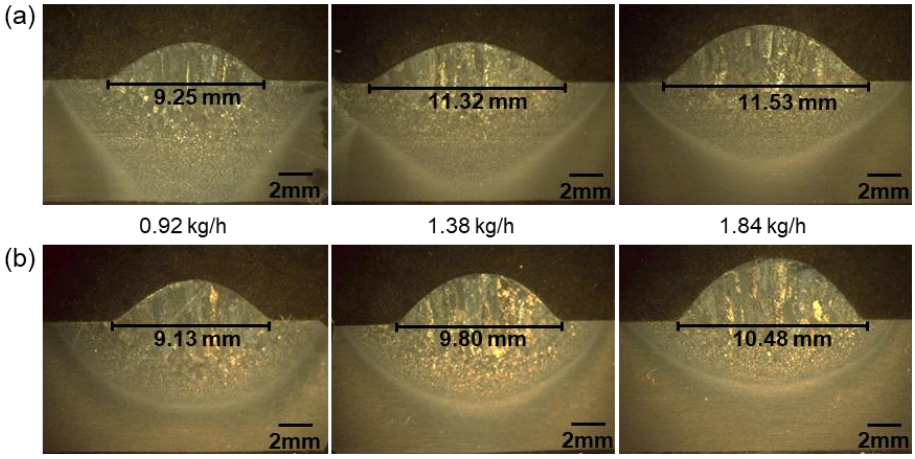


Figure 3-10 Cross-section of the beads at different deposition rates obtained with (a) 1.2 mm wire, and (b) 2.4 mm wire at the current of 250 A.

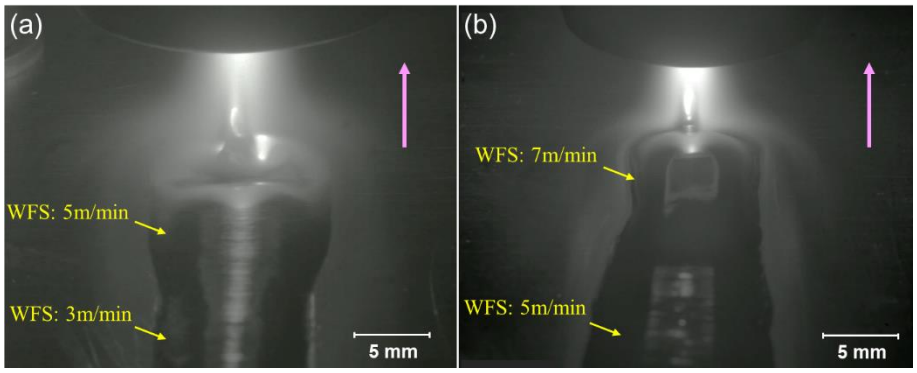


Figure 3-11 Bead shape changes with the increasing WFS during the deposition of 1.2 mm wire at 250 A: (a) bead width increases as the WFS increases from 3 to 5 m/min, and (b) bead width decreases as the WFS increases from 5 to 7 m/min. The pink arrows indicate the torch travel direction.

3.1.3.3 Keyhole behaviour

The keyhole is formed under a combined effect of intensive energy and arc pressure, where the intensive energy melts the workpiece, and the high pressure of the plasma jet produces a funnel-shaped cavity in the melt pool [17,18]. Specifically, the arc pressure is considered to be the dominant driven force for the keyhole formation [19,20], which can be expressed as [21]:

$$p = p_e + p_g = \frac{\mu_0 I^2}{4\pi^2}\left(\frac{1}{r_2^2} - \frac{1}{r_1^2}\right) + \frac{1}{2}\rho_g u_z^2 \quad \textbf{(3-3)}$$

where p_e is the pressure caused by electromagnetic force, p_g is the pressure caused by plasma gas flow, μ_0 is the magnetic permeability, I is the current, r_1 and r_2 are the radius of the arc at the workpiece and electrode, respectively, ρ_g is the plasma gas density, and u_z is the flow velocity of the plasma gas. It can be seen that the arc pressure consists of the pressure caused by electromagnetic force and the pressure caused by plasma gas force, where the former depends on the current and the latter depends on the plasma gas flow velocity. Therefore, a high current process and small nozzle diameter are likely to induce keyholes in the substrate or underlying layers. This is undesirable in WAAM, as it will limit the maximum energy input that can be used and consequently will limit the deposition rate. Figure 3-12 shows the keyhole appearances obtained with a stationary and a moving torch respectively without feeding the wire. In Figure 3-12a, there is a large depression in the centre of the melt pool due to the high arc pressure, where the liquid metal has been pushed away from the centre. In Figure 3-12b, the keyhole caused visible defects which were not subsumed by the liquid metal before solidification took place.

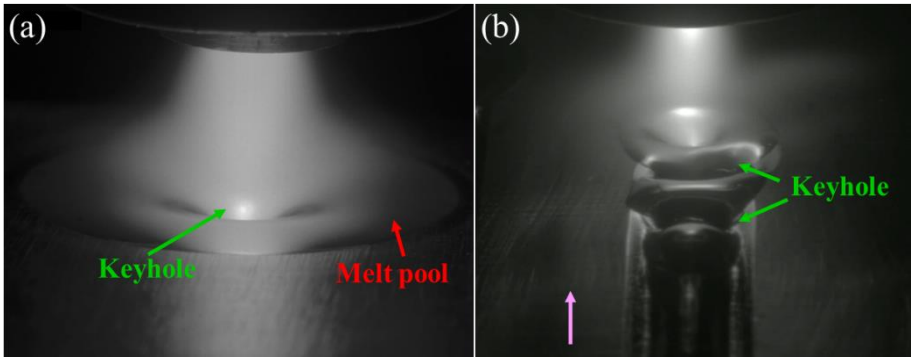


Figure 3-12 Keyhole appearance with (a) a stationary and (b) a moving plasma torch.

Figure 3-13 shows the cross-section of the samples under different currents and nozzle sizes with a stationary plasma torch. Note that no wire was fed in this case. From Figure 3-13a, it can be seen that there is a funnel-shaped cavity in each sample with a 3.0 mm nozzle, and the cavity becomes larger as the current increases. The formation of the cavity is due to incomplete closure of the keyhole

caused by the displacement of the liquid metal by arc pressure. Both energy input and arc pressure (p_e) increase as the current increases, which results in a greater keyhole size and consequently a larger cavity. However, there is no cavity formed at the current of 200 and 250 A with 3.9 mm nozzle, as shown in Figure 3-13b. This shows that the keyhole susceptibility decreases with an increase in nozzle size. This is because when the area of the nozzle exit increases, the flow velocity of the plasma gas decreases, which reduces the arc pressure (p_g) and leads to a lower likelihood of keyhole formation.

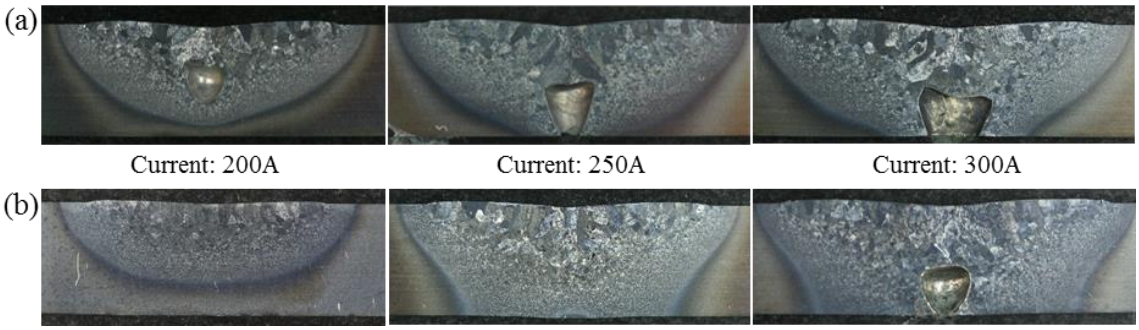


Figure 3-13 Cross-section of the samples with different currents and nozzle diameters: (a) 3.0 mm nozzle, and (b) 3.9 mm nozzle. The plasma torch was stationary.

Some experiments with a moving plasma torch were also conducted without feeding the wire, and the appearance of the samples is shown in Figure 3-14. It can be seen from Figure 3-14a that by using a 3.0 mm nozzle there is no obvious defect at a current of 200 A, but a defect caused by keyhole was generated at a current of 260 A. However, when using a 3.9 mm nozzle, no defect was found at both 200 and 260 A, as shown in Figure 3-14b. Generally, the nozzles used in the traditional PTA welding and cutting processes are less than 3.0 and 1.5 mm, respectively. Therefore, the nozzles used in the above experiments are relatively large. A 3.9 mm nozzle was adopted in all the following experiments of this study to decrease the likelihood of keyhole formation.

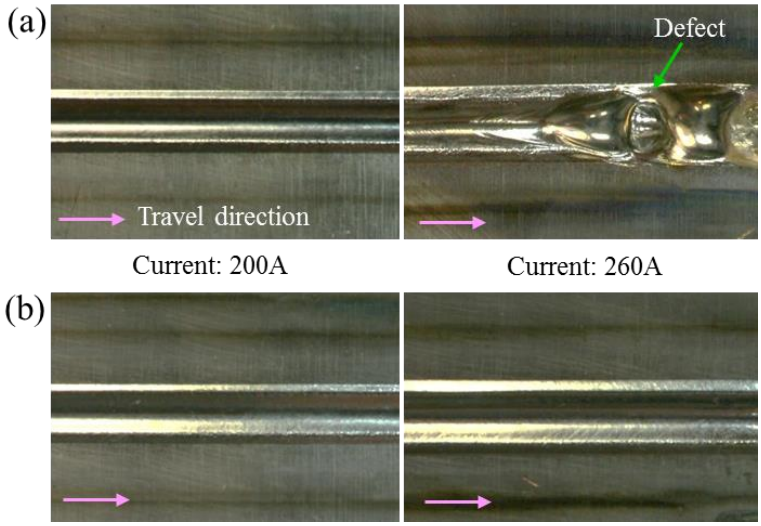


Figure 3-14 Appearance of the samples obtained with different currents and nozzle diameters: (a) 3.0 mm nozzle, and (b) 3.9 mm nozzle. The torch travel speed was 9.0 mm/s in these cases.

In the previous experiments, there was no wire feeding. However, the keyhole behaviour may change with the presence of a filler wire as the wire can obscure the plasma arc and reduce its impact on the workpiece. Figure 3-15 shows the deposition process using wires with diameters of 1.2, 1.6, 2.0 and 2.4 mm. In these cases, the deposition rate and current were the same. It can be seen that the keyhole is quite significant when using a 1.2 mm wire (Figure 3-15a), but it becomes smaller with a 1.6 mm wire (Figure 3-15b). For 2.0 and 2.4 mm wires, the keyhole formation was completely suppressed (Figure 3-15c and 3-15d). This is attributed to the screening of the plasma arc by the wire. With thin wires, only a small portion of the arc energy interacts directly with the wire, and most of it reaches the workpiece. However, as the wire diameter increases, the ability of the wire to obscure the arc increases and less energy is available to heat up the underlying workpiece, and a significant proportion of the electromagnetic force acts directly on the wire. This changes the energy balance between workpiece and wire while simultaneously suppressing the keyhole formation.

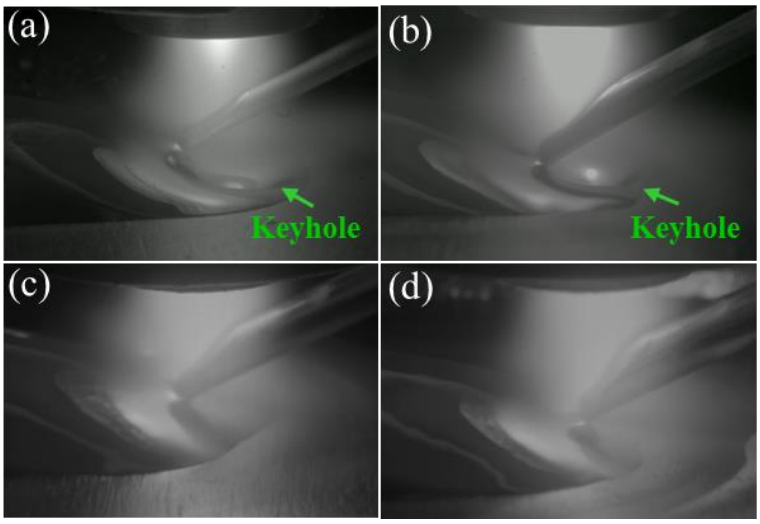


Figure 3-15 Effect of wire size on keyhole formation at 300 A for the following wire diameters: (a) 1.2 mm, (b) 1.6 mm, (c) 2.0 mm, and (d) 2.4 mm.

3.1.3.4 Wire feeding position

In wire based AM processes, there are mainly three types of metal transfer modes, which are surface tension transfer (also known as liquid bridge transfer), droplet surface tension transfer (also known as intermediate transfer), and free space droplet transfer (also named as droplet transfer) [22]. The stability of the process and the metal transfer mode are largely governed by the wire feeding position [12]. Figure 3-16 shows the deposition process and the bead width with different wire feeding positions at two different WFSs with a 1.2 mm wire. At a low WFS of 3.2 m/min (Figure 3-16a), the wire can be melted solely by the arc regardless of the wire feeding position. However, at a very low position (h=0 mm), the droplet touches the melt pool, which leads to a droplet surface tension transfer mode. When the wire feeding position is higher, the metal transfer turns into a free space droplet transfer mode. From Figure 3-16c, it can be seen that the bead width does not change so much with the increase of wire feeding position. At a high WFS of 4.4 m/min (Figure 3-16b), when the wire feeding position is low ($0 \leq h < 2.5$mm), the wire passes through the plasma arc and reaches the melt pool, leading to a surface tension transfer mode. As the wire feeding position increases from 2.5 to 3.0 mm, the metal transfer changes from a droplet surface tension to a free space droplet transfer mode.

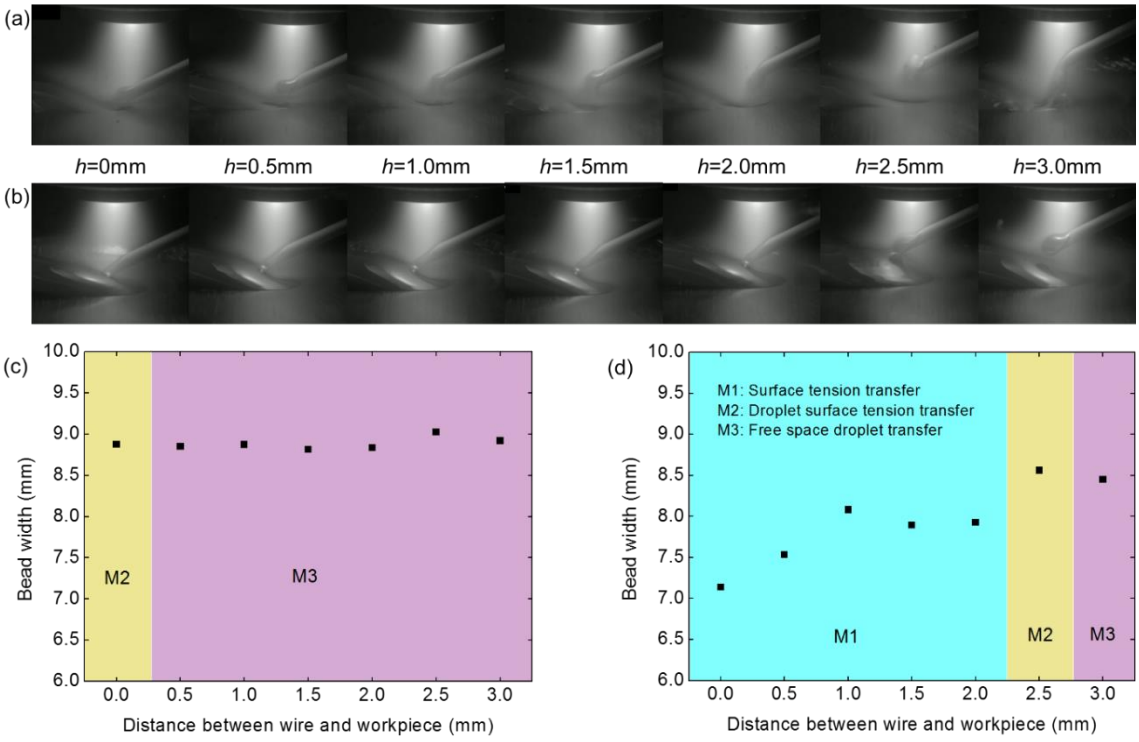


Figure 3-16 Deposition process with different wire feeding positions at the WFS of (a) 3.2 m/min (deposition rate: 0.98 kg/h), and (b) 4.4 m/min (deposition rate: 1.35 kg/h) with a 1.2 mm wire. Bead width and metal transfer mode as a function of *h*: (c) WFS=3.2 m/min, (d) WFS=4.4 m/min.

When the WFS is low, the wire is fully melted by the arc before it reaches the melt pool, which does not affect the metal transfer behaviour significantly. However, when the WFS is high, the metal transfer mode is affected by the wire feeding position. This is mainly because there is a temperature gradient in the PTA, where the temperature increases from the bottom to the top region [13]. In the high WFS case, when the wire feeding position is low, the wire could not be fully melted only by the arc, which means that additional energy needs to be taken from the melt pool. This depletion of energy from the melt pool by the wire results in a narrow bead shape. However, when the wire is positioned in the upper region of the PTA near the cathode where the arc is more focused, the wire could be completely melted by the PTA without interacting with the melt pool. This is the main reason that the bead width obtained with surface tension transfer mode is narrower than

with droplet surface tension and free space droplet transfer modes, as shown in Figure 3-16d.

The same experiment was replicated for 2.4 mm wire with the same deposition rates as those of 1.2 mm wire, and the results are shown in Figure 3-17. At both WFSs of 0.8 m/min (Figure 3-17a) and 1.1 m/min (Figure 3-17b), as the wire feeding position increases from 0 to 3 mm, the metal transfer changes from surface tension transfer mode to droplet surface tension transfer mode, and then to free space droplet transfer mode. Similarly to the previous case, the bead width in surface tension transfer mode is lower than in droplet surface tension and free space droplet transfer modes (Figure 3-17c and 3-17d). This is attributed to the depletion of heat from the melt pool by the wire as discussed earlier.

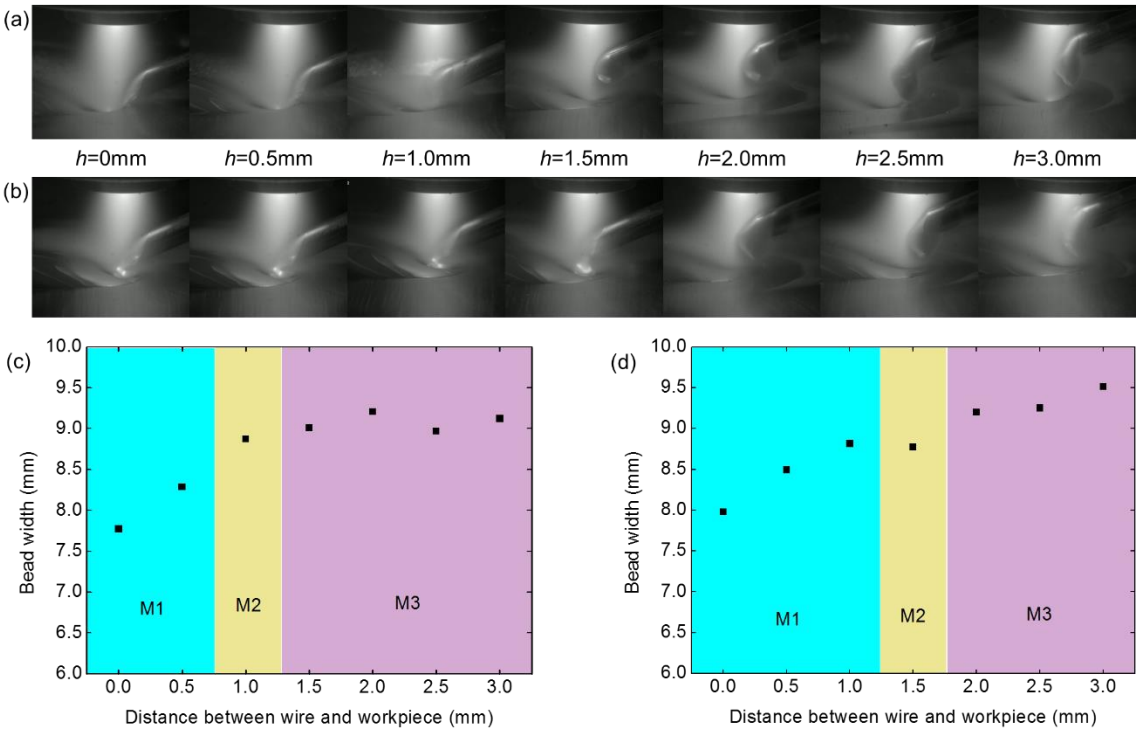


Figure 3-17 Deposition process with different wire feeding positions at the WFS of (a) 0.8 m/min (deposition rate: 0.98 kg/h), and (b) 1.1 m/min (deposition rate: 1.35 kg/h) with a 2.4 mm wire. Bead width and metal transfer mode as a function of *h*: (c) WFS=0.8 m/min, (d) WFS=1.1 m/min.

By comparing the results obtained with 1.2 mm and 2.4 mm wires, it can be seen that at two different deposition rates of 0.98 and 1.35 kg/h, the droplet surface

tension transfer mode occurred at the *h* of 0 and 2.5 mm respectively for 1.2 mm wire. However, this transfer mode occurred at two very close wire feeding positions (at the *h* of 1.0 and 1.5 mm, respectively) for 2.4 mm wire. This means that the transition of the metal transfer mode depends on the wire diameter, and 1.2 mm wire is more sensitive to the wire feeding position than 2.4 mm wire as the deposition rate increases. This is mainly because that the thick wire interacts more with the arc than the thin wire due to the bigger projected area and longer interaction time (attributed to lower WFS used for the same deposition rate), which means that it interacts less with the melt pool. This also can be seen from Figures 3-16b and 3-17b where the 1.2 mm wire reaches the middle part of the melt pool in surface tension transfer mode, while the 2.4 mm wire reaches the leading edge of the melt pool. The lower likelihood of interaction of thicker wire with the melt pool makes the process less sensitive to the variation of the transfer mode.

It can be seen that compared to surface tension transfer mode, the beads obtained with droplet surface tension and free space droplet modes are wider. Because of the erratic mode of the free space droplet transfer, spatter occurs occasionally in this case. Therefore, droplet surface tension transfer is recommended in the PTA deposition process, which not only gives a wider bead but also gives a more stable process. In addition, this mode is easier to be detected compared to other transfer modes, and therefore it is preferable in terms of process monitoring with closed-loop feedback system when using robotic processes [12].

Based on the obtained results, it can be seen that thicker wire is more efficient in terms of achieving a high deposition rate (Figure 3-5). For a fixed current, a considerably higher build rate can be achieved with bigger diameter wire (e.g., 3.8 kg/h for 2.4 mm wire versus 2.9 kg/h for 1.2 mm wire for 300 A). Alternatively, for a given build rate, the current required is lower as the wire diameter increases. This means that with thicker wires we can achieve a higher deposition rate using the same energy input, or we can use a lower energy input to achieve the same deposition rate. Also, the thick wire can block more arc than the thin wire, which

can mitigate the keyhole. In addition, as the deposition rate increases the metal transfer is not so sensitive to the wire feeding position for the thick wire. This means that in order to keep the same metal transfer mode in a part building process, the wire feeding position for thick wire does not need to be adjusted oftentimes as the WFS changes. However, at the same current and deposition rate, the bead shape obtained with the thinner wire has a higher aspect ratio, which is better for the surface finish of the component. In practice, thicker wires are more challenging for the feeding system due to their stiffness. For example, the 2.4 mm diameter wire was very hard to manipulate, especially when building parts with complex shapes, which required continuous rotation of the wire position around the plasma torch. Therefore, there will be a trade-off between the hardware and the thickest wire that can be used, meaning that the hardware of the system needs to be improved in order to use thicker wires.

3.1.4 Conclusions

1. For all the four wire sizes investigated in this study, more material could be melted with increasing current due to higher heat input. At the same current, the maximum deposition rate increases linearly with the wire size, which is caused by direct heating of the wire by the arc and lower amount of heat being transferred to the workpiece. A very high deposition rate of 3.8 kg/h was achieved at the current of 300 A using 2.4 mm wire.
2. For the same current and deposition rate, the bead obtained with 1.2 mm wire exhibited a higher aspect ratio than with 2.4 mm wire. Therefore, this wire allows the achievement of lower surface waviness during part building. Besides, the 1.2 mm wire was much easier to manipulate than the 2.4 mm wire.
3. Both the heat input and electromagnetic force increase with the increasing arc current, leading to the formation of the keyhole. The keyhole formation can be mitigated by using larger diameter nozzles due to the lower pressure of plasma gas. Keyhole can also be mitigated by using thicker wires due to the screening of the arc.

4. As the wire feeding position becomes higher from the substrate, the metal transfer changes from surface tension transfer mode to droplet surface tension transfer mode and then to a free space droplet transfer mode, which leads to an increasing bead width. The droplet surface tension transfer mode was found to give the most optimum bead shape and stable deposition with high enough tolerance. As the deposition rate increases, the metal transfer mode of thin wire is more sensitive to the wire feeding position than thick wire.

3.1.5 Acknowledgement

Chong Wang would like to express his gratitude to Cranfield University and China Scholarship Council (No. 201706450041) for funding his research studies. The authors would like to thank NEWAM (EP/R027218/1) and WAAMMat programmes for financial support. The authors also would like to thank Flemming Nielsen, Nisar Shah, John Thrower, and Steve Pope for the technical support.

3.1.6 References

[1] W.E. Frazier, Metal additive manufacturing: A review, J. Mater. Eng. Perform. 23 (2014) 1917–1928.

[2] T. DebRoy, H.L. Wei, J.S. Zuback, T. Mukherjee, J.W. Elmer, J.O. Milewski, A.M. Beese, A. Wilson-Heid, A. De, W. Zhang, Additive manufacturing of metallic components – Process, structure and properties, Prog. Mater. Sci. 92 (2018) 112–224.

[3] T.D. Ngo, A. Kashani, G. Imbalzano, K.T.Q. Nguyen, D. Hui, Additive manufacturing (3D printing): A review of materials, methods, applications and challenges, Compos. Part B Eng. 143 (2018) 172–196.

[4] D. Herzog, V. Seyda, E. Wycisk, C. Emmelmann, Additive manufacturing of metals, Acta Mater. 117 (2016) 371–392.

[5] X. Shi, S. Ma, C. Liu, C. Chen, Q. Wu, X. Chen, J. Lu, Performance of high layer thickness in selective laser melting of Ti6Al4V, Materials 9 (2016) 975.

[6] S.W. Williams, F. Martina, A.C. Addison, J. Ding, G. Pardal, P. Colegrove, Wire + arc additive manufacturing, Mater. Sci. Technol. 32 (2016) 641–647.

[7] J. Ding, P. Colegrove, F. Martina, S. Williams, R. Wiktorowicz, M.R. Palt, Development of a laminar flow local shielding device for wire + arc additive manufacture, J. Mater. Process. Technol. 226 (2015) 99–105.

[8] B.W. Shinn, D.F. Farson, P.E. Denney, Laser stabilisation of arc cathode spots in titanium welding, Sci. Technol. Weld. Join. 10 (2005) 475–481.

[9] F. Martina, J. Mehnen, S.W. Williams, P. Colegrove, F. Wang, Investigation of the benefits of plasma deposition for the additive layer manufacture of Ti-6Al-4V, J. Mater. Process. Technol. 212 (2012) 1377–1386.

[10] Y. Wang, B. Qi, B. Cong, M. Yang, F. Liu, Arc characteristics in double-pulsed VP-GTAW for aluminum alloy, J. Mater. Process. Technol. 249 (2017) 89–95.

[11] Y. Li, L. Wang, C. Wu, A novel unified model of keyhole plasma arc welding, Int. J. Heat Mass Transf. 133 (2019) 885–894.

[12] S. Ríos, P.A. Colegrove, S.W. Williams, Metal transfer modes in plasma Wire + Arc additive manufacture, J. Mater. Process. Technol. 264 (2019) 45–54.

[13] S.C. Chu, S.S. Lian, Numerical analysis of temperature distribution of plasma arc with molten pool in plasma arc melting, Comput. Mater. Sci. 30 (2004) 441–447.

[14] A. Caballero, J. Ding, Y. Bandari, S. Williams, Oxidation of Ti-6Al-4V during wire and arc additive manufacture, 3D Print. Addit. Manuf. 6 (2019) 91–98.

[15] P.W. Fuerschbach, G.A. Knorovsky, A study of melting efficiency in plasma arc and gas tungsten arc welding, Weld. J. 70 (1991) 287–297.

[16] J.N. DuPont, A.R. Marder, Thermal efficiency of arc welding processes. Weld. J. 74 (1995) 406–416.

[17] X. Jian, C.S. Wu, Numerical analysis of the coupled arc-weld pool-keyhole behaviors in stationary plasma arc welding, Int. J. Heat Mass Transf. 84 (2015) 839–847.

[18] T.Q. Li, C.S. Wu, J. Chen, Transient variation of arc heat flux and pressure distribution on keyhole wall in PAW, Weld. World. 60 (2016) 363–371.

[19] D. Wu, A. Van Nguyen, S. Tashiro, X. Hua, M. Tanaka, Elucidation of the weld pool convection and keyhole formation mechanism in the keyhole plasma arc welding, Int. J. Heat Mass Transf. 131 (2019) 920–931.

[20] T.Q. Li, C.S. Wu, Y.H. Feng, L.C. Zheng, Modeling of the thermal fluid flow and keyhole shape in stationary plasma arc welding, Int. J. Heat Fluid Flow. 34 (2012) 117–125.

[21] D.S. Dai, Y.L. Song, H. Zhang, Y.F. Zhu, Study on arc force in plasma welding, Trans. China Weld. Inst. 23 (2002) 51–54.

[22] R. Hu, X. Chen, G. Yang, S. Gong, S. Pang, Metal transfer in wire feeding-based electron beam 3D printing: Modes, dynamics, and transition criterion, Int. J. Heat Mass Transf. 126 (2018) 877–887.

3.2 Process characteristics of wire and plasma arc additive manufacture with a vertical wire feed

Chong Wang, Wojciech Suder, Jialuo Ding, Goncalo Pardal, Stewart Williams

Welding Engineering and Laser Processing Centre, Cranfield University, Cranfield, Bedfordshire, MK43 0AL, UK

Abstract: Wire + arc additive manufacture (WAAM) is suitable for building large engineering structures with high deposition rates and relatively low costs. In order to mitigate the keyhole formation and achieve uniform beads at different travel directions, a new plasma transferred arc (PTA) deposition process with the wire positioned perpendicularly to the workpiece and the plasma torch inclined was investigated and compared with the traditional PTA deposition process. The effect of travel direction on the bead shape was studied. The keyhole formation and maximum wire feeding rate that can be achieved were compared between the new and traditional processes. In addition, the metal transfer behaviour as a function of different process parameters was studied. The results show that owing to the inclined plasma torch, the arc pressure acting directly on the workpiece in the new process is lower than that in the traditional process, leading to a lower likelihood of keyhole formation. The new process is not truly omnidirectional, and the travel direction with torch trailing is optimum for the new process, which produces better bead geometry than other travel directions. The process parameters, including wire feed speed, current, and plasma gas flowrate have significant effect on the forces acting the droplets, which determine the droplet transfer behaviour and consequently the bead appearance.

Keywords: Wire + arc additive manufacture; Vertical wire; Travel direction; Keyhole formation; Metal transfer mode.

3.2.1 Introduction

Wire + arc additive manufacture (WAAM) has developed rapidly during the last decade as a flexible process that can be used to fabricate medium to large metallic components (metres in scale) with high deposition rate and relatively low equipment cost [1]. Compared with traditional subtractive manufacture where the parts are machined from solid billets or forgings, WAAM reduces a great deal of material wastage and lead time [2]. In WAAM process, an electric arc such as gas metal arc (GMA) [3], gas tungsten arc (GTA) [4,5] and plasma transferred arc (PTA) [6,7] is used as the heat source to melt the metallic wire, whilst the motion can be provided by a CNC or a robotic manipulator. Martina et al. [8] demonstrated first the benefits of using PTA to build titanium parts, which gives a higher maximum bead width and better stability than other WAAM processes. However, in the traditional PTA deposition process, the plasma torch is positioned vertically and the wire is fed slantwise, meaning that the deposition process is very sensitive to the wire feeding position with respect to the workpiece surface [9,10]. Furthermore, unlike in the GMA deposition process which is omnidirectional, different travel directions result in different bead shapes in the traditional PTA deposition process. In practice, this is overcome by the rotation of the end-effector during variable direction deposition, which complicates the tool-path planning when building complex structures. In addition, the perpendicular configuration of the torch to the workpiece induces high arc pressure on the liquid metal at high currents, which increases the likelihood of generating depression or even keyhole in the melt pool and therefore limits the maximum productivity [9]. However, with a vertical wire feed and inclined torch, the process should be more omnidirectional, and the arc column will not be as focused as in the traditional configuration, which should reduce the likelihood of keyhole formation.

To achieve uniform beads in different travel directions, many studies have been carried out in additive manufacture (AM) processes. Wu et al. [11] studied the effect of wire feeding direction and wire feeding angle on the GTA deposition process. They found that the beads had low quality at low (30°-50°) and high

(70°) wire feeding angles, and the bead geometry varied considerably in different wire feeding directions (i.e. travel directions), but a uniform bead shape could be obtained at the wire feeding angle of 60° in any wire feeding direction. However, the process window used was very narrow in their study, meaning that uniform deposits in different travel directions cannot be achieved after changing any process variables used. To eliminate the disadvantages of the commonly-used lateral wire feeding, Wang et al. [12] developed a laser wire setup, in which the laser and wire were integrated coaxially. The results showed that a uniform bead shape with a smooth bead surface was obtained in different travel directions. Fu et al. [13] proposed a laser deposition process with a vertical wire and three axisymmetric inclined lasers. A complex component was built successfully with uniform bead shape using this process, which demonstrated the benefit of perpendicular wire setup with respect to the workpiece. Similarly, Huft [14] developed a PTA deposition process with a vertical wire and three axisymmetric inclined plasma torches, which significantly reduced the sensitivity of the process to travel direction. However, this process is complex due to the interactions between the arcs and the complex energy profile. In addition, the results showed a relatively high remelting, which would indicate low process efficiency.

In this study, a PTA process with an inclined torch is proposed, meaning there is a change in the arc profile compared to the traditional process. As a result, two factors related to the heat source will be changed. One is the arc pressure, and the other is the energy distribution. For the arc pressure, it plays a dominant role in keyhole formation. Wang et al. [9] reported that a higher arc pressure increases the likelihood of keyhole formation, which reduces the process stability and even causes defects during the deposition process. Therefore, a low arc pressure leading to a keyhole-free process is desired in the PTA deposition process. As for the energy distribution, it might affect the melting behaviour of the wire and consequently the maximum feeding rate that can be achieved. The higher the wire melting efficiency, the higher the deposition rate that can be achieved for the same applied power, which reduces distortion and thermal damage in the material and decreases the overall costs. However, compared to the traditional

PTA deposition process, it is unclear how this new process with the vertical wire and inclined torch will affect the keyhole formation and deposition rate.

In addition, the metal transfer behaviour has an important effect on the process stability and bead formation. Wu et al. [15] claimed that in the GTA deposition process, the metal transfer is determined by different forces acting on the droplet, and any change of these forces alters the resultant force, which will affect the metal transfer behaviour and the final bead appearance. Compared to the GTA-based process, the forces in PTA-based process are more complicated due to the constricted plasma gas flow. In particular, when the wire is fed vertically, the direction and the magnitude of different forces will be changed, which should considerably influence the metal transfer and melt pool behaviour. Geng et al. [16] showed that the droplet transfer changed from bridging to globular as the distance from the wire tip to the melt pool surface increased in the GTA deposition process, thus leading to a lower bead quality. Ríos et al. [10] claimed that the stability of the PTA deposition process for titanium is critically dependent on the metal transfer mode, which is governed by the wire feeding position. Spatter occurs when the wire position is too high, whilst the wire tip hits the bottom of the melt pool when the wire position is too low. A similar phenomenon was reported by Wang et al. [9], who additionally found that the beads obtained with the droplet surface tension or free space droplet transfer modes are flatter than those obtained with the surface tension transfer mode.

In this study, a PTA-based WAAM process with a vertical wire and inclined torch for the deposition of Ti-6Al-4V is investigated. The effect of travel direction on bead shape was studied. In addition, the comparison between this new and the traditional processes, in terms of keyhole formation and maximum wire feeding rate that can be achieved, was conducted. Furthermore, the effect of different process parameters, including wire feed speed (WFS), current, and plasma gas flowrate on the metal transfer behaviour and bead appearance was investigated.

3.2.2 Experimental procedure

3.2.2.1 Materials and setup

Figure 3-18 shows the experimental setup for the proposed PTA deposition process. Ti-6Al-4V wire with a diameter of 1.6 mm was used as feedstock, which was fed perpendicularly to the substrate. The substrate used was also Ti-6Al-4V with dimensions of 300 mm × 200 mm ×7 mm, which was clamped on an aluminium workbench. Both plasma gas and shielding gas used for the plasma torch were pure argon. For the WAAM system, a 6-axis Fanuc robot and a plasma power source (EWM Tetrix 352) were used. The plasma torch and wire were fixed to the robot using a customised bracket, where the angle of the torch and the position of the wire was adjustable. The deposition was conducted in a flexible tent, which was filled with argon to protect the material from oxidation. The oxygen level in the tent was maintained below 500 ppm as checked by an oxygen analyser. During the experiment, an AMV 4000 arc monitor was used to record the current and voltage, and a CMOS process camera was fixed perpendicular to the torch-wire plane to record the arc behaviour and metal transfer.

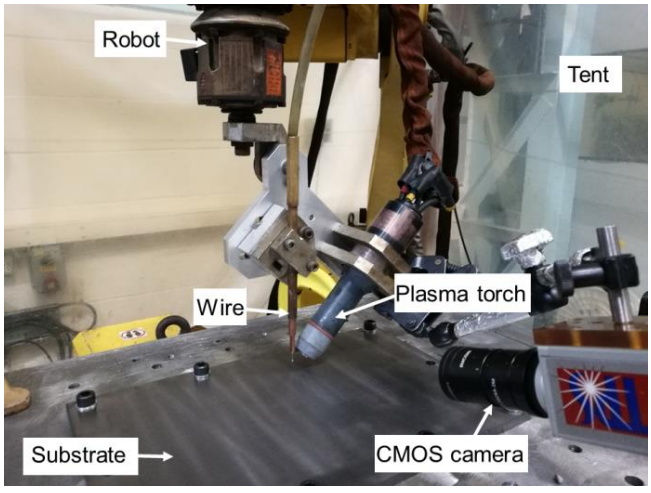


Figure 3-18 Experimental setup for the PTA-based WAAM system with a vertical wire and inclined torch.

3.2.2.2 Methods

As shown in Figure 3-19, the distance between the wire and the copper nozzle defined as *d*, the distance between the copper nozzle and the substrate defined

as *h*, and the torch angle (the angle between the plasma torch and the substrate) defined as *α* were varied during the experiment. Based on the output from preliminary trials, some process parameters were fixed in all the deposition processes in order to obtain acceptable bead profiles, as shown in Table 3-3.

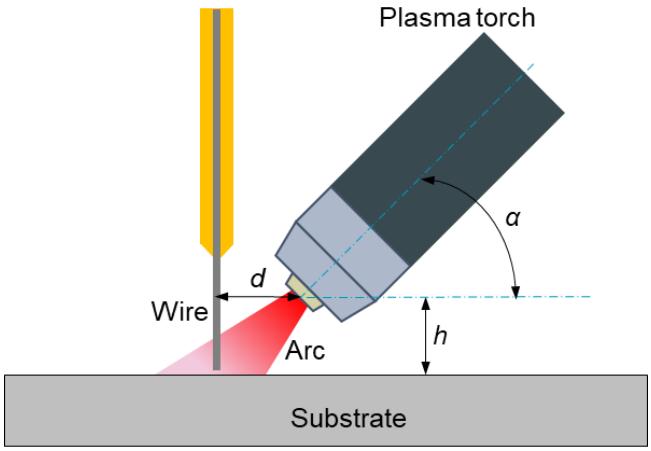


Figure 3-19 Schematic showing the definition of different parameters for the deposition process.

Table 3-3 Fixed parameters used in all experiments.

Parameters	Value
Torch travel speed	4.5 mm/s
Shielding gas flowrate	8 L/min
Bead length	100 mm
Copper nozzle to substrate stand-off (*h*)	8 mm
Copper nozzle diameter	3.9 mm

Firstly, the effect of travel direction on the bead shape was studied with the new process. Three different travel directions, i.e. torch leading, torch trailing, and torch on the side, were examined. The process parameters used in these three cases, including the torch angle (*α*), current, WFS, wire to nozzle distance (*d*), and plasma gas flowrate are shown in Table 3-4. Based on the obtained results

(explained in Section 3.2.3.1), the travel direction with torch trailing was used in all the following experiments.

Table 3-4 Parameters used for the study of travel direction effect.

Parameters	Value
Torch angle (α)	45°
Current	200 A
WFS	2.5 m/min
Wire to nozzle distance (d)	7.5 mm
Plasma gas flowrate	0.8 L/min

Secondly, some deposits were conducted with both the new process (i.e. vertical wire and inclined torch) and the traditional process (i.e. vertical torch and inclined wire) to compare the keyhole behaviour and the maximum feeding rate that can be achieved. To compare keyhole behaviour, the current used was 200 A, and the WFS used was 1.5 m/min for both processes. To compare the maximum feeding rate that can be achieved, the WFS was increased from a low value to a limit value where no more wire could be melted as identified by the process camera.

Thirdly, the effect of different process parameters on metal transfer behaviour was investigated. All the parameters are shown in Table 3-5. Amongst these experimental cases, the effect of WFS on the metal transfer was studied by comparing the results from Cases 1-3. Similarly, the effects of arc current (Cases 3-5) and plasma gas flowrate (Cases 3, 6, 7) were also studied.

Table 3-5 Parameters used for the metal transfer behaviour study.

Case	WFS (m/min)	Current (A)	Plasma gas flowrate (L/min)	Torch angle (°)	Wire to nozzle distance (mm)
1	3.5	200	0.8	30	5
2	3	200	0.8	30	5
3	2.5	200	0.8	30	5
4	2.5	180	0.8	30	5
5	2.5	160	0.8	30	5
6	2.5	200	0.7	30	5
7	2.5	200	0.6	30	5

3.2.3 Results and discussion

3.2.3.1 Effect of travel direction on bead shape

The processes with the vertical wire and vertical torch will be referred to as the new process and the traditional process, respectively. Figure 3-20 shows the new deposition processes with different travel directions, and Figure 3-21 shows the corresponding cross-sections of the deposited beads. Although the wire could be fully melted in the melt pool in all the three cases (Figure 3-20), the obtained bead shapes are significantly different (Figure 3-21). The bead achieved with torch leading (Figure 3-21a) is much narrower and higher than those of the other cases (Figure 3-21b and 3-21c). This is mainly attributed to the relative position between the arc and the melt pool. For the travel direction with torch leading, the PTA moves away from it after the melt pool is generated. For the other two cases, the PTA passes through it after the melt pool is generated. As a result, the melt pool absorbs less energy in the first case than in the other two cases, which limits its spread in the transverse direction, resulting in a relatively narrow and tall bead shape. In addition, as shown in Figure 3-21b, the bead obtained with the torch on the side exhibits an asymmetric profile. This is primarily caused by two reasons.

First, the temperature of the workpiece on the left side of the bead is higher than that of the right side due to the occurrence of the arc root. This means that the stronger heat sink on the right side promotes faster solidification of the molten material, resulting in smaller width on the right part of the bead. Second, the molten material is blown away to the left side by the arc pressure.

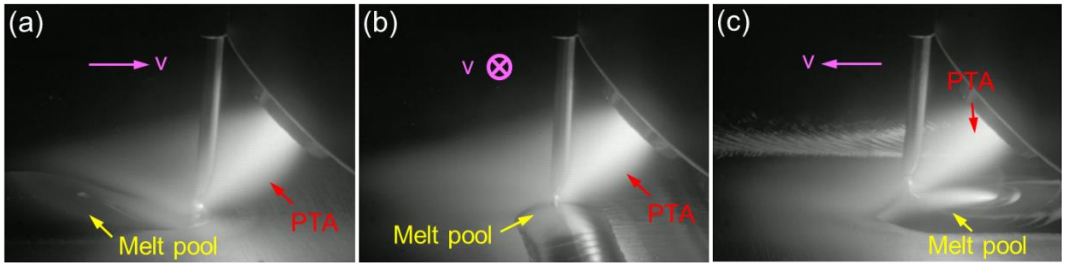


Figure 3-20 Deposition processes at different travel directions (indicated by the pink arrows): (a) torch leading, (b) torch on the side, and (c) torch trailing.

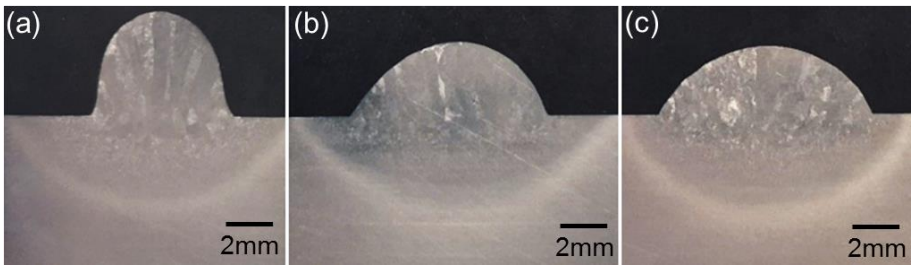


Figure 3-21 Cross-section of the beads obtained with different travel directions: (a) torch leading, (b) torch on the side, and (c) torch trailing.

From the results obtained, one can see that different bead shapes were achieved at different travel directions with the new process, which means that the process is not omnidirectional. This is because the energy source distribution is not axisymmetric about the vertical axis, which means that the arc energy is absorbed by different parts of the melt pool in different travel directions, resulting in different bead shapes.

In WAAM, the surface waviness of a component is dictated by the bead shape. Wang et al. [9] reported that a flatter bead results in a lower surface waviness for the same cross-sectional area, meaning less material needs to be machined off. Therefore, the bead obtained with the travel direction of torch leading will result

in a higher surface waviness than in the other two cases. In addition, a symmetric bead shape is required when building real components, which means the bead obtained with the travel direction of the torch on the side is not desired. Therefore, the travel direction with torch trailing seems to be the most suitable for this new process, and this configuration will be further studied.

3.2.3.2 Comparison with the traditional process

3.2.3.2.1 Keyhole behaviour

Figure 3-22 shows the comparison of the melting behaviour between the new and traditional processes for the same process parameters. It can be seen that there is no depression in the melt pool in the new process (Figure 3-22a), whilst a keyhole is generated in the traditional process (Figure 3-22b). It is reported that keyhole formation in the PTA-based processes is caused by the energy input and arc pressure, and the latter is the more dominant factor [17-20]. Here, the energy input was the same for the two cases, and therefore the keyhole generated in the second case was caused by a higher arc pressure compared to that in the first case. By comparing the two processes, one can see that the arc column in the new process is longer and impinges the surface at an angle. Actually, the arc pressure acting directly on the workpiece is expressed as:

$$p_n = p\sin\alpha \quad \textbf{(3-4)}$$

where p_n is the arc pressure normal to the workpiece, whilst p is the total arc pressure, and α is the torch angle. Therefore, the arc pressure acting directly on the workpiece increases as the torch angle increases from 0° to 90°. Specifically, at a torch angle of 30°, the arc pressure acting directly on the workpiece in the new process will be reduced by 50% compared to that in the traditional process. In addition, the longer arc column will also reduce the arc pressure [21]. Therefore, for the same process parameters, the new process has a lower arc pressure exerted in the normal to the surface than that of the traditional process, leading to a lower likelihood of keyhole formation. In WAAM, the keyhole is undesirable as it can induce defects in parts, which means that the deposition process needs to be operated below the keyhole threshold, limiting the maximum

current and deposition rate that can be used. Hence, inclining the torch can potentially allow higher currents to be used, leading to higher deposition rates.

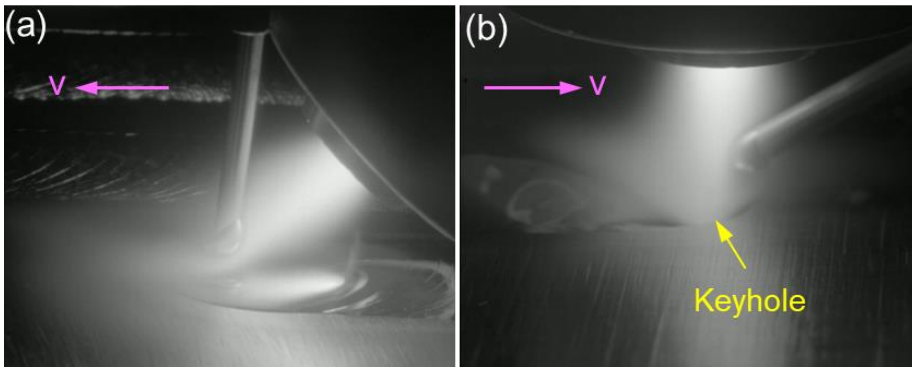


Figure 3-22 Comparison of the deposition processes between the (a) new process and (b) traditional process.

3.2.3.2.2 Deposition rate

During the experiment, it was found that the torch angle significantly affects the maximum wire feeding rate that can be achieved as it determines the regions of the melt pool and arc column that the wire could intercept. Figure 3-23 shows the deposition processes with different torch angles. Due to the lack of access, in each case the wire was positioned as close as practically possible to the plasma torch, which resulted in different distances (*d*) between the wire and copper nozzle. The distances (*d*) for the torch angles of 30°, 45° and 60° were 5, 7.5, and 10 mm, respectively. This led to different melting behaviour, as shown in Figure 3-23. At a torch angle of 60° (Figure 3-23a), the wire could not reach the PTA centre, leading to a partially melted wire and an unstable process. Besides, the keyhole was formed in this case. When the torch angle was reduced to 45° (Figure 3-23b), the wire could not be fully melted by the PTA before reaching the melt pool. This means that the wire needed to acquire additional energy from the melt pool to be fully melted. At a torch angle of 30° (Figure 3-23c), the wire was fully melted by the PTA before reaching the melt pool.

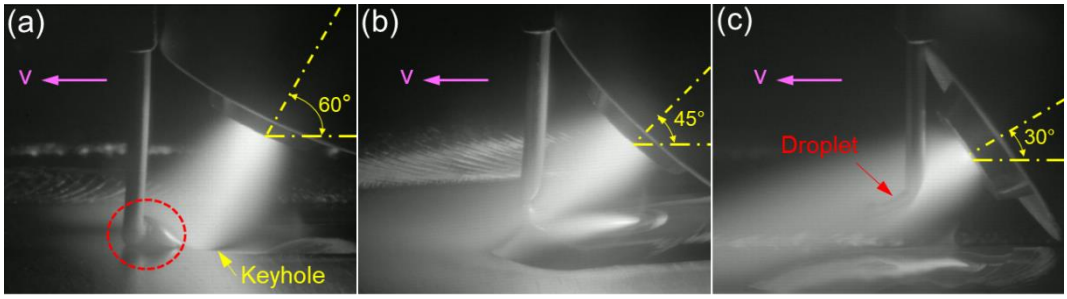


Figure 3-23 Deposition processes at different torch angles: (a) 60°, (b) 45°, and (c) 30°.

The difference in melting behaviour is attributed to the different positions of the wire in the arc column. It is known that there is a steep temperature gradient in the PTA column with the temperature reaching the highest point near the cathode [22]. Therefore, the closer the wire is to the copper nozzle (or cathode), the easier the wire can be melted. Wang et al. [9] also reported that the wire feeding position has a significant effect on the melting behaviour and melting efficiency in the PTA deposition process. For the same WFS, as the distance between the wire and copper nozzle increases, the metal transfer changes from free space mode to surface tension mode. This results in a lower melting efficiency as the wire takes additional energy from the melt pool in the latter transfer mode. In the three cases shown in Figure 3-23, the wire could be melted entirely by the PTA only in the last case due to possibility of positioning the wire in the closest proximity of the arc column, hence reaching the hottest region and the highest melting efficiency. Therefore, a torch angle of 30° was used in the following experiments to study the deposition rate.

Figure 3-24 shows the maximum wire feeding rates obtained with the new and the traditional processes at the same current of 200 A. The distance between the wire and the copper nozzle used was the same for both processes. In order to achieve the maximum deposition rate, both processes were operated near the melting threshold, which means that at this high WFS the wire could not be melted entirely in the arc column and reached the melt pool. It can be seen that the maximum wire feeding rates achieved with the same energy input were similar (around 3.0 kg/h). It is reported by Wang et al. [9] that the maximum wire feeding

rate that can be achieved increases with the energy input. Therefore, when the wire feeding position and the energy input are the same in the new and traditional processes, similar deposition rates will be achieved.

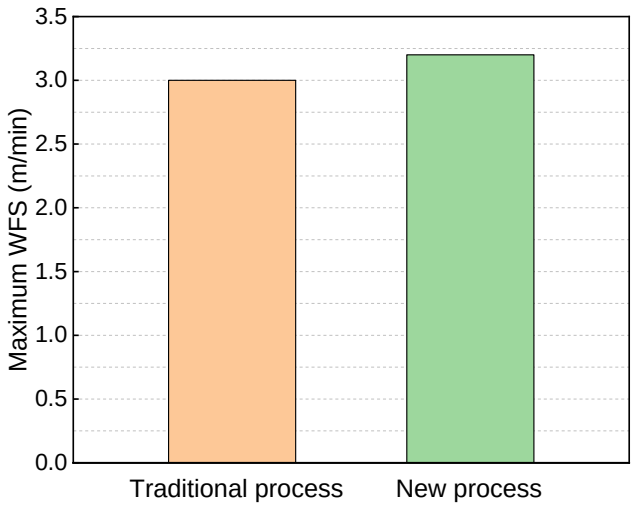


Figure 3-24 Maximum wire feeding rates obtained with the new and traditional processes at the same current of 200 A.

3.2.3.3 Metal transfer behaviour

3.2.3.3.1 Effect of WFS

Figure 3-25 shows the effect of WFS on metal transfer behaviour. At a WFS of 2.5 m/min (Figure 3-25a), the droplets were small when detaching from the wire tip. The WFS was relatively low in this case, and the wire was melted entirely by the PTA. The droplet transfer period was around 128 ms, and the voltage was stable during the transfer period. When the WFS was increased to 3.0 m/min (Figure 3-25b), the droplets became larger than those in the first case. The droplet transfer period increased to 585 ms, which is four times longer than in the first case. It is noteworthy that at the time intervals of 469 and 585 ms, the droplet touched the melt pool, leading to a noticeable change in arc voltage, from 28 to 24 V, due to the shortening of the arc column. This means that the droplets were large enough to bridge the arc gap and provided an easier path for the current to flow from the electrode to the workpiece. This phenomenon was also reported by Ríos et al. [10], who showed that such monitoring of voltage can be used to detect

the metal transfer mode in real-time to control the deposition process. At a WFS of 3.5 m/min (Figure 3-25c), the relatively high WFS resulted in more wire being fed at a given time. The wire could not be fully melted in the middle of the arc column and passed across the whole arc column to the other side. This resulted in a slow accumulation of the liquid metal at the wire tip and growth of large droplets.

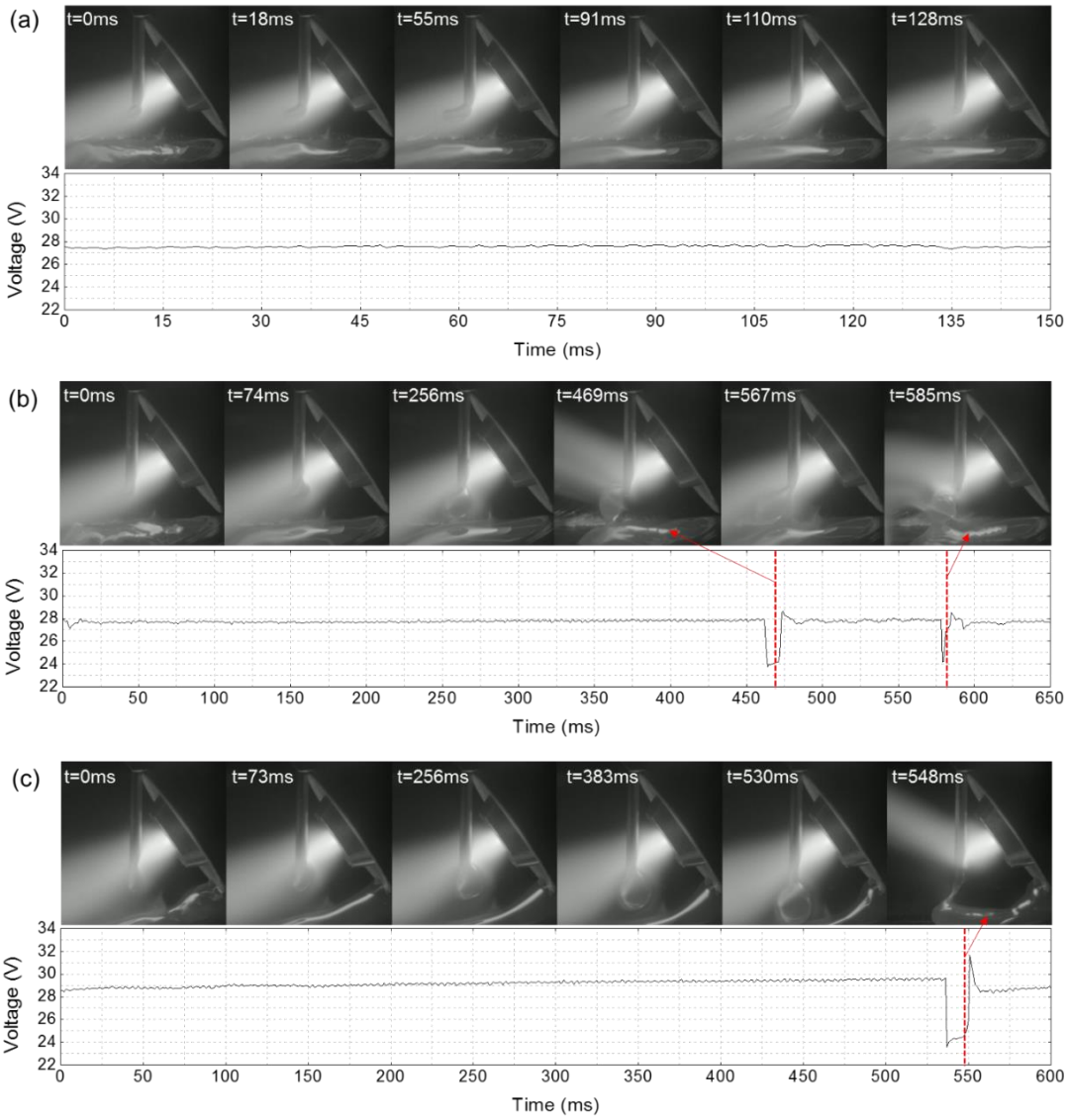


Figure 3-25 Droplet transfer and voltage waveform at different WFSs: (a) 2.5 m/min, (b) 3.0 m/min, and (c) 3.5 m/min.

At low WFSs, the droplets detached from the wire in the middle part of the arc column where the arc pressure could overcome the surface tension and remove

them. However, at high WFSs the wire can only be fully melted after passing the hottest part of the arc column, and lower arc pressure could not detach droplets which grew to large sizes until in contact with the melt pool. The wire melting and metal transfer behaviour play a critical role in the bead formation, which will be discussed later in Section 3.2.3.3.4.

3.2.3.3.2 Effect of current

Figure 3-26 shows the effect of current on the metal transfer behaviour. At a relatively low current of 160 A (Figure 3-26a), the surface tension of the droplets was high due to the low energy input, and the arc pressure was relatively low. Therefore, the arc pressure could not detach the droplets from the wire tip, and the wire passed across the entire arc column. As a result, large droplets and long transfer period (876 ms) occurred in this case. At a current of 180 A (Figure 3-26b), the wire could be melted more easily due to the increased energy input. In addition, the increased arc pressure and decreased surface tension made the droplets easier to detach from the wire tip, as reflected by the smaller droplet size and shorter transfer period. When the current was increased to 200 A, the high arc pressure and low surface tension led to a significant decrease in both droplet size and transfer period, as shown in Figure 3-26c.

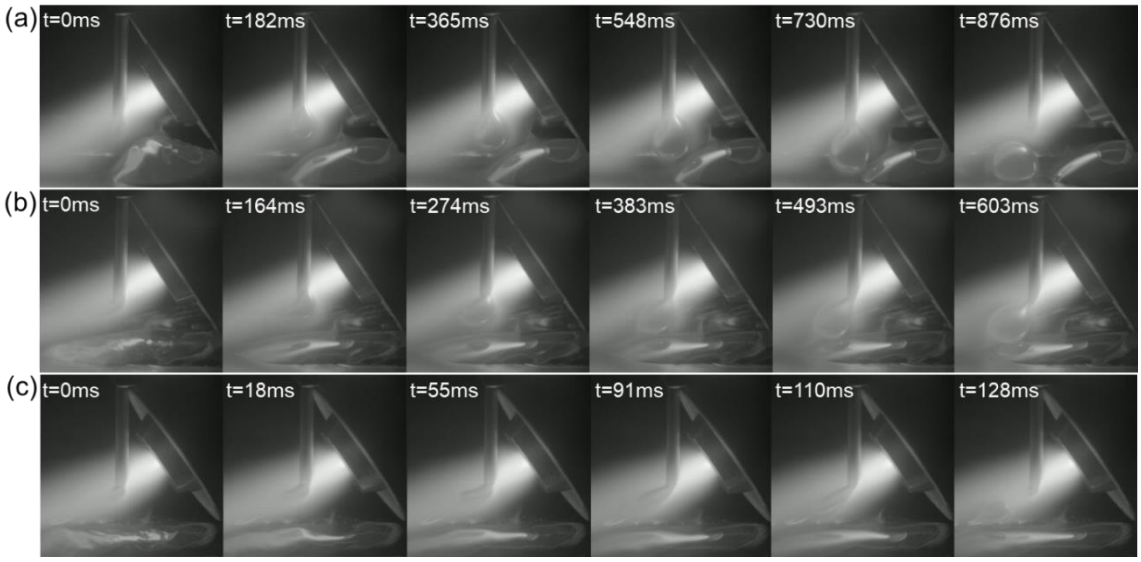


Figure 3-26 Droplet transfer at different levels of current: (a) 160 A, (b) 180 A, and (c) 200 A.

The effect of current on the metal transfer behaviour can be explained by analysing forces acting on the droplets. From Equation (3-3), it can be seen that the electromagnetic force increases with increasing current, resulting in a higher arc pressure (p_e). In addition, the temperature of the droplets also increases with increasing current, resulting in lower surface tension. Therefore, increasing the current makes the droplets easier to detach from the wire.

3.2.3.3.3 Effect of plasma gas flowrate

Figure 3-27 shows the effect of plasma gas flowrate on metal transfer behaviour. At a plasma gas flowrate of 0.6 L/min (Figure 3-27a), the droplets were relatively large with a transfer period of 420 ms. When the plasma gas flowrate was increased to 0.7 L/min (Figure 3-27b), the droplet size decreased, and the transfer period of the droplet reduced to 219 ms. As shown in Figure 3-27c, when the plasma gas flowrate was further increased to 0.8 L/min, much smaller droplets and higher frequency than in the previous two cases were observed.

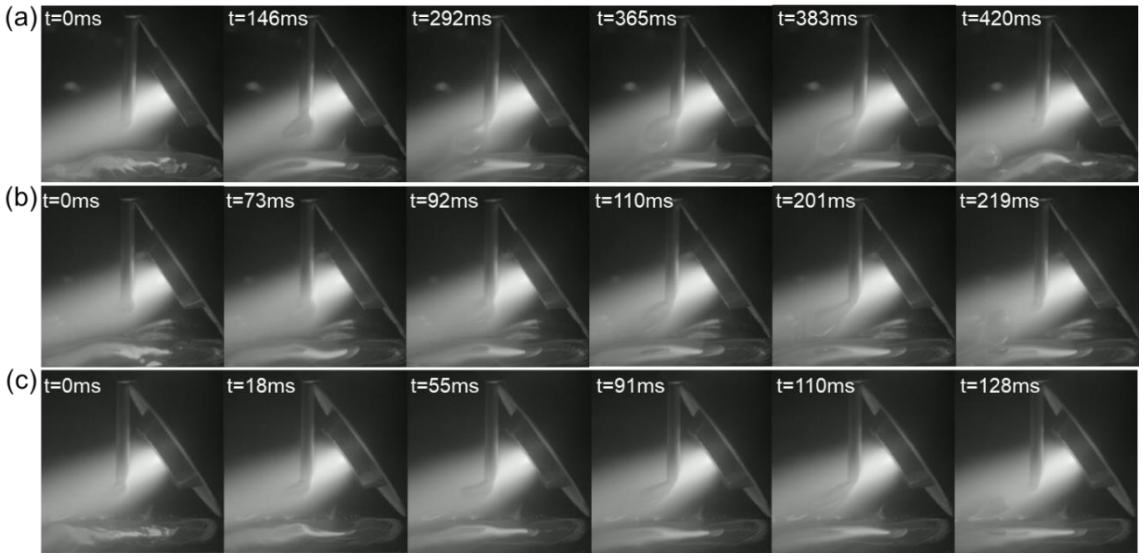


Figure 3-27 Droplet transfer with different plasma gas flowrates: (a) 0.6 L/min, (b) 0.7 L/min, and (c) 0.8 L/min.

From Equation (3-3), it can be seen that the arc pressure (p_g) increases with increasing plasma gas flowrate due to the increased plasma drag force. At a low plasma gas flowrate, the relatively low arc pressure struggled to detach droplets

and they grew up to a large size. The droplets could only be detached when in contact with the melt pool, leading to a large droplet and low transfer frequency. However, at a high plasma gas flowrate, the high arc pressure had enough force to flow off the droplets from the wire tip before they could grow up to a significant size, resulting in a high droplet transfer frequency.

3.2.3.3.4 Forces acting on droplets

In arc based processes, different forces act on a droplet and the detachment of the droplet is driven by their balance. For example, in the traditional GTA deposition process where the torch is normal to the surface and the wire is inclined at an angle of 30°, the resultant force acting on a droplet in the vertical direction is expressed by [15]:

$$F = \left(F_g + F_{em} + F_a + F_p sin30°\right) - \left(F_v + F_\sigma sin30°\right) \quad \textbf{(3-5)}$$

where F_g is the gravitational force, F_{em} is the electromagnetic force, F_a is the plasma drag force, F_p is the driving force of the wire, F_v is vapour jet force, and F_σ is surface tension. This equation also applies to the PTA deposition process as they both share the same mechanism of arc generation. From Equation (3-5), it can be seen that the gravitational force, electromagnetic force, plasma drag force, and the driving force of the wire act as detaching force, whilst vapour jet force and surface tension act as opposing force. Figure 3-28 schematically shows the difference in the forces acting on a droplet in the traditional and new PTA deposition processes. One can see that the directions of most of the forces have been changed in the new process compared to those in the traditional process, which will inevitably result in a different resultant force. Due to the relatively low WFS in WAAM and low volume of metal vapour produced, the driving force of the wire and the vapour jet force can be neglected. In addition, the arc pressure is composed of electromagnetic force and plasma drag force. Therefore, the main forces acting on the droplets in the PTA deposition process are arc pressure, surface tension, and gravitational force.

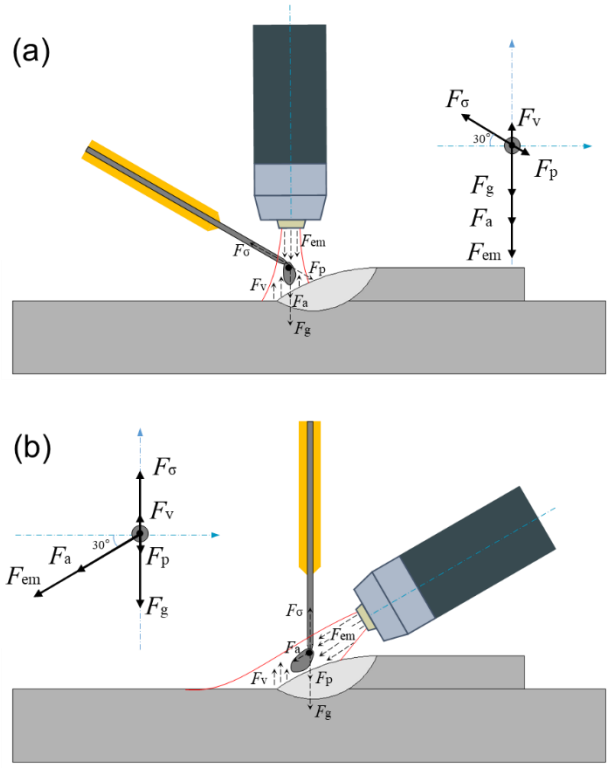


Figure 3-28 Forces acting on a droplet in (a) the traditional PTA deposition process, and (b) the new PTA deposition process.

For both processes, the arc pressure and gravitational force are detaching force, whilst the surface tension is opposing force. However, the different directions of the forces between the two processes make the droplets move along different directions after detachment. In the traditional process, the directions of both arc pressure and gravitational force are normal to the workpiece, meaning that they will push the droplets to go to the melt pool vertically. While in the new process, the arc pressure and gravitational force have different directions. Therefore, the movement direction of the droplets depends on the net effect of these two forces. For example, depending on the current, the droplets will land in different parts of the melt pool, as shown in Figure 3-25. Therefore, compared to the new process, the detachment force is higher in the traditional process and the droplets will go to the melt pool without the risk of being blown away.

In the PTA deposition process, the bead appearance is largely dependent on the metal transfer behaviour. Figure 3-29 shows the bead appearance obtained with

the corresponding processes as presented in Figures 3-25 to 3-27. In Figure 3-29a, periodic ripples can be observed on the bead surface, and they become larger as the WFS increases from 2.5 to 3.0 m/min due to the decreased droplet transfer frequency. At a WFS of 3.5 m/min, the energy input was not high enough to generate a melt pool, resulting in humps of molten metal on the substrate. It can be seen from Figure 3-29b that reducing current has a similar effect on the bead appearance as increasing WFS. As the current decreases from 200 to 180 A, the droplets become larger and the transfer frequency becomes lower, resulting in larger ripples on the bead surface. At a current of 160 A, disconnected humps are present due to the low energy input. Figures 3-29(a3) and 3-29(b3) prove that the energy input per unit volume of deposited wire controls the melt pool temperature and bead appearance. In Figure 3-29c, the decreased plasma gas flowrate has little effect on the bead appearance due to the little variation in droplet transfer behaviour (see Figure 3-27), but in general plasma gas is important as it controls the arc pressure which is the main droplet detaching force in this new process.

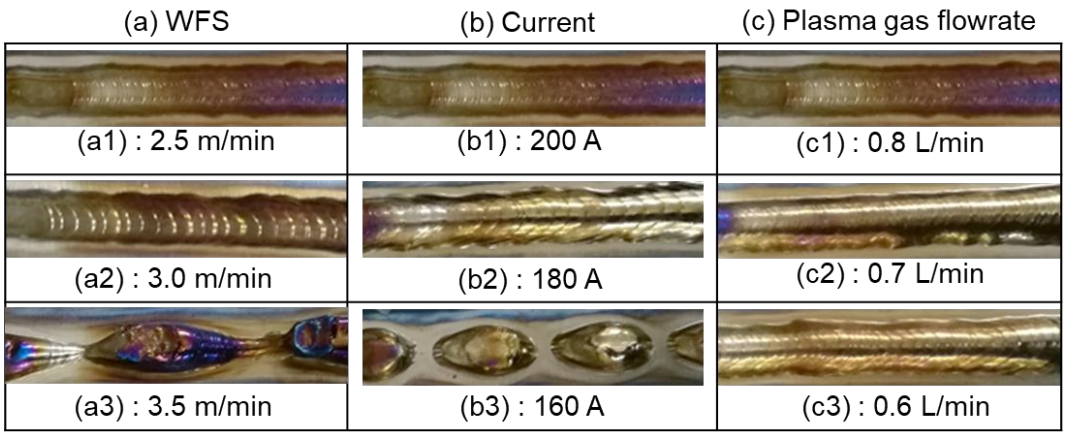


Figure 3-29 Bead appearance as a function of different process parameters: (a) WFS, (b) current, and (c) plasma gas flowrate. All parameters used in each case can be seen in Table 3-5.

From Figure 3-29, one can see that the beads obtained with the new process exhibit relatively low surface finish. This is because in these cases the metal transfer mode was dominated by the free space droplet transfer, which is not as

stable as droplet surface tension transfer and surface tension transfer [9]. In addition, the movement direction of the droplets is determined by the net effect of arc pressure and gravitational force, which is not constant and can vary with many process parameters. By contrast, in the traditional process the droplet movement direction is perpendicular to the workpiece, and it has low sensitivity to the process parameters. Figure 3-30 shows a typical traditional deposition process and the obtained bead appearance. All the parameters used in this case were the same as those in Figure 3-29(a1). It can be seen that the bead obtained with the traditional process is more regular than that obtained with the new process.

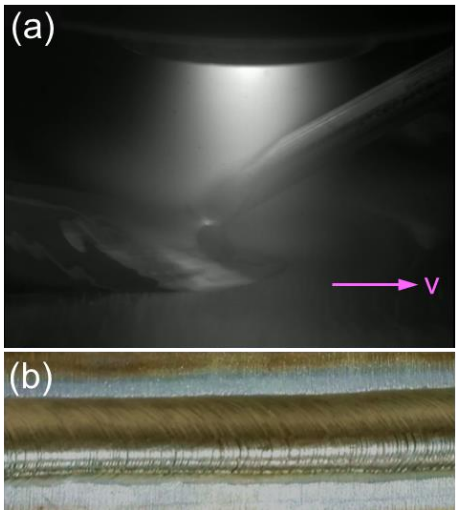


Figure 3-30 The (a) deposition process and (b) bead appearance obtained with the traditional process at a current of 200 A, WFS of 2.5 m/min, and plasma gas flowrate of 0.8 L/min.

Based on the above results and discussion, it can be concluded that the new PTA deposition process has both advantages and disadvantages compared to the traditional process. Unfortunately, the new process is not omnidirectional, and different bead profiles were achieved at different travel directions. The best bead quality in terms of flatness and symmetric bead shape can be obtained with the travel direction of torch trailing. This is similar to the traditional process where a travel direction with torch trailing is also commonly used because it gives higher tolerance and better bead quality compared to the other two travel directions

[11,23]. Furthermore, due to the inclined plasma torch, the arc pressure acting directly on the workpiece in the new process is lower than in the traditional process, resulting in a lower likelihood of keyhole formation. Similar wire feeding rates were obtained at the same energy input and wire feeding position between the two processes. Moreover, the droplet transfer behaviour is sensitive to many process parameters in the new process, and the movement direction of the droplet after detachment from the wire is determined by the resultant force of all the forces acting on it. Different bead appearances can be generated depending on the corresponding metal transfer behaviour, but in general the beads obtained with the new process have lower uniformity than those obtained with the traditional process.

3.2.4 Conclusions

In this study, a PTA deposition process of Ti-6Al-4V with a vertical wire and inclined torch was investigated and compared with the traditional process. The main conclusions can be drawn as follows.

1. Different bead profiles were obtained at different travel directions, meaning the new PTA deposition process is not omnidirectional. The travel direction with torch trailing is optimum in this new process as it produces higher width-to-height ratio and symmetric bead geometry compared to the other two travel directions.
2. Compared to the traditional process, the new process results in a lower likelihood of keyhole formation for the same current due to lower arc pressure acting directly on the workpiece surface, which potentially improves the possibility of achieving higher current and deposition rate.
3. The position of the wire in the arc column affects the melting of wire significantly. The closer the wire is to the copper nozzle, the easier the wire can be melted. For the same current and wire feeding position, similar maximum deposition rates can be obtained with the new and the traditional PTA deposition processes.

4. The droplet transfer behaviour is determined by all the forces acting on it, which are sensitive to different process parameters. Increasing the WFS or decreasing the current and plasma gas flowrate can result in a larger droplet and a lower transfer frequency.
5. Compared to the traditional process where the droplets are always pushed into the melt pool vertically, the movement direction of the droplets in the new process is not specific due to the different directions of the arc pressure and gravitational force. As a result, the beads obtained with the new process have lower uniformity compared to those obtained with the traditional process.

3.2.5 Acknowledgement

Chong Wang would like to thank Welding Engineering and Laser Processing Centre (WELPC) of Cranfield University and China Scholarship Council (No. 201706450041) for funding his research studies. The authors would like to express their gratitude to EPSRC funding NEWAM (EP/R027218/1). The technical support from Nielsen Flemming and Nisar Shah are also much appreciated.

3.2.6 References

[1] S.W. Williams, F. Martina, A.C. Addison, J. Ding, G. Pardal, P. Colegrove, Wire + arc additive manufacturing, Mater. Sci. Technol. 32 (2016) 641–647.

[2] X. Xu, J. Ding, S. Ganguly, C. Diao, S. Williams, Oxide accumulation effects on wire + arc layer-by-layer additive manufacture process, J. Mater. Process. Technol. 252 (2018) 739–750.

[3] B. Cong, J. Ding, S. Williams, Effect of arc mode in cold metal transfer process on porosity of additively manufactured Al-6.3%Cu alloy, Int. J. Adv. Manuf. Technol. 76 (2015) 1593–1606.

[4] Z. Qi, B. Cong, B. Qi, H. Sun, G. Zhao, J. Ding, Microstructure and mechanical properties of double-wire + arc additively manufactured Al-Cu-Mg alloys, J. Mater. Process. Technol. 255 (2018) 347–353.

[5] B. Wu, Z. Pan, D. Ding, D. Cuiuri, H. Li, Z. Fei, The effects of forced interpass cooling on the material properties of wire arc additively manufactured Ti6Al4V alloy, J. Mater. Process. Technol. 258 (2018) 97–105.

[6] X. Bai, P. Colegrove, J. Ding, X. Zhou, C. Diao, P. Bridgeman, J. Hönnige, H. Zhang, S. Williams, Numerical analysis of heat transfer and fluid flow in multilayer deposition of PAW-based wire and arc additive manufacturing, Int. J. Heat Mass Transf. 124 (2018) 504–516.

[7] X. Xu, S. Ganguly, J. Ding, S. Guo, S. Williams, F. Martina, Microstructural evolution and mechanical properties of maraging steel produced by wire + arc additive manufacture process, Mater. Charact. 143 (2018) 152–162.

[8] F. Martina, J. Mehnen, S.W. Williams, P. Colegrove, F. Wang, Investigation of the benefits of plasma deposition for the additive layer manufacture of Ti-6Al-4V, J. Mater. Process. Technol. 212 (2012) 1377–1386.

[9] C. Wang, W. Suder, J. Ding, S. Williams, The effect of wire size on high deposition rate wire and plasma arc additive manufacture of Ti-6Al-4V, J. Mater. Process. Tech. 288 (2021) 116842.

[10] S. Ríos, P.A. Colegrove, S.W. Williams, Metal transfer modes in plasma Wire + Arc additive manufacture, J. Mater. Process. Technol. 264 (2019) 45–54.

[11] Q. Wu, J. Lu, C. Liu, X. Shi, Q. Ma, S. Tang, H. Fan, S. Ma, Obtaining uniform deposition with variable wire feeding direction during wire-feed additive manufacturing, Mater. Manuf. Process. 32 (2017) 1881–1886.

[12] Y.K. Wang, S. Shi, G. Fu, C.S. Li, Research on the key process parameters in direct laser deposition using coaxial inside-beam wire feeding, Appl. Mech. Mater. 43 (2011) 401–404.

[13] J. Fu, L. Gong, Y. Zhang, Q. Wu, X. Shi, J. Chang, J. Lu, Microstructure and mechanical properties of Ti-6Al-4V fabricated by verticalwire feeding with axisymmetric multi-laser source, Appl. Sci. 7 (2017) 227.

[14] N. Huft, Investigation of multiple torch PAW-based additive manufacturing, PhD thesis, Montana Technological University, 2019.

[15] B. Wu, D. Ding, Z. Pan, D. Cuiuri, H. Li, J. Han, Z. Fei, Effects of heat accumulation on the arc characteristics and metal transfer behavior in Wire Arc Additive Manufacturing of Ti6Al4V, J. Mater. Process. Technol. 250 (2017) 304–312.

[16] H. Geng, J. Li, J. Xiong, X. Lin, F. Zhang, Optimization of wire feed for GTAW based additive manufacturing, J. Mater. Process. Technol. 243 (2017) 40–47.

[17] X. Jian, C.S. Wu, Numerical analysis of the coupled arc-weld pool-keyhole behaviors in stationary plasma arc welding, Int. J. Heat Mass Transf. 84 (2015) 839–847.

[18] T.Q. Li, C.S. Wu, J. Chen, Transient variation of arc heat flux and pressure distribution on keyhole wall in PAW, Weld. World. 60 (2016) 363–371.

[19] D. Wu, A. Van Nguyen, S. Tashiro, X. Hua, M. Tanaka, Elucidation of the weld pool convection and keyhole formation mechanism in the keyhole plasma arc welding, Int. J. Heat Mass Transf. 131 (2019) 920–931.

[20] T.Q. Li, C.S. Wu, Y.H. Feng, L.C. Zheng, Modeling of the thermal fluid flow and keyhole shape in stationary plasma arc welding, Int. J. Heat Fluid Flow. 34 (2012) 117–125.

[21] D.S. Dai, Y.L. Song, H. Zhang, Y.F. Zhu, Study on arc force in plasma welding, Trans. China Weld. Inst. 23 (2002) 51–54.

[22] S.C. Chu, S.S. Lian, Numerical analysis of temperature distribution of plasma arc with molten pool in plasma arc melting, Comput. Mater. Sci. 30 (2004) 441–447.

[23] S.H. Mok, G. Bi, J. Folkes, I. Pashby, Deposition of Ti-6Al-4V using a high power diode laser and wire, Part I: Investigation on the process characteristics, Surf. Coatings Technol. 202 (2008) 3933–3939.

4 The interaction between the PTA and laser

4.1 Finite element analysis of thermal behaviour in hybrid plasma arc-laser melting of Ti-6Al-4V

Chong Wang, Guangyu Chen, Jialuo Ding, Wojciech Suder, Xin Chen, Chenglei Diao, Stewart Williams

Welding Engineering and Laser Processing Centre, Cranfield University, Cranfield, Bedfordshire, MK43 0AL, UK

Abstract: Hybrid plasma transferred arc (PTA)-laser additive manufacture has the ability to build large-scale metal components with high deposition rates and near-net shape. However, the process is complex with many process parameters to understand, which determine the thermal behaviour and thus the final structure and properties of the deposited components. In this work, a three-dimensional steady-state finite element (FE) model was built to calculate the melt pool geometry, cooling rate, thermal gradient and solidification rate in hybrid PTA-laser melting process of Ti-6Al-4V. The simulated results for different process parameters agreed well with the corresponding experimental measurement. It was found that the melt pool geometry was more sensitive to laser power and travel speed compared to arc-laser separation distance and laser beam size. Faster travel speed and lower laser power enhanced the cooling rate and therefore can result in smaller grain size. Increasing the laser power could reduce the thermal gradient, but had little effect on solidification rate, which could potentially promote the grain morphology from columnar to equiaxed transition (CET). In addition, increasing the travel speed could increase both the thermal gradient and the solidification rate, having little effect on promoting CET.

Keywords: PTA-laser hybrid melting; Steady-state FE model; Melt pool geometry; Cooling rate; Thermal gradient.

4.1.1 Introduction

Additive manufacture (AM) is a transformative approach to produce industrial parts, which offers unrivalled benefits in comparison with the traditional subtractive manufacture, such as low material waste, short lead time, and high design flexibility [1]. Normally, there are three types of heat sources for metal AM, which are laser [2,3], electron beam [4,5], and electric arc [6-8]. Each of them offers a different set of benefits and challenges. For example, the arc based processes have relatively high efficiency and deposition rate, whilst the laser based processes are well known for their high accuracy. Hybrid arc-laser AM processes were developed to combine the advantages of both electric arc and laser, which have the potential to achieve both high deposition rate and near-net shape [9,10]. In hybrid arc-laser AM, the structure and properties of the deposited components are determined by the thermal conditions, such as melt pool geometry, cooling rate, and thermal gradient. For example, the generated melt pool plays a significant role in determining the deposited bead shape and consequently the surface finish of the deposited parts [7]. The cooling rate and thermal gradient govern the microstructural evolution, which considerably affects the mechanical properties [11]. Therefore, in order to build a defect-free and structurally sound component, the process needs to be controlled precisely by appropriate selection of different process parameters, such as travel speed, laser power, laser beam size, and the separation distance between the arc and laser.

Compared to the AM processes with a single heat source, the hybrid arc-laser process is more complicated owing to the double number of process variables that can be changed. Therefore, it is time-consuming and expensive to select different variables by trial and error. Moreover, measuring the thermal conditions accurately (e.g. thermal gradient and solidification rate) during deposition is quite challenging [12]. Finite element (FE) model has been demonstrated to be an effective way to provide detailed information of the thermal behaviour for AM processes. For example, Xiong et al. [13] built a three-dimensional (3D) FE model to investigate the effect of substrate preheating on the thermal behaviour in wire + arc additive manufacture (WAAM). They found that substrate preheating

resulted in a smoother thermal cycle and led to a decrease in the cooling rate of the melt pool. In addition, the thermal behaviour as a function of different variables in selective laser melting (SLM) process has been studied using FE model [14-16]. However, these models are based on transient analysis, which still require relatively long computational time. Most importantly, in many AM processes, apart from the initiation and termination of a deposit, steady-state conditions are reached pretty quickly due to the long deposition time and constant travel speed. Therefore, steady-state FE models can be more effective in reducing the computational time. Ding [17] built a 3D steady-state FE model for WAAM and reported that it saves more than 99% computational time in the thermal analysis compared to the transient model without compromising the accuracy. Such a steady-state FE model could be potentially used as a process control tool to efficiently predict thermal conditions needed for a particular structure and property.

So far, most of the hybrid arc-laser configurations have been used for welding applications [18-20]. However, the purpose of using the hybrid process in welding is different from that in AM, leading to different optimum processing conditions. In hybrid arc-laser welding, the laser with small beam size in keyhole regime is used to increase the weld penetration, whilst the arc is used to enhance the gap-filling capability, which consequently improves the welding efficiency as well as process tolerance. Also, in some gas metal arc (GMA) welding cases, a laser is used to stabilise the arc thus to improve the process stability and weld quality [21]. Therefore, the distance between the arc and laser is very close in hybrid welding process. In AM, however, the arc is used to melt the feedstock efficiently and generate the melt pool, whilst the laser is used to control the melt pool size precisely. In addition, a flat bead profile with low penetration is favourable in AM [7]. Therefore, the laser with a conduction regime is desired in hybrid arc-laser AM, and the separation distance between the two heat sources is relatively high.

As mentioned above, due to the short arc-laser separation distance and high penetration depth, a combined volumetric heat source model or two separate volumetric heat source models with very close distance are normally used to

simulate the thermal conditions in hybrid arc-laser welding. For example, Chen et al. [22] used a combined volumetric heat source model (double ellipsoidal + conical) in FE simulation to study the hybrid arc-laser welding process of 316 steel and achieved an accurate weld cross-sectional geometry. Kong et al. [23] simulated the hybrid arc-laser welding process of mild steel with two separate volumetric heat source models (double ellipsoidal and cylindrical), and found that the fusion zone and heat-affected zone (HAZ) obtained with the FE model and experimental measurement were in good agreement. However, in their models many characteristic parameters are needed to define the heat source (i.e. four parameters for double ellipsoidal model only). Furthermore, in welding or AM process, the energy produced by the heat source (arc or laser) is transferred from the surface of the workpiece to the bottom. Therefore, physically the surface heat source could be more suitable to describe the laser and arc energy. Moreover, the characteristic parameter needed for the surface heat source model is only the diameter, which can be obtained easily by the experimental measurement. Therefore, two independent surface heat source models are more suitable to describe the laser and arc energy in hybrid arc-laser AM simulation. Nevertheless, the heat convection effect in the melt pool is not considered in a typical FE analysis with surface heat source model, which might affect the accuracy of the results. This can be compensated by artificially increasing the thermal conductivity in the melt pool [24,25], which has been adopted in this study.

Here, a 3D steady-state FE model was established to study the thermal behaviour, including melt pool shape, cooling rate, thermal gradient and solidification rate of Ti-6Al-4V in hybrid plasma transferred arc (PTA)-laser melting process. The FE model was first calibrated and validated by experimental autogenous welds. After validation, the effect of different process parameters, including laser power, travel speed, laser beam size, and arc-laser separation distance on the thermal behaviour was investigated quantitatively.

4.1.2 Experimental procedure

4.1.2.1 Materials and setup

Figure 4-1 shows the setup for the hybrid PTA-laser system. The material used was Ti-6Al-4V plate with the dimensions of 200 mm × 50 mm × 13 mm. An EMW power supply was used to produce the PTA, of which the current and voltage were recorded by an arc monitor (AMV 4000). Pure argon was used for both shielding gas and plasma gas for the plasma torch. Also, a continuous wave IPG fibre laser with a maximum output power of 8 kW was used. The laser head was inclined to prevent the back reflection, whilst the plasma torch was inclined to avoid the burning by the laser beam. The motion of the system was provided by a 6-axis Fanuc robot. The experiment was carried out in an argon-filled tent to avoid oxidation of the material. A CMOS process camera (Xiris XVC-1000) was used to monitor the melt pool.

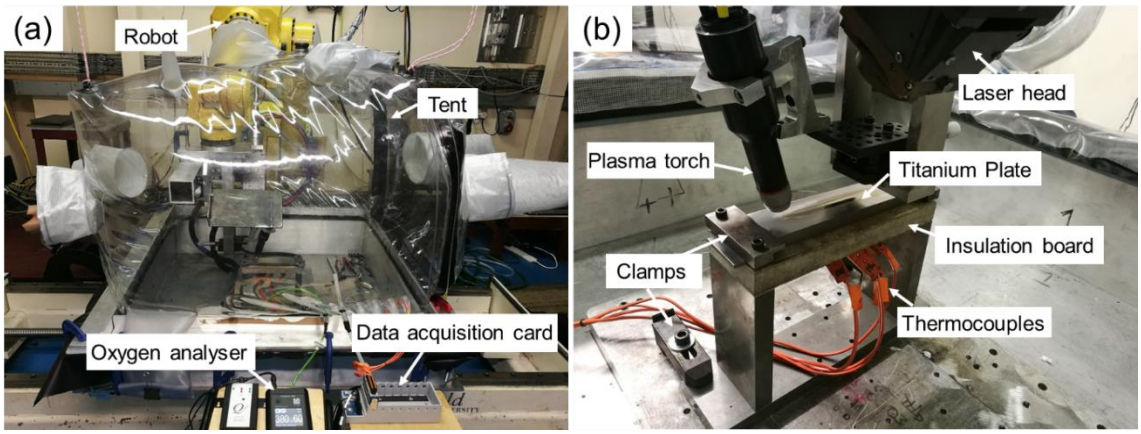


Figure 4-1 (a) Experimental setup for the hybrid PTA-laser system, and (b) the configuration inside the tent.

In order to record the thermal cycle, four channels were machined at the bottom of the plate, into which type-R thermocouples were inserted, as shown in Figure 4-1b. The thermocouples were located at the mid-width of the plate and 3 mm below the top surface to minimise the risk of damaging by the heat sources. The spacing between every two adjacent thermocouples was 15 mm. An insulation board was placed under the titanium plate to support it. The middle part of the insulation board was removed to allow the thermocouples to go through. The

titanium plates were clamped at both sides to secure them. Some process parameters were kept constant during the experiments, as shown in Table 4-1.

Table 4-1 Fixed parameters used during the experiments.

Parameters (unit)	Value
Copper nozzle diameter (mm)	3.9
Electrode diameter (mm)	4
Angle of electrode tip (°)	40
Nozzle to plate stand-off (mm)	8
Plasma gas flowrate (L/min)	0.8
Shielding gas flowrate (L/min)	8
Oxygen level in tent (ppm)	<500
Angle of plasma torch (°)	20
Angle of laser head (°)	30
Fibre diameter of laser (μm)	300

4.1.2.2 Methods

To calibrate and validate the FE model, a set of autogenous welds were performed. All the important parameters such as current, voltage, laser power, laser beam diameter (defocused), arc-laser separation distance and travel speed were measured, as shown in Table 4-2. Amongst these experimental cases, Case 1 was used for the calibration of the FE model. Other cases with different process parameters (Cases 2 to 5) were used for the validation of the model. In this study, the laser leading configuration was used in all the modelling and experiments. After welding, all samples were cross-sectioned, hot mounted, grinded, polished, and etched to check the dimensions of the melted region using a stereo microscope.

Table 4-2 Parameters used in the experiments for calibration and validation of the FE model.

	Current (A)	Voltage (V)	Laser power (W)	Travel speed (mm/s)	Separation distance (mm)	Laser beam diameter (mm)
Case 1	160	19	2500	4.5	10	6
Case 2	160	19	4500	4.5	10	6
Case 3	160	19	2500	6.5	10	6
Case 4	160	19	2500	4.5	16	6
Case 5	160	19	2500	4.5	10	12

4.1.3 Finite element model

4.1.3.1 Geometrical model and FE mesh

A 3D steady-state FE model was established using the commercial software ABAQUS. The dimensions of the titanium plate in the model were the same as those in the experiments. Figure 4-2 shows the mesh arrangement for the FE model, with a forced convection/diffusion brick element type (DCC3D8). The model had a total number of 463590 nodes and 439400 elements. Due to the high temperature gradient in the heat source zone, higher mesh density was used (grid size of 0.5 mm) in this area. In addition, in order to improve the computing efficiency, the mesh was set coarser at a further distance from the heat source, with a grid size of 3 and 5 mm at the two sides of the plate, respectively.

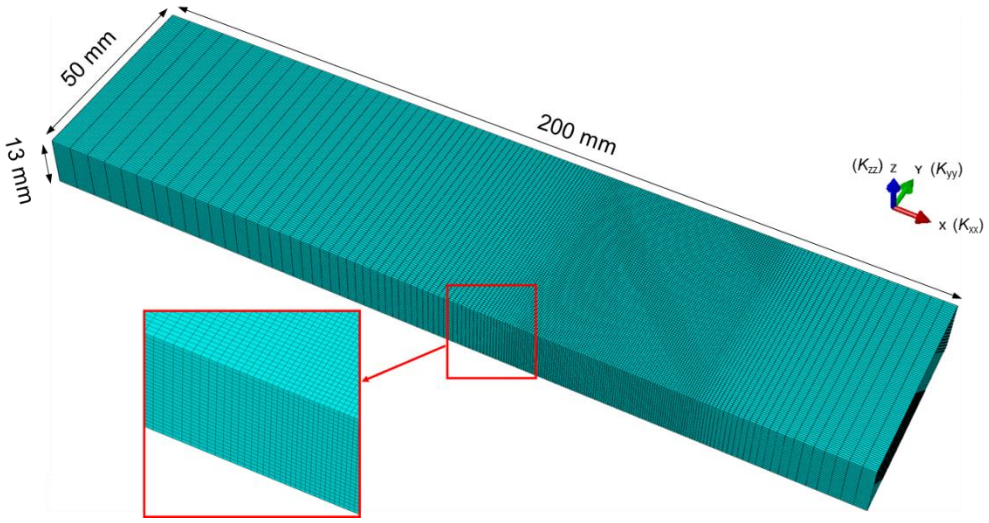


Figure 4-2 Geometry and mesh used in the FE model.

4.1.3.2 Heat source model

Two separate circular surface heat source models with Gaussian distribution were used for the PTA and laser. The power density distribution of the PTA or laser is described as follows:

$$q(x,y) = \frac{3Q}{\pi r_0^2} \exp\left(-3\frac{r^2}{r_0^2}\right) \quad \textbf{(4-1)}$$

$$r^2 = (x - x_0 - v_t t)^2 + (y - y_0)^2 \quad \textbf{(4-2)}$$

where r is the radial distance from a given point to the heat source centre, the point $(x_0 + v_t t,\ y_0)$ is the current location of the heat source centre, r_0 is the effective radius and defines the region where 95% of the heat flux is applied, v_t is the travel speed, t is time, and Q is heat input. In this study, the radii of the PTA and laser used were 6 and 3 mm respectively. For the PTA, the heat input, Q_a, is expressed by:

$$Q_a = \eta_a UI \quad \textbf{(4-3)}$$

where U and I are the arc voltage and arc current respectively, η_a is arc efficiency. For the laser, the heat input, Q_l, is expressed by:

$$Q_l = \eta_l P_l \quad \textbf{(4-4)}$$

where η_l is laser absorptivity, P_l is the applied laser power.

Unlike the conventional transient FE model which uses a Lagrangian reference frame to simulate the moving heat source, the steady-state model uses an Eulerian reference frame where the material "flows" through the mesh [17]. A mass flow rate per area, f, is utilised to represent the heat source movement, which is defined by:

$$f = -v_t \rho \quad \textbf{(4-5)}$$

where ρ is the material density.

4.1.3.3 Boundary and initial conditions

Both convection and radiation were considered on the external surfaces of the plate to simulate the heat loss to the environment, which is defined by:

$$k(\nabla T \cdot n) - q + \mu(T - T_0) + \varepsilon_0 \sigma(T^4 - T_0^4) = 0 \quad \textbf{(4-6)}$$

where k is the thermal conductivity, n is the unit outward normal vector, q is the heat flux received by the surface (only top surface in this case), μ is the convection coefficient, ε_0 is the emissivity coefficient, σ is the Stefan-Boltzmann constant (5.67×10^{-8} $W\cdot m^{-2}\cdot K^{-4}$), and T_0 is the initial temperature. Here, the convection coefficient and the emissivity used were 15 $W\cdot m^{-2}\cdot K^{-1}$ and 0.8, respectively, and the initial ambient temperature was set as 20 °C.

4.1.3.4 Material properties

The material used in this study was Ti-6Al-4V. The temperature-dependent material properties, including specific heat, density, and conductivity, are required for the FE model, which are taken from Ref. [26]. Artificial thermal conductivity was used in the melt pool to compensate for the convection effect. Specifically, an orthotropic conductivity (k_{xx}, k_{yy}, k_{zz}) was used for the calibration of the model,

where k_{xx}, k_{yy}, and k_{zz} represent the component of the thermal conductivity in X, Y, and Z direction, respectively, as indicated in Figure 4-2.

4.1.3.5 Model calibration

It was found that the heat input primarily determines the melt pool volume as well as the thermal cycle. Since the arc current, arc voltage, and applied laser power were known from measurements (see Case 1), the only parameters determining the heat input are arc efficiency and laser absorptivity. These two parameters were adjusted until the melt pool volume and thermal cycle in the FE model matched the experiment. The arc efficiency used was 0.64, which is in keeping with the values measured by Fuerschbach and Knorovsky [27], ranging from 0.5-0.75. The laser absorptivity used was 0.5, which also agrees with the values of a fibre laser in conduction mode for titanium, ranging from 0.38-0.51 [28-31]. The orthotropic artificial conductivity was then used to calibrate the melt pool geometry. More specifically, the melt pool size in one certain dimension can be increased by increasing the conductivity in this direction, which then is compensated by the melt pool size in the remaining dimensions. In this study, the values of k_{xx}, k_{yy}, and k_{zz} were 100, 150, and 30 $W \cdot m^{-1} \cdot K^{-1}$, respectively. It should be mentioned that the same values of artificial conductivity were used in all other modelling cases.

Figure 4-3 shows the melt pools obtained with the FE model and the experiment (Case 1). It can be seen from both simulation and experiment that the laser produced much smaller melt pool compared to the PTA, but the two melt pools were connected and formed one elongated melt pool.

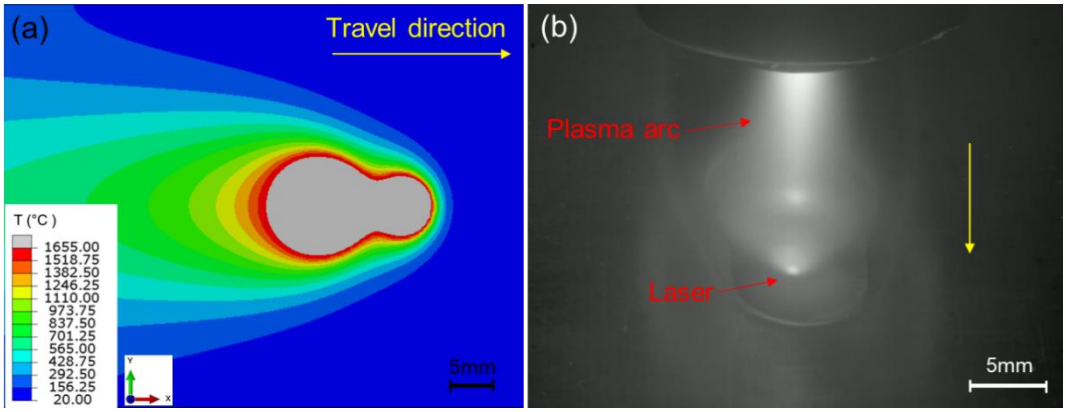


Figure 4-3 The melt pool obtained with (a) FE model, and (b) experiment. The yellow arrows indicate the travel direction.

Figure 4-4 shows the comparison of the melt pool, HAZ, and thermal cycle between the FE model and experiment, and Table 4-3 shows the dimensions of the melt pool and HAZ. For Ti-6Al-4V, the fusion line at cross-section is difficult to identify due to the smooth transition of microstructure. Many researchers reported that it is close to the interface between columnar and equiaxed grains [24,32,33], and therefore a red dashed line was drawn to indicate the fusion line (Figure 4-4a), which can be used to identify the depth of the melt pool. The width of the melt pool can be identified easily by visual check from the top surface of the plate. Since the fusion line is not particularly precise, HAZ was also compared, as presented in Figure 4-4b. The temperature in the HAZ boundary used was the α-dissolution temperature (747 ºC), at which α phase starts to dissolve into β phase [32]. From Figure 4-4b and Table 4-3, it can be seen that the HAZ in the model and experiment matches well. Figure 4-4c shows the comparison of the melt pool at the top surface, where both the shape and the dimensions show a good agreement. Figure 4-4d shows that the thermal cycle obtained with the FE model is in a good agreement with the experimental measurement, except for the peak temperature. This is because the melt pool centreline was not perfectly in the mid-width of the plate during welding, and thus the thermocouple location was a bit further to the melt pool than expected, leading to a slight decrease in the measured peak temperature.

Table 4-3 The dimensions of melt pool and HAZ obtained with experiment and FE model.

	Dimensions (mm)	Experiment	FE model
Melt pool	Width	11.4	12.2
	Depth	2.0	2.2
	Length	20.3	20.4
HAZ	Width	18.1	17.8
	Depth	7.0	7.3

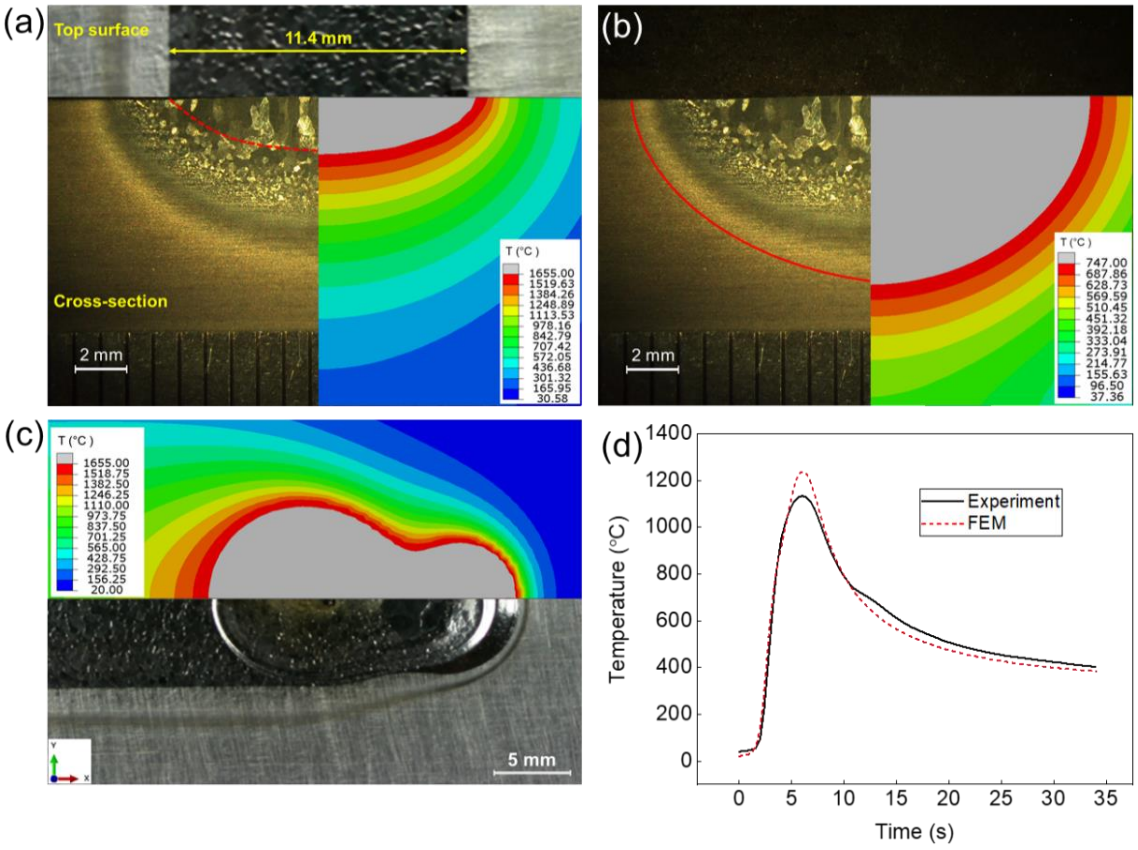


Figure 4-4 Comparison between simulation and experimental results: (a) melt pool at cross-section, (b) HAZ at cross-section, (c) melt pool at top surface, and (d) thermal cycle.

4.1.4 Results and discussion

4.1.4.1 Model validation

Figure 4-5 shows the comparison of the melt pool and HAZ between experiment and FE model. All the parameters used for these cases are presented in Table 4-2. It can be seen from Figure 4-5a and 4-5b that the width and depth of melt pool and HAZ obtained with the model are in good agreement with those obtained in the experiment. Moreover, Figure 4-5c shows that the length of the melt pools matches well. It should be noted that there is a tiny difference in the connected region of the melt pools between experiment and FE model (Figure 4-5c). This is because the flow interaction between the two melt pools could not be represented very well in the FE model due to the high surface tension of the material, leading to a smoother melt pool boundary in the experiment than in the model. In general, the simulated results are in good agreement with the experimental results, confirming the validity of the FE model.

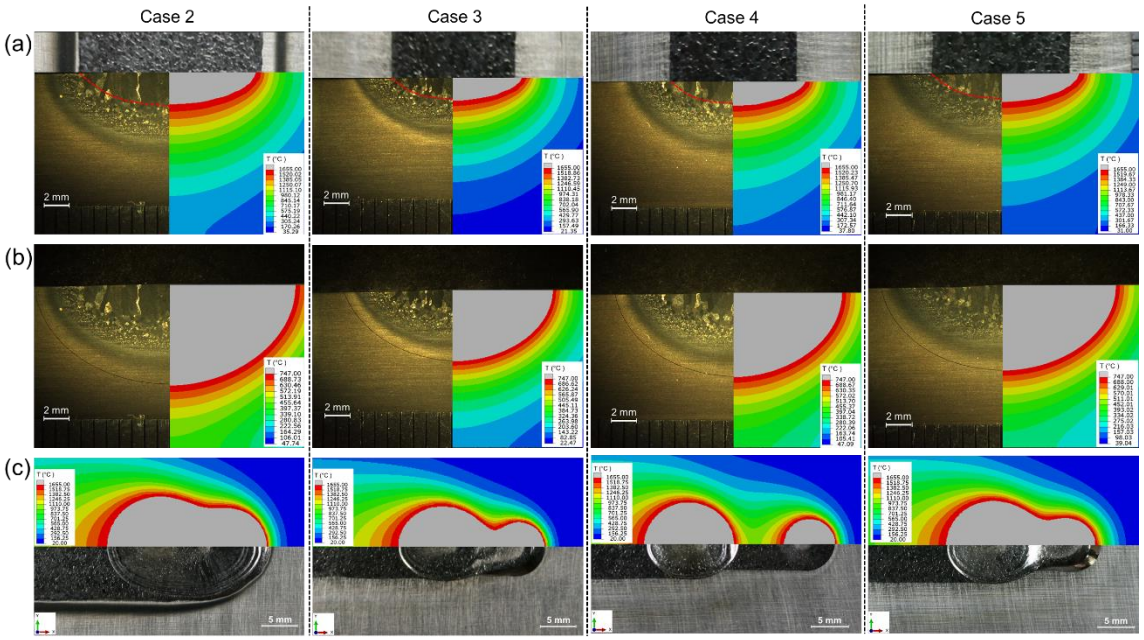


Figure 4-5 Comparison of melt pool and HAZ between simulation and experiment with different process parameters (Cases 2 to 5 in Table 4-2): (a) melt pool at cross-section, (b) HAZ at cross-section, and (c) melt pool form top view.

4.1.4.2 Melt pool geometry

The melt pool size is one of the primary parameters in AM, as it determines the geometry of the deposited bead, which is a fundamental building block for built parts [7]. Amongst the three dimensions (width, depth, and length) of the melt pool, the width and depth are most important as they determine the printing resolution and remelting into the underlying layers or baseplate, and therefore are emphatically discussed in this study.

Figure 4-6 shows the melt pool dimensions as a function of applied laser power. It can be seen that both the melt pool width and depth increase linearly with the laser power due to the increased heat input. Figure 4-7 shows the corresponding melt pool geometries presented in Figure 4-6. When the laser power was low (500 W), the laser could not generate a melt pool, but just preheated the workpiece. As the laser power increased to 1500 W, two separate melt pools were generated by the PTA and laser respectively. With the further increase of laser power from 2500 to 5500 W, the two separate melt pools merged into one deeper and wider melt pool. Here, the applied arc power was constant (3040 W). Due to the laser leading configuration used in this study, the arc interacted on an already hot or melted workpiece preheated by the laser. Therefore, a relatively large melt pool was generated by the PTA.

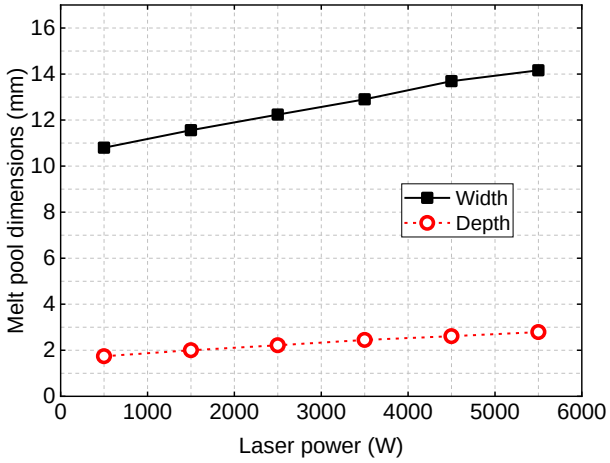


Figure 4-6 The effect of laser power on the melt pool dimensions (all the process parameters used except laser power are the same as those of Case 1 in Table 4-2).

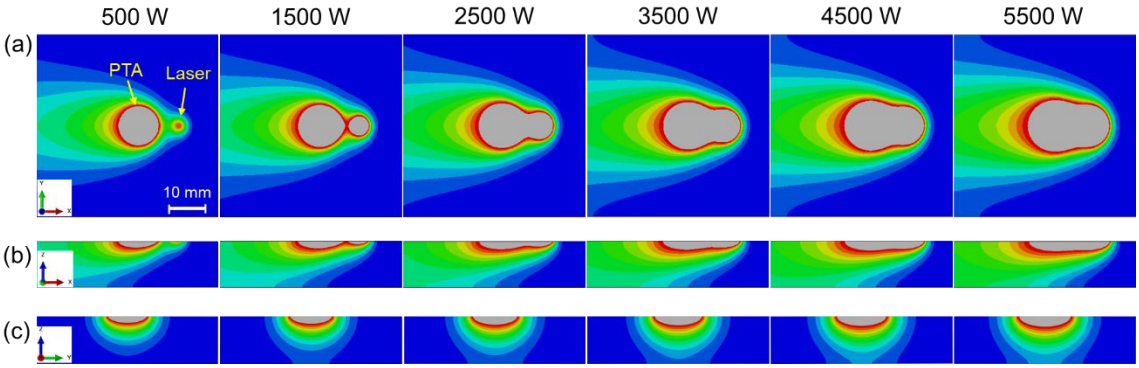


Figure 4-7 The effect of laser power on the melt pool geometry from different views: (a) top surface, (b) longitudinal section, and (c) cross-section.

Figure 4-8 presents the effect of travel speed on the melt pool dimensions. It can be seen that both the melt pool width and depth are inversely proportional to the travel speed, especially the melt pool width, which reduces significantly from 14.3 to 9.5 mm as the travel speed increases from 2.5 to 11 mm/s. This is attributed to the decreased heat input per unit length (also referred to as line energy, Λ), which is inversely proportional to the travel speed, as given by:

$$\Lambda = \frac{Q_a + Q_l}{v_t} \quad \textbf{(4-7)}$$

Therefore, increasing travel speed at constant power results in a decrease in line energy, leading to a smaller melt pool. Figure 4-9 shows the corresponding melt pool geometries presented in Figure 4-8. It can be seen that the melt pool becomes smaller with the increasing travel speed. Compared to the depth and width, the total length of the melt pool has no significant variation due to the fixed separation distance between the two heat sources.

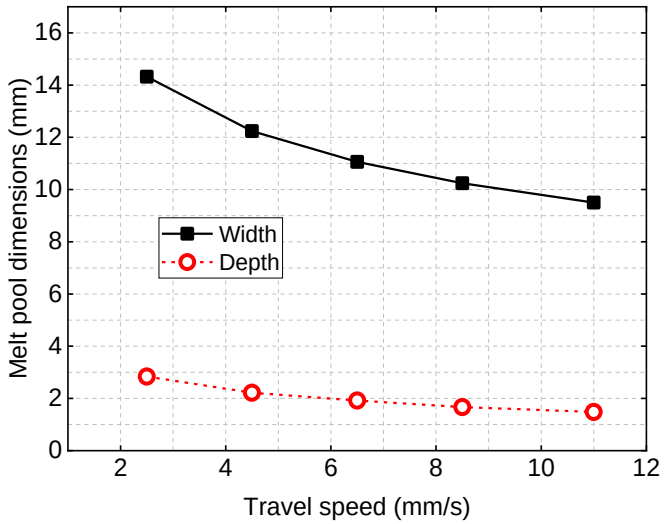


Figure 4-8 The effect of travel speed on the melt pool dimensions (all the process parameters used except travel speed are the same as those of Case 1 in Table 4-2).

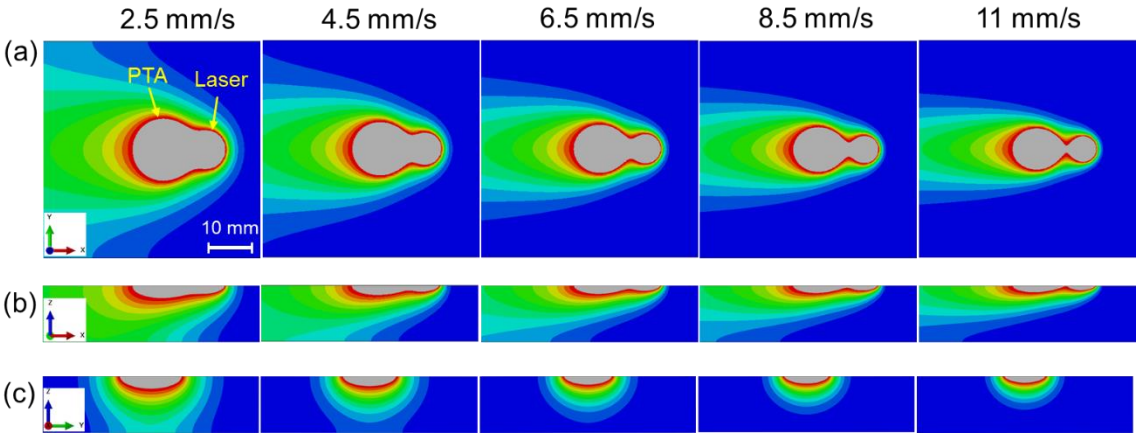


Figure 4-9 The effect of travel speed on the melt pool geometry from different views: (a) top surface, (b) longitudinal section, and (c) cross-section.

Figure 4-10 shows the variation in melt pool dimensions with the arc-laser separation distance, and Figure 4-11 presents the corresponding melt pool geometries. In general, the increasing separation distance does not affect the melt pool width and depth significantly but leads to an increase in its total length. As the separation distance increases from 0 to 8 mm, there is one large melt pool. However, as it increases to beyond 12 mm, two separate melt pools occur. In these cases, the total applied power is constant with 3040 and 2500 W for arc power and laser power, respectively. The slight decrease in melt pool width and depth is caused by the increase in melt pool length, according to the energy conservation law.

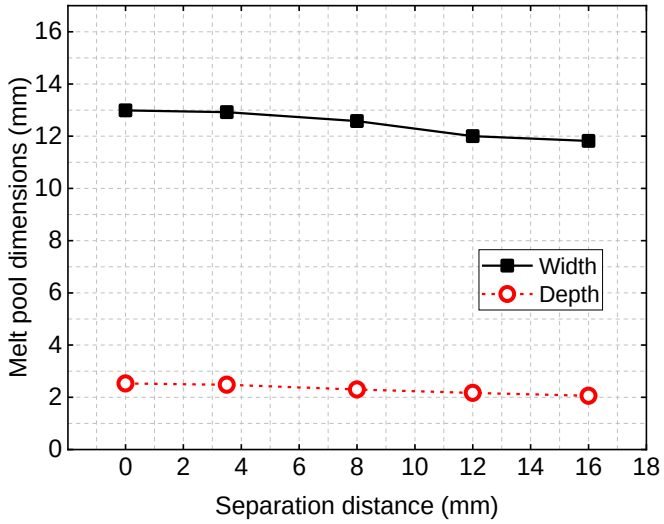


Figure 4-10 The effect of the separation distance between the PTA and laser on the melt pool dimensions (all the process parameters used except separation distance are the same as those of Case 1 in Table 4-2).

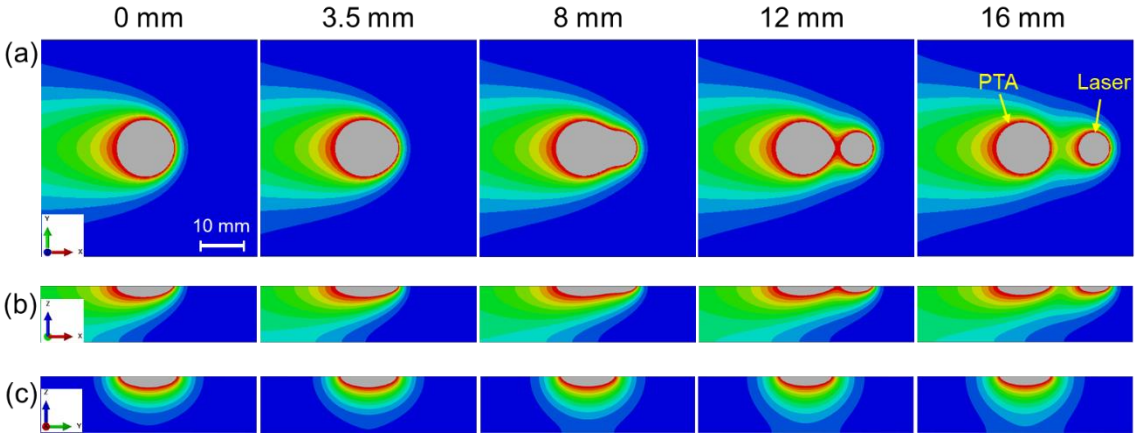


Figure 4-11 The effect of arc-laser separation distance on the melt pool geometry from different views: (a) top view, (b) longitudinal section, and (c) cross-section.

Figure 4-12 shows the melt pool dimensions as a function of the laser beam diameter. It can be seen that the laser beam size has a minor effect on both the melt pool width and depth. Figure 4-13 shows the melt pool geometry produced by two extreme beam diameters of 4 and 12 mm. From Figure 4-13a and 4-13b, it can be seen that increasing the laser beam size leads to an increase in width and decrease in depth at the front part of the melt pool (i.e. the melt pool generated by the laser). However, this has very little effect on the rear part of the melt pool, which determines the final melt pool width and depth in the hybrid process. This indicates that compared to the laser power (Figure 4-6), the laser beam size has much less effect on the melt pool dimensions in hybrid PTA-laser melting process with a laser leading configuration.

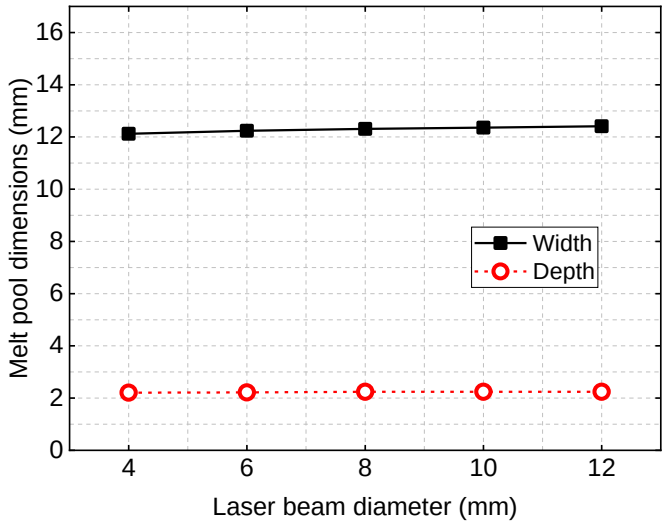


Figure 4-12 The effect of the laser beam diameter on the melt pool dimensions (all the process parameters used except laser beam diameter are the same as those of Case 1 in Table 4-2).

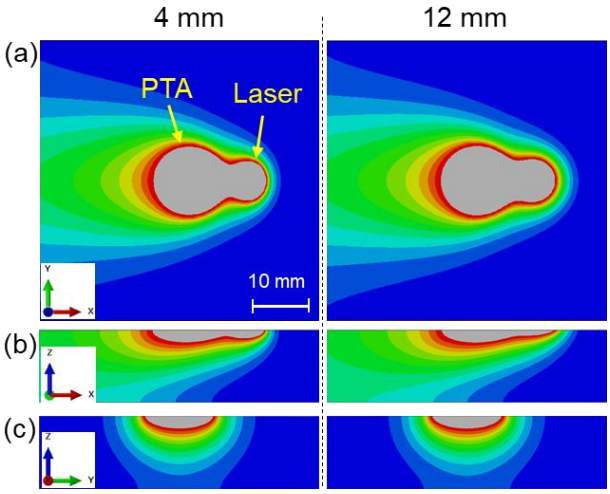


Figure 4-13 The melt pool geometry obtained with the laser beam diameters of 4 and 12 mm from different views: (a) top view, (b) longitudinal section, and (c) cross-section.

From the above analysis and discussion, we know that the melt pool width and depth are more sensitive to laser power and travel speed than to the separation distance and laser beam size. This is because the former two varibles determine the line energy input during the process, whilst the latter two variables determine the energy distribution. Therefore, it can be concluded that in hybrid PTA-lasers

melting process the melt pool width and depth are mainly governed by the energy input and not respond significantly to the energy distribution.

In AM, the ability to achieve good surface finish of the deposited parts is of critical concern. Lower surface waviness is more desired as it results in less material to be machined off, which is more cost-effective and environmentally friendly. It is reported that the surface finish of the deposited parts is controlled by the bead shape. For the same cross-sectional area, a lower surface waviness of the deposited component can be achieved with a flatter bead shape [7]. Although the deposited material was not considered in this FE model, it still can be used to approximate the behaviour of melt pool variation for different process parameters. From Figures 4-6 and 4-8, we can know that in hybrid PTA-laser AM the deposited beads would become wider with the increasing laser power and decreasing travel speed. Due to the mass conservation, the bead height would decrease with increasing width. Consequently, flatter beads should lead to better surface finish when building parts. This is consistent with Martina et al. [34] who investigated the effect of different process parameters on the effective wall width in the PTA deposition process of Ti-6Al-4V, and found that that the wall width increased with increasing heat input (caused by increased current or decreased travel speed). As for the arc-laser separation distance and laser beam size, they have little effect on the melt pool width and therefore would not influence the bead shape and final surface finish of the deposited parts significantly.

4.1.4.3 Cooling rate and solidification parameters

Metallurgical variables such as cooling rate ($\frac{\partial T}{\partial t}$), thermal gradient ($G_0$), and solidification rate (R_0) determine the microstructure during the deposition process. For example, the cooling rate and thermal gradient at the start of solidification control the grain size, grain morphology and texture, while the post-solidification cooling rate controls the fine-scale microstructure [11,35]. Therefore, it is of vital importance to predict and control the essential metallurgical variables for different process parameters.

In the established FE model, the artificial conductivity was used in the melt pool to compensate for the heat convection effect, which helps to achieve more accurate melt pool geometry. However, the temperature distribution in the melt pool might not be very precise. Therefore, for the analysis of cooling rate and thermal gradient, the temperature above the melting point will not be discussed. In addition, the temperature used for solidification parameters is in the mushy zone and near solidus (T_s=1625°C). The position selected is at the mid-width and on the top surface of the plate.

4.1.4.3.1 Cooling rate

Figure 4-14 shows the thermal cycle after solidification as a function of different process parameters. It can be seen that compared to laser power and travel speed, the separation distance and laser beam diameter have very little effect on the thermal cycle. As mentioned earlier, this is because the latter two variables do not change the total amount of heat input into the workpiece. In general, laser power and travel speed are two primary process variables affecting the thermal conditions in the hybrid PTA-laser process. Therefore, the effect of these two variables on the cooling rate and solidification parameters will be discussed.

Ti-6Al-4V is a two-phase (alpha and beta) titanium alloy. The cooling rate at the melting point determines the beta gain size, whilst the cooling rate at the beta transus temperature (T_t=997°C) determines the alpha grain size [11]. The role of laser power and travel speed on the cooling rate at these two temperatures are shown in Figure 4-15. The selected position exhibits a lower cooling rate with higher laser power or lower travel speed. This is owing to the increased heat input with the increasing laser power and decreasing travel speed, resulting in slower heat dissipation. In addition, the comparison of Figure 4-15a and 4-15b reveals that changing travel speed is more effective than laser power to control the cooling rate. Moreover, it can be seen that in both cases, for the same process parameters the cooling rate at T_s is always higher than that at T_t. This is also revealed in Figure 4-14a and 4-14b that the higher the temperature, the higher the cooling rate.

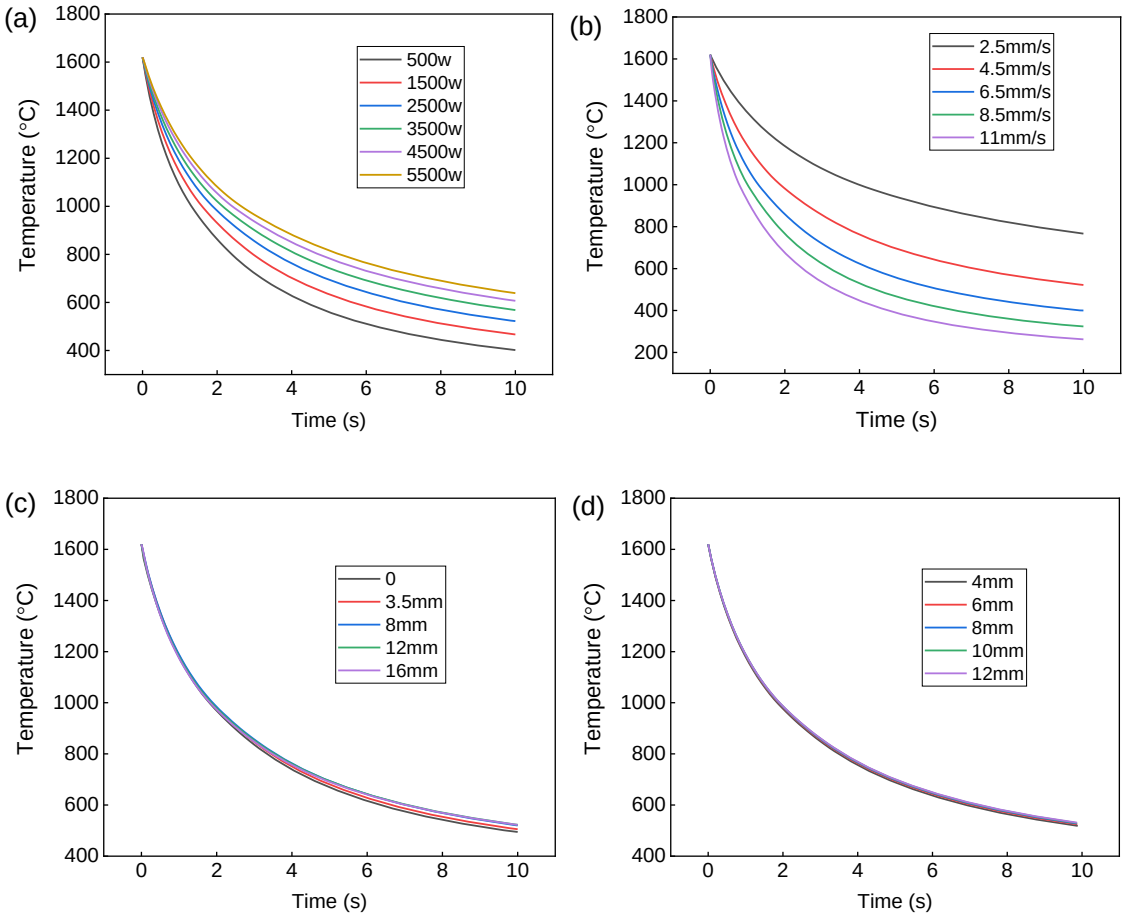


Figure 4-14 The thermal cycle as a function of different process parameters: (a) laser power, (b) travel speed, (c) separation distance, and (d) laser beam diameter.

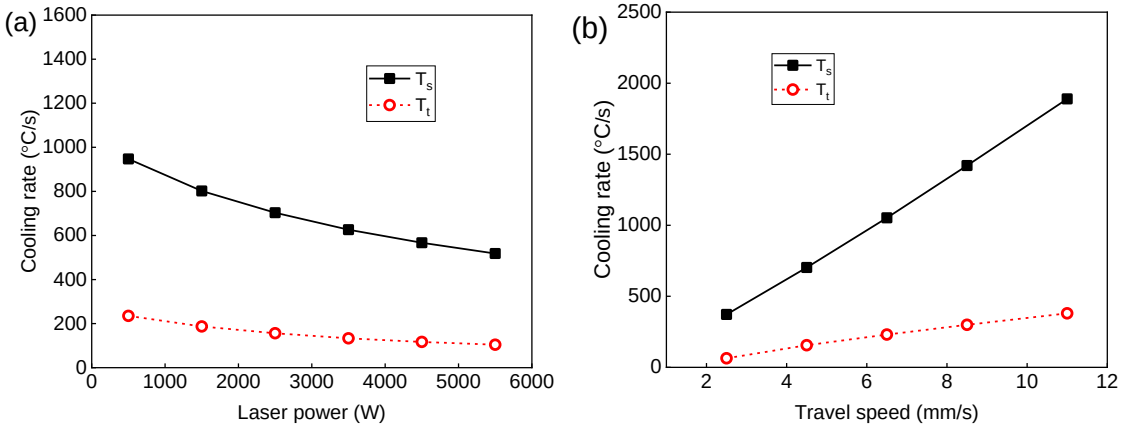


Figure 4-15 The effect of (a) laser power, and (b) travel speed on cooling rate.

It is well known that grain size tends to decrease with the increasing cooling rate [35]. Therefore, it can be concluded that smaller grain size can be achieved with lower laser power and higher travel speed in the hybrid PTA-laser process. This can be validated from the experimental data. For example, larger beta grains are observed in Case 2 (laser power of 4500 W, Figure 4-5) compared to Case 1 (laser power of 2500 W, Figure 4-4). Also, smaller beta grains are observed in Case 3 (Figure 4-5) compared to those in Case 1 (Figure 4-4), where the travel speeds used in the two cases were 6.5 and 4.5 mm/s, respectively. It should be mentioned that the cooling rates observed in these cases are higher than those reported for the PTA deposition process (e.g. 186-270°C/s in Ref. [36]). This is because the cases studied here are conducted on the baseplate which results in a 3D heat transfer, whilst in the reported case the study was conducted on the previously deposited layers with relatively thin width where a two-dimensional (2D) heat transfer occurs.

4.1.4.3.2 Solidification parameters

Figure 4-16 shows the variation in solidification rate with the increase of laser power and travel speed. The solidification rate does not change significantly with the laser power. This is because these cases were conducted at a constant travel speed. The relationship between the solidification rate and the travel speed is expressed as:

$$R_0 = v_t sin\theta \quad \textbf{(4-8)}$$

where v_t is travel speed, and θ is the angle between the travel direction and the tangential direction at a location on the solidification front, as indicated in Figure 4-17. Since the selected position is at the top surface of the plate in the cases studied here, θ does not change significantly with the increase in laser power. Therefore, the solidification rate remains almost unchanged for the entire range of laser power. However, the solidification rate increases significantly with increasing travel speed, which also can be explained by Equation (4-8).

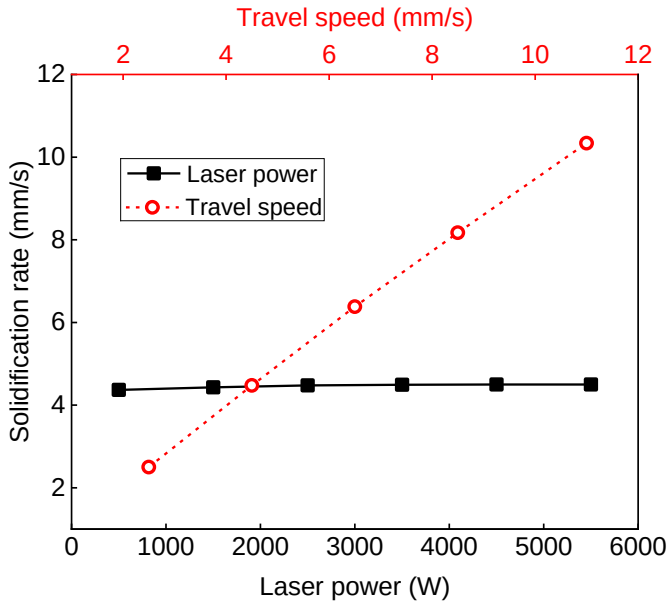


Figure 4-16 The effect of laser power on solidification rate (travel speed was kept fixed), and the effect of travel speed on solidification rate (laser power was kept fixed).

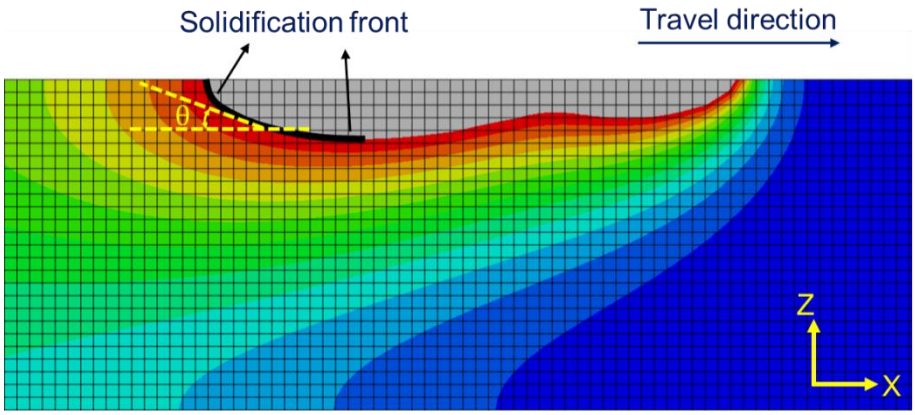


Figure 4-17 Melt pool contour including the solidification front and the angle θ.

The thermal gradient can be achieved by differentiating the temperature-distance curve. Also, it is determined by the cooling rate and solidification rate, which is expressed as:

$$G_0 = \frac{1}{R_0}\frac{\partial T}{\partial t} \quad \textbf{(4-9)}$$

Therefore, if the cooling rate and solidification rate are known, the thermal gradient at the solidification front can also be calculated according to Equation (4-9). Figure 4-18 shows the thermal gradient as a function of laser power and travel speed. It can be seen that the thermal gradient increases with increasing travel speed and with decreasing laser power, meaning that a higher heat input would result in a lower thermal gradient.

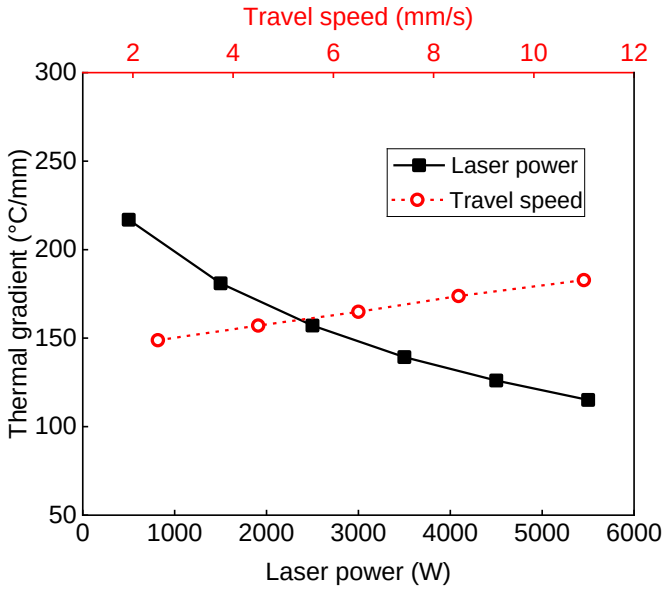


Figure 4-18 The effect of laser power on thermal gradient (travel speed was kept fixed), and the effect of travel speed on thermal gradient (laser power was kept fixed).

One of the significant challenges in AM is to avoid columnar grains as they can cause anisotropy in mechanical property [12]. The grain morphology from columnar to equiaxed transition (CET) is promoted by a high solidification rate and low thermal gradient [35]. This means CET can be achieved by manipulating the process parameters. The almost unchanged solidification rate and the decreased thermal gradient indicate that increasing the laser power is capable of improving the CET in the hybrid PTA-laser process. However, both the solidification rate and thermal gradient increase with the increasing travel speed, showing no evidence of the effect of travel speed on promoting CET. A similar phenomenon was observed by Bermingham et al. [12], who found that both

thermal gradient and solidification rate increase with the increase of travel speed in gas tungsten arc (GTA) deposition of Ti-6Al-4V. In fact, a solidification map was developed for Ti-6Al-4V based on solidification rate and thermal gradient, which can be used for the grain morphology prediction [35]. For example, using this map, Bontha et al. [37,38] modelled the solidification conditions for laser wire deposition process of Ti-6Al-4V, and concluded that increasing laser power could promote CET due to the decrease in thermal gradient. However, opposite results were found for the travel speed effect on promoting CET. It was found in this study that increasing the travel speed would only promote CET slightly in the hybrid PTA-laser process.

4.1.5 Conclusions

In this study, a 3D steady-state FE model was developed, validated, and used to calculate the melt pool geometry, cooling rate and solidification parameters in hybrid PTA-laser melting process of Ti-6Al-4V. The effect of laser power, travel speed, laser beam size, and arc-laser separation distance on the thermal behaviour was examined. The key findings were drawn as follows.

1. The established FE model was accurate enough to predict the thermal behaviour for various process variables in hybrid PTA-laser melting process.
2. In this hybrid process, the melt pool geometry responds more significantly to the energy input compared to energy distribution. The width and depth of the melt pool increase with the increasing laser power and decreasing travel speed due to the increased energy input, whilst they are not sensitive to the arc-laser separation distance and laser beam size owing to the unchanged energy input.
3. The cooling rate decreases with the increasing laser power and decreasing travel speed at both melting point and beta transus temperature, which is because of the slower heat dissipation caused by the increased heat input. At the same processing condition, a higher temperature results in a higher cooling rate. Increased cooling rate leads

to smaller beta grain sizes in Ti-6Al-4V, which was validated by the experimental data.

4. In the hybrid PTA-laser process, the solidification rate increases significantly with the travel speed but has a minor response to the laser power. A lower thermal gradient was achieved with a higher laser power or a lower travel speed. By using the solidification map of Ti-6Al-4V, it was found that it is better to control the CET by changing laser power due to the decreased thermal gradient than by changing the travel speed.

4.1.6 Acknowledgement

Chong Wang would like to acknowledge China Scholarship Council (No. 201706450041) and Cranfield University for funding his research studies. The authors would like to thank EPSRC for sponsoring this research (NEWAM: EP/R027218/1). The authors also would like to thank John Thrower, Nielsen Flemming, Nisar Shah, and Steve Pope for the technical assistance.

4.1.7 References

[1] D. Herzog, V. Seyda, E. Wycisk, C. Emmelmann, Additive manufacturing of metals, Acta Mater. 117 (2016) 371–392.

[2] E. Liverani, S. Toschi, L. Ceschini, A. Fortunato, Effect of selective laser melting (SLM) process parameters on microstructure and mechanical properties of 316L austenitic stainless steel, J. Mater. Process. Technol. 249 (2017) 255–263.

[3] E. Brandl, F. Palm, V. Michailov, B. Viehweger, C. Leyens, Mechanical properties of additive manufactured titanium (Ti-6Al-4V) blocks deposited by a solid-state laser and wire, Mater. Des. 32 (2011) 4665–4675.

[4] M. Galati, L. Iuliano, A literature review of powder-based electron beam melting focusing on numerical simulations, Addit. Manuf. 19 (2018) 1–20.

[5] R. Hu, X. Chen, G. Yang, S. Gong, S. Pang, Metal transfer in wire feeding-based electron beam 3D printing: Modes, dynamics, and transition criterion, Int. J. Heat Mass Transf. 126 (2018) 877–887.

[6] Z. Qi, B. Cong, B. Qi, H. Sun, G. Zhao, J. Ding, Microstructure and mechanical properties of double-wire + arc additively manufactured Al-Cu-Mg alloys, J. Mater. Process. Technol. 255 (2018) 347–353.

[7] C. Wang, W. Suder, J. Ding, S. Williams, The effect of wire size on high deposition rate wire and plasma arc additive manufacture of Ti-6Al-4V, J. Mater. Process. Tech. 288 (2021) 116842.

[8] B. Cong, J. Ding, S. Williams, Effect of arc mode in cold metal transfer process on porosity of additively manufactured Al-6.3%Cu alloy, Int. J. Adv. Manuf. Technol. 76 (2015) 1593–1606.

[9] J. Näsström, F. Brueckner, A.F.H. Kaplan, Laser enhancement of wire arc additive manufacturing, J. Laser Appl. 31 (2019) 022307.

[10] F. Kong, H. Zhang, G. Wang, Numerical simulation of transient multiphase field during hybrid plasma-laser deposition manufacturing, J. Heat Transfer. 130 (2008) 1–7.

[11] J. Gockel, J. Beuth, K. Taminger, Integrated control of solidification microstructure and melt pool dimensions in electron beam wire feed additive manufacturing of ti-6al-4v, Addit. Manuf. 1 (2014) 119–126.

[12] M.J. Bermingham, D.H. StJohn, J. Krynen, S. Tedman-Jones, M.S. Dargusch, Promoting the columnar to equiaxed transition and grain refinement of titanium alloys during additive manufacturing, Acta Mater. 168 (2019) 261–274.

[13] J. Xiong, Y. Lei, R. Li, Finite element analysis and experimental validation of thermal behavior for thin-walled parts in GMAW-based additive manufacturing with various substrate preheating temperatures, Appl. Therm. Eng. 126 (2017) 43–52.

[14] J. Li, Z. Wei, L. Yang, B. Zhou, Y. Wu, S.G. Chen, Z. Sun, Finite element analysis of thermal behavior and experimental investigation of Ti6Al4V in selective laser melting, Optik 207 (2020) 163760.

[15] Y. Chen, H. Chen, J.Q. Chen, J. Xiong, Y. Wu, S.Y. Dong, Numerical and experimental investigation on thermal behavior and microstructure during selective laser melting of high strength steel, J. Manuf. Process. 57 (2020) 533–542.

[16] Y. Li, D. Gu, Parametric analysis of thermal behavior during selective laser melting additive manufacturing of aluminum alloy powder, Mater. Des. 63 (2014) 856–867.

[17] J. Ding, P. Colegrove, J. Mehnen, S. Ganguly, P.M.S. Almeida, F. Wang, S. Williams, Thermo-mechanical analysis of Wire and Arc Additive Layer Manufacturing process on large multi-layer parts, Comput. Mater. Sci. 50 (2011) 3315–3322.

[18] B. Acherjee, Hybrid laser arc welding: State-of-art review, Opt. Laser Technol. 99 (2018) 60–71.

[19] X. Chen, Z. Mu, R. Hu, L. Liang, A.B. Murphy, S. Pang, A unified model for coupling mesoscopic dynamics of keyhole, metal vapor, arc plasma, and weld pool in laser-arc hybrid welding, J. Manuf. Process. 41 (2019) 119–134.

[20] B. Ribic, R. Rai, T. DebRoy, Numerical simulation of heat transfer and fluid flow in GTA/Laser hybrid welding, Sci. Technol. Weld. Join. 13 (2008) 683–693.

[21] X. Cai, H. Li, H. Wei, L. Yang, Y. Gao, Effect of laser on the welding process of short-circuiting transfer MIG welding of aluminum alloys, Int. J. Adv. Manuf. Technol. 75 (2014) 1829–1836.

[22] L. Chen, G. Mi, X. Zhang, C. Wang, Numerical and experimental investigation on microstructure and residual stress of multi-pass hybrid laser-arc welded 316L steel, Mater. Des. 168 (2019) 107653.

[23] F. Kong, J. Ma, R. Kovacevic, Numerical and experimental study of thermally induced residual stress in the hybrid laser-GMA welding process, J. Mater. Process. Technol. 211 (2011) 1102–1111.

[24] V.D. Fachinotti, A. Cardona, B. Baufeld, O. Van Der Biest, Finite-element modelling of heat transfer in shaped metal deposition and experimental validation, Acta Mater. 60 (2012) 6621–6630.

[25] A. Askari, S. Das, Practical numerical analysis of a crack near a weld subjected to primary loading and hydrogen embrittlement, J. Mater. Process. Technol. 173 (2006) 1–13.

[26] J. Ahn, E. He, L. Chen, R.C. Wimpory, J.P. Dear, C.M. Davies, Prediction and measurement of residual stresses and distortions in fibre laser welded Ti-6Al-4V considering phase transformation, Mater. Des. 115 (2017) 441–457.

[27] P.W. Fuerschbach, G.A. Knorovsky, A study of melting efficiency in plasma arc and gas tungsten arc welding, Weld. J. 70 (1991) 287–297.

[28] H. Kwon, W.K. Baek, M.S. Kim, W.S. Shin, J.J. Yoh, Temperature-dependent absorptance of painted aluminum, stainless steel 304, and titanium for 1.07 μm and 10.6 μm laser beams, Opt. Lasers Eng. 50 (2012) 114–121.

[29] C.D. Boley, S.A. Khairallah, A.M. Rubenchik, Calculation of laser absorption by metal powders in additive manufacturing, Appl. Opt. 54 (2015) 2477–2482.

[30] C.D. Boley, S.C. Mitchell, A.M. Rubenchik, S.S.Q. Wu, Metal powder absorptivity: modeling and experiment, Appl. Opt. 55 (2016) 6496.

[31] F. Lia, J. Park, J. Tressler, R. Martukanitz, Partitioning of laser energy during directed energy deposition, Addit. Manuf. 18 (2017) 31–39.

[32] E. Brandl, V. Michailov, B. Viehweger, C. Leyens, Deposition of Ti-6Al-4V using laser and wire, part I: Microstructural properties of single beads, Surf. Coatings Technol. 206 (2011) 1120–1129.

[33] S. Mishra, T. DebRoy, Measurements and Monte Carlo simulation of grain growth in the heat-affected zone of Ti-6Al-4V welds, Acta Mater. 52 (2004) 1183–1192.

[34] F. Martina, J. Mehnen, S.W. Williams, P. Colegrove, F. Wang, Investigation of the benefits of plasma deposition for the additive layer manufacture of Ti-6Al-4V, J. Mater. Process. Technol. 212 (2012) 1377–1386.

[35] P.A. Kobryn, S.L. Semiatin, Microstructure and texture evolution during solidification processing of Ti-6A1-4V, J. Mater. Process. Technol. 135 (2003) 330–339.

[36] J. Lin, Y. Lv, D. Guo, X. Wu, Z. Li, C. Liu, B. Guo, G. Xu, B. Xu, Enhanced strength and ductility in thin Ti-6Al-4V alloy components by alternating the thermal cycle strategy during plasma arc additive manufacturing, Mater. Sci. Eng. A. 759 (2019) 288–297.

[37] S. Bontha, N.W. Klingbeil, P.A. Kobryn, H.L. Fraser, Thermal process maps for predicting solidification microstructure in laser fabrication of thin-wall structures, J. Mater. Process. Technol. 178 (2006) 135–142.

[38] S. Bontha, N.W. Klingbeil, P.A. Kobryn, H.L. Fraser, Effects of process variables and size-scale on solidification microstructure in beam-based fabrication of bulky 3D structures, Mater. Sci. Eng. A. 513–514 (2009) 311–318.

5 Wire based PTA-laser hybrid additive manufacture

5.1 Wire based plasma arc and laser hybrid additive manufacture of Ti-6Al-4V

Chong Wang, Wojciech Suder, Jialuo Ding, Stewart Williams

Welding Engineering and Laser Processing Centre, Cranfield University, Cranfield, Bedfordshire, MK43 0AL, UK

Abstract: In this study, a novel wire based plasma transferred arc (PTA)-laser hybrid additive manufacture process was proposed for deposition of large-scale titanium parts with high deposition rate and near-net shape. The optimum processing conditions, including the heat source configuration, wire feeding position, and arc-to-laser separation distance, were investigated. The benefits of using the hybrid process over the single PTA and laser deposition processes on their own were studied. The results show that compared to the single PTA process, the hybrid process has extended energy distribution and melt pool size, giving more interaction time of the wire with the heat sources and therefore a higher deposition rate. Compared to the laser process, the hybrid process has a much higher wire melting efficiency and tolerance to wire positioning accuracy. Owing to more distributed energy across the two heat sources, the likelihood of keyhole formation in the hybrid process is lower than that in the single PTA process. The best configuration for the hybrid process is the PTA leading, combined with front feeding of the wire. In this configuration, the PTA is used to melt the feedstock and the laser is used to control the melt pool size, which allows independent control of deposition rate and bead shape. A set of multi-layer walls was built to demonstrate the feasibility of this process for the manufacture of engineering parts. The results show that the achieved flat beads are very desirable for low surface waviness and lead to near-net-shape deposition. The main limitation of the hybrid process is remelting into the underlying layer. To overcome this, a multi-energy source process with more evenly distributed energy has been proposed.

Keywords: Plasma arc-laser hybrid additive manufacture; Wire + arc additive manufacture; Wire + laser additive manufacture; Multi-energy source.

5.1.1 Introduction

Directed energy deposition (DED) additive manufacture (AM) has developed rapidly due to advantages such as short lead times compared to forgings, low material waste compared to machining, and high design flexibility [1-3]. Wire based DED AM processes have much higher deposition rates and lower material waste in comparison with powder based processes, leading to the potential to produce large-scale and near-net-shape metallic components in many industry sectors including aerospace, aviation, and power generation [4-7]. Depending on the power source, there are three principal types of wire based DED AM processes, which are electron beam freeform fabrication (EBF^3) [8], wire + laser additive manufacture (WLAM) [9], and wire + arc additive manufacture (WAAM) [10]. EBF^3 is conducted in a vacuum chamber resulting in relatively high equipment cost, low duty cycles, long cooling times and therefore is not widely used. In WLAM, near-net-shape components can be achieved due to the independent control of total laser power and power distribution (principally beam size) which allows achievement of stable melting without keyhole formation. However, due to the low absorptivity of lasers in many metals, very high laser powers are required for high build rates in the WLAM process. This leads to much higher costs, and there is a lot of reflected power to manage. In WAAM, using the plasma transferred arc (PTA) process reasonable deposition rates can be achieved (e.g. 1 kg/h for titanium) due to the high energy transfer efficiency of the electric arc compared to lasers, making large-scale parts achievable in reasonable times [10]. In principle, it is possible to increase the deposition rate further in the PTA process but, unlike the WLAM process, it is not possible to vary the energy distribution greatly. Therefore, the high current required for higher deposition rates increases the likelihood of keyhole formation due to high arc pressure, limiting the deposition rate [11]. Comparing WLAM and WAAM processes, one can see that each process has its own advantages and disadvantages. Therefore, a wire based PTA-laser hybrid AM process was

investigated to combine the advantages of both power sources and thus to build parts with higher deposition rates, no defects, and near-net shape.

For the arc-laser hybrid AM process, there have been only a few research papers published in the past few years. Näsström et al. [12,13] investigated cold metal transfer (CMT) arc-laser hybrid AM process of steel, comparing the deposited components obtained with only CMT, CMT with leading laser, and CMT with trailing laser. They found that the CMT arc with trailing laser configuration improved the process stability and consequently improved the surface finish and geometric feature capability. Pardal et al. [14] studied the benefits of introducing a concentric laser as a secondary power source in CMT based WAAM of titanium. Compared to the CMT process alone, the hybrid process stabilised the arc, leading to an improved bead shape, as well as a higher deposition rate. Zhang et al. [15] investigated gas metal arc (GMA)-laser hybrid AM of aluminium and obtained similar results. They found that compared to the GMA process, the surface quality of the components was improved significantly by adding a laser, and the efficiency of material utilisation was increased by 15%. It is noteworthy that the above studies [12-15] were focused mainly on the improvement of the surface finish of the GMA based WAAM process by addition of the laser. This is because the GMA process with a consumable electrode is not very stable [16], which results in a relatively rough surface finish. In addition, in some materials with a low work function such as titanium, the cathode spot is not fixed on one point and electrons can be extracted from a large area, leading to arc wandering [14]. In addition, the high surface tension of titanium leads to difficulties with droplet detachment as well as large spatter in the GMA process. Hence it is difficult to deposit titanium with GMA process. However, in arc processes with a non-consumable electrode such as gas tungsten arc (GTA) and PTA, the electrons are emitted from the tungsten electrode (thermionic emission) and the arc is stable, which are suitable for deposition of titanium.

Miao et al. [17] compared the microstructure and mechanical properties of aluminium parts deposited by both the GTA-laser hybrid AM process and GTA based WAAM process. They found that the addition of the laser led to more

uniform element distribution and finer grains caused by the strengthened fluid flow and high cooling rate in the laser-affected zone. This resulted in an improved hardness and strength of the samples. Wu et al. [18] studied the microstructure and mechanical properties of Al-Cu alloy deposited by GTA-laser hybrid AM process and stated that the grain size is smaller and Cu element distributes more homogenously in the laser-arc-affected zone compared to arc-affected zone in each layer. The main focus of research on GTA-laser hybrid AM presented to date [17,18] has been on improvement of microstructure and mechanical properties by introducing the additional low power laser source (less than 500 W). However, there is no studies reporting on how to increase deposition rate through the addition of a laser source. Compared to the GTA based WAAM process, PTA based process has a higher stand-off distance due to the more concentrated arc column, which gives a higher tolerance in terms of wire feeding position and layer height errors. Therefore, the PTA-laser hybrid AM process is expected to provide more benefits than GTA based hybrid AM process.

In this study, a PTA-laser hybrid AM process was investigated for the deposition of Ti-6V-4V. The effect of different processing conditions, including the configuration of the laser and PTA powers sources, wire feeding direction, wire feeding position, and arc-laser separation distance on the deposition process (e.g. metal transfer and bead appearance) were studied. The benefits of using the hybrid process over PTA and laser processes on their own were investigated. Three multi-layer single-pass walls were deposited to evaluate the geometric quality of the parts and to study the limitations of the standard hybrid deposition process. A further adaptation of the arc-laser hybrid concept was developed to overcome the observed limitations. This is a multi-energy source (MES) concept utilising three power sources (one PTA and two separate lasers).

5.1.2 Experimental procedure

5.1.2.1 Materials and setup

Ti-6Al-4V wire with a diameter of 1.2 mm was used as the feedstock material, and Ti-6Al-4V plate with dimensions of 300 mm × 200 mm × 7 mm was used as

the substrate. The PTA was generated by a EWM Tetrix 552 power supply. Pure argon was used for both plasma gas and shielding gas for the plasma torch with the flowrates of 0.8 and 8 L/min, respectively. The tungsten electrode had a diameter of 4 mm with a tip angle of 40° and a set-back of 2.4 mm. The copper orifice had a diameter of 3.9 mm, and the stand-off distance between the orifice and workpiece was 8 mm. A continuous-wave fibre laser (IPG YLR-8000, wavelength: 1.07μm) with a maximum power of 8 kW was used for the laser source. The laser is delivered through a fibre with a core diameter of 0.3 mm, and the focal lengths of the collimation lens and focusing lens are 125 and 250 mm respectively. The optical setup gives a laser beam with a focal spot diameter of 0.6 mm. The laser defocusing was applied during all depositions.

Figure 5-1 shows the experimental setup for the PTA-laser hybrid AM system. The deposition was conducted in an enclosed tent to prevent the material from oxidation, which was purged with argon until the oxygen level was below 500 ppm as verified by an oxygen analyser. A 6-axis Fanuc robot was used to provide motion for the system, and the robot's end-effector was enclosed in the tent. A Dinse wire feeder was used to feed the wire. The arc current and voltage were recorded by an arc monitor (Triton Electronics AMV4000). The plasma torch was inclined at an angle of 20° to protect it from the burning by the laser beam. The laser head was inclined at an angle of 30° to prevent back reflection. The deposition process, including the metal transfer and melt pool behaviour, was monitored using a CMOS process camera (Xiris XVC-1000).

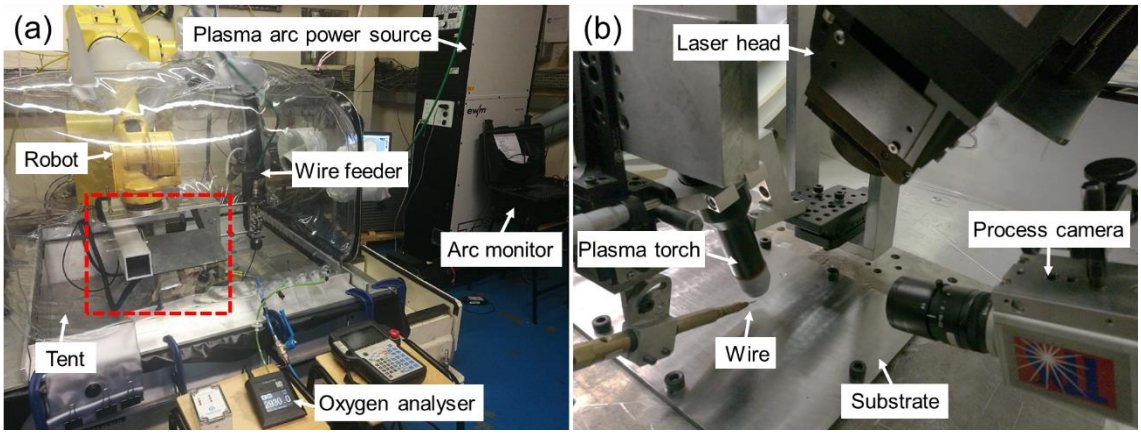


Figure 5-1 (a) Experimental setup for PTA-laser hybrid AM system, and (b) view from inside of the tent, which is indicated by a red dashed square in (a).

5.1.2.2 Methods

5.1.2.2.1 Processing conditions in the hybrid process

As shown in Figure 5-2, two different configurations regarding the relative position of the wire, plasma torch, and laser head were used, in which the wire was either irradiated by the PTA first (Figure 5-2a) or by the laser first (Figure 5-2b). Note that the wire feeding angles were slightly different in the two configurations in order to feed the wire properly. When considering the wire feeding direction, there are four configurations for the wire and power sources: wire front feeding with PTA leading (a1), wire back feeding with laser leading (a2), wire front feeding with laser leading (b1), and wire back feeding with PTA leading (b2). Based on the outcome of initial optimisation (explained in Section 5.1.3.1.1), the configuration with wire front feeding and PTA leading (a1) was used for the remaining experiments. It should be noted that the substrate was fixed during all the depositions. Therefore the travel direction mentioned in this study is based on the movement of the wire, plasma torch and laser head.

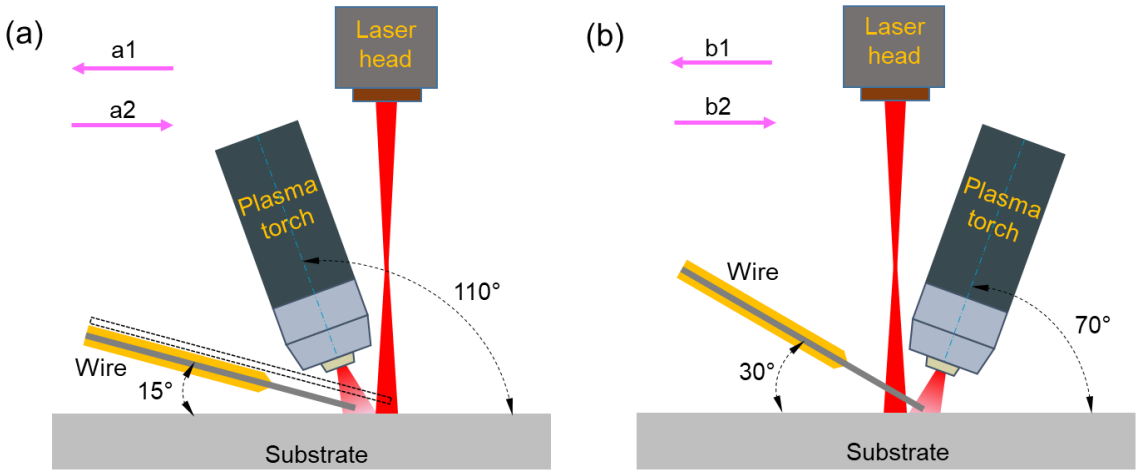


Figure 5-2 Different configurations and travel directions (indicated by pink arrows) used: (a) the wire is first irradiated by the PTA, and (b) the wire is first irradiated by the laser.

To investigate the tolerance of the hybrid process to wire positioning accuracy and process robustness, some deposits were conducted with different wire feeding positions. In this procedure, the distance (d_1) between the wire tip and the workpiece was increased from 0 to 4 mm with an increment of 1 mm. The wire melting and melt pool behaviour were recorded by the process camera. In order to study the effect of the separation distance between the power sources on the deposition process and bead appearance, a set of beads was deposited by increasing the arc-laser separation distances (d_2) from 10 to 18 mm with an increment of 2 mm. The definition of d_1 and d_2 is illustrated in Figure 5-3. Table 5-1 shows the parameters that were maintained constant.

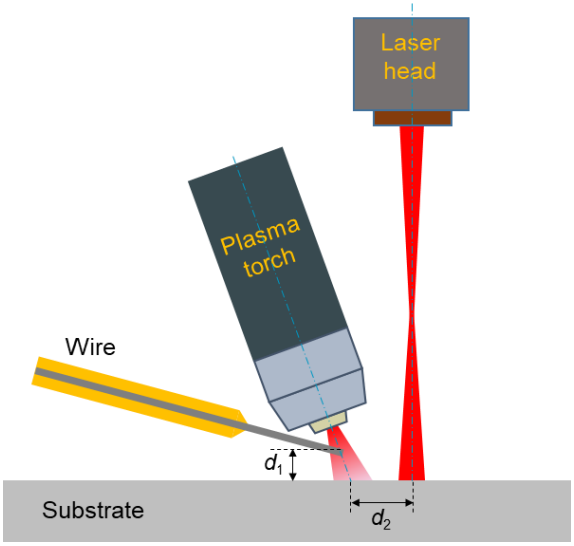


Figure 5-3 Illustration of the definition of d_1 and d_2.

Table 5-1 Fixed process parameters used during the experiments.

Parameters	Value (unit)
Travel speed (TS)	4.5 mm/s
Wire feed speed (WFS)	4 m/min
Laser beam diameter	12 mm
Arc current	200 A

5.1.2.2.2 Deposition rate in different AM processes

The deposition rate, R, is expressed by:

$$R = \frac{\pi d_w^2 v_w \rho_w}{4} \quad \textbf{(5-1)}$$

where d_w is the wire diameter, v_w is WFS, ρ_w is the density of the wire. Therefore, for a given wire, the deposition rate is only controlled by WFS. First, the limit of deposition rate for the same applied power was achieved for each process separately, i.e. PTA and laser. In each case, a maximum WSF was found at a given power, above which the wire could not be melted anymore, as established from the video recordings. The power was increased from 2 to 8 kW

with an increment of 2 kW. Next, the deposition rate of the hybrid process was compared with those of laser and PTA on their own for the same power output of 8 kW. In the hybrid process, the ratio between the laser power and the PTA power was varied but for a constant total power of 8 kW. For each ratio, the maximum WFS was recorded and compared. It should be mentioned that in this series of experiments, the wire feeding position was lifted up to make sure that both the PTA and laser can irradiate on the wire, which is indicated by the dashed outline as shown in Figure 5-2a.

In order to achieve the exact power needed from the PTA power supply, several deposits were conducted with different currents, where the current and voltage were recorded by arc monitor. The output power of the power supply, P_o, is given by:

$$P_o = UI \tag{5-2}$$

where U and I are arc voltage and current, respectively. Based on Equation (5-2) and the data obtained from the arc monitor, the output power of the PTA as a function of current was obtained, as shown in Figure 5-4.

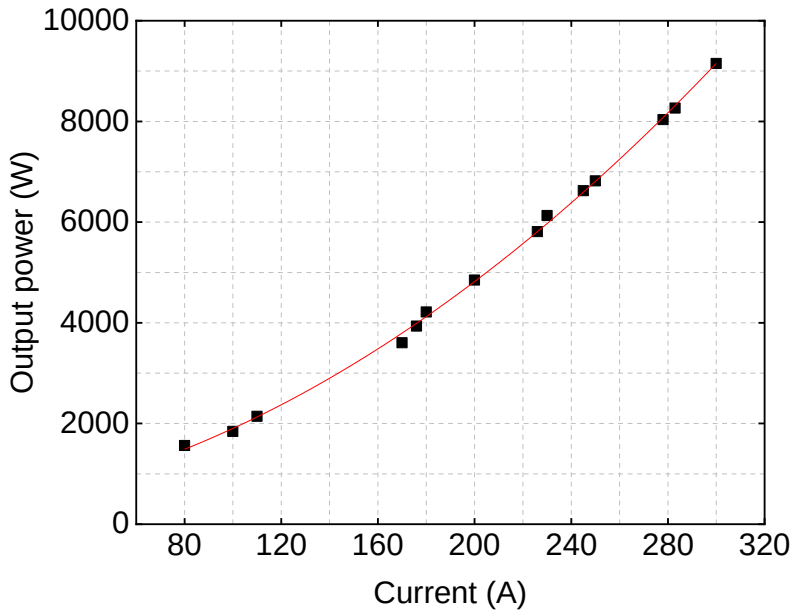


Figure 5-4 Measured output power of PTA as a function of applied current.

5.1.2.2.3 Tolerance of WLAM

To compare the tolerance of the hybrid process with WLAM process in terms of wire positioning accuracy, some additional deposits were conducted with WLAM. In this case, the distance from the wire tip to the substrate was increased from 0 to 4 mm with an increment of 1 mm. The WFS and TS used were 2 m/min and 4.5 mm/s, respectively. A 4 kW laser power with a defocused laser beam diameter of 8 mm was used.

5.1.2.2.4 Limitation of WAAM

To study the limit of WAAM process due to keyhole formation, some experiments with varying power input and deposition rate were conducted with WAAM and hybrid processes. In the wire based AM processes, the ratio of WFS to TS is an important parameter, which determines the cross-sectional area of the bead. During the deposition, if we neglect vaporisation of the material or spatter, the volume of melted wire and the deposited bead will be the same. In a unit time, they can be expressed as:

$$\frac{\pi d_w^2}{4} v_w = A_b v_t \quad \textbf{(5-3)}$$

where A_b is the cross-sectional area of the bead (not including the remelting area, as shown in Figure 5-5), and v_t is TS. From Equation (5-3), the ratio of WFS to TS can be expressed as:

$$\frac{v_w}{v_t} = \frac{4A_b}{\pi d_w^2} \quad \textbf{(5-4)}$$

It can be seen that for a given wire diameter, the WFS to TS ratio is proportional to the cross-sectional area (A_b) of the bead.

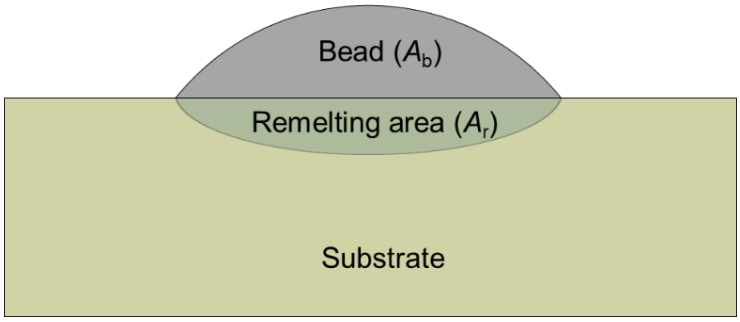


Figure 5-5 Schematic diagram showing the deposited bead with a cross-sectional area of A_b and remelting area of A_r.

In order to achieve the same bead shape (i.e. bead height and bead width) with different processes, the WFS to TS ratio should be the same. In addition, the heat input per unit length should be the same. Therefore, the WFS and TS were increased proportionally to achieve higher deposition rates (controlled by WFS). Meanwhile, the heat input was increased proportionally from a low value to a limit value marked by the onset of keyhole formation. The experiment was first conducted for WAAM and then compared with the hybrid process.

5.1.2.2.5 Multi-layer wall building

To evaluate the geometric quality of the components deposited by the hybrid process, three multi-layer single-pass walls were deposited at different deposition rates. The process parameters used are listed in Table 5-2. The parts were cross-sectioned, mounted, polished, and etched after being deposited to check the profile and surface waviness.

Table 5-2 Process parameters used for deposition of the multi-layer single-pass walls.

Parameters (unit)	Wall 1	Wall 2	Wall 3
TS (mm/s)	4.5	4.5	4.5
WFS (m/min)	4	6	8
Arc current (A)	200	240	280
Laser beam diameter (mm)	12	12	12
Laser power (kW)	3	5	5

5.1.2.2.6 Multi-energy source deposition

In AM, the deposition process efficiency can be reflected by the energy needed for deposition of per unit mass of material, which is defined by:

$$e = \frac{P_a}{R} \tag{5-5}$$

where P_a is the total applied power of the process, and R is the deposition rate. It can be seen that the lower the value of e, the higher the deposition process efficiency. The initial results show that with the standard PTA-laser hybrid configuration, the remelting ratio is high, resulting in low deposition process efficiency (explained in Section 5.1.3.3). To overcome the low process deposition efficiency and to reduce the remelting depth of the process, the energy distribution needs to be adjusted so that more energy is applied to the edges of the melt pool generated by the PTA. To achieve this, we investigated a MES concept [19], where three or more energy sources are combined to give an adaptable and optimised power density profile. The specific arrangement used for this initial investigation is shown in Figure 5-6. The PTA source was leading, and two laser sources were placed at the edges of the melt pool. The distance between the two lasers was 8 mm. Due to the practical limitations of this complex setup, back wire feeding was used.

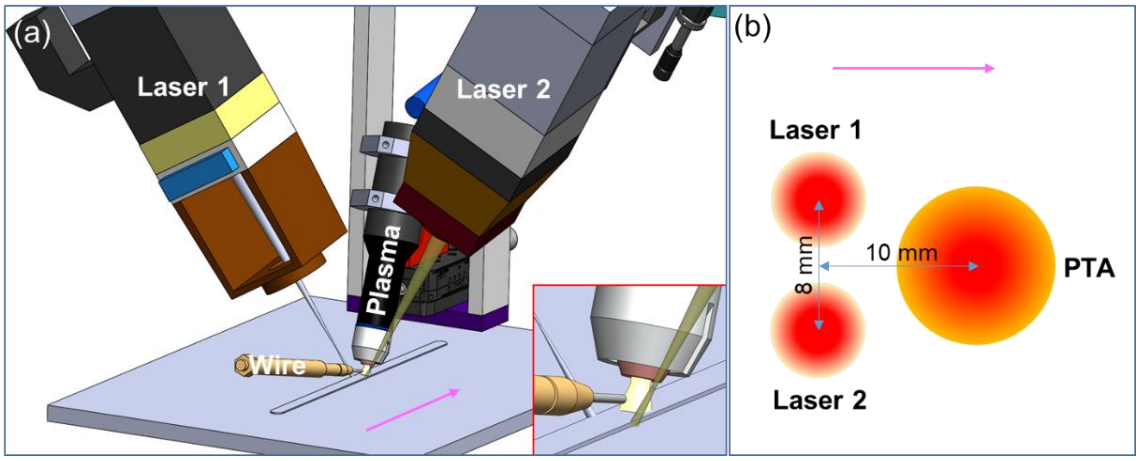


Figure 5-6 Schematic shows (a) the configuration of MES with one PTA and two separate lasers, and (b) the relative position of the three energy sources. Pink arrows indicate the travel direction.

To compare the benefits of using MES over the standard hybrid process, a deposit was also conducted using the standard PTA-laser hybrid process. In both configurations, the WFS, TS, arc current and the total applied power of laser are the same except for the laser energy distribution. All the parameters used for the two processes are shown in Table 5-3.

Table 5-3 Process parameters used for the standard PTA-laser hybrid process and MES deposition process.

Parameters (unit)	Standard hybrid process	MES
TS (mm/s)	4.5	4.5
WFS (m/min)	4	4
Arc current (A)	200	200
Laser beam diameter (mm)	12	Laser 1: 6
		Laser 2: 6
Laser power (kW)	3	Laser 1: 1.5
		Laser 2: 1.5

5.1.3 Results and discussion

5.1.3.1 Processing conditions of the hybrid AM

5.1.3.1.1 Configuration

Figure 5-7 shows the hybrid deposition processes with front feeding configurations. In Figure 5-7a, the PTA was leading. It can be seen that the wire was melted by the PTA with small droplets being transferred into the melt pool. The laser was placed behind the PTA to make the bead wider by adding more power into the melt pool. The small droplets appear to be in continuous contact with the melt pool, which ensures smooth metal transfer. This resulted in a wide and smooth bead, as shown in Figure 5-7c. In contrast, large droplets generated in the laser leading configuration, which resulted in a less smooth bead with large ripples on the surface, as shown in Figure 5-7d. The high laser power, in this case, was sufficient to melt the wire. However, as shown in Figure 5-7b, the high surface tension of titanium and the lack of arc pressure that would push the droplets towards the melt pool resulted in large droplets with a lower detachment frequency.

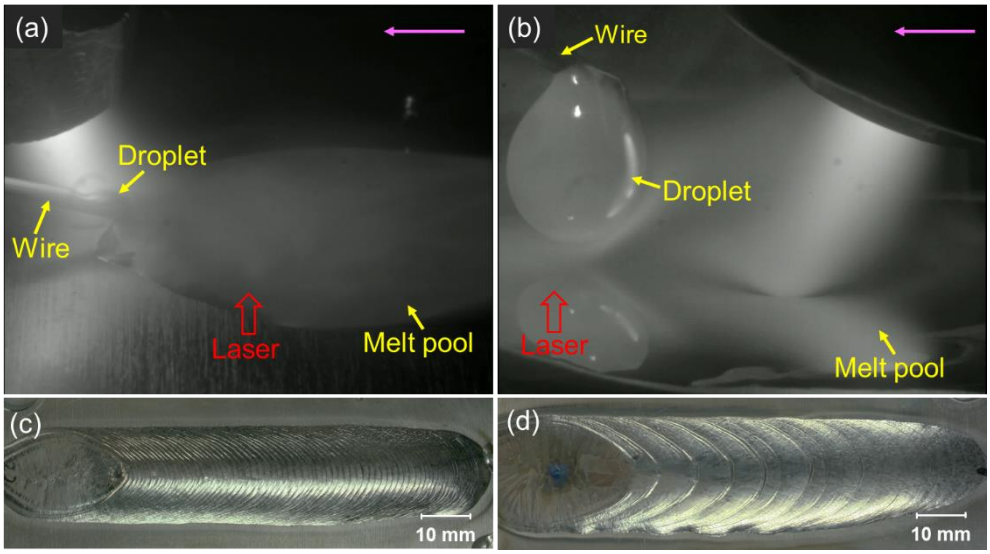


Figure 5-7 The effect of wire orientation and leading source on the deposition process and bead appearance for 7 kW laser and 200 A current: (a) wire melted by the PTA, and (b) wire melted by the laser. (c) and (d) show the bead appearance obtained with (a) and (b) respectively. Pink arrows indicate the travel direction.

In the first case (Figure 5-7a), the stable metal transfer was attributed to the arc pressure produced by PTA, which pushed the small droplet into the melt pool regularly. In the second case (Figure 5-7b), however, there was no detachment force for the droplet when the wire was melted. Therefore, the droplet kept growing and detached from the wire only when touching the melt pool. In this case, the gravitational force and the surface tension from the melt pool were the main detachment forces. The large droplets with low detachment frequency in the second case induced oscillations in the melt pool. Therefore the configuration with the wire being melted by the PTA is more suitable for the hybrid process.

Figure 5-8 shows the hybrid deposition process where the arc pressure is used to transfer the metal from the wire. As indicated by the blue arrow in Figure 5-8a, the contact tip is in very close proximity to the deposited bead when the wire is in the back feeding position, leading to a lower tolerance in wire position compared to the front feeding position shown in Figure 5-8b. Therefore, the configuration of wire front feeding with PTA leading was selected for further experiments.

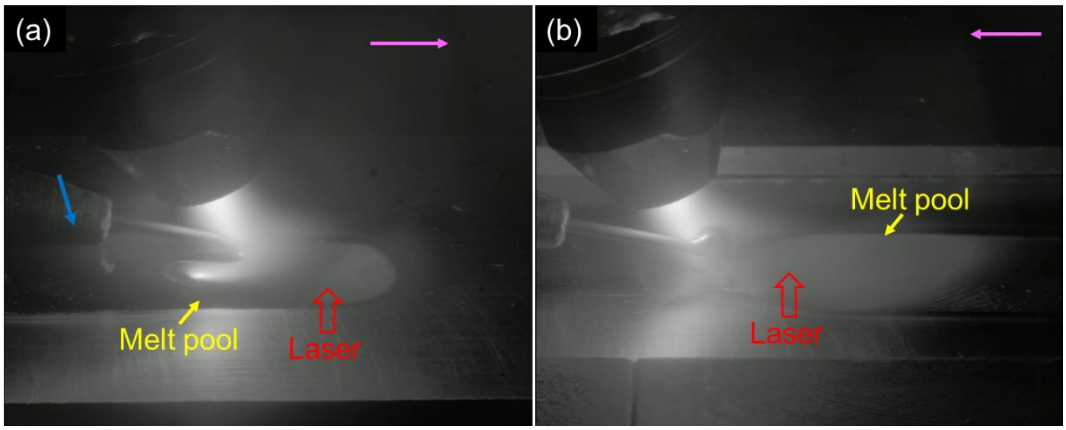


Figure 5-8 The effect of wire feeding direction on the hybrid deposition process: (a) back feeding, and (b) front feeding. The laser power used in both cases was 3 kW.

5.1.3.1.2 Wire feeding position

Figure 5-9 shows the hybrid deposition process with different wire feeding positions with respect to the surface of the workpiece, and Figure 5-10 shows the bead appearance and bead width obtained with the corresponding positions.

When the wire feeding position was too low (d_1=0, Figure 5-9a), the wire stabbed the workpiece before it could be fully melted, increasing the likelihood of bending and misaligning of the wire. The bead obtained with this process is shown in Figure 5-10(a1), which had irregular edges. However, when the wire feeding position became higher (from 1 to 4 mm), the metal was transferred to the metal pool in regular intervals, which led to a good bead appearance, as shown in Figure 5-10(a2-a5). It also can be seen from Figure 5-10b that the bead width increases very slightly (from 12.83 to 13.54 mm) as the wire feeding position changes from 1 to 4 mm. This is attributed to the improvement in melting efficiency as the wire feeding position becomes higher [11]. With the low position, some of the wire is melted in the melt pool, leading to lower process efficiency and a narrower bead. When the position is higher, all the wire is melted in the arc, resulting in higher process efficiency and wider bead. In general, it can be concluded that the hybrid process has high tolerance to the wire feeding position since the metal transfer behaviour and the bead shape did not change significantly when the distance between wire tip and workpiece changed from 1 to 4 mm.

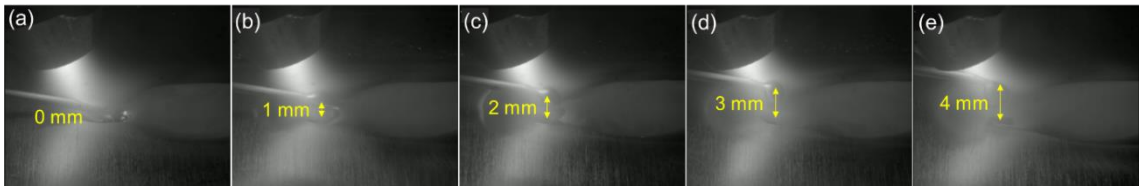


Figure 5-9 The effect of wire-workpiece distance on the deposition process: (a) d_1=0, (b) d_1=1 mm, (c) d_1=2 mm, (d) d_1=3 mm, and (e) d_1=4 mm.

In addition, the beads deposited by the hybrid process have smooth surface even for settings of wire where large droplets are formed. For example, even when the droplets impact the melt pool with high energy from a high position (d_1=4 mm), the melt pool was still stable (Figure 5-9e), and the bead surface was smooth (Figure 5-10(a5)). This is because the wire is melted by PTA, which takes advantage of the high tolerance of PTA and the additional energy from the laser then expands and stabilises the melt pool, which means that any oscillations in the melt pool dampen down before the onset of solidification.

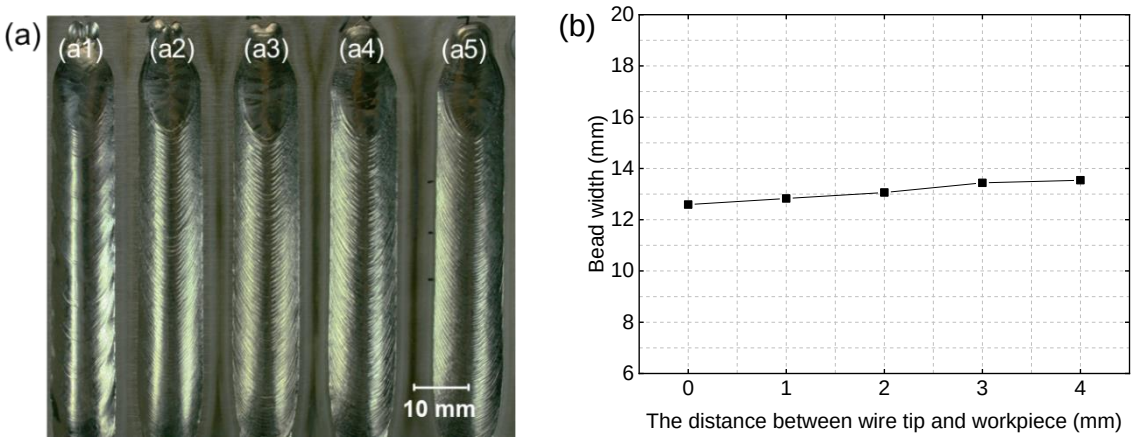


Figure 5-10 (a) Bead appearance and (b) bead width obtained with different wire-workpiece distances: (a1) d_1=0, (a2) d_1=1 mm, (a3) d_1=2 mm, (a4) d_1=3 mm, and (a5) d_1=4 mm.

5.1.3.1.3 Arc-laser separation distance

Figure 5-11 shows the deposition process with different separation distances between PTA and laser, and Figure 5-12 shows the corresponding bead appearances and bead widths. It can be seen from Figure 5-11a that when the two heat sources were relatively close to each other (d_2=10 mm), there was just one common melt pool formed. However, when the separation distance increased to 14 mm (Figure 5-11c), a clear narrowing with two separated melt pools could be observed. This means that the melt pool generated by the PTA lost a significant amount of energy and almost solidified before the laser impinged on it. As the separation distance further increased (Figure 5-11d and 5-11e), the gap between the two melt pools became larger. It should be noted that this effect is dependent on the energy and spot size of the laser and PTA.

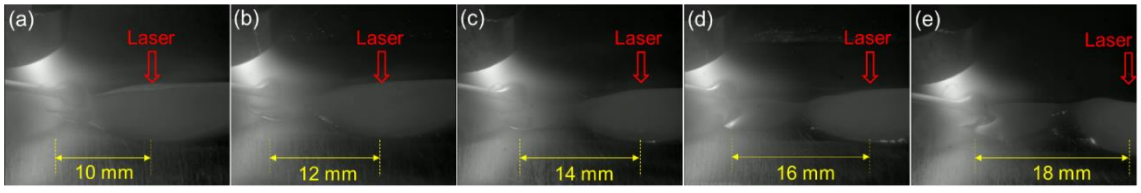


Figure 5-11 The effect of arc-laser separation distance on the deposition process: (a) d_2=10 mm, (b) d_2=12 mm, (c) d_2=14 mm, (d) d_2=16 mm, and (e) d_2=18 mm.

It can be seen from Figure 5-12a that the separation distance also affects the final bead shape. The beads are irregular when two separated melt pools are formed, and this becomes worse as the separation distance increases. Also, beyond a certain distance, the initiation and termination of the beads are unacceptable due to the non-uniform shape (Figure 5-12(a3-a5)).

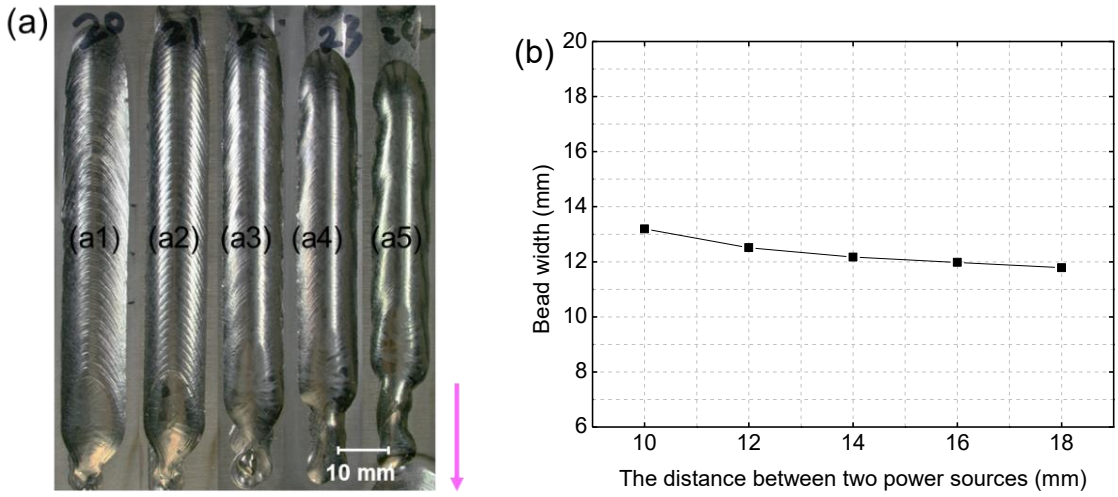


Figure 5-12 The effect of arc-laser separation distance on (a) bead appearance, and (b) bead width. The pink arrow indicates the deposition direction.

As shown in Figure 5-12b, the bead width decreases as the separation distance increases. This is because as the separation distance increases, energy is lost through conduction, so the melt pool becomes smaller. When the laser then adds more energy again, it has to firstly replace this lost energy to get the melt pool back to the original size generated by the PTA. Any remaining energy then broadens the melt pool. The closer the laser is to the PTA source then the less the thermal losses are before the addition of the laser energy. Therefore, the bead width gets smaller as the separation distance increases. Based on the presented analysis, the separation distance should be as low as practically possible, which will give a uniform and wide bead appearance. However, if the separation distance is too low, the likelihood of damaging plasma torch by the laser reflection is very high. Therefore, in this study, a minimum separation distance of 10 mm was used.

5.1.3.2 Benefits of the hybrid process

5.1.3.2.1 Deposition rate

Figure 5-13 shows the maximum deposition rates achieved with different applied powers for the processes of the PTA and laser on their own. It can be seen that the deposition rate increases linearly with the applied power for both processes. Also, for a given power, the deposition rate obtained with PTA is always higher than that of the laser. This is because the beam size of the PTA is smaller than that of the laser (12 mm in this case), and therefore the wire absorbs more power directly from the former power source. Figure 5-14 shows a schematic of the wire under a power source beam. The power absorbed (P) per unit length by wire is the projected area under the beam (width times length of wire exposed) times power density. For round wire, the width is the same as the diameter. Then, P can be expressed as:

$$P = \eta_1 d_w D E \quad \textbf{(5-6)}$$

where η_1 is the absorption coefficient, D is the power source beam diameter, E is the power density. E is expressed by:

$$E = \frac{4P_a}{\pi D^2} \quad \textbf{(5-7)}$$

where P_a is the applied power. By substituting Equation (5-7) into Equation (5-6), the power absorbed per unit length by wire can be further expressed as:

$$P = \frac{4\eta_1 d_w P_a}{\pi D} \quad \textbf{(5-8)}$$

Assuming the same absorption coefficient for the PTA and laser, it can be seen that for the same applied power, more power is absorbed by the wire in the case with smaller beam size. This also means that more power goes to the workpiece in the case with a larger beam size, which is dissipated through thermal conduction. This can be clearly seen from Figure 5-15 in that a much wider melt pool was generated with the laser (Figure 5-15b) compared to that with the PTA (Figure 5-15a) at the same applied power. Actually, if the laser beam size is the

same as that of the PTA size, then the difference is solely down to the absorption coefficient. The absorption of laser energy in titanium is quite high (around 0.4) compared to many other metals (e.g., 0.3 for stainless steel and 0.15 for aluminium) [20], but still likely to be lower than PTA on its own (0.5-0.75) [21]. Therefore, higher deposition rates can be obtained with the PTA compared to that with the laser at the same applied power due to the more direct absorption of energy by the wire from the PTA.

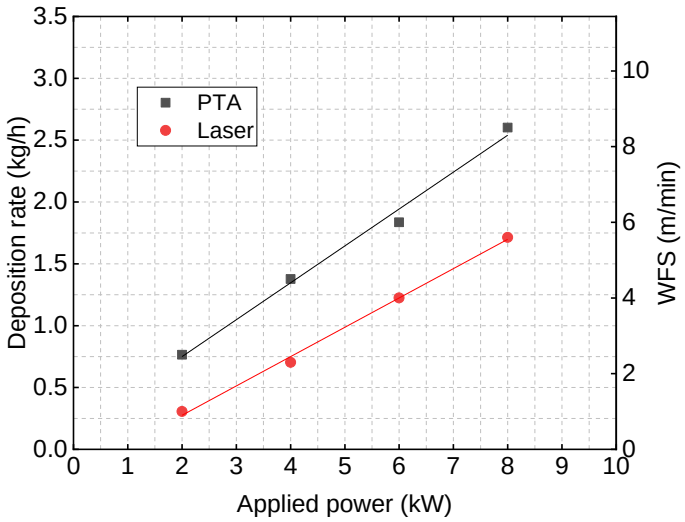


Figure 5-13 Comparison of maximum deposition rates obtained with a single laser and a single PTA processes.

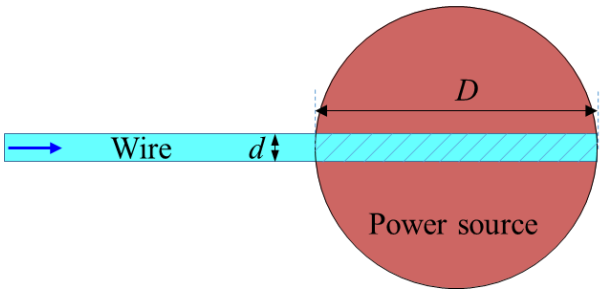


Figure 5-14 Schematic shows the wire under a single power source (PTA or laser). Blue arrow indicates wire feeding direction.

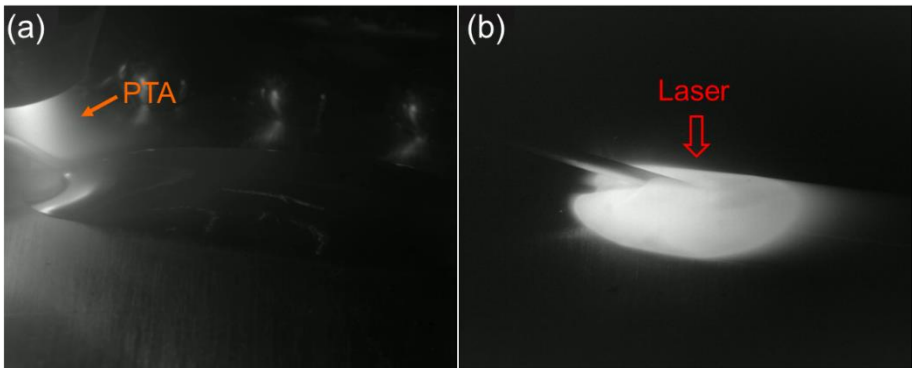


Figure 5-15 The deposition processes with the power source of (a) PTA, and (b) laser, at the same applied power of 6 kW.

Figure 5-16 shows the maximum deposition rates obtained with the hybrid process and compared with PTA only and laser only processes. The total power input for each process is 8 kW, which means that in the hybrid process the power ratio between the laser and the PTA was varied to maintain the same total power. It can be seen that the maximum deposition rate obtained with the hybrid process was around 0.5 kg/h higher than that of PTA only process (2.6 kg/h), with the lowest deposition rate being the laser only process (1.7 kg/h).

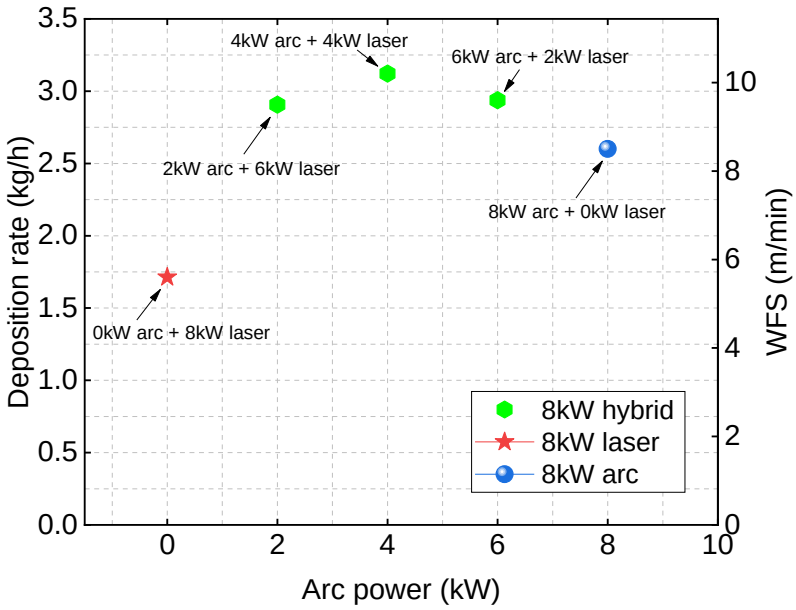


Figure 5-16 Comparison of maximum deposition rates obtained with the hybrid process, PTA only process, and laser only process with a total power input of 8 kW in each case.

Figure 5-17 shows the corresponding hybrid and PTA only deposition processes as presented in Figure 5-16. In each case, the WFS is the maximum limit for the applied power to achieve a stable process. For the hybrid process, although all three cases have the same total applied power input, the contribution of each power source for the melting of wire is different in each case. As shown in Figure 5-17a, when the arc power is low (2 kW), the PTA preheats the wire but the laser provides most of the energy needed for melting of the wire. In this case, there is no melt pool generated under the arc, and all the melt pool is under the laser. A similar phenomenon occurs in the second case (Figure 5-17b), but with hotter wire reaching the laser due to the higher arc power (4 kW). As shown in Figure 5-17c, however, with a high arc power of 6 kW, most of the wire is melted by PTA before reaching the melt pool, and the rest of the wire is melted by the laser. In this case, the PTA provides a large proportion of energy needed to melt the wire, and there is a melt pool formed under the PTA. As for the PTA only deposition process (Figure 5-17d), most of the wire is melted by the arc, and the rest is melted by the melt pool.

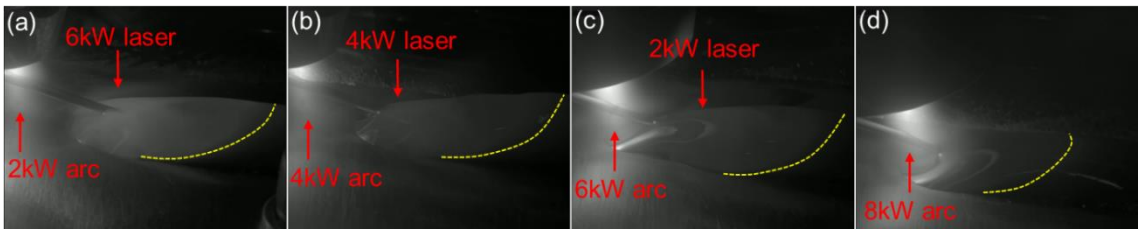


Figure 5-17 Hybrid and PTA only deposition process with a total power input of 8 kW: (a) 2 kW arc and 6 kW laser, (b) 4 kW arc and 4 kW laser, (c) 6 kW arc and 2 kW laser, and (d) 8 kW arc. Yellow dashed line indicates the melt pool boundary.

The deposition rate of the hybrid process is higher than that of the laser process on its own as it is a combination of the PTA and the laser. For the PTA only process, the deposition rate is limited by the melting of the wire. For a given wire thickness, there is a minimum time for the wire to melt determined by energy conduction from the top to the bottom. To achieve higher deposition rates, the wire needs to be fed at higher speeds, reducing the effective interaction time for the relatively small PTA. In the hybrid case, the energy distribution is extended

and the wire passes into the laser after the arc and continues to be melted there. It can be seen from Figure 5-17 that the melt pools in all the three hybrid cases are longer than that in the PTA only process. Also, Figure 5-18 schematically shows the positions of the wire in the hybrid and PTA only processes. It can be seen that both the power source and the hot melt pool provide energy for the melting of the wire in the two cases. However, the length of the wire surrounded by the power source and melt pool in the hybrid process (L1 in Figure 5-18a) is longer than that in the PTA only process (L2 in Figure 5-18b), which gives more time for the energy conduction from the top to the bottom of the wire for the hybrid process, allowing more wire to be melted at the same total applied power. Therefore, compared to the PTA only process, a higher deposition rate was obtained in the hybrid process due to the extended energy distribution and melt pool size.

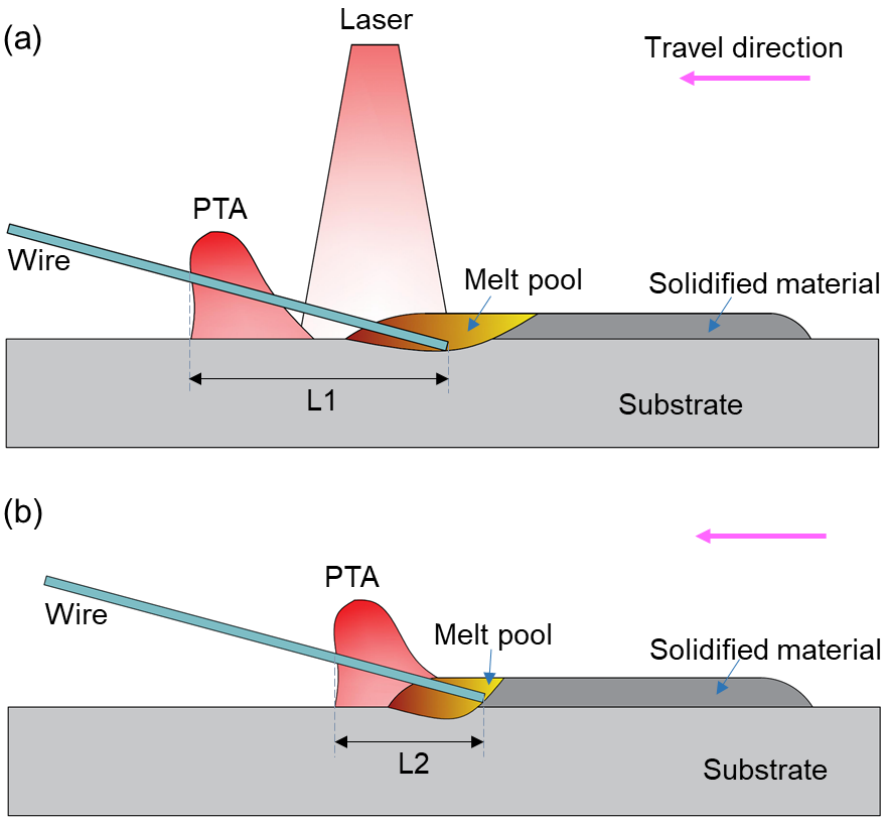


Figure 5-18 Schematic shows the positions of the wire in (a) the hybrid PTA-laser process, and (b) single PTA process.

5.1.3.2.2 Tolerance of WLAM

As described in Section 5.1.3.1.2, in the hybrid process the wire is melted by PTA, which has high tolerance to the wire feeding position. In WLAM, however, the deposition process is very sensitive to the wire feeding position. Figure 5-19 shows the deposition processes and the corresponding bead appearances with different wire feeding positions. When the wire feeding position was very low (d_1=0), the wire stabbed the melt pool. This did not cause any major problems but induced irregular oscillations in the melt pool, which is however not reflected on the bead shape. When the distance between the wire tip and workpiece was increased to 1-2 mm, the process was in the optimum configuration, leading to smooth and uniform bead appearances. When this distance was increased further (d_1=3 mm, d_1=4 mm), large droplets started to form at the tip of the wire, causing significant oscillations in the melt pool with a fixed period. This is attributed to the high surface tension of titanium and lack of detachment force apart from the gravitational force. This shows that the processing window for the wire feeding position in WALM is very narrow, ranging only from 1 to 2 mm. When the wire position is out of this range, the process is unstable and deposited beads are unacceptable. Similar phenomena were also reported by other researchers [22-25]. Hence the hybrid process benefits not only from higher melting efficiency but also from the electromagnetic force of arc and the shear force of plasma gas which helps droplet detachment and does not require the wire to be in direct contact with the melt pool.

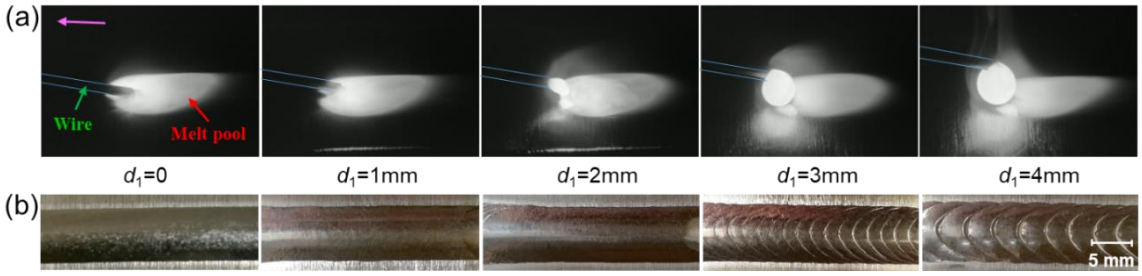


Figure 5-19 Tolerance of WLAM to wire-workpiece distance: (a) d_1=0, (b) d_1=1 mm, (c) d_1=2 mm, (d) d_1=3 mm, and (e) d_1=4 mm.

5.1.3.2.3 Limitation of WAAM

The arc pressure provides a detachment force for the metal transfer, however it also can cause some issues. As reported in Ref. [11], the arc pressure increases with the increasing current owing to the increasing electromagnetic force. Above a certain level, a keyhole is formed, which can cause defects in the beads. Figure 5-20 shows two deposited beads obtained at two different levels of current. It can be seen that the bead is smooth and uniform at a current of 205 A (Figure 5-20a), however when the current is increased to 283 A severe defects are formed, caused by keyhole formation (Figure 5-20b). The maximum deposition rate that can be achieved with the WAAM process is directly proportional to the current of the PTA. Hence keyhole formation limits the deposition rate.

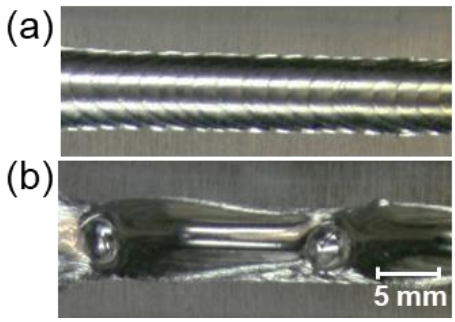


Figure 5-20 The effect of current on keyhole formation: (a) bead with a good appearance at 205 A, and (b) bead with defects at 283 A.

Figure 5-21 shows the power required for a particular deposition rate and the corresponding beads for WAAM and hybrid processes. The hybrid process can be used as an extension of the WAAM process to increase the deposition rate. At a very low power input (1.67 kW, point A), the energy was just enough to melt the wire, but there was no melt pool generated on the substrate due to the conduction loss, leading to an irregular bead (Figure 5-21 b1). The maximum deposition rate that could be achieved with WAAM process, on the other hand, without any defects was 0.54 kg/h. As the power input exceeded 5.83 kW (point B), keyhole defects started to appear in the melt pool, as shown in Figure 5-21 b2. However, with the same total power input of 5.83 kW (arc power of 4.16 kW and laser power of 1.67 kW), there was no keyhole formed in the hybrid process, and the bead was smooth and uniform (Figure 5-21 b3). For the hybrid process,

even with a total power input of 11.67 kW (arc power of 5.83 kW and laser power of 5.84 kW, point C), there still was no keyhole and a regular bead could be formed (Figure 5-21 b4). This means that by adding the laser, the deposition rate could be doubled (from 0.54 to more than 1.08 kg/h in this case) without the risk of keyhole formation.

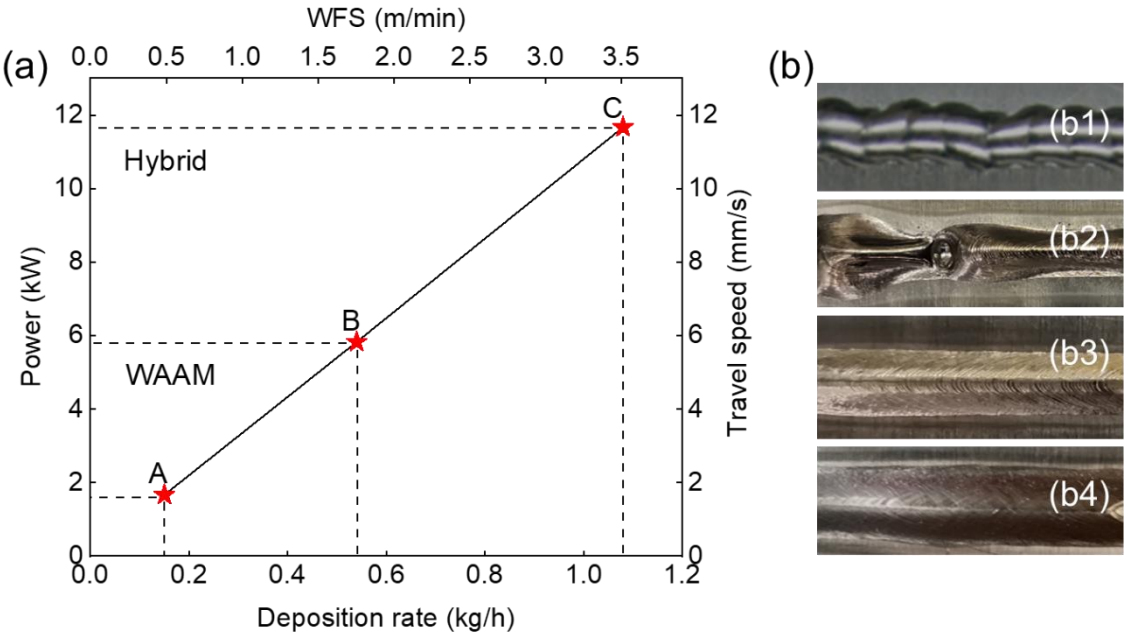


Figure 5-21 (a) Deposition rate and (b) bead appearance at different applied powers obtained with WAAM and hybrid processes.

The total energy in the hybrid process is distributed between arc and laser, which means that the arc current is lower than that in the WAAM process with same total power input, leading to a lower arc pressure in the former process. As a result, the likelihood of keyhole formation in the hybrid process is very low, which therefore extends the deposition rate. It should be mentioned that the deposition rates obtained with both PTA and hybrid processes are relatively low. This is because the ratio of WTS to TS is low in this case to achieve a small bead cross-sectional area.

From the above analysis, one can see that the PTA-laser hybrid AM process combines the advantages of both power sources. In the hybrid process, the PTA is used to melt the wire and the laser is used to better control the melt pool.

Compared to a laser, a PTA has higher efficiency and process tolerance. Therefore, its energy is utilised to initiate the melt pool, melt the wire and ensure efficient metal transfer. Compared to a PTA, a laser in conduction regime does not produce keyhole. Therefore, the laser energy is added to the PTA source so that a higher deposition rate can be achieved without the generation of keyhole defects. Additionally, the extended energy distribution and melt pool size allow achievement of higher deposition rates compared to either process on its own.

5.1.3.3 Multi-layer wall building

Figure 5-22 shows the cross-sections of the three multi-layer single-pass walls with different widths and deposition rates. The properties of the walls are summarised in Table 5-4. It can be seen that all the walls have a good surface finish, especially wall 1 and wall 2, which have near-net shape. This means that such parts would require little or none post-machining. Also, the relatively high deposition rate of 2.4 kg/h (wall 3) of the hybrid process means shorter deposition time and lower cost of parts compared to the normally used one in WAAM ranging from 0.4 to 1.2 kg/h. In addition, the effective wall width can easily go up to 18.6 mm (wall 3) in the hybrid process. The much higher bead width could be achieved as compared to WAAM process with still better deposition rate and surface quality, meaning that the hybrid process has a larger working envelope than WAAM.

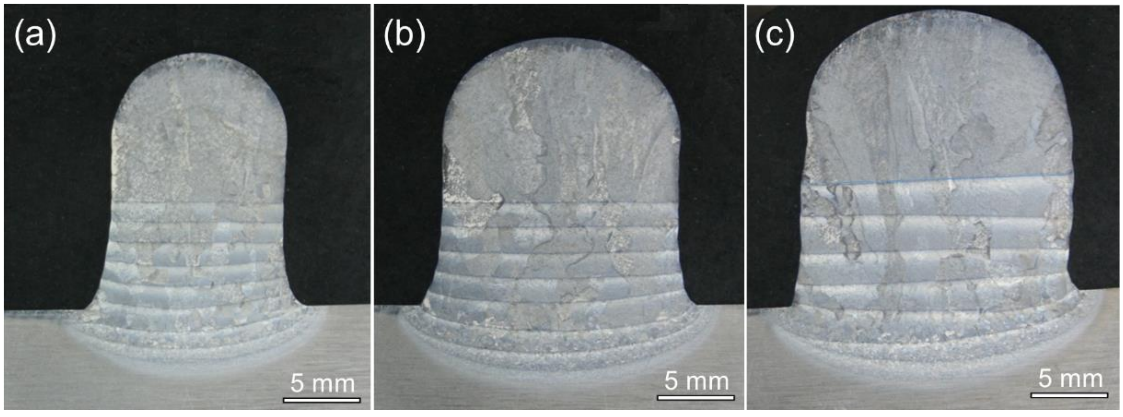


Figure 5-22 The cross-sections of the multi-layer single-pass walls with different WFSs show good surface finish: (a) wall 1: 4 m/min, (b) wall 2: 6 m/min, and (c) wall 3: 8 m/min. The parameters used are shown in Table 5-2.

Table 5-4 Geometric properties of the multi-layer single-pass walls.

Parameters (unit)	Wall 1	Wall 2	Wall 3
Total layer number	10	9	8
Total height (mm)	17.1	18.2	19.8
Average layer height (mm)	1.7	2.0	2.5
Width (mm)	11.5	15.8	18.6
Deposition rate (kg/h)	1.2	1.8	2.4

As described above, the PTA-laser hybrid AM process has many benefits. However, there are some limitations of the process. For DED AM processes, it is very desirable to minimise dilution or remelting ratios. Energy used for melting previous layers is effectively wasted and leads to a very inefficient process. Furthermore, it can cause problems with undesirable microstructures forming and therefore properties if the deposited material goes through many thermal cycles. Finally, it can cause severe problems with residual stresses and distortion. From Figure 5-22, it can be seen that the remelting area of the workpiece is significant, which indicates the previous few layers will be remelted when depositing the subsequent layer. This is also indicated by looking at the overall deposition process efficiency. For wall 2, for example, the total power input is 11.4 kW with a deposition rate of 1.8 kg/h, giving a process efficiency of 22.3 MJ/kg for the deposited material. This compares with typical values of 17.0 MJ/kg for a single-pass wall in PTA based WAAM process from the literature [26]. This is because for both the PTA and laser the highest power density is on the deposit centreline. Thus much energy is concentrated in the melt pool centreline during the hybrid deposition process.

5.1.3.4 Multi-energy source deposition

Figure 5-23 shows a comparison of the standard PTA-laser hybrid process and the MES deposition process and the cross-section of the beads obtained with the

two processes. From Figure 5-23c and 5-23d, it can be seen that the bead obtained with the MES process exhibited a wider and shallower profile. It is clear it will be possible to increase the WFS and therefore to increase the deposition rate and the deposition process efficiency. It can also be seen that both the remelting depth and the heat-affected zone (HAZ) are shallower for the MES process compared to the standard PTA-laser hybrid process. This means the MES process is capable of achieving a high deposition rate and high process efficiency. Further studies of the MES concept will be done in the future.

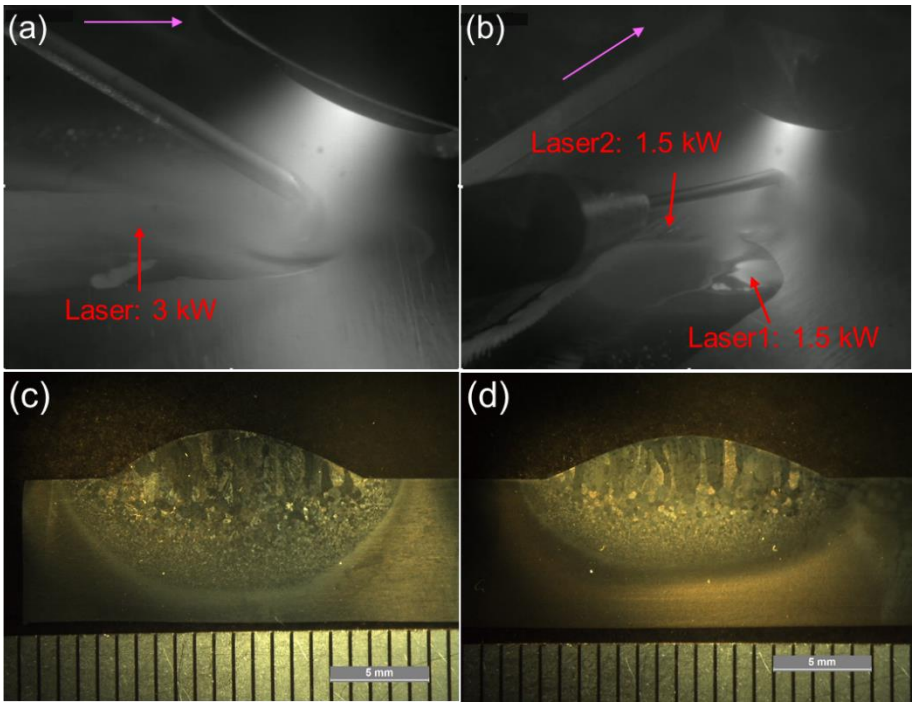


Figure 5-23 The deposition process with (a) one PTA (200 A) and one laser (3 kW), and (b) one PTA (200 A) and two lasers (1.5 kW for each laser). (c) and (d) shows the cross-section of the deposited beads obtained with (a) and (b) respectively.

5.1.4 Conclusions

1. For the same applied power, more power can be absorbed directly by the wire from the power source in the PTA process compared to that in the laser process, giving a higher deposition rate. A higher deposition rate can be achieved for the PTA-laser hybrid process compared to the PTA and laser processes alone. Compared to the laser process, the high deposition

rate of the hybrid process is attributed to the combination of the PTA and the laser. Compared to the PTA process, the higher deposition rate is attributed to the extended energy distribution and melt pool size of the hybrid process, allowing higher melting rates for the wire.

2. The deposition rate in the PTA process is limited by keyhole formation, whereas in the hybrid process the range could be significantly expanded by the addition of the laser power. This is due to the lower arc current and hence arc pressure in the hybrid process for the same overall power input.
3. The tolerance to wire positioning of the hybrid process is increased compared to the WLAM process due to the PTA melting the wire.
4. The optimum configuration for the PTA-laser hybrid AM process is PTA leading with the wire fed from the front, giving a stable deposition process as well as a good bead appearance.
5. The separation distance between the laser and arc is very important. Too short distance increases the likelihood of damage of the plasma torch whilst too excessive distance results in narrowing and in certain cases separation of the melt pool into two.
6. The PTA-laser hybrid process has limitations in terms of deposition process efficiency leading to a high remelting ratio. This is due to there being too much energy on the deposit centreline. To overcome this, a new concept of using a MES was introduced with two laser sources placed either side and just behind the PTA. With this concept, the remelting ratio was significantly improved.

5.1.5 Acknowledgement

Chong Wang would like to express his gratitude to Welding Engineering and Laser Processing Centre (WELPC) of Cranfield University as well as China Scholarship Council (No. 201706450041) for funding his research studies. The research was also supported by EPSRC funding NEWAM (EP/R027218/1). The authors also would like to thank John Thrower, Nielsen Flemming, Nisar Shah, Steve Pope, and Tracey Roberts for their technical support. In addition, special appreciation goes towards Dr. Jan Hönnige for designing the setup.

5.1.6 References

[1] T. DebRoy, H.L. Wei, J.S. Zuback, T. Mukherjee, J.W. Elmer, J.O. Milewski, A.M. Beese, A. Wilson-Heid, A. De, W. Zhang, Additive manufacturing of metallic components – Process, structure and properties, Prog. Mater. Sci. 92 (2018) 112–224.

[2] X. Guan, Y.F. Zhao, Numerical modeling of coaxial powder stream in laser-powder-based Directed Energy Deposition process, Addit. Manuf. 34 (2020) 101226.

[3] A. Singh, S. Kapil, M. Das, A comprehensive review of the methods and mechanisms for powder feedstock handling in directed energy deposition, Addit. Manuf. 35 (2020) 101388.

[4] B. Baufeld, E. Brandl, O. Van Der Biest, Wire based additive layer manufacturing: Comparison of microstructure and mechanical properties of Ti-6Al-4V components fabricated by laser-beam deposition and shaped metal deposition, J. Mater. Process. Technol. 211 (2011) 1146–1158.

[5] D. Ding, Z. Pan, D. Cuiuri, H. Li, Wire-feed additive manufacturing of metal components: technologies, developments and future interests, Int. J. Adv. Manuf. Technol. 81 (2015) 465–481.

[6] Z. Qi, B. Cong, B. Qi, H. Sun, G. Zhao, J. Ding, Microstructure and mechanical properties of double-wire + arc additively manufactured Al-Cu-Mg alloys, J. Mater. Process. Technol. 255 (2018) 347–353.

[7] B. Cong, Z. Qi, B. Qi, H. Sun, G. Zhao, J. Ding, A comparative study of additively manufactured thin wall and block structure with Al-6.3%Cu alloy using cold metal transfer process, Appl. Sci. 7 (2017) 1–11.

[8] K.M. Taminger, R.A. Hafley, Electron beam freeform fabrication for cost effective near-net shape manufacturing, NATO/RTOAVT-139 specialists' meeting on cost effective manufacture via net shape processing, Amsterdam, 2006.

[9] E. Brandl, F. Palm, V. Michailov, B. Viehweger, C. Leyens, Mechanical properties of additive manufactured titanium (Ti-6Al-4V) blocks deposited by a solid-state laser and wire, Mater. Des. 32 (2011) 4665–4675.

[10] S.W. Williams, F. Martina, A.C. Addison, J. Ding, G. Pardal, P. Colegrove, Wire + arc additive manufacturing, Mater. Sci. Technol. 32 (2016) 641–647.

[11] C. Wang, W. Suder, J. Ding, S. Williams, The effect of wire size on high deposition rate wire and plasma arc additive manufacture of Ti-6Al-4V, J. Mater. Process. Tech. 288 (2021) 116842.

[12] J. Näsström, F. Brückner, A.F.H. Kaplan, Measuring the effects of a laser beam on melt pool fluctuation in arc additive manufacturing, Rapid Prototyp. J. 25 (2019) 488–495.

[13] J. Näsström, F. Brueckner, A.F.H. Kaplan, Laser enhancement of wire arc additive manufacturing, J. Laser Appl. 31 (2019) 022307.

[14] G. Pardal, F. Martina, S. Williams, Laser stabilization of GMAW additive manufacturing of Ti-6Al-4V components, J. Mater. Process. Technol. 272 (2019) 1–8.

[15] Z. Zhang, C. Sun, X. Xu, L. Liu, Surface quality and forming characteristics of thin-wall aluminium alloy parts manufactured by laser assisted MIG arc additive manufacturing, Int. J. Light. Mater. Manuf. 1 (2018) 89–95.

[16] P.J. Modenesi, J.H. Nixon, Arc instability phenomena in GMA welding, Weld. J. (Miami, Fla). 73 (1994) 2195–2245.

[17] Q. Miao, D. Wu, D. Chai, Y. Zhan, G. Bi, F. Niu, G. Ma, Comparative study of microstructure evaluation and mechanical properties of 4043 aluminum alloy fabricated by wire-based additive manufacturing, Mater. Des. 186 (2020) 108205.

[18] D. Wu, D. Liu, F. Niu, Q. Miao, K. Zhao, B. Tang, G. Bi, G. Ma, Al–Cu alloy fabricated by novel laser-tungsten inert gas hybrid additive manufacturing, Addit. Manuf. 32 (2020) 100954.

[19] S.W. Williams, W.J. Suder, Additive manufacture, Patent, International publication number: WO 2020/038671 A1.

[20] H. Kwon, W.K. Baek, M.S. Kim, W.S. Shin, J.J. Yoh, Temperature-dependent absorptance of painted aluminum, stainless steel 304, and titanium for 1.07 μm and 10.6 μm laser beams, Opt. Lasers Eng. 50 (2012) 114–121.

[21] P.W. Fuerschbach, G.A. Knorovsky, A study of melting efficiency in plasma arc and gas tungsten arc welding, Weld. J. 70 (1991) 287–297.

[22] A.S. Salminen, V.P. Kujanpää, Effect of wire feed position on laser welding with filler wire, J. Laser Appl. 15 (2003) 2–10.

[23] W.U.H. Syed, L. Li, Effects of wire feeding direction and location in multiple layer diode laser direct metal deposition, Appl. Surf. Sci. 248 (2005) 518–524.

[24] W.U.H. Syed, A.J. Pinkerton, L. Li, A comparative study of wire feeding and powder feeding in direct diode laser deposition for rapid prototyping, Appl. Surf. Sci. 247 (2005) 268–276.

[25] S. Takushima, D. Morita, N. Shinohara, H. Kawano, Y. Mizutani, Y. Takaya, Optical in-process height measurement system for process control of laser metal-wire deposition, Precis. Eng. 62 (2020) 23–29.

[26] X. Zhang, F. Martina, J. Ding, X. Wang, S.W. Williams, Fracture toughness and fatigue crack growth rate properties in wire + arc additive manufactured Ti-6Al-4V, Fatigue Fract. Eng. Mater. Struct. 40 (2017) 790–803.

5.2 Bead shape control in wire based plasma arc and laser hybrid additive manufacture of Ti-6Al-4V

Chong Wang, Wojciech Suder, Jialuo Ding, Stewart Williams

Welding Engineering and Laser Processing Centre, Cranfield University, Cranfield, Bedfordshire, MK43 0AL, UK

Abstract: Wire base plasma transferred arc (PTA)-laser hybrid additive manufacture has the potential to build large-scale metal components with high deposition rates and near-net shape. However, the process is complex and it is not well understood on how to control the bead shape, which is essential for the deposition of different engineering structures. Therefore, in this study, the effect of different process parameters, including laser power, energy distribution between the PTA and laser, wire feed speed, travel speed, and laser beam size on the deposition process and bead shape was investigated. The results show that the optimum operating regime for the process is with the wire being melted by the PTA and the melt pool being controlled by the laser, which gives a good bead shape as well as a stable deposition process. The bead dimensions are significantly affected by the laser power and travel speed due to the large variation in energy input. The effect of wire feed speed is more complex with the bead width initially increasing to a maximum and then decreasing as the wire feed speed increases. The laser beam size has a very minor effect on the bead shape, but a small beam size will result in an irregular bead appearance due to the unstable process caused by the high power density. In addition, a procedure for controlling the bead shape in the hybrid process was proposed, and its feasibility was demonstrated by the two deposited multi-layer single-pass walls.

Keywords: Wire based additive manufacture; PTA-laser hybrid additive manufacture; Bead shape; Titanium

5.2.1 Introduction

Compared to traditional subtractive and formative manufacture methods, additive manufacture (AM) is attracting more attention due to the massive reduction of wasted material, relatively short lead-time, no mould and die needed, and high design flexibility [1-3]. In metal AM, powder or wire is commonly used as a feedstock, melted by a heat source of laser, electron beam or electric arc. Amongst different AM techniques, wire + arc additive manufacture (WAAM) is most cost-effective due to lower cost of wire compared to powder and higher efficiency of electric arc compared to laser and electron beam, and therefore is suitable for deposition of large structural parts with high deposition rate [4]. In plasma transferred arc (PTA) based WAAM, typical deposition rates of titanium are 0.4-1.2 kg/h. Much higher deposition rates can be achieved (e.g. Norsk Titanium [5]) but at the cost of low surface quality, resulting in significant material needing to be machined off. Wire based PTA-laser hybrid AM has shown the potential to build large-scale parts with high deposition rate and near-net shape. It combines the advantages of both heat sources and shows more benefits than PTA or laser deposition processes on their own. During the deposition process, a single bead is the smallest and fundamental unit of a part. Therefore, it is critical to understand how individual process parameters affect the bead shape and how to achieve targeted bead dimensions in order to achieve a reliable process for deposition of a wide range of geometries.

Wire based PTA-laser hybrid AM process has not been studied widely. So far, most of the parametric studies on bead shape using arc-laser hybrid heat sources are focused on welding applications [6-9]. However, in hybrid welding the laser beam is generally used for its deep penetration capability, and hence the laser is operated with small beam size in the keyhole regime [10]. In hybrid AM, however, the laser is used to provide additional energy and support the arc in melting the wire and spread the melt pool. Therefore, conduction regime is more appropriate in hybrid AM process. In addition, in a large number of hybrid welding cases, a much lower volume of filler wire is required compared to an AM process. Therefore, the different practical requirements between welding and AM lead to

different optimum working conditions, meaning that the results obtained in a welding process might not be applicable to an AM process. To the best knowledge of the authors, no systematic study about bead shape control in arc-laser hybrid AM has been reported.

There has been a lot of effort dedicated to developing such process understanding in wire based arc or laser AM processes. Dinovitzer et al. [11] used a Taguchi method to study the effect of different process parameters, including wire feed speed (WFS), travel speed (TS), and current on the bead geometry in gas tungsten arc (GTA) deposition process. They concluded that the bead width decreased whilst the bead height increased with the increase of WFS. The TS had a major effect on bead width but a minor effect on bead height. In addition, the bead width increased with increasing current. Such process understanding is required to develop process algorithms for the deposition of engineering parts. However, the selected process window was quite narrow (e.g. current ranged only from 50 to 59 A) in their study. Martina et al. [12] investigated the PTA deposition of titanium for a much wider range of parameters (e.g. current ranged from 120 to 300 A). They found that the effective wall width increased with increasing current and decreasing TS, and the layer height increased with increasing WFS and decreasing current. In addition to arc based deposition processes, bead shape control in laser wire deposition process was also studied. Schulz et al. [13] achieved process maps using a semi-analytical approach to study the bead width as a function of WFS, laser power, and laser intensity distribution in laser wire deposition process and achieved similar results as described in arc based processes in Refs. [11,12]. In addition, they reported that the process was sensitive to the ratio of WFS to TS, where a low ratio led to the formation of droplets and process instabilities. Abioye et al. [14] developed a process map to predict the process characteristics and bead geometry in laser wire deposition process and achieved the relationship between the input parameters (WFS, TS, and laser power) and the resulting bead properties (contact angle, width-height aspect ratio, and dilution ratio). Mok et al. [15] studied the influence of laser power, TS, and WFS on the bead shape, and claimed that

the bead width was mainly determined by laser power whilst the bead height was affected more significantly by TS than by laser power.

Similar work needs to be done for the wire based PTA-laser hybrid AM process to achieve desired bead shapes for the deposition of complex components. It is known that WFS and TS are two of the most critical process parameters that need to be considered to control the bead shape. In addition, the energy is provided by both the PTA and laser in the hybrid AM process, which contribute to the melting of wire and spread of melt pool. Therefore, the influence of both heat sources needs to be considered. Nevertheless, there are different operating ranges for the two heat sources. For example, in a PTA deposition process, a keyhole can be formed at high current levels caused by high arc pressure, which can result in defect formation [16], whilst excessive power density in a laser based process can lead to vaporisation and melt pool instabilities. Therefore, in the hybrid process, for a given total power input the process stability and the bead shape will vary depending on the ratio of arc power to laser power. However, how these parameters affect the deposition process and the bead shape is not understood. Also, a procedure for selecting different process parameters needs to be developed to provide references for controlling the bead shape in the PTA-laser hybrid AM process.

In this study, the effect of different process variables, including laser power, the ratio of arc power to laser power, WFS, TS, and laser beam size on the bead shape formation of Ti-6Al-4V in wire based PTA-laser hybrid AM process was studied systematically. The goal was to understand the effect of each process parameters on the bead shape and to develop a procedure for the selection of process parameters to achieve a targeted bead shape in the hybrid deposition process.

5.2.2 Experimental procedure

5.2.2.1 Materials and setup

The base material and wire used was Ti-6Al-4V. The diameter of the wire was 1.2 mm, and the dimensions of the substrate were 300 mm × 200 mm × 7 mm.

Before deposition, the substrate was first ground and then cleaned with acetone to remove any surface contamination. Figure 5-24 shows the experimental setup for the wire based PTA-laser hybrid AM system. The PTA was generated by a EWM Tetrix 552 power supply. Pure argon was used for both shielding gas (flowrate: 8 L/min) and plasma gas (flowrate: 0.8 L/min) for the plasma torch. An AMV 4000 arc monitor was connected to the plasma arc power supply to recorder the arc voltage and arc current. An IPG fibre laser with a wavelength of 1070 nm and a maximum power of 8 kW was used. The laser beam used in this study was defocused (i.e. out of the focal position, see Figure 5-25). The laser head was inclined at an angle of 30° to prevent back reflection. The wire was fed using a Dinse wire feeder. A 6-axis Fanuc robot with mounted plasma torch and laser head was used to control the deposition path. The experiments were conducted in a flexible tent enclosure filled with pure argon. During the deposition, the oxygen level in the tent was controlled to be below 500 ppm as verified by a PurgEye 600 oxygen analyser. A CMOS process camera (Xiris XVC-1000) was fixed perpendicular to the travel direction to monitor the melt pool behaviour and metal transfer process.

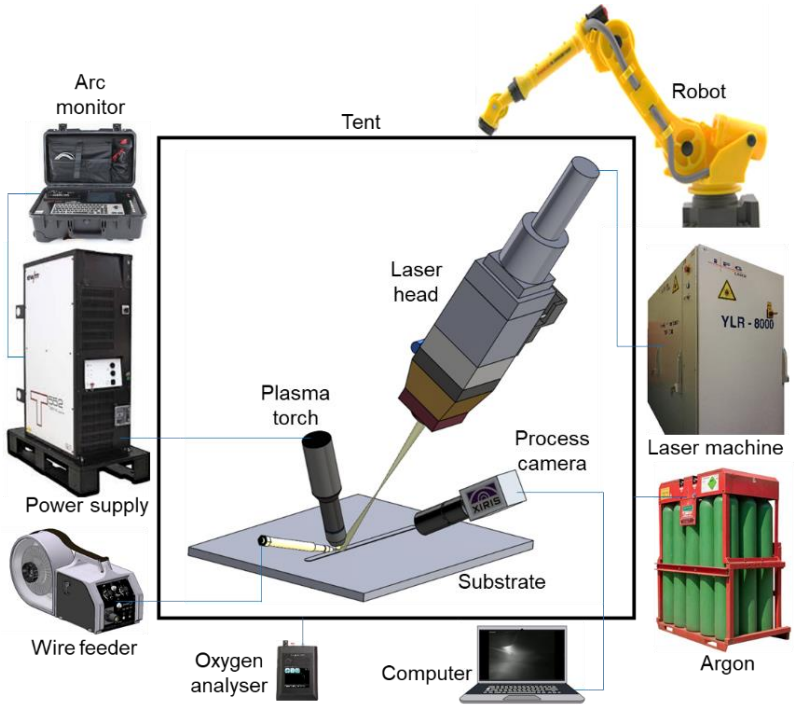


Figure 5-24 Experimental setup for the wire based PTA-laser hybrid AM system.

Figure 5-25 schematically shows the configuration used, which is the optimum for the hybrid deposition process according to Section 5.1, allowing high process tolerance and high deposition rate. In this configuration, the wire was irradiated by the PTA and the laser was placed behind the PTA. The plasma torch was positioned with a stand-off distance of 8 mm and inclination angle of 20° to ensure enough access for the wire and avoid laser reflection. The wire feeding angle was 15°. The distance (d_1) between the wire tip and the substrate was 2 mm, whilst the separation distance (d_2) between the PTA and the laser was 10 mm.

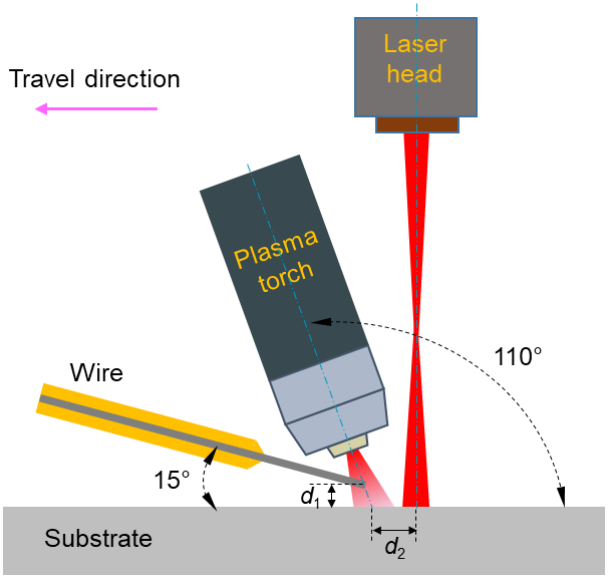


Figure 5-25 Configuration for the wire based PTA-laser hybrid deposition process (side view).

5.2.2.2 Methods

The bead shape was characterised by two features, which are bead width and bead height, as illustrated in Figure 5-26. In the first experiment, the effect of laser power on bead shape was investigated. The laser power was increased from 1 to 7 kW with an increment of 2 kW at constant other conditions, as shown in Table 5-5 (case 2 to case 5). In addition, a deposit just with PTA and without any laser was conducted as a reference (case 1, Table 5-5).

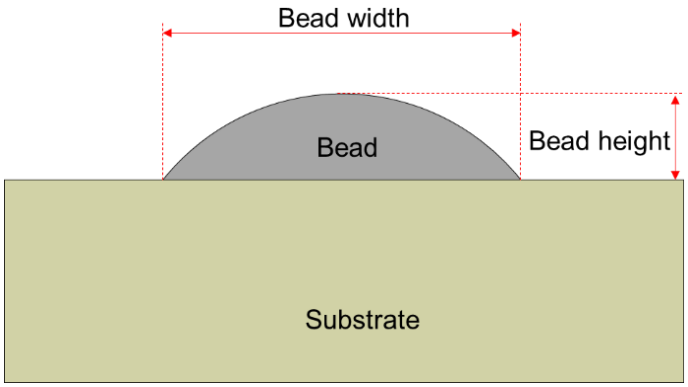


Figure 5-26 Schematic diagram of the cross-section showing the bead width and bead height.

In the next experiment, the effect of the ratio of arc power to laser power on the bead shape was investigated (case 6 to case 11, Table 5-5). The laser power was increased from 0 to 5 kW, whilst the arc power was reduced from 8 to 3 kW, maintaining the total power input constant at 8 kW. The output power of the PTA was calculated based on applied voltage and current, measured by the arc monitor. To study the effect of WFS on bead shape, the WFS was increased from 2 to 6 m/min with an increment of 1 m/min (case 12 to case 16, Table 5-5). Also, to study the effect of TS on bead shape, the TS was increased from 4 to 12 mm/s with an increment of 2 mm/s by keeping other parameters fixed (case 17 to case 21, Table 5-5).

To study the effect of laser beam size on bead shape, the laser beam diameter was increased from 2 to 12 mm with an increment of 2 mm (case 22 to case 27, Table 5-5). In addition, some deposits with different laser beam diameters (5, 12, and 15.6 mm) were conducted at different laser powers.

In addition, two multi-layer single-pass walls with the same bead shape but different deposition rates were deposited to prove that the bead shape in the hybrid process can be controlled according to a proposed procedure.

After deposition, some beads and the two single-pass walls were cross-sectioned, hot mounted, ground, polished, and etched in Kroll's reagent to check their properties (e.g. profile and remelting region).

Table 5-5 Process parameters used to study the effect of each parameters on the bead shape.

Parametric study	Case	Arc current (A)	Arc power (kW)	Laser power (kW)	WFS (m/min)	TS (mm/s)	Laser beam diameter (mm)
Laser power	1	200	4.8	0	4	4.5	12
	2	200	4.8	1	4	4.5	12
	3	200	4.8	3	4	4.5	12
	4	200	4.8	5	4	4.5	12
	5	200	4.8	7	4	4.5	12
Ratio of arc power to laser power	6	276	8	0	4	4.5	12
	7	254	7	1	4	4.5	12
	8	230	6	2	4	4.5	12
	9	205	5	3	4	4.5	12
	10	176	4	4	4	4.5	12
	11	143	3	5	4	4.5	12
WFS	12	200	4.8	3	2	4.5	12
	13	200	4.8	3	3	4.5	12
	14	200	4.8	3	4	4.5	12
	15	200	4.8	3	5	4.5	12
	16	200	4.8	3	6	4.5	12
TS	17	200	4.8	5	4	4	12
	18	200	4.8	5	4	6	12
	19	200	4.8	5	4	8	12
	20	200	4.8	5	4	10	12
	21	200	4.8	5	4	12	12
Laser beam size	22	200	4.8	5	4	4.5	2
	23	200	4.8	5	4	4.5	4
	24	200	4.8	5	4	4.5	6
	25	200	4.8	5	4	4.5	8
	26	200	4.8	5	4	4.5	10
	27	200	4.8	5	4	4.5	12

5.2.3 Results and discussion

5.2.3.1 Different process parameters on bead shape

5.2.3.1.1 Effect of laser power

Figure 5-27 shows the deposition process and the resulting cross-sections of the beads obtained with different laser powers. The corresponding bead dimensions are plotted in Figure 5-28. It can be seen that initially the bead was narrow and tall with only PTA (i.e. laser power of 0 kW). The bead shape did not change significantly (bead width increased from 7.23 to 7.45 mm) with an extra 1 kW laser power, suggesting this laser power was not high enough to expand the melt pool in the transverse direction. It is worth mentioning that because this WFS was relatively high, close to the limit for this current, the first two macrographs exhibited low remelting into the substrate, as almost the entire arc power was utilised for melting the wire. When the laser power was increased from 1 to 3 kW, the melt pool became much wider, leading to a sudden increase in bead width (Figure 5-28a). The melt pool became wider and shallower remarkably with a further increase of laser power to 7 kW. As for the bead height, it decreased constantly due to a fixed deposition rate (controlled by WFS), as shown in Figure 5-28b.

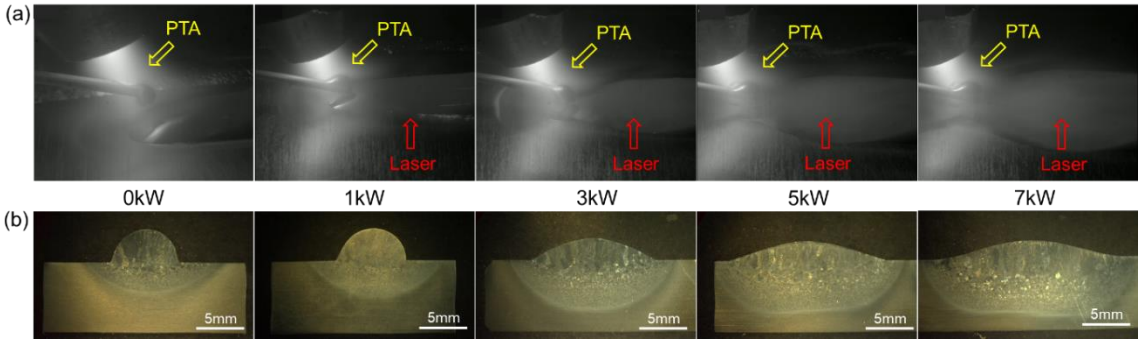


Figure 5-27 The effect of laser power on (a) deposition process, and (b) bead shape with a constant arc power of 4.8 kW.

It also can be seen from Figure 5-27b that the remelting into the substrate increases with the increase of laser power. In particular, at a laser power of 5 and 7 kW, the penetration depth was very high. This leads to remelting of several

layers lying below the layer being deposited during the deposition process. Such a process will result in low deposition process efficiency and high distortion, as revealed in Section 5.1. Therefore, in this case a laser power of 3-5 kW is optimum, and then further increase will cause too much remelting.

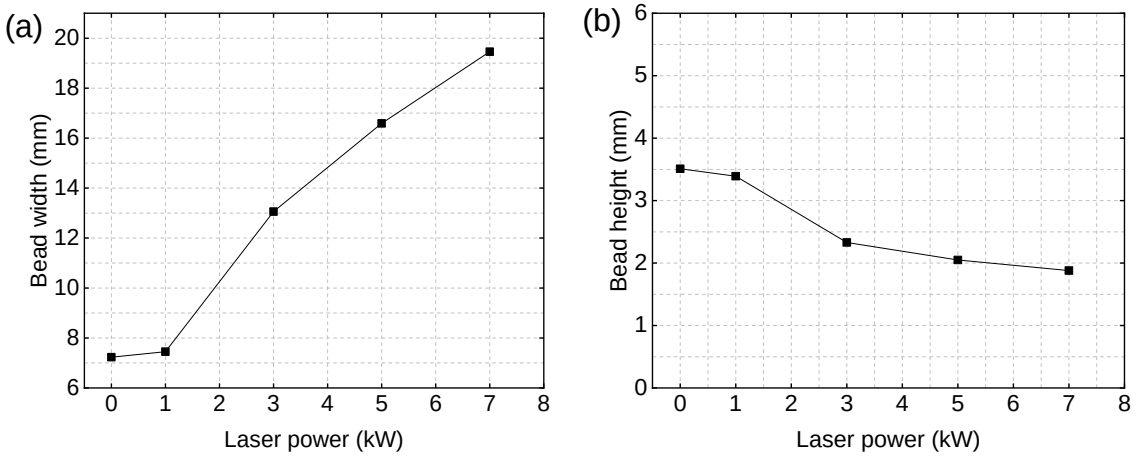


Figure 5-28 The effect of laser power on (a) bead width, and (b) bead height. All the parameters used are shown in Cases (1-5) of Table 5-5.

5.2.3.1.2 Effect of ratio of arc power to laser power

Figure 5-29 shows the deposition process with different ratios of arc power to laser power. It is known that the arc pressure increases with increasing arc current due to the increased electromagnetic force [16]. When the arc power (mainly controlled by current) was set to 8 kW, the high arc pressure caused a large depression in the melt pool (Figure 5-29a). The depression became smaller and then disappeared as the arc power reduced, as shown in Figure 5-29(b-e). However, when the arc power was too low (Figure 5-29f), the wire could not be fully melted by the PTA and stabbed the melt pool, which induced oscillations in the melt pool. If the wire reaches the melt pool, it takes excessive heat from the melt pool, reducing the melting efficiency and in extreme cases can lead to misalignment of the wire [16].

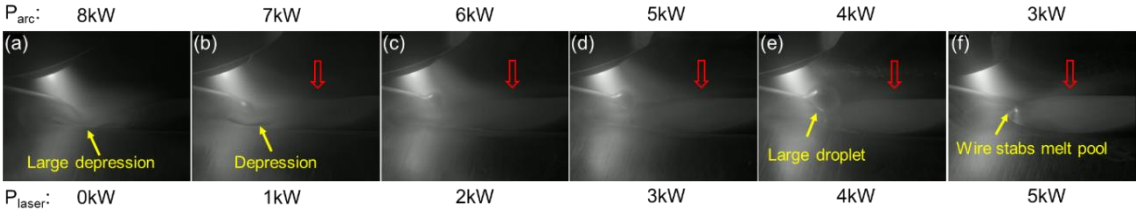


Figure 5-29 The deposition processes with different ratios of arc power to laser power at a constant total applied power of 8 kW. Red arrows indicate the laser positions.

Figure 5-30 shows the bead dimensions obtained with the processes as presented in Figure 5-29. The bead becomes wider and shallower as the ratio of arc power to laser power reduces. This is because the reducing arc power and increasing laser power cause less depression in the melt pool, which changes the energy source profile, leading to a change in bead shape. When the arc power is high, high depression results in a three-dimensional energy source profile with relatively low energy at the surface, leading to a narrow bead. As the arc power reduces and laser power increases, the depression reduces and finally disappears. Consequently, the energy source goes shallower and becomes a two-dimensional surface energy source. This results in more energy at the surface and leads to lower penetration and wider bead. To compensate for the increased bead width, the bead height decreases constantly according to the conservation of mass (Figure 5-30b). It has been shown in the literature that the bead shape affects the surface quality of deposited parts. Wang et al. [16] described that at the same cross-sectional area, a flatter bead leads to a lower surface waviness. Although the bead becomes flatter with increasing laser power and decreasing arc power (Figure 5-30), too low arc power, at a certain point, will lead to an unstable deposition process with wire stabbing the melt pool (Figure 5-29f). Therefore, in the PTA-laser hybrid deposition process, it is desired that when the arc power is just enough to melt the wire and the laser power is adjusted to control the melt pool width, but not too high thus to avoid excessive remelting into the underlying layers.

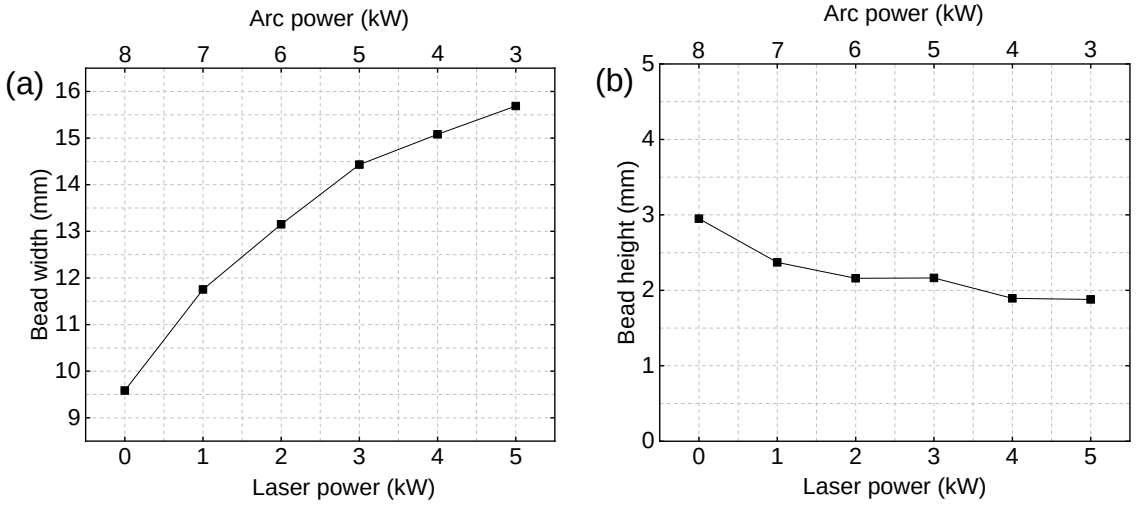


Figure 5-30 The effect of the ratio of arc power to laser power on (a) bead width, and (b) bead height. All the parameters used are shown in Cases (6-11) of Table 5-5.

5.2.3.1.3 Effect of wire feed speed

Figure 5-31 shows the deposition processes with different WFSs. When the WFS was low (2 m/min, Figure 5-31a), the wire was fully melted even without reaching the centre of arc column. The arc pressure induced a depression in the exposed workpiece surface. As the WFS increased from 3 to 4 m/min (Figure 5-31b and 5-31c), the wire could no longer be melted immediately at the edge of the arc column and started protruding to the opposite side, shielding the workpiece and dispersing the plasma force. Hence the depression gradually decreased and eventually disappeared at the WFS of 4 m/min. However, when the WFS reached 5-6 m/min, the wire could no longer be melted entirely by the PTA and reached the laser-generated melt pool (Figure 5-31d and 5-31e).

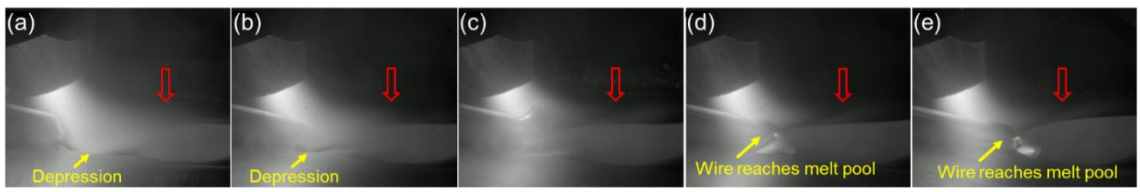


Figure 5-31 The hybrid deposition processes at different WFSs: (a) 2 m/min, (b) 3 m/min, (c) 4 m/min, (d) 5 m/min, and (e) 6 m/min. Red arrows indicate the laser positions.

Figure 5-32 shows the bead width and bead height as a function of WFS. It can be seen that the bead width rises first and then declines as the WFS increases (Figure 5-32a). A similar result was obtained in the PTA deposition process by Martina et al. [12]. However, the authors did not explain this phenomenon. Wang et al. [16] studied the effect of WFS on bead shape in the PTA deposition of Ti-6Al-4V, and also achieved a similar result. They stated that the increase of the bead width was attributed to the improved melting efficiency caused by lower thermal conduction of wire as compared to the workpiece. The reduction of bead width was attributed to the excessive heat taken from the melt pool by the wire. As for the bead height, it constantly increases due to the increased feeding rate, as shown in Figure 5-32b. It should be mentioned that the largest bead width was obtained at the WFS of 4 m/min, where the arc power is just enough to fully melt the wire (Figure 5-31c). This confirms the conclusion obtained in Section 5.2.3.1.2 that in the PTA-laser hybrid AM process the arc power is optimum when it is just sufficient for melting the wire provided no significant depression is instigated in the melt pool. In general, there is a small effect of WFS on the bead width (8% variation, Figure 5-32a), depending on whether the wire is melted directly by the PTA or it needs some extra heat from the laser-generated melt pool.

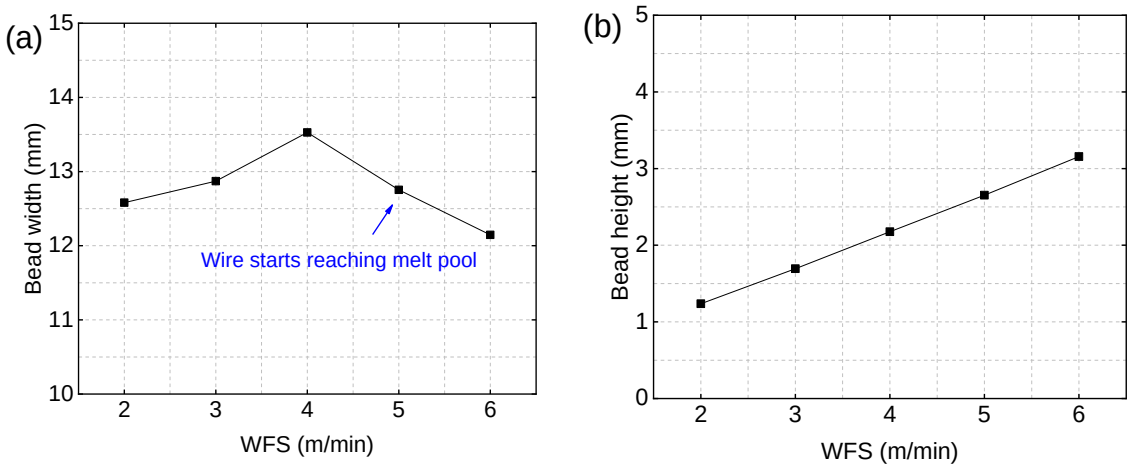


Figure 5-32 The effect of WFS on (a) bead width, and (b) bead height. All the parameters used are shown in Cases (12-16) of Table 5-5.

5.2.3.1.4 Effect of travel speed

Figure 5-33 shows the deposition processes at different TSs. It can be seen that the wire could be fully melted by the PTA in all cases, meaning that the TS does not have a significant effect on the wire melting behaviour. As described in Section 5.1, this configuration is best for the PTA-laser hybrid process as the wire can be transferred into the melt pool smoothly by arc pressure and the process has high tolerance in terms of wire feeding space. Therefore, Figure 5-33 demonstrates that such a configuration is insensitive to TS.

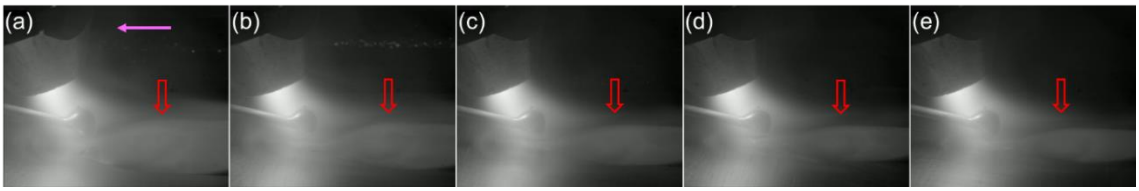


Figure 5-33 Hybrid deposition processes at different TSs: (a) 4 mm/s, (b) 6 mm/s, (c) 8 mm/s, (d) 10 mm/s, and (e) 12 mm/s. Pink arrow indicates the travel direction whilst the red arrows indicate the laser positions.

Figure 5-34 shows the bead dimensions obtained with the processes as presented in Figure 5-33. It can be seen that both bead width and bead height decrease with the increase of TS. The heat input per unit length, Λ, is inversely proportional to the TS, which is given by:

$$\Lambda = \frac{P_a}{v_t} \tag{5-9}$$

where P_a is the total applied power, and v_t is TS. Therefore, increasing the TS reduces the heat input per unit length, leading to a reduction in bead width. During the deposition, if the material vaporisation and spatter are neglected, the material deposited per unit length (i.e. cross-sectional area of the bead), A_b, can be expressed by:

$$A_b = \frac{A_w v_w}{v_t} \tag{5-10}$$

where v_w is WFS, and A_w is the cross-sectional area of the wire. If TS increases, the material deposited per unit length decreases and therefore both the bead width and bead height decrease.

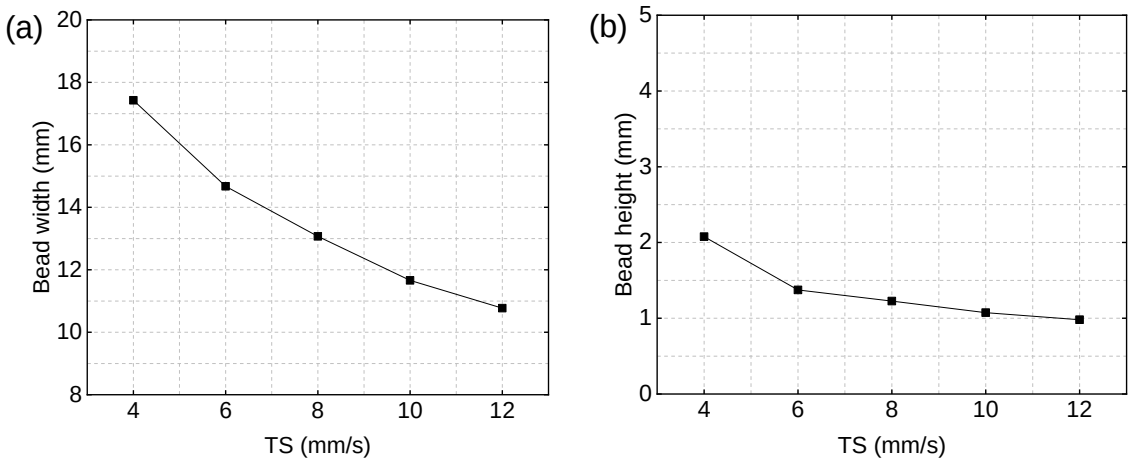


Figure 5-34 The effect of TS on (a) bead width, and (b) bead height. All the parameters used are shown in Cases (17-21) of Table 5-5.

5.2.3.1.5 Effect of laser beam size

One of the biggest benefits of laser is independent control of beam size and power, which allows the power density and beam size to be independently varied. Figure 5-35 shows the bead width as a function of laser beam diameter in the hybrid deposition process. It can be seen that the same bead width of 16.9 mm was obtained with the laser beam diameter varying from 6 to 12 mm. A slightly narrower bead width (16.1 mm) was obtained at a small laser beam diameter of 4 mm due to the energy losses by vaporisation, as indicated in Figure 5-38. By comparing Figure 5-28 and Figure 5-35, one can see that the bead shape is more responsive to the total applied power than the laser beam size. It should be mentioned that the almost unchanged bead width with the variation in laser beam diameter (Figure 5-35) only happens when the laser beam size is smaller than the melt pool that is generated. The fact that the melt pool with up to four-time wider width than the laser beam diameter (bead width of 16 mm at the laser beam diameter of 4 mm) was achieved suggests that the melt flow was dominant in the bead formation in these cases. However, if the beam size is bigger than the

natural melt pool size, then the laser beam size would control the width, as demonstrated by the multi-energy source (MES) approach in Section 5.1.

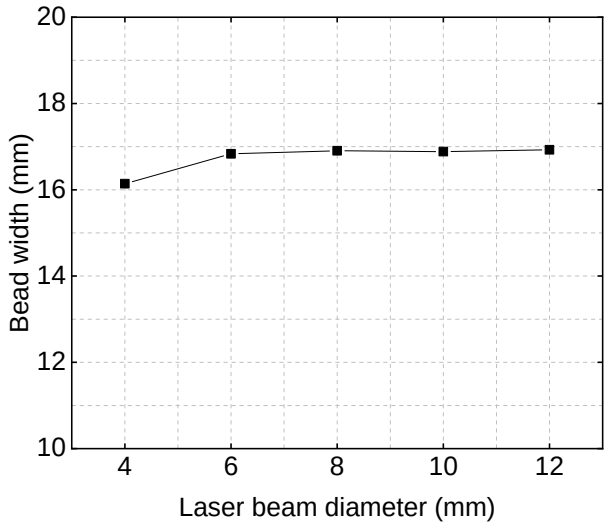


Figure 5-35 The effect of laser beam size on bead width at an arc power of 4.8 kW and laser power of 5 kW. All the parameters used are shown in Cases (23-27) of Table 5-5.

Figure 5-36 exhibits the cross-section of the corresponding beads described in Figure 5-35. It can be seen that all the penetrations on the workpiece had similar depth. Normally, the penetration depth is proportional to power density and interaction time in laser welding [17]. The power density is defined as the ratio of laser power to laser beam area which, for a circular beam, is given by:

$$E = \frac{4P_l}{\pi d_l^2} \quad \textbf{(5-11)}$$

where P_l and d_l are the laser power and laser beam diameter, respectively. The interaction time, t_i, is defined as the ratio of laser beam diameter to travel speed, which is given by:

$$t_i = \frac{d_l}{v_t} \quad \textbf{(5-12)}$$

In these cases (Figure 5-35), the laser power and travel speed were fixed. Therefore, the power density reduced quadratically and the interaction time

increased linearly as the laser beam diameter increased, meaning that the penetration depth should decrease as the beam diameter increases [18]. However, in this study there is PTA in front of the laser, which adds significant portion of heat to the melt pool, compensating for the deficiency of laser power and reducing the impact of laser beam size on penetration depth.

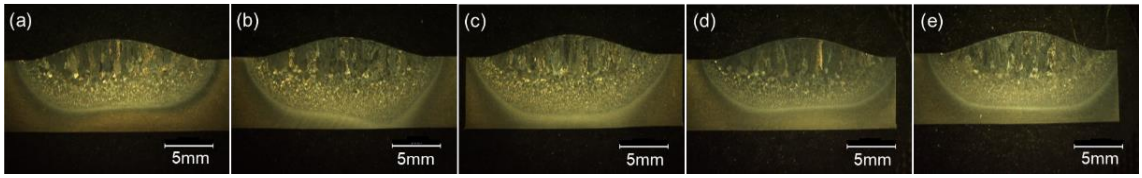


Figure 5-36 The cross-section of the beads obtained with different laser beam diameters: (a) 4 mm, (b) 6 mm, (c) 8 mm, (d) 10 mm, and (e) 12 mm.

The laser power used in the cases of Figures 5-35 and 5-36 was constant. Figure 5-37 shows the effect of laser beam size on the bead width at different laser powers. It can be seen that the laser beam size had a very little effect on the bead width even at a wide range of laser power. Specifically, at the same laser power, the difference of the bead width obtained with different laser beam sizes was always less than 1 mm.

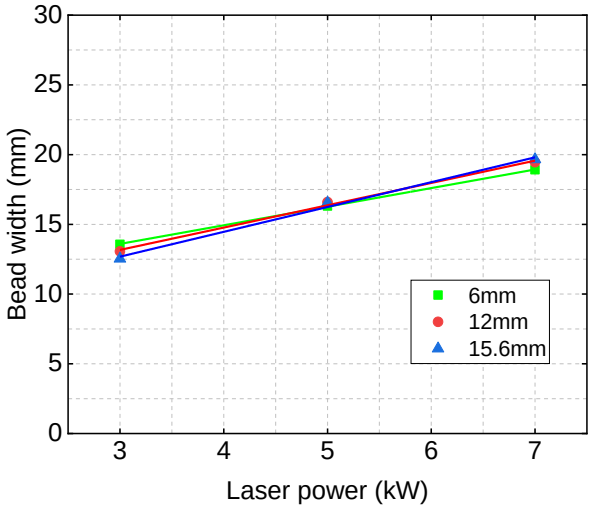


Figure 5-37 The effect of laser beam size on bead width at different laser powers.

In a laser based process, the process stability is, to a large extent, dependent on the power density. Depending on the power density, there are two different

regimes, known as keyhole and conduction. In general, the conduction regime exhibits still melt pool controlled by the thermal phenomena, whilst the keyhole regime is associated with vapour plume which interacts with the incoming laser beam and can induce agitated and dynamic melt pool [19]. Figure 5-38 shows the hybrid deposition processes at different laser beam diameters and the resulting bead appearances. It can be seen that the beam diameter had a significant effect on both the process stability and bead appearance. Much smoother beads were achieved with larger beam diameters and therefore lower power density. When the laser beam diameter reduced to 6 mm, the onset of vaporisation occurred, evident as a bright glowing spot in the laser interaction point. This vapour plume induced random oscillation in the melt pool, resulting in a less uniform bead. Specifically, the bead obtained with the laser beam diameter of 2 mm was not straight, which is unacceptable for the deposition of parts.

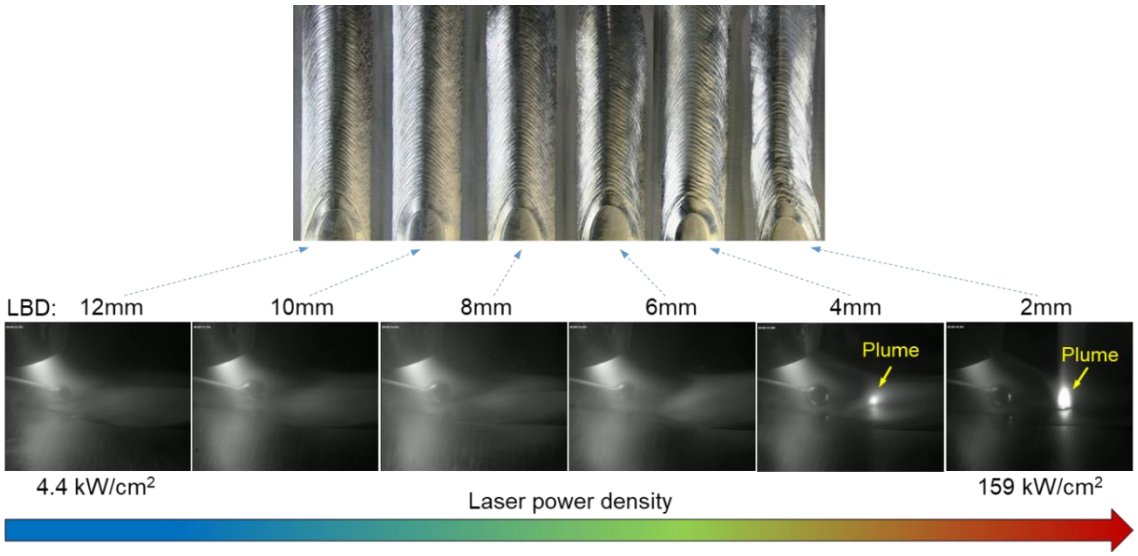


Figure 5-38 The effect of laser beam size on the deposition process and bead appearance at a constant laser power of 5 kW and arc power of 4.8 kW. Note, LBD stands for laser beam diameter.

5.2.3.2 Procedure for bead shape control

When depositing a high-value part, a specific deposition rate and bead dimensions are needed. Based on the results presented in earlier sections, a procedure for the selection of different process parameters to achieve a targeted

deposition rate and bead shape in the hybrid process is proposed as shown in Figure 5-39, which will be introduced in detail.

When the bead dimensions are given, the cross-sectional area of the bead will be fixed. In addition, the deposition rate, *R*, is expressed as:

$$R = \frac{\pi d_w^2 v_w \rho_w}{4} \quad \textbf{(5-13)}$$

where ρ_w is the density of the wire, d_w is wire diameter, and v_w is WFS. Therefore, for a given wire, the deposition rate is only dependent on the WFS. From Equation (5-10), one can see that when the cross-sectional area of the bead and the WFS are confirmed, the TS can be achieved. In the hybrid deposition process, the PTA is used to melt the wire to take advantage of its high efficiency and arc pressure, giving smooth metal transfer. As discussed in Section 5.2.3.1.2, if the arc current is too low, the wire cannot be fully melted. If the current is too high, there is a large depression formed on the substrate or underlying layers, reducing the process stability (Figure 5-29). Therefore, there is an optimum arc current for each given WFS. In fact, Wang et al. [16] obtained the maximum WFSs for different sizes of wires at different levels of current in the PTA deposition process, which provides a reference for the selection of arc current for the hybrid process. Furthermore, the laser is used to control the melt pool size in the hybrid process. Therefore, once the WFS, TS, and current are fixed, the only way to control the bead shape is to adjust the laser power (Figure 5-28). As discussed in Section 5.2.3.1.5, for a given current and laser power, the bead width changes very slightly with the laser beam size. However, the bead quality is dependent on it (Figure 5-38). Therefore, to achieve a smooth and uniform bead, an optimum laser beam size should be used. In addition, when choosing the laser beam size, the bead width needs to be taken into consideration. The laser beam should not be too small to avoid low process stability and low bead quality, and it should not be much larger than the bead width to avoid excessive energy losses. After all the parameters have been confirmed, the deposited bead will be examined to see

if it meets the targeted dimensions. If not, the laser power will be adjusted slightly until the targeted dimensions are achieved.

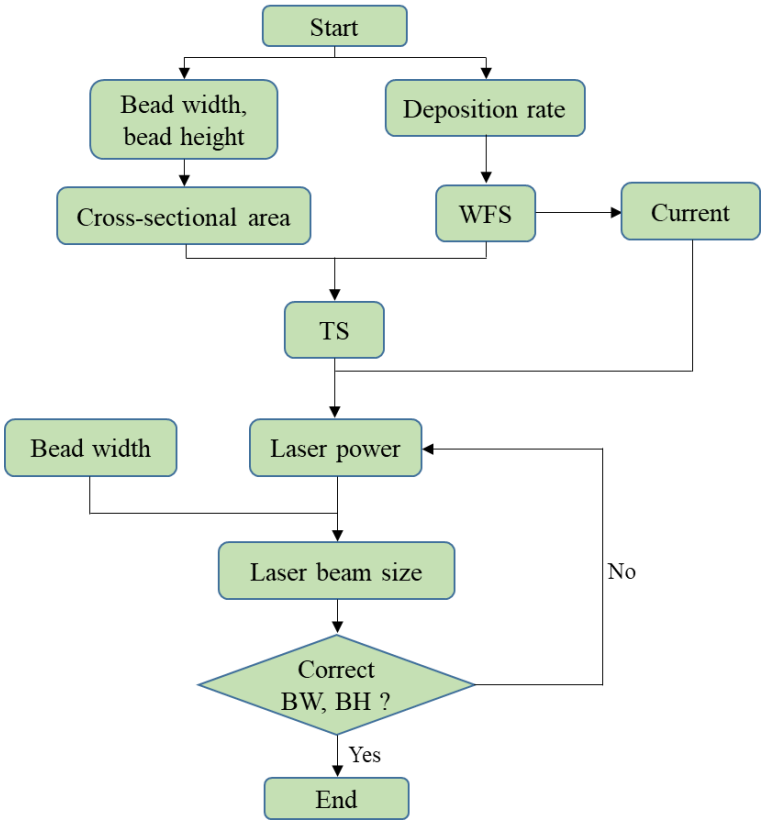


Figure 5-39 Procedure for bead shape control in wire based PTA-laser hybrid AM process. Note: BW and BH stand for bead width and bead height, respectively.

Overall, the hybrid deposition process should be operated in the most optimum regime with the PTA melting the feedstock wire and laser controlling the melt pool. Actually, increasing the TS does not have any effect on deposition rate or building time but mainly on the possible range of bead widths for a given process. In some cases, faster TSs are required to achieve narrow beads and maintain high deposition rates. An appropriate arc power needs to be selected to ensure the melting of the wire. The laser power should be optimum to provide just the right amount of heat for the required bead width and remelting ratio. Ideally, the laser beam size should be in the order of magnitude of the bead width to minimise the risk of vaporisation and unnecessary convective flow.

5.2.3.3 Multi-layer single-pass walls

To demonstrate the feasibility and repeatability of the proposed procedure, two multi-layer single-pass walls were deposited using the hybrid process. The target was to deposit two walls with the same bead dimensions (width of 12 mm and height of 1.6 mm) but different deposition rates (1.2 and 1.8 kg/h respectively). The parameters used for the two walls are listed in Table 5-6.

Table 5-6 Process parameters used for the deposition of multi-layer single-pass walls.

Parameters (unit)	Wall 1	Wall 2
TS (mm/s)	4.5	6.75
WFS (m/min)	4	6
Arc current (A)	200	270
Laser beam diameter (mm)	12	12
Laser power (kW)	3	3.5

The resulting walls are shown in Figure 5-40, and the dimensions are summarised in Table 5-7. It can be seen that both walls exhibit good surface finish. The two walls have a similar profile, with small differences in layer height and width. In both cases, the real widths are slightly lower than the target. This is caused by the difference in bead dimensions between the first layer deposited on a substrate and subsequent layers. Note that the parameters selected for this test were developed based on bead-on-plate experiments. In general, the achieved dimensions of the walls are very close to the target, which indicates that it is feasible to use this procedure to control the bead shape in the PTA-laser hybrid AM process.

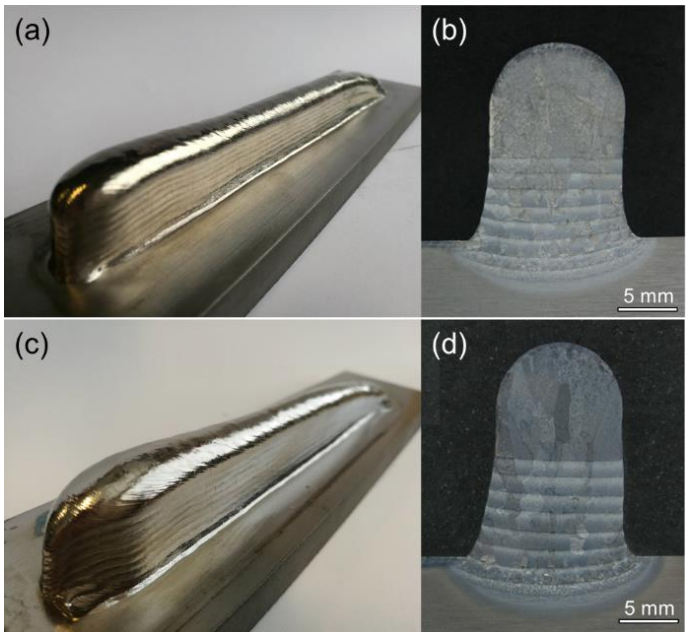


Figure 5-40 Two single-pass multi-layer walls with the same width but different deposition rates: (a) Wall 1 and (b) its cross-section at a deposition rate of 1.2 kg/h, and (c) Wall 2 and (d) its cross-section at a deposition rate of 1.8 kg/h.

Table 5-7 Features of the two multi-layer single-pass walls.

Parameters (unit)	Wall 1	Wall 2
Total layer number	10	10
Total height (mm)	17.1	18.2
Average layer height (mm)	1.7	1.8
Width (mm)	11.5	11.1
Deposition rate (kg/h)	1.2	1.8

5.2.4 Conclusions

1. The best operating regime for the PTA-laser hybrid AM process is that the wire is melted by the PTA and the melt pool is controlled by the laser. For a given WFS, the arc current is optimum when it just fully melts the wire and does not create depression or keyhole in the melt pool. Also, the laser

power should be adjusted to achieve the required bead width but not too high to avoid too much remelting on the previous layers.

2. In wire based PTA-laser hybrid AM process, the bead width is affected significantly by the laser power and TS. More specifically, at a constant arc current, the bead width increases while the bead height decreases with increasing laser power due to the increased heat input. Both bead width and height decrease with the increase of TS, which is caused by the decreased heat input and decreased deposited material per unit length.
3. The WFS has a relatively complex effect on the bead width. The bead width initially increases with increasing WFS and then decreases at a certain point. The increasing stage is owing to the increasing melting efficiency, whilst the decreasing stage is due to the wire reaching the melt pool, which takes a large amount of heat from the melt pool.
4. The laser beam size has very little effect on the bead dimensions, which suggests convection dominates the melt pool. However, it affects the process stability and the bead quality significantly. Larger beam results in a lower likelihood of vaporisation and better surface quality due to the lower power density.
5. A procedure for selecting process parameters for the achievement of required bead dimensions and deposition rate was proposed. Its feasibility was demonstrated by the deposition of two multi-layer single-pass walls with the same bead dimensions but different deposition rates.

5.2.5 Acknowledgement

Chong Wang would like to thank Welding Engineering and Laser Processing Centre (WELPC) of Cranfield University and China Scholarship Council (No. 201706450041) for funding his research studies. The authors acknowledge the funding from EPSRC (NEWAM programme: EP/R027218/1). The authors also would like to express their gratitude to John Thrower, Nielsen Flemming, and Nisar Shah for setting up the hybrid additive manufacture system, and Steve Pope and Tracey Roberts for etching the samples.

5.2.6 References

[1] T. DebRoy, H.L. Wei, J.S. Zuback, T. Mukherjee, J.W. Elmer, J.O. Milewski, A.M. Beese, A. Wilson-Heid, A. De, W. Zhang, Additive manufacturing of metallic components – Process, structure and properties, Prog. Mater. Sci. 92 (2018) 112–224.

[2] D. Herzog, V. Seyda, E. Wycisk, C. Emmelmann, Additive manufacturing of metals, Acta Mater. 117 (2016) 371–392.

[3] T. DebRoy, T. Mukherjee, J.O. Milewski, J.W. Elmer, B. Ribic, J.J. Blecher, W. Zhang, Scientific, technological and economic issues in metal printing and their solutions, Nat. Mater. 18 (2019) 1026–1032.

[4] S.W. Williams, F. Martina, A.C. Addison, J. Ding, G. Pardal, P. Colegrove, Wire + arc additive manufacturing, Mater. Sci. Technol. 32 (2016) 641–647.

[5] Norsk Titanium receives Thales Alenia Space contract to build structural additive manufactured components for orbital missions. https://www.businesswire.com/news/home/20160713005335/en/Norsk-Titanium-Receives-Thales-Alenia-Space-Contract-to-Build-Structural-Additive-Manufactured-Components-for-Orbital-Missions.

[6] S. Katayama, Y. Naito, S. Uchiumi, M. Mizutani, Physical phenomena and porosity prevention mechanism in laser-arc hybrid welding, Trans. JWRI 35 (2006) 13–18.

[7] Y.B. Chen, Z.L. Lei, L.Q. Li, L. Wu, Experimental study on welding characteristics of CO_2 laser TIG hybrid welding process, Sci. Technol. Weld. Join. 11 (2006) 403–411.

[8] M. A. Kesse, Laser-TIG hybrid welding process, Master's thesis, Lappeenranta University of Technology, 2013.

[9] C. Emmelmann, M. Kirchhoff, N. Petri, Development of plasma-laser-hybrid welding process, Phys. Procedia. 12 (2011) 194–200.

[10] X. Chen, Z. Mu, R. Hu, L. Liang, A.B. Murphy, S. Pang, A unified model for coupling mesoscopic dynamics of keyhole, metal vapor, arc plasma, and weld pool in laser-arc hybrid welding, J. Manuf. Process. 41 (2019) 119–134.

[11] M. Dinovitzer, X. Chen, J. Laliberte, X. Huang, H. Frei, Effect of wire and arc additive manufacturing (WAAM) process parameters on bead geometry and microstructure, Addit. Manuf. 26 (2019) 138–146.

[12] F. Martina, J. Mehnen, S.W. Williams, P. Colegrove, F. Wang, Investigation of the benefits of plasma deposition for the additive layer manufacture of Ti-6Al-4V, J. Mater. Process. Technol. 212 (2012) 1377–1386.

[13] M. Schulz, F. Klocke, J. Riepe, N. Klingbeil, K. Arntz, Process optimization of wire-based laser metal deposition of titanium, J. Eng. Gas Turbines Power. 141 (2019) 052102.

[14] T.E. Abioye, J. Folkes, A.T. Clare, A parametric study of Inconel 625 wire laser deposition, J. Mater. Process. Technol. 213 (2013) 2145–2151.

[15] S.H. Mok, G. Bi, J. Folkes, I. Pashby, Deposition of Ti-6Al-4V using a high power diode laser and wire, Part I: Investigation on the process characteristics, Surf. Coatings Technol. 202 (2008) 3933–3939.

[16] C. Wang, W. Suder, J. Ding, S. Williams, The effect of wire size on high deposition rate wire and plasma arc additive manufacture of Ti-6Al-4V, J. Mater. Process. Tech. 288 (2021) 116842.

[17] W.A. Ayoola, W.J. Suder, S.W. Williams, Parameters controlling weld bead profile in conduction laser welding, J. Mater. Process. Technol. 249 (2017) 522–530.

[18] W. Suder, S. Williams, Parameter selection in laser welding using the power factor concept, ICALEO, LIA, 103 (2010) 654–659.

[19] E. Goncalves Assuncao, Investigation of conduction to keyhole mode transition, PhD thesis, Cranfield University, 2012.

6 Summary, Conclusions, and Future work

6.1 Summary

It was originally hypothesised that through a thorough understanding of the PTA process and PTA-laser hybrid process, a major improvement to the DED AM, in terms of net-shape and deposition rate can be achieved. The key findings of this thesis presented in the previous chapters support this hypothesis.

Prior to examining the PTA-laser hybrid deposition process, it is necessary to have a comprehensive understanding of the limitations of using a single PTA heat source for high deposition rate applications. Therefore, Chapter 3 (Papers 1 and 2) was concerned with characterising the single PTA deposition process, in which Paper 1 investigated the traditional PTA process and Paper 2 focused on a new PTA process with the vertical wire.

It has been found that there are limitations of using a single PTA heat source to achieve high deposition rates and high process tolerance. First, during the deposition, the energy distribution between the wire and workpiece plays a significant role in determining the melting efficiency and bead shape. Too much energy distributed on the workpiece will result in high penetration depth and low melting efficiency, while too much energy distributed on the wire will result in low temperature in the melt pool and therefore a narrow bead shape. Therefore, there is a balance in terms of achieving a high deposition rate and a flat bead shape. Second, the normal way to increase the deposition rate in the PTA process is using a higher level of current. However, high current is accompanied by a keyhole in the melt pool, which is attributed to the arc pressure. As keyhole can introduce defects, the maximum deposition rate is limited by the current threshold before the keyhole formation. Third, the traditional configuration of the PTA process could not produce uniform beads at different travel directions, meaning it is not omnidirectional. In practice, this requires rotation of the wire with respect to the plasma torch when the travel direction is altered, leading to extra complications during programming the tool path.

Based on the obtained results in Paper 1 and Paper 2, optimum operating conditions have been found to mitigate these limitations for the single PTA deposition process. It was found that one of the effective ways of improving the melting efficiency (or deposition rate) is by melting the feedstock more efficiently and reducing the remelting into the workpiece. The investigation of the wire size effect on the deposition rate showed that higher melting efficiency could be achieved using a thicker wire due to the larger projected area under the arc column, leading to more effective absorptivity of energy directly from the PTA. It is recommended that the wire is fully melted by the PTA without reaching the melt pool. Otherwise, a narrower bead will be achieved due to the heat acquired by the wire from the melt pool, which is not desired to build real parts (Paper 1). In addition, the keyhole is formed due to the high arc pressure, which is mainly caused by the electromagnetic force and plasma gas force. Therefore, to reduce the likelihood of keyhole formation, some process parameters need to be optimised for the generation of lower arc pressure by reducing these two forces. For example, lower current can be used to reduce electromagnetic force, and larger copper nozzle and lower plasma gas flowrate can be used to reduce the plasma gas force (Paper 1 and Paper 2). Moreover, in order to achieve the omnidirectionality of the PTA process, a novel configuration with the vertical wire and inclined torch was examined. It has been demonstrated that although this process is not completely omnidirectional and therefore could not produce uniform beads in different travel directions without adjusting the position of the wire, it could mitigate the keyhole formation due to the lower arc pressure acting directly on the melt pool (Paper 2).

Although there are limitations of using a single PTA heat source, it is an excellent source for melting wire due to the high efficiency and high tolerance in terms of wire feeding space. However, on its own, it is hard to control deposition rate and melt pool (or thermal balance) independently. Similarly, the laser has relatively low efficiency and low tolerance for melting wire compared to the PTA, but it has higher accuracy of controlling the melt pool due to the independent control of bead size and power. However, it is also difficult to control the deposition rate

and melt pool independently with the laser heat source only. This is because with a single axisymmetric heat source, when changing heat input everything else, such as bead shape, remelting, and thermal balance will also change. Therefore, in order to decouple the deposition rate and bead shape, a hybrid AM approach with the PTA and laser heat sources was proposed.

Before the PTA-laser hybrid deposition process was developed, the interaction between the two heat sources on the material response was investigated using a FE model to better understand the hybrid process. Chapter 4 (Paper 3) presented the development, validation and utilisation of this FE model. Due to the use of a steady-state approach, this model is much more efficient compared to the commonly-used transient-state model in terms of the computational time. Also, compared to the volumetric heat source model normally used in hybrid welding, two independent surface heat source models are more suitable to describe the PTA and laser in this hybrid AM process.

It has been proved that the FE model can provide useful knowledge of the response of melt pool shape to process parameters for the hybrid AM process. For example, it was found that amongst the four variables (laser power, travel speed, laser beam size, and arc-laser separation distance) investigated, laser power and travel speed were determining parameters for the melt pool geometry (Paper 3). This has been proved in Paper 4 and Paper 5, which demonstrated that this FE model is a viable tool for better understanding the PTA-laser hybrid deposition process. In addition, this model was capable of predicting many other thermal conditions, such as cooling rate, solidification rate, and thermal gradient, in the PTA-laser hybrid process, which are important for the microstructural development and mechanical properties.

Chapter 5 (Papers 4 and 5) was then concerned with the PTA-laser hybrid deposition process, in which Paper 4 presented the development of this hybrid process and Paper 5 examined the bead shape control of this process.

For the PTA-laser hybrid deposition process, the optimum processing conditions have been obtained, and the benefits of the hybrid process over the PTA and

laser processes on their own have been demonstrated (Paper 4). In addition, using the PTA to melt the wire and the laser to control the melt pool, it was possible to control the deposition rate and bead shape independently in the hybrid process (Paper 5). This process showed high flexibility in terms of controlling the deposition rate and thermal conditions. For example, the energy ratio between both heat sources can be varied without affecting the total energy input. This means if more wire is needed but at a high cooling rate, then the arc energy can be increased along with the WFS and laser energy reduced accordingly to maintain the total energy input. In addition, by properly controlling the current, WFS, TS, laser power, etc., high deposition rate with wide and shallow bead shape can be achieved. Using the PTA-laser hybrid process, it was possible to build near-net-shape titanium parts at high deposition rates, as demonstrated by the multi-layer walls deposited. In other words, this will enable us to improve the deposition rate and consequently reduce the lead-time and overall costs.

The standard PTA-laser hybrid deposition process exhibited some limitations such as relatively low process deposition efficiency due to too much energy concentrated in the melt pool centreline. A multi-energy source (MES) approach was proposed to expand the capabilities of the hybrid process. Preliminary results from the MES study showed high promise of the process, which will be studied in the future.

Overall, the key findings of the thesis demonstrate that near-net-shape titanium parts at high deposition rates can be achieved with the PTA-laser hybrid process. The results of this thesis can also provide effective guidance for fabricating other materials such as steel, aluminium, etc. In addition, we can also apply the knowledge to the cross-disciplinary subjects, which can contribute both to academics and industry.

6.2 Conclusions

- The limits of the PTA process in terms of the deposition rate and process tolerance have been understood. It was found that a higher deposition rate can be achieved with a thicker wire because of the increased melting

efficiency. The processing conditions, such as WFS and wire feeding position, affect the melting and transfer behaviour of wire and distribution of heat between workpiece and wire, which have a significant effect on bead shape and resulting surface waviness of deposited components. The keyhole in the PTA process, observed at high currents, is primarily caused by the high arc pressure driven by electromagnetic force and plasma gas force. Therefore, it is effective to mitigate the keyhole formation by reducing these two forces.

- Using a novel PTA configuration with the vertical wire and inclined torch, the likelihood of keyhole formation was reduced significantly due to the lower vertical component of the arc pressure acting directly on the melt pool. Unfortunately, this configuration is not omnidirectional, and therefore uniform beads could not be achieved at different travel directions.
- A 3D steady-state FE model was developed, validated and used to predict the thermal behaviour in PTA-laser hybrid melting process. The effect of laser power, travel speed, arc-laser separation distance and laser beam size on melt pool geometry, cooling rate, solidification rate and thermal gradient has been studied, which provided a reference for the bead shape control and microstructural development in hybrid PTA-laser deposition process.
- A wire based PTA-laser hybrid deposition process was developed, and the optimum processing conditions were obtained. By comparing the hybrid process with the PTA and laser deposition processes on their own, it was found the hybrid process exhibited higher deposition rate and process tolerance, and allowed the independent control of deposition rate and bead shape. In addition, a MES approach was introduced to overcome the limits of the standard hybrid process, such as high remelting and low cooling rate.
- Precise control of the bead shape in the PTA-laser hybrid deposition process was possible by appropriate selection of different process variables. It was found that the best operating regime for the hybrid

process is achieved when the PTA is operated at low current to provide just enough energy to fully melt the wire and the laser is set up in conduction regime just to develop and control the melt pool but without excessive remelting to the underlying layers.

6.3 Future work

A number of areas of this research can be continued by the author or others, which are listed below:

6.3.1 FE modelling

In this work, the steady-state FE model established was capable of predicting the thermal behaviour of the hybrid PTA-laser melting process. However, the deposited material was not considered, which is needed when building a part layer by layer. Therefore, in the future, this model will be used in a multi-layer structure to investigate its feasibility in real AM application. Besides, in the current work, the same value of artificial conductivity was used for different processing conditions. In the real situation, however, different process parameters result in different fluid flow behaviour and heat convection effects. This is why the calculated melt pool geometries for some process parameters had different discrepancies compared with the experimental measurements. Therefore, in the future, artificial conductivity needs to be adjusted according to the process parameters used to achieve more accurate results. One possible way is to use the computational fluid dynamics (CFD) model to study the heat convection effect for different process parameters, and then import the obtained results in the FE model.

6.3.2 Wire preheating for higher deposition rate

In the hybrid PTA-laser AM process, the wire is melted by the PTA while the melt pool is controlled by the laser, which means that the maximum deposition rate is primarily determined by the PTA. In order to further improve the deposition rate as well as to keep a relatively high melting efficiency but without the risk of inducing keyhole by applying excessive current, external preheating of wire (e.g.

from resistance heat) could be used. With this approach, the proportion of heat used for melting of wire by the main arc would be lower, as compensated by the wire preheating system. This is likely to reduce the remelting and formation of keyhole defects caused by the PTA. Therefore, in the future, the optimum preheating temperature and arc current used for different WFSs and the benefits on deposition rate should be investigated.

6.3.3 Multi-energy source

Preliminary results from the MES approach with one PTA and two lasers showed that by precisely controlling the energy distribution, high process deposition efficiency and good bead shape could be achieved. This configuration needs to be further studied to understand the optimum processing conditions, such as the relative position between the three heat sources, the energy ratio between the three heat sources, the laser beam size, etc. Also, the bead shape control in this process needs to be investigated. In addition, to reduce the level of complexity when using two lasers and one PTA, a more compact version of MES with intelligent control of energy distribution using scanning laser optics should be investigated. This could give higher flexibility in delivering an accurate amount of energy while keeping the setup relatively simple.

6.3.4 Mechanical properties and microstructure

The microstructure and mechanical properties of the deposited parts are of great concern, as they determine the performance and structural integrity. Compared to the traditional WAAM process, the thermal conditions in the hybrid PTA-laser deposition process are different due to higher heat input and thus influence the resulting microstructure and mechanical properties. Therefore, a full characterisation of the microstructure and mechanical properties of the deposited parts produced by the hybrid process is necessary. In addition, some cold work methods, such as rolling and peening to improve the mechanical properties and reduce the texture, or some other methods, such as promoting CET by optimising thermal conditions and material compositions, need to be carried out.